

SWITCH MODE CONVERTER BASED DAMPING OF PWM CONVERTER
WITH LCL TYPE FILTER FOR GRID INTERFACE OF RENEWABLE ENERGY
SYSTEMS

A THESIS SUBMITTED TO
THE GRADUATE SCHOOL OF NATURAL AND APPLIED SCIENCES
OF
MIDDLE EAST TECHNICAL UNIVERSITY

BY
SEBAHATTİN NADİR USLUER

IN PARTIAL FULFILLMENT OF THE REQUIREMENTS
FOR
THE DEGREE OF MASTER OF SCIENCE
IN
ELECTRICAL AND ELECTRONICS ENGINEERING

DECEMBER 2014

Approval of the thesis:

**SWITCH MODE CONVERTER BASED DAMPING OF PWM CONVERTER
WITH LCL TYPE FILTER FOR GRID INTERFACE OF RENEWABLE
ENERGY SYSTEMS**

submitted by **SEBAHATTİN NADİR USLUER** in partial fulfillment of the requirements for the degree of **Master of Science in Electrical and Electronics Engineering Department, Middle East Technical University** by,

Prof. Dr. Gülbin Dural Ünver
Dean, Graduate School of **Natural and Applied Sciences**

Prof. Dr. Gönül Turhan Sayan
Head of Department, **Electrical and Electronics Engineering**

Assoc. Prof. Dr. Ahmet M. Hava
Supervisor, **Electrical and Electronics Eng. Dept., METU**

Examining Committee Members:

Prof. Dr. Muammer Ermiş
Electrical and Electronics Engineering Dept., METU

Assoc. Prof. Dr. Ahmet M. Hava
Electrical and Electronics Engineering Dept., METU

Prof. Dr. A. Nezhî Güven
Electrical and Electronics Engineering Dept., METU

Assoc. Prof. Dr. Umut Örgüner
Electrical and Electronics Engineering Dept., METU

Eyyup Demirkutlu, M.Sc.
ADULARYA Energy Electric Gen. and Mining Inc.

Date: 04/12/2014

I hereby declare that all information in this document has been obtained and presented in accordance with academic rules and ethical conduct. I also declare that, as required by these rules and conduct, I have fully cited and referenced all material and results that are not original to this work.

Name, Last name : Sebahattin Nadir Usluer

Signature :

ABSTRACT

SWITCH MODE CONVERTER BASED DAMPING OF PWM CONVERTER WITH LCL TYPE FILTER FOR GRID INTERFACE OF RENEWABLE ENERGY SYSTEMS

Usluer, Sebahattin Nadir

M.S., Department of Electrical and Electronics Engineering
Supervisor: Assoc. Prof. Dr. Ahmet M. Hava

December 2014, 214 pages

This thesis involves design and simulation for switch mode converter based damping of three-phase *LCL*-filtered PWM converter widely used for grid-interface of renewable energy systems. The study involves the resonance damping of high power voltage source converters connected to the grid via *LCL* filters. The design is verified by means of detailed computer simulations. The study considers eliminating the resonant harmonics which results in overvoltage/current stresses and leads to the failure of the converter. Several power ratings and operating conditions are considered to provide a thorough performance evaluation of the designed system.

Keywords: Grid-connected VSC, PWM, two-level VSC, *LCL* filter, resonance of *LCL* filter, switch mode converter, filter damping, active damping, passive damping, wind energy

ÖZ

YENİLENEBİLİR ENERJİ SİSTEMLERİNİN ŞEBEKE ARAYÜZÜ İÇİN LCL TİPİ SÜZGEÇLİ PWM ÇEVİRİCİNİN ANAHTARLAMALI ÇEVİRİCİ TEMELLİ SÖNÜMLENDİRİLMESİ

Usluer, Sebahattin Nadir

Yüksek Lisans, Elektrik ve Elektronik Mühendisliği Bölümü
Tez Yöneticisi: Doç. Dr. Ahmet M. Hava

Aralık 2014, 214 sayfa

Bu tez, yenilenebilir enerji sistemlerinin şebeke arayüzünde kullanılan üç fazlı, *LCL* tipi süzgeçli darbe genişlik modülasyonu (DGM, Pulse-width Modulation, PWM) çeviricisinin tasarımını ve ayrıntılı benzetim çalışmalarını içermektedir. Bu çalışma, yüksek güçlü, gerilim kaynaklı çeviricilerin *LCL* tipi süzgeç üzerinden şebekeye bağlanması durumunda oluşan rezonansın anahtarlama çevirici temelli söndürülmesini içerir. Tasarım çalışmaları, ayrıntılı bilgisayar benzetimleri aracılığıyla doğrulanacaktır. Bu çalışmada çeviricinin arızalanıp devre dışı kalmasına yol açan yüksek gerilim/akım streslerinin kaynağı olan rezonans harmoniklerinin söndürülmesi ele alınacaktır. Bu çalışmada, tasarımı yapılan sistemin tamamıyla eksiksiz ve kapsamlı bir başarımlı değerlendirilmesini sunabilmek amacıyla çeşitli güç değeri ve farklı çalışma koşulları göz önünde bulundurulacaktır.

Anahtar Kelimeler: Şebekeye bağlı GKE, DGM, iki seviyeli GKE, *LCL* süzgeç, *LCL* süzgeç rezonansı, anahtarlama çevirici, süzgeç söndürülmesi, aktif söndürme, pasif söndürme, rüzgar enerjisi

*To My Wife
and To My Parents*

ACKNOWLEDGEMENTS

I would like to thank my supervisor, Assoc. Prof. Dr. Ahmet M. Hava for his support, encouragement, guidance, and critiques on this study throughout my graduate education.

I would like to express my sincere gratitude to my beloved wife Nurbanu for her endless love, support, and encouragements in all aspects of my life.

I express my deepest gratitude to my parents for their unconditional support and patience throughout my life.

I would like to acknowledge thanks to my friends Emre Kantar and Barış Çiftçi for their help and support.

I wish to thank to Middle East Technical University Department of Electrical and Electronics Engineering faculty and staff for their help throughout my graduate studies.

TABLE OF CONTENTS

| | |
|--|------|
| ABSTRACT | v |
| ÖZ..... | vi |
| ACKNOWLEDGEMENTS..... | viii |
| TABLE OF CONTENTS | ix |
| LIST OF TABLES..... | xiii |
| LIST OF FIGURES | xiv |
| LIST OF ABBREVIATIONS..... | xxi |
| CHAPTERS..... | 1 |
| 1. INTRODUCTION..... | 1 |
| 1.1. Background and Motivation..... | 1 |
| 1.2. Scope of the Thesis | 5 |
| 1.3. Thesis Outline | 8 |
| 2. WIND ENERGY CONVERSION SYSTEMS | 11 |
| 2.1. Introduction..... | 11 |
| 2.2. Wind Turbine Concepts | 12 |
| 2.2.1. Fixed Speed Wind Turbines | 14 |
| 2.2.2. Partial Variable Speed Wind Turbines | 15 |
| 2.2.3. Variable Speed Wind Turbines with Partial-scale Converter | 15 |
| 2.2.4. Variable Speed Wind Turbines with Full-scale Converter | 16 |
| 2.3. Grid Connection Requirements..... | 17 |
| 2.3.1. Power Quality..... | 18 |
| 2.3.2. Demands to Grid Connection | 25 |
| 2.3.3. Grid Types..... | 28 |
| 2.4. Power Converter Topologies | 32 |
| 2.4.1. Back-to-back PWM-VSI..... | 34 |
| 2.4.2. Tandem Converter..... | 36 |

| | | |
|--------|--|-----|
| 2.4.3. | Matrix Converter | 37 |
| 2.4.4. | Multilevel Converter..... | 38 |
| 2.4.5. | Resonant Converter | 40 |
| 2.4.6. | Comparison of Power Converters..... | 41 |
| 2.5. | Review of Back-to-back WECS..... | 44 |
| 2.5.1. | Requirements on the Power Converter..... | 45 |
| 2.5.2. | Determination of the Converter Topology | 48 |
| 2.6. | Cost and Efficiency Evaluation of WECS | 52 |
| 2.7. | Trends in WECS..... | 53 |
| 2.8. | Summary | 56 |
| 3. | DESIGN AND CONTROL OF GRID-CONNECTED PWM-VSI..... | 59 |
| 3.1. | System Description | 60 |
| 3.1.1. | Determination of the Switching Frequency..... | 62 |
| 3.1.2. | Determination of the Controller | 63 |
| 3.1.3. | Determination of the Grid Side Filter..... | 64 |
| 3.1.4. | Mathematical Model of the L Filter | 66 |
| 3.1.5. | Mathematical Model of the <i>LCL</i> Filter..... | 67 |
| 3.1.6. | Frequency Characteristics of the <i>LCL</i> Filter..... | 68 |
| 3.2. | Hardware Design Review..... | 73 |
| 3.2.1. | DC-link Capacitor Design Review | 73 |
| 3.2.2. | <i>LCL</i> Filter Design Review | 74 |
| 3.3. | Control Overview and Controller Design | 80 |
| 3.3.1. | Space Vector Transformations of Three-phase Systems..... | 83 |
| 3.3.2. | Phase Locked Loop | 88 |
| 3.3.3. | Current Control..... | 90 |
| 3.3.4. | DC Voltage Control..... | 98 |
| 3.4. | Stability Assessment | 99 |
| 3.5. | Summary and Conclusion | 102 |
| 4. | RESONANCE DAMPING METHODS | 105 |
| 4.1. | Natural Damping | 107 |
| 4.2. | Passive Damping | 109 |

| | | |
|----------|---|-----|
| 4.3. | Active Damping | 113 |
| 4.4. | Advanced Passive Damping..... | 118 |
| 4.4.1. | Design of Advanced Passive Damping Methods | 118 |
| 4.4.2. | Frequency Characteristics of Advanced Passive Damping Methods | 122 |
| 4.5. | Switch Mode Converter Based Damping..... | 124 |
| 4.5.1. | Design of SMCD Methods | 126 |
| 4.5.1.1. | Design of Transformer-coupled SAF Based Damping..... | 126 |
| 4.5.1.2. | Design of Directly-connected SAF Based Damping | 129 |
| 4.5.2. | Control of SMCD Methods | 131 |
| 4.5.2.1. | Control of Transformer-coupled SAF Based Damping..... | 131 |
| 4.5.2.2. | Control of Directly-connected SAF Based Damping | 132 |
| 4.6. | Summary and Conclusion | 134 |
| 5. | VERIFICATION OF DAMPING METHODS | 135 |
| 5.1. | Simulation Results of Passive Damping | 137 |
| 5.2. | Simulation Results of Advanced Passive Damping Methods..... | 140 |
| 5.3. | Power Loss and Efficiency Analyses of Passive Damping Methods..... | 148 |
| 5.4. | Simulation Results of SMCD Methods..... | 150 |
| 5.4.1. | Stability Analysis of SMCD Methods..... | 152 |
| 5.4.2. | Dynamic Load Analysis of SMCD Methods | 157 |
| 5.4.3. | Grid Current THD Analysis of SMCD Methods..... | 159 |
| 5.4.4. | Efficiency Analysis of SMCD Methods..... | 161 |
| 5.5. | Verification of SMCD Methods for 3L PWM-VSI | 161 |
| 5.5.1. | 3L 3 MW TC-SAF Compensated System under GCF | 164 |
| 5.5.2. | 3L 3 MW TC-SAF Compensated System under CCF | 166 |
| 5.5.3. | 3L 3 MW DC-SAF Compensated System under GCF..... | 168 |
| 5.5.4. | 3L 3 MW DC-SAF Compensated System under CCF..... | 170 |
| 5.5.5. | 3L 3 MW DC-SAF Compensated System under Grid Harmonic Distortion | 172 |
| 5.5.6. | 3L 3 MW DC-SAF Compensated System under Grid Unbalance..... | 175 |
| 5.6. | Summary and Conclusion | 177 |

| | |
|--|-----|
| 6. PERFORMANCE AND COST EVALUATION OF DAMPING METHODS..... | 179 |
| 6.1. Introduction | 179 |
| 6.2. Dynamic Performance Comparison | 180 |
| 6.3. Grid Current THD Comparison..... | 184 |
| 6.4. Comparison of Power Losses..... | 187 |
| 6.5. Efficiency Comparison..... | 188 |
| 6.6. Performance Evaluation | 189 |
| 6.7. Cost Evaluation | 193 |
| 7. CONCLUSION AND FUTURE WORK..... | 199 |
| REFERENCES | 207 |

LIST OF TABLES

TABLES

| | |
|---|-----|
| Table 2.1 Categories, typical characteristics, origins, and consequences of variations in the supply voltage | 19 |
| Table 2.2 Individual harmonic voltage values at the supply terminals as percent of nominal voltage, U_n | 24 |
| Table 2.3 Current distortion limits set by IEEE-STD-519 [21]..... | 31 |
| Table 2.4 Technical information on WTs and WT generators | 50 |
| Table 2.5 ABB's LV full-scale wind power converters | 51 |
| Table 2.6 IGBT electrical characteristics | 51 |
| Table 3.1 Technical information of suitable DC-link capacitors | 74 |
| Table 5.1 Parameters of the simulated 3 MW PWM-VSI..... | 135 |
| Table 5.2 Simulation parameters for TC-SAF and DC-SAF compensated 3 MW PWM-VSI..... | 152 |
| Table 5.3 Switching states for 2L PWM-VSI..... | 163 |
| Table 5.4 Switching states for 3L PWM-VSI..... | 164 |
| Table 5.5 The summary of proposed series active filters | 178 |
| Table 6.1 Parameters of the simulated 1 MW PWM-VSI..... | 180 |
| Table 6.2 Capacity factors calculated using different power levels | 192 |
| Table 6.3 Operational efficiencies of 1 MW PWM-VSI with different damping methods for various capacity factors | 193 |
| Table 6.4 Operational current harmonic distortion ratings of 1 MW PWM-VSI with different damping methods for various capacity factors | 193 |
| Table 6.5 Initial cost analysis of 1 MW PWM-VSI for various damping methods | 195 |
| Table 6.6 Annual power losses of PD, TC-SAF, and DC-SAF compensated systems for various capacity factors..... | 196 |
| Table 6.7 Return on investment calculation of SMCD methods..... | 196 |

LIST OF FIGURES

FIGURES

| | |
|---|----|
| Figure 1.1 Global cumulative installed wind capacity (<i>source</i> GWEC) | 2 |
| Figure 1.2 Block diagram of a typical wind turbine | 3 |
| Figure 1.3 Two-level PWM-VSI connected to the grid via <i>LCL</i> filter | 4 |
| Figure 1.4 Inherent resonance problem of <i>LCL</i> filter | 4 |
| Figure 1.5 Efficiency variation of (a) 1 MW and (b) 3 MW converters vs. switching frequency..... | 8 |
| Figure 2.1 The conversion of wind power to electric power in WECS [15] | 12 |
| Figure 2.2 Possible technical solutions for WECS [16] | 13 |
| Figure 2.3 Main parts of a wind turbine [17]..... | 13 |
| Figure 2.4 Schematic of a fixed speed WT with reactive power compensation and soft-start features [18]..... | 14 |
| Figure 2.5 Schematic of a partial variable speed WT with variable rotor | 15 |
| Figure 2.6 Schematic of a variable speed WT with partial-scale converter [18]..... | 16 |
| Figure 2.7 Schematic of a variable speed WT with full-scale converter [18] | 17 |
| Figure 2.8 Harmonic standards for grid integration of WTs | 23 |
| Figure 2.9 Power control characteristics of a WECS | 26 |
| Figure 2.10 Reactive power exchange for WECS in the PCC in Turkey | 26 |
| Figure 2.11 Reactive power exchange against utility voltage | 27 |
| Figure 2.12 Fault ride-through capability of grid-connected WTs [23] | 28 |
| Figure 2.13 First order equivalent of the grid | 29 |
| Figure 2.14 Development of power semiconductors in the past and in the future | 32 |
| Figure 2.15 Two-level (2L) back-to-back PWM-VSI [26]..... | 34 |
| Figure 2.16 3L back-to-back PWM-VSI [26]..... | 35 |
| Figure 2.17 Back-to-back PWM-VSIs fed by a multi-phase machine and connected in parallel [26]..... | 36 |

| | |
|--|----|
| Figure 2.18 Tandem converter topology [16]..... | 37 |
| Figure 2.19 Ideal matrix converter topology [16] | 38 |
| Figure 2.20 Multilevel converters topologies for 3L converter a) Cascaded H-bridge b) Diode clamped c) Flying capacitor | 39 |
| Figure 2.21 Natural clamped converter topology and the switch configuration [16] | 40 |
| Figure 2.22 A general design schematic of a WECS [26]..... | 45 |
| Figure 2.23 Demands to power electronics in a WT [28]..... | 46 |
| Figure 2.24 Market shares of the WT manufacturers based on the installed capacity | 48 |
| Figure 2.25 Development of wind turbines [28] | 55 |
| Figure 3.1 Full-scale WECS analyzed in this thesis..... | 60 |
| Figure 3.2 Efficiency analysis of 3 MW 2L PWM-VSI for SPWM, SVPWM, and DPWM1 methods | 63 |
| Figure 3.3 <i>LCL</i> Filter and bank of <i>LC</i> trap filters..... | 65 |
| Figure 3.4 The basic <i>LCL</i> filter configuration with short-circuited grid side..... | 68 |
| Figure 3.5 The frequency characteristics of the <i>L</i> filter and the <i>LCL</i> filter | 69 |
| Figure 3.6 Grid side voltage and current waveforms of the insufficiently damped <i>LCL</i> filter | 70 |
| Figure 3.7 Capacitor voltage waveform of the insufficiently damped <i>LCL</i> filter | 70 |
| Figure 3.8 The simple passive damping schematic | 71 |
| Figure 3.9 The extinction of resonant harmonics after the implementation of simple passive damping..... | 72 |
| Figure 3.10 Ripple attenuation rate against <i>r</i> | 78 |
| Figure 3.11 Overall control scheme of grid-connected, <i>LCL</i> filtered PWM-VSI..... | 80 |
| Figure 3.12 Two loop cascaded control structure..... | 81 |
| Figure 3.13 Stationary <i>abc</i> -frame and stationary $\alpha\beta$ -frame..... | 84 |
| Figure 3.14 Vector diagram of PWM-VSC control structure..... | 86 |
| Figure 3.15 Phase locked loop in synchronous reference frame | 88 |
| Figure 3.16 Current control using (a) converter current feedback (CCF) and (b) grid current feedback (GCF) | 91 |

| | |
|--|-----|
| Figure 3.17 PWM update methods (a) single-update with sampling at the start (b) single-update with sampling in the middle [64] | 93 |
| Figure 3.18 Double update PWM method | 93 |
| Figure 3.19 Single-phase block diagram of current control loop | 95 |
| Figure 3.20 Simplified single-phase block diagram of current control loop | 95 |
| Figure 3.21 Eight possible space vectors for a three-phase PWM-VSI..... | 96 |
| Figure 3.22 Modulation waveforms of (a) SVPWM and (b) DPWM1 | 98 |
| Figure 3.23 Block diagram of DC-link voltage control loop..... | 99 |
| Figure 3.24 Bode diagram of the undamped and passively damped <i>LCL</i> filter | 101 |
| Figure 3.25 Pole-zero diagram of the undamped and passively damped <i>LCL</i> filter | 101 |
| Figure 3.26 Voltage oriented current control of a three-phase PWM-VSI with <i>LCL</i> filter..... | 103 |
| Figure 4.1 Bode diagrams of undamped, passively damped and actively damped <i>LCL</i> filter..... | 106 |
| Figure 4.2 Block diagram of CCF control | 108 |
| Figure 4.3 Modified block diagram of CCF control | 108 |
| Figure 4.4 Simple PD structure applied on a 2L PWM-VSI | 110 |
| Figure 4.5 Simple passive damping with <i>LCL</i> filter (a) Single-phase representation (b) Block diagram representation..... | 111 |
| Figure 4.6 Bode plots of the passively damped <i>LCL</i> filter for various R_d | 112 |
| Figure 4.7 Pole-zero diagram of the passively damped <i>LCL</i> filter for various R_d ... | 113 |
| Figure 4.8 Block diagram of AD loop with the <i>LCL</i> plant | 114 |
| Figure 4.9 Block diagram of GCF with AD loop | 115 |
| Figure 4.10 Block diagram of CCF with AD loop..... | 116 |
| Figure 4.11 Pole and zero locations under GCF with AD, CCF with and without AD | 117 |
| Figure 4.12 Advanced passive damping methods (a) Type 1, (b) Type 2, (c) Type 3, and (d) Type 4..... | 119 |
| Figure 4.13 Bode plots of investigated advanced passive damping methods..... | 122 |
| Figure 4.14 Tuning of the damping capacitor value for Type 2 | 123 |
| Figure 4.15 Bode plots of advanced passive damping methods, Type 2 tuned | 124 |

| | |
|--|-----|
| Figure 4.16 Single-phase equivalent circuit of SAF compensated system..... | 125 |
| Figure 4.17 Single-phase equivalent circuit of SAF compensated system at the resonant frequency..... | 125 |
| Figure 4.18 Grid-connected 2L three-phase VSI with TC-SAF based damping..... | 126 |
| Figure 4.19 Single-phase representation of TC-SAF compensated system | 127 |
| Figure 4.20 Bode plots of TC-SAF compensated and undamped <i>LCL</i> filters..... | 128 |
| Figure 4.21 Grid-connected 2L three-phase VSI with DC-SAF based damping | 129 |
| Figure 4.22 Single-phase representation of DC-SAF compensated system | 130 |
| Figure 4.23 Bode plots of DC-SAF compensated and undamped <i>LCL</i> filters | 130 |
| Figure 4.24 Block diagram of PWM-VSI with TC-SAF..... | 131 |
| Figure 4.25 Block diagram of PWM-VSI with DC-SAF | 133 |
| Figure 5.1 2L PWM-VSI simulation model in SIMPLORER..... | 136 |
| Figure 5.2 Passively damped system steady-state waveforms | 137 |
| Figure 5.3 Activation of PD from undamped condition | 138 |
| Figure 5.4 Current and voltage waveforms during the transition from undamped to passively damped condition and vice versa..... | 139 |
| Figure 5.5 Load dynamic response of passively damped system from 20% load to rated load then to 20% load again..... | 139 |
| Figure 5.6 FFT analysis on grid current of passively damped system | 140 |
| Figure 5.7 Steady-state waveforms of advanced passive damping Type 1 | 141 |
| Figure 5.8 Steady-state waveforms of advanced passive damping Type 2 | 142 |
| Figure 5.9 Steady-state waveforms of advanced passive damping Type 3 | 143 |
| Figure 5.10 Steady-state waveforms of advanced passive damping Type 4 | 144 |
| Figure 5.11 Dynamic load response of advanced passive damping Type 1 | 145 |
| Figure 5.12 Dynamic load response of advanced passive damping Type 2..... | 145 |
| Figure 5.13 Dynamic load response of advanced passive damping Type 3 | 146 |
| Figure 5.14 Dynamic load response of advanced passive damping Type 4..... | 146 |
| Figure 5.15 Activation and deactivation of the advanced passive damping methods in the presence of resonance | 147 |
| Figure 5.16 THD performances of passive damping methods | 148 |

| | |
|---|-----|
| Figure 5.17 Power Losses of passive damping methods for various load percentages | 149 |
| Figure 5.18 Efficiencies of passively damped systems for various load percentages | 149 |
| Figure 5.19 One phase of TC-SAF simulation model | 150 |
| Figure 5.20 DC-SAF simulation model | 151 |
| Figure 5.21 Activation of TC-SAF Based System from undamped condition | 153 |
| Figure 5.22 Activation of DC-SAF Based System from undamped condition | 153 |
| Figure 5.23 TC-SAF compensated system steady-state waveforms..... | 154 |
| Figure 5.24 SIT waveforms at steady-state..... | 155 |
| Figure 5.25 Auxiliary converter output waveforms at steady-state | 155 |
| Figure 5.26 DC-SAF compensated system steady-state waveforms | 156 |
| Figure 5.27 Auxiliary converter output voltage at steady-state | 157 |
| Figure 5.28 Auxiliary DC-bus voltage waveform | 157 |
| Figure 5.29 Load dynamic response of TC-SAF compensated system from 20% load to rated load then 20% load again..... | 158 |
| Figure 5.30 Load dynamic response of DC-SAF compensated system from 20% load to rated load then 20% load again..... | 158 |
| Figure 5.31 FFT analysis of TC-SAF grid current | 159 |
| Figure 5.32 FFT analysis of DC-SAF grid current | 160 |
| Figure 5.33 THD ratings of TC-SAF compensated and DC-SAF compensated systems under various load conditions | 160 |
| Figure 5.34 Efficiency ratings of TC-SAF and DC-SAF compensated systems under various load conditions | 161 |
| Figure 5.35 3L PWM-VSI simulation model in SIMPLORER..... | 163 |
| Figure 5.36 Activation of TC-SAF on 3L PWM-VSI under GCF | 164 |
| Figure 5.37 Steady-state waveforms of TC-SAF compensated 3L PWM-VSI under GCF..... | 165 |
| Figure 5.38 Activation of TC-SAF on 3L PWM-VSI under CCF..... | 166 |
| Figure 5.39 Steady-state waveforms of TC-SAF compensated 3L PWM-VSI under CCF..... | 167 |

| | |
|--|-----|
| Figure 5.40 Activation of DC-SAF on 3L PWM-VSI under GCF..... | 168 |
| Figure 5.41 Steady-state waveforms of DC-SAF compensated 3L PWM-VSI under GCF..... | 169 |
| Figure 5.42 Activation of DC-SAF on 3L PWM-VSI under GCF for $f_{sw}=600$ Hz . | 170 |
| Figure 5.43 Activation of DC-SAF on 3L PWM-VSI under CCF | 171 |
| Figure 5.44 Steady-state waveforms of DC-SAF compensated 3L PWM-VSI under CCF..... | 171 |
| Figure 5.45 Simulation model of harmonic injection to grid voltage..... | 172 |
| Figure 5.46 Activation of DC-SAF on 3L PWM-VSI under distorted grid condition | 173 |
| Figure 5.47 Grid current and voltage of 3L 3 MW DC-SAF compensated system with CCF under distorted grid condition | 174 |
| Figure 5.48 PLL angle waveform under distorted grid condition | 174 |
| Figure 5.49 Activation of DC-SAF on 3L PWM-VSI under voltage unbalance condition | 175 |
| Figure 5.50 Grid current and voltage of 3L 3 MW DC-SAF compensated system with CCF under distorted grid condition under voltage unbalance condition..... | 176 |
| Figure 5.51 PLL angle waveform under voltage unbalance condition..... | 177 |
| Figure 6.1 Load dynamic response of naturally damped system from 20% load to rated load then to 20% load again..... | 181 |
| Figure 6.2 Load dynamic response of actively damped system from 20% load to rated load then to 20% load again..... | 181 |
| Figure 6.3 Load dynamic response of passively damped system from 20% load to rated load then to 20% load again..... | 182 |
| Figure 6.4 Load dynamic response of TC-SAF compensated system from 20% load to rated load then 20% load again..... | 183 |
| Figure 6.5 Load dynamic response of DC-SAF compensated system from 20% load to rated load then 20% load again..... | 183 |
| Figure 6.6 Grid current FFT result of naturally damped system | 184 |
| Figure 6.7 Grid current FFT result of actively damped system..... | 185 |
| Figure 6.8 Grid current FFT result of passively damped system | 185 |

| | |
|--|-----|
| Figure 6.9 Grid current FFT result of TC-SAF compensated system..... | 186 |
| Figure 6.10 Grid current FFT result of DC-SAF compensated system | 186 |
| Figure 6.11 THD comparison of damping methods under various load conditions | 187 |
| Figure 6.12 Power loss comparison of damping methods under various load conditions..... | 188 |
| Figure 6.13 Efficiency comparison of damping methods under various load conditions..... | 189 |
| Figure 6.14 (a) Power curve (b) Annual energy production and capacity factor of MWT62/1.0..... | 190 |
| Figure 6.15 Modified power curve of MWT62/1.0 | 191 |

LIST OF ABBREVIATIONS

| | |
|--------|---|
| 2L | Two-level |
| 3L | Three-level |
| AD | Active Damping |
| CCF | Converter Current Feedback |
| DPWM1 | Discontinuous Pulse-width Modulation 1 |
| EMC | Electromagnetic Compatibility |
| EMI | Electromagnetic Interference |
| ESR | Equivalent Series Resistance |
| GCF | Grid Current Feedback |
| IGBT | Insulated Gate Bipolar Transistor |
| MOSFET | Metal Oxide Semiconductor Field Effect Transistor |
| PD | Passive Damping |
| PWM | Pulse-width Modulation |
| RMS | Root Mean Square |
| SAF | Series Active Filter |
| SCC | Short-circuit Power |
| SCR | Short-circuit Ratio |
| SVPWM | Space Vector Pulse-width Modulation |
| THD | Total Harmonic Distortion |
| TSO | Transmission System Operator |
| VSC | Voltage Source Converter |
| VSI | Voltage Source Inverter |
| WECS | Wind Energy Conversion System |
| WT | Wind Turbine |

CHAPTER 1

INTRODUCTION

1.1. Background and Motivation

Wind power is a clean, free, and fast growing renewable energy source which has been used in windmills to grind grain, wind pumps to extract groundwater, and transportation using ships for centuries. After the discovery of electricity, wind power ceased to be a local energy source instead it became an energy source that can be transferred to distant areas. Nowadays, small residential or utility scale wind generation has turned out to be very popular so as to minimize the dependence of electricity production on fossil fuels.

An increased investment in wind power generation is seen from the global cumulative installed wind capacity in Figure 1.1 [1]. The cumulative installed capacity increases with an average growth rate of 26.2%/year, although the growth rate of 2013 is only 12.5%. The total installed wind capacity is almost 318 GW by the end of 2013. Moreover, global installed wind power capacity will double in five years according to Global Wind Energy Council (GWEC). Besides, governments encourage the investors by supplying grants, reducing taxes, and paying higher prices for the electricity produced from renewable energy sources. The reduced installation cost of wind turbines (WTs) over time is also very attractive.

Despite the upward trend in wind energy production, the technology used in wind turbines is not unique. A variety of designs both in control of WT and in power conversion are utilized. This makes WTs and wind energy conversion remarkable application areas. The number of academic publications on wind energy conversion and control has also increased recently due to enlarged interest on wind power.

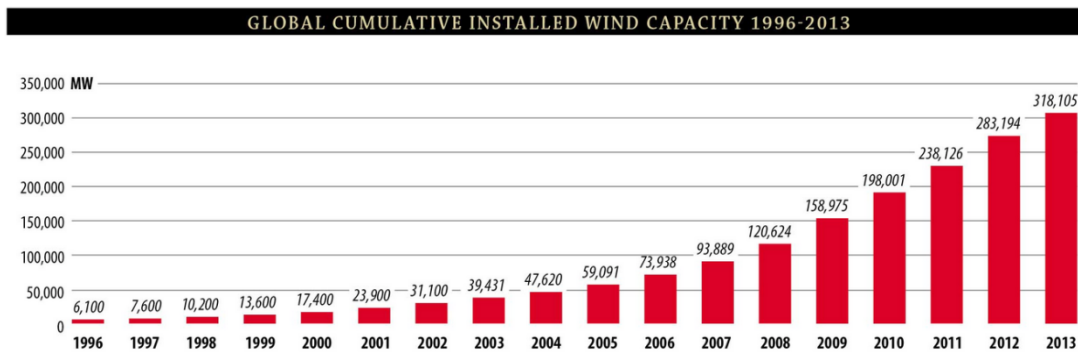


Figure 1.1 Global cumulative installed wind capacity (*source GWEC*)

Figure 1.2 demonstrates the block diagram of a WT. The conversion of wind power to the utility scale electric power is summarized with the presentation of major equipments used in WTs. The kinetic energy of the wind is converted to mechanical energy and subsequently to electrical energy by electrical generators whose rotor is connected to the blades via a mechanical shaft. The use of gearbox providing a transition from low speed to high speed is optional depending on the design of the generator. The conversion of varying frequency electric power to the fixed frequency utility interface is achieved using power electronics converters. Generator side converter and the grid side converter act together to convert the unregulated power at the generator terminals to well-regulated utility scale power. Mostly, the connection to the utility is exerted via step-up transformers. Specifically for wind turbines, the power electronics converter systems are named as wind energy conversion systems (WECS). In addition to WECS control, pitch angle of the blades is also controlled for regulation of the wind power at high wind speeds.

The use of grid-connected pulse-width modulation (PWM) voltage source inverters (VSIs) has been increasing in recent years. Especially for WECS, design economics and controllability of the system are two main factors to select the proper topology for the application. The back-to-back inverter based direct energy conversion systems meet the industrial standards and provide cost effective solutions. The most

adopted topology on the market is still two-level; although, a trend towards multilevel inverters to manage the increasing power levels is observed for wind turbines [2]. The power rating of wind turbines typically starts from 500kW and increases up to several megawatts.

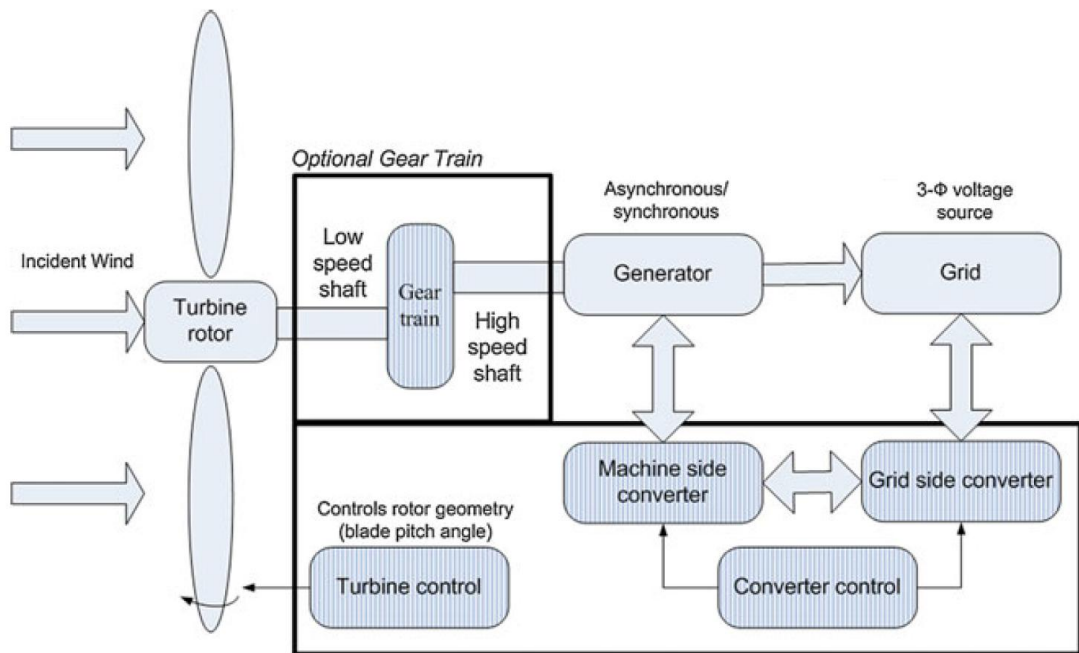


Figure 1.2 Block diagram of a typical wind turbine

Grid side harmonic filters are used at the output of the VSIs to achieve a satisfactory attenuation of switching ripples. The vast amount of PWM ripple at the carrier frequency and its multiples with the sideband harmonics in the inverter's output current is removed via grid side filters; hence, total harmonic distortion (THD) value of the grid current is minimized. Modern power electronic converters use *LCL* filters which are clearly superior to standard *L* filters in terms of size, weight, dynamic response, and PWM ripple reduction [3]-[8]. In Figure 1.3, the well-known two-level PWM-VSI topology with grid connection via an *LCL* filter is illustrated.

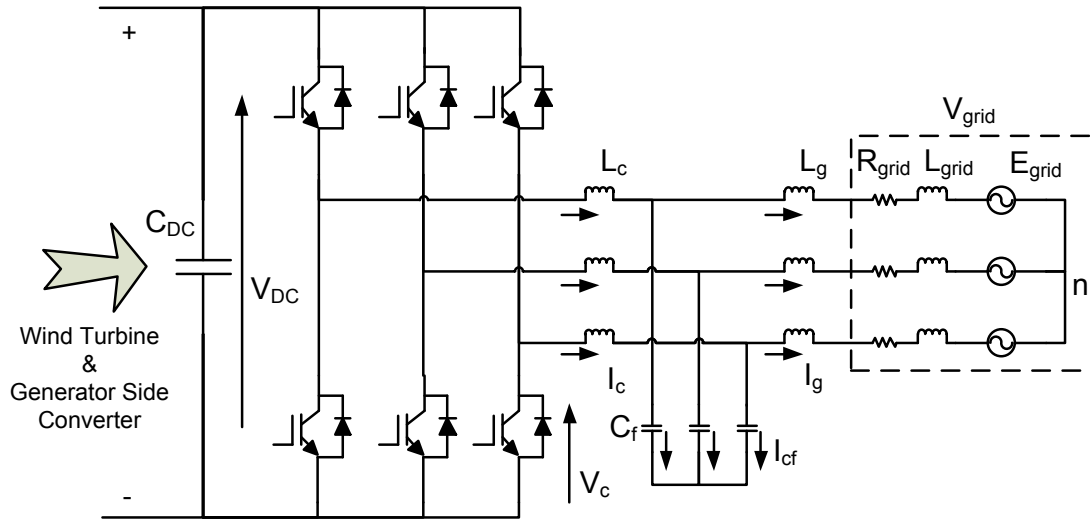


Figure 1.3 Two-level PWM-VSI connected to the grid via *LCL* filter

Despite the advantages of *LCL* filters, a resonance problem affecting the stability of the overall system constitutes a major issue which has to be dealt with. *LCL* filters are high order low-pass filters with first-order characteristics at low frequency range. The frequency characteristic of an *LCL* filter is shown in Figure 1.4.

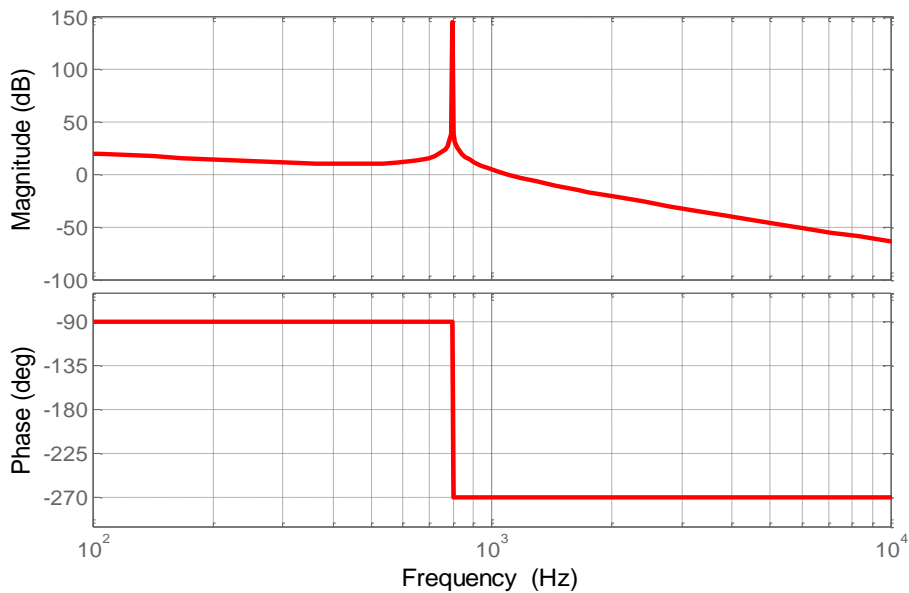


Figure 1.4 Inherent resonance problem of *LCL* filter

At the resonant frequency defined in (1.1), the ideal *LCL* filter behaves as an infinite gain amplifier for the harmonics excited by the inverter or grid originated harmonics. These undesired harmonic components at the resonant frequency should be suppressed to avoid overvoltage/current stresses and failure of the inverter. Therefore, the *LCL* filter should be damped with proper damping methods in order to operate safely.

$$f_{res} = \frac{1}{2\pi} \sqrt{\frac{L_c + L_g}{L_c L_g C_f}} \quad (1.1)$$

For high power systems, the efficiency of the grid side converter is very important. The switching frequency of the converter is limited to a few kilohertz in order to decrease the switching losses of the semiconductors hence increase the efficiency. However, passively damping the *LCL* filter's resonance by inserting resistive elements into the filter produces undesirable losses which may increase up to 2% of the converter's rated power. The losses are converted to heat and the cooling expenses of the converter raise. Besides, the efficiency target is not satisfied.

On the other hand, the low switching frequency of the converter reduces the controller bandwidth considerably. Therefore, the resonant frequency of the *LCL* filter and the switching frequency get closer. Actively damping the *LCL* filter's resonance via additional voltage/current feedback from filter capacitor or via complex state observers is not applicable due to limited phase margin of the controller.

Despite the resistive losses produced by passive damping, the resonant frequency of the *LCL* filter should be suppressed properly using passive damping as the simplest and generally applied solution for high power systems.

1.2. Scope of the Thesis

Resonance damping methods of *LCL* filter are primarily investigated in this thesis. The design of *LCL* filter and control of multi-megawatt grid side converters are also

stated throughout this study. As alternative to classical damping methods, two novel damping methods based on switch mode converters are presented and analyzed deeply. The comparison of damping methods soon to be mentioned is given to present a complete analysis on the resonance damping of *LCL* filter.

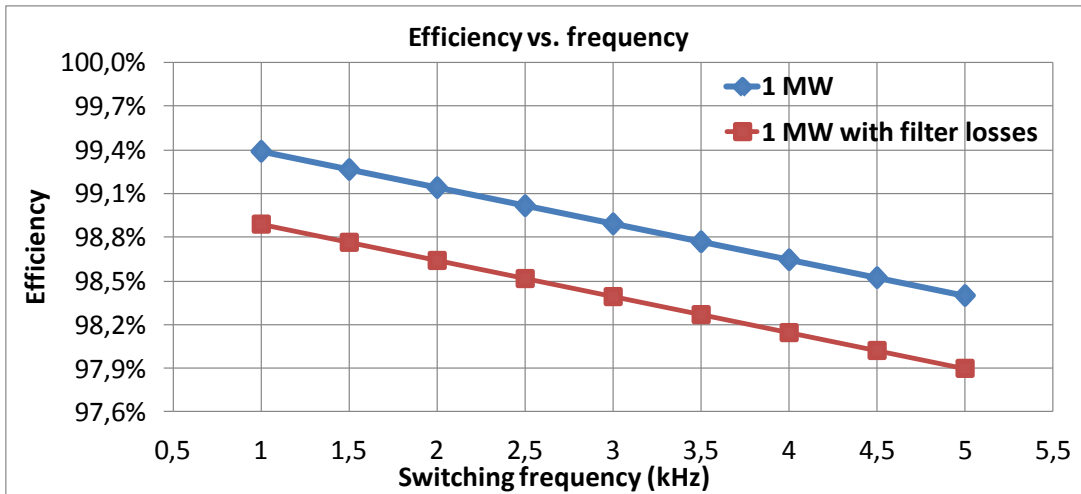
Resonance damping methods can be classified into four main categories: natural damping (ND), passive damping (PD), active damping (AD), and switch mode converter based damping (SMCD). Various studies proposing the abovementioned damping solutions have been conducted in the literature [4]-[11]. ND approaches using the converter side current feedback are applicable for small power rated inverters up to several tens of kilowatts [6], [8], [9]. Medium power inverters up to several hundred kilowatts with *LCL* line filters can be damped using AD methods [5], [9]. AD methods employ a modified current regulator via an additional feedback from the filter capacitor not to excite any harmonics around the resonant frequency owing to the high PWM carrier frequency. Nonetheless, applications involving multi-megawatt inverters allow only a few kilohertz switching frequency in order to reduce the semiconductor losses hence increase the efficiency. Consequently, the controller bandwidth is limited and the resonant harmonics cannot be controlled (or suppressed) using AD. PD methods are valid for inverters having both small and high power ratings [7], [10]. However, the losses due to PD resistors can exceed 1% of the inverter's rated power [4] and reduce the efficiency significantly. At this point, the use of SMCD methods comes in to discussion. Auxiliary PWM converters and reactive components can replace the damping resistors by reducing power losses extensively while maintaining the stability of the overall system [11], [12].

The switching frequency is a limiting factor on the efficiency target of the WECS. Figure 1.5 (a) illustrates the variation in the efficiency against switching frequency in 1 kHz - 5 kHz range for a 1 MW grid side converter. The losses due to semiconductor switching and conduction possess the majority of the losses. Apart from the semiconductor losses, the losses due to grid side filters present an important portion. Figure 1.5 shows the efficiency results obtained only by calculating the semiconductor losses and obtained by calculating both the semiconductor losses and

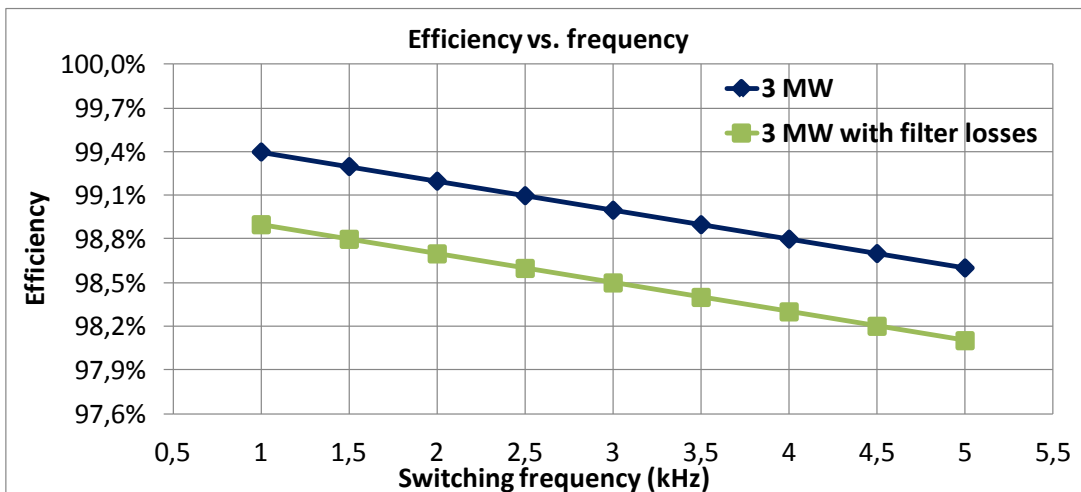
grid side filter losses. The selected converter topology is two-level and the applied PWM method is space vector PWM (SVPWM). The gate resistances are selected as default values of the loss calculating software whereas the modulation index and power factor are selected according to the specifications of the wind energy conversion given in the following chapters. At full load condition, 0.5% of the system's rated power is lost on the filter elements [13]. By assuming the filter losses constant against the frequency, approximate efficiency results are shown. Similar to Figure 1.5 (a), the variation in the efficiency against switching frequency in 1 kHz – 5 kHz range for a 3 MW grid side converter is shown in Figure 1.5 (b). It should be noted that the efficiency curves given in Figure 1.5 does not count for the passive damping losses. The calculation of passive damping losses and the effect of passive damping on the system's efficiency are presented in the subsequent chapters.

By observing the efficiency reduction due to increased switching frequency, it can be inferred that each WECS design must have a predefined efficiency target. For multi-megawatt systems, this target is set as high as 98-99% since the losses beyond 1-2% of the system brings extra cost in cooling and design. Selecting the switching frequency close to 2 kHz for the 1 MW system and around 1 kHz for the 3 MW system leads to enhanced efficiency rating hence decreased losses.

Due to limited switching frequency of high power systems, resonance damping is ensured by passive damping elements. The increased losses due to passive damping are not desired; therefore, innovative damping methods shall be applied. Design and control of novel SMCD methods are investigated in this thesis. Two distinct topologies are examined: transformer-coupled SAF (TC-SAF) based damping and directly-connected SAF (DC-SAF) based damping. A detailed analysis of these methods in terms of steady-state THD and efficiency ratings, dynamic performances, and power ratings is presented. As 3 MW being a common power rating in the wind energy market [14], SAF compensated 3 MW inverters are investigated in this study. Besides, resonance damping methods presented in this study are compared and contrasted on 1 MW PWM-VSI to depict a thorough analysis.



(a)



(b)

Figure 1.5 Efficiency variation of (a) 1 MW and (b) 3 MW converters vs. switching frequency

1.3. Thesis Outline

This thesis consists of seven chapters. First chapter introduces the background and motivation. The increasing use of wind turbines and development of power electronics in wind energy conversion systems (WECS) are stated. The difficulties in designing high power grid-connected converters are presented. The augmented use

of *LCL* filters for grid connection and the inherent resonance problem brought by *LCL* filters are also stated in the first chapter.

Chapter 2 includes an overview of WECS and grid connection requirements of the multi-megawatt wind turbines. Wind turbine (WT) topologies together with the power conversion strategies are described briefly. Power quality issues and grid codes specific to Turkish Wind Turbines Network Regulation are stated. Grid types depending on the stiffness criterion and grid current harmonics regulation are identified. Besides, commonly used power converter topologies in WTs are investigated. The pros and the cons of each topology are pointed out clearly. An expanded review on back-to-back connected converters is given. Requirements on the power converters and determining factors for the converter topology are stated. Literature review of the biggest manufacturer's WT generators and WECS is conducted. Technical data of IGBTs used in the designs throughout this thesis are given. The cost and efficiency evaluation of the present WECS are stated and new trends in WECS are discussed at the end of the chapter.

Chapter 3 presents a review on the hardware and controller design. Hardware design based on the converter efficiency and converter optimization is stated. The requirements of the converter are gathered and then the efficiency target is determined. Switching frequency and DC-link capacitor selection are mentioned. The mathematical model of the system is given and the behavior of the system is observed. The design of grid side *LCL* filter and the control of grid side converter are given. The main blocks of the controller are discussed. Space vector transformations from three-phase to two-phase signals are reviewed. The grid phase angle determination using phase locked loop (PLL) is stated. AC currents and DC voltage control loops are examined together with the tuning of the controllers. Moreover, the stability assessment of the system using pole-zero diagrams is given.

In the 4th chapter, an overview of damping methods for power converters with *LCL* line filters is given. Besides, advanced passive damping methods mostly used in high power systems are examined. Switch mode converter based resonance damping (SMCD) of high power, grid-connected, *LCL* filtered inverters are presented. The

need for alternative damping methods is described. The theories of two distinct SMCD methods, namely transformer-coupled series active filter (TC-SAF) based damping and directly-connected series active filter (DC-SAF) based damping are investigated. Mathematical models of these methods are given and the frequency responses are plotted. Moreover, control of the proposed damping methods is discussed.

Chapter 5 deals with the detailed analysis of resonance damping methods based on stability, power quality, dynamic response, and efficiency. The analysis is conducted via computer simulations on a 3 MW system. The verification and detailed performance analysis of SMCD methods are given. Dynamic load, grid current THD, and efficiency analyses on a 3 MW system are clarified and two SMCD methods are compared. The proposed methods are also verified on a three-level (3L) 3 MW system. Moreover, 3L 3 MW DC-SAF compensated system is performed under distorted and unbalanced grid conditions separately.

The comparison of natural damping (ND), active damping (AD), passive damping (PD), and novel switch mode converter based damping (SMCD) methods is conducted on a 1 MW system via computer simulations in Chapter 6. Dynamic load responses, grid current THD values for various load conditions, and total power losses are compared and contrasted. Besides, the cost and efficiency evaluation of these methods are established and a summary of the investigated damping methods is given.

Finally, in the 7th chapter, the conclusion of the thesis is presented and future works are stated.

CHAPTER 2

WIND ENERGY CONVERSION SYSTEMS

2.1. Introduction

In conventional power systems, electric power supplied by large power plants is transferred towards consumption centers over long distance transmission cables. The quality of the power is continuously monitored by control centers to regulate the power system. However, distributed generation systems including both renewable and non-renewable energy sources such as wind turbines, photovoltaic generators, wave generators, small hydro plants, and gas/steam powered combined heat and power stations are being used nowadays. A wider use of renewable energy sources in distribution networks are forecasted in the near future.

An increased attention on the wind energy conversion systems has led to significant development on power electronics in the last thirty years. The wind turbine technology started in the 1980's with a few tens of kW power capacity and multi-MW wind turbines are installed today. In the earlier works, the generators were directly connected to the grid hence wind turbines were incapable of adjusting active and reactive power and controlling the voltage and frequency. As the technological improvements on power electronics increased, the need for a controlled interface between the wind energy sources and the grid is satisfied. Therefore, the wind energy is easily transferred to the power system by means of controlling active and reactive power.

2.2. Wind Turbine Concepts

Wind power is received by specially designed blades placed on top of a tower. In modern wind turbines, the number of the blades is usually selected as three. The rotational speed of multi-MW wind turbines is typically 10-15 rpm as the tip-speed of the blades should be lower than half of the speed of sound. This means that the rotational speed decreases as the radius of the blade increases. The low speed of the blade is increased via a gearbox. The mechanical power is then converted to electrical power by means of an electric generator as shown in Figure 2.1 [15].

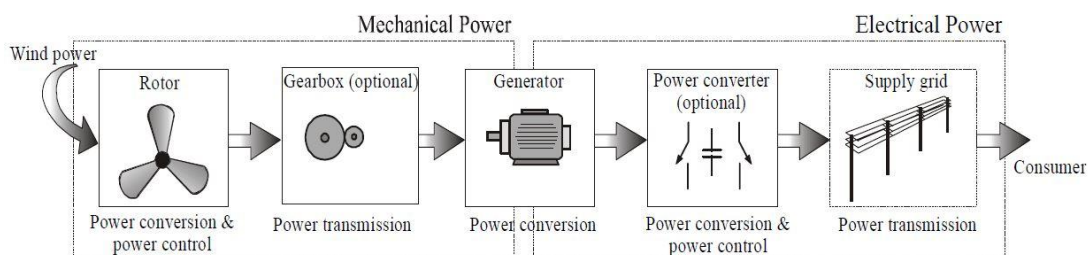


Figure 2.1 The conversion of wind power to electric power in WECS [15]

Multi-pole generators may also be used to eliminate the gearbox; however, such specially designed machines may not be effective in terms of cost. Figure 2.2 demonstrates the possible technical solutions of converting wind power to electrical power having constant voltage and frequency [16]. In today's wind turbines, the power transferred to the grid can be controlled at high wind speed. The control can be done either by active stall or pitch control. As the power generated is proportional with the cube of wind speed, the wind turbine should be shut off to protect the entire system when the wind power goes higher. The speed where the wind turbine stops generating power is named as cut-out speed. Based on the speed control and power conversion criteria, wind turbines can be classified into four groups: fixed speed wind turbine, partial variable speed wind turbine, variable speed wind turbine with partial-scale converter and variable speed wind turbine with full-scale converter.

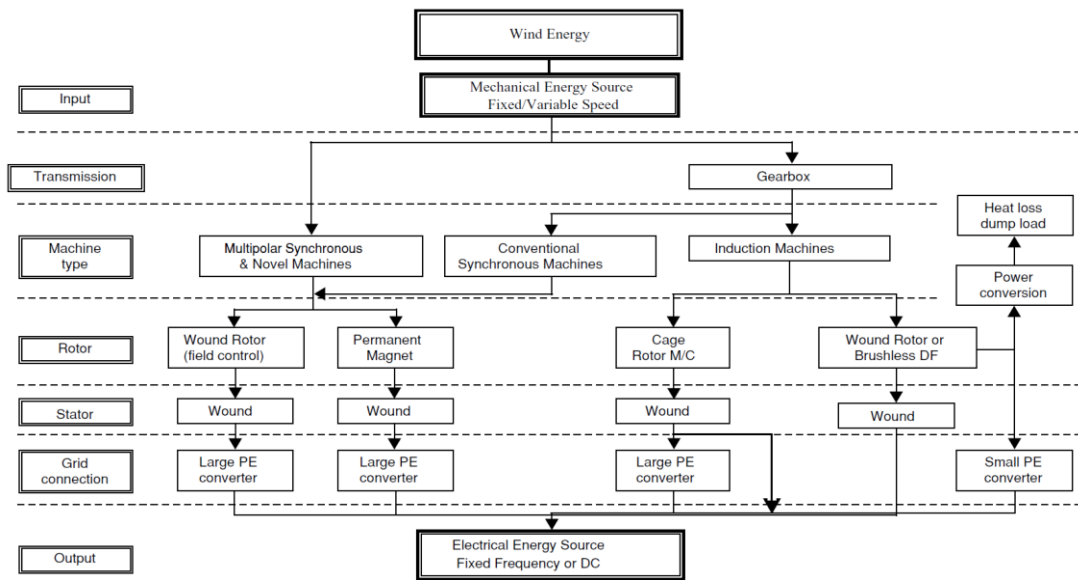


Figure 2.2 Possible technical solutions for WECS [16]

Figure 2.3 below shows the main parts of a typical variable speed wind turbine (WT) with active stall control [17].

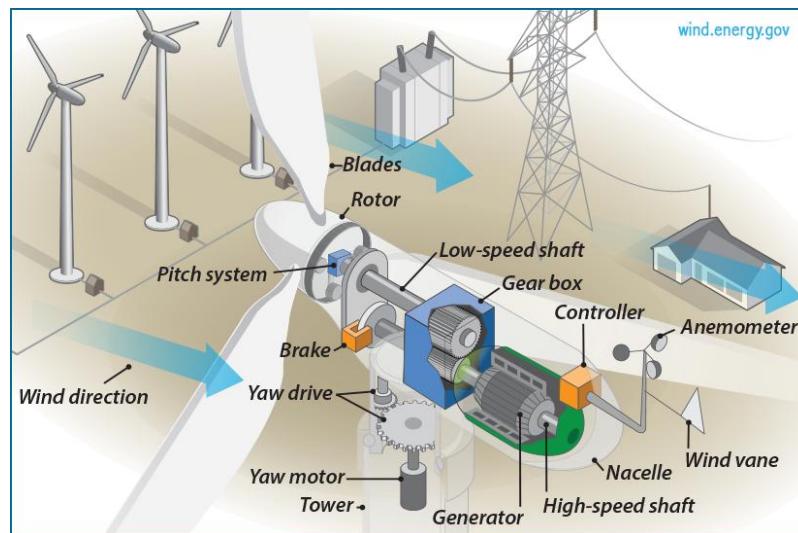


Figure 2.3 Main parts of a wind turbine [17]

2.2.1. Fixed Speed Wind Turbines

In this type of WTs, squirrel cage induction generators are connected to the grid via transformers as shown in Figure 2.4 [18]. The frequency of the grid establishes the rotational speed of the stator thus of the rotor. The speed of the generator is determined by the pole pair number and the frequency of the grid. The speed limitation may be set aerodynamically by stall control, active stall control or pitch control.

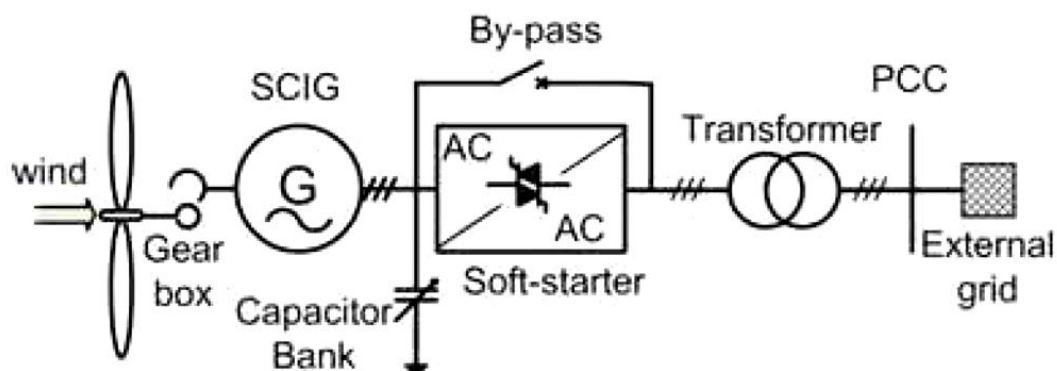


Figure 2.4 Schematic of a fixed speed WT with reactive power compensation and soft-start features [18]

The very first WT were using this type of design. The reactive power demand from the generator to the grid is supplied by a reactive power compensator, simply by switching a capacitor bank in the case of a variation in production. A soft-starter is also applied to provide a smooth operation. The variations in speed cause voltage fluctuations at the output of the generator. Hence, the stiffness of the grid becomes very important.

This type of WTs cannot be connected to weak grids and don't support speed control. The mechanical structure of the WT must be able to withstand mechanical stresses resulting from wind draft and torque pulsations too.

2.2.2. Partial Variable Speed Wind Turbines

The generator of a partial variable speed WT is connected to the grid through a transformer as in the case of fixed speed WT. In this configuration, the speed can be controlled partially by varying the rotor resistance connected to the rotor terminals as shown in Figure 2.5. Above the synchronous speed, the rotor resistance is controlled via power electronics; hence, the slip is changed. Due to variable slip, the power transferred to the grid can also be controlled typically up to 10% of the synchronous speed. The capacitor bank provides the reactive power needed by the generator and smooth grid operation is performed by the soft-start circuit.

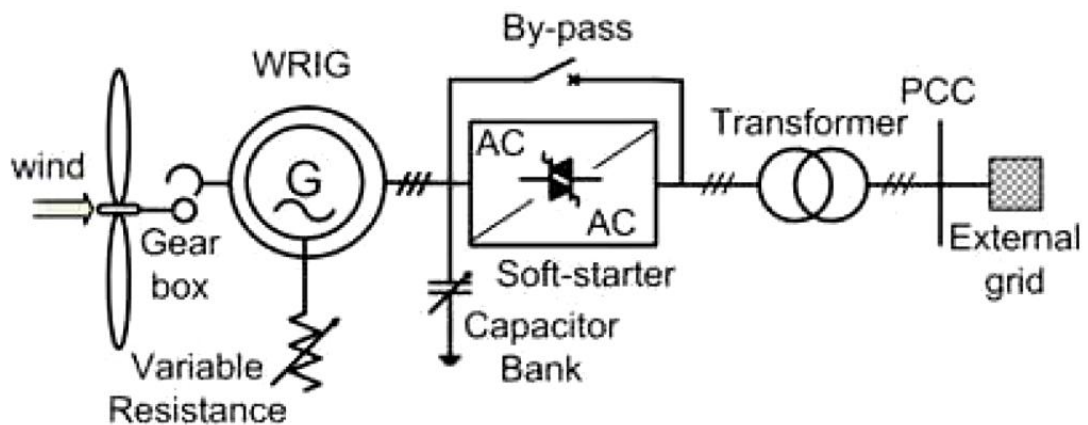


Figure 2.5 Schematic of a partial variable speed WT with variable rotor resistance [18]

2.2.3. Variable Speed Wind Turbines with Partial-scale Converter

A wound rotor induction generator is placed so as to convert mechanical power to electrical power. A partial-scale power converter is connected to the rotor terminals controlling the frequency of the rotor; hence, the rotor speed. This type of WT is mostly known as doubly-fed induction generator (DFIG). Figure 2.6 shows a DFIG wind turbine power schematic. The power rating of the converter is approximately %30 of the generator's nominal power [18].

The speed range of the WT is typically $\pm 30\%$ around the synchronous speed. The speed of the rotor is widely controlled and the reactive power compensation can be handled by the converter. Besides, the resistive losses of partial variable speed WT due to additional rotor resistances are eliminated. The small-scale power converter is an attractive approach from the cost perspective. However, the use of slip-rings and the fact that the DFIG-WT is prone to grid faults are the main disadvantages.

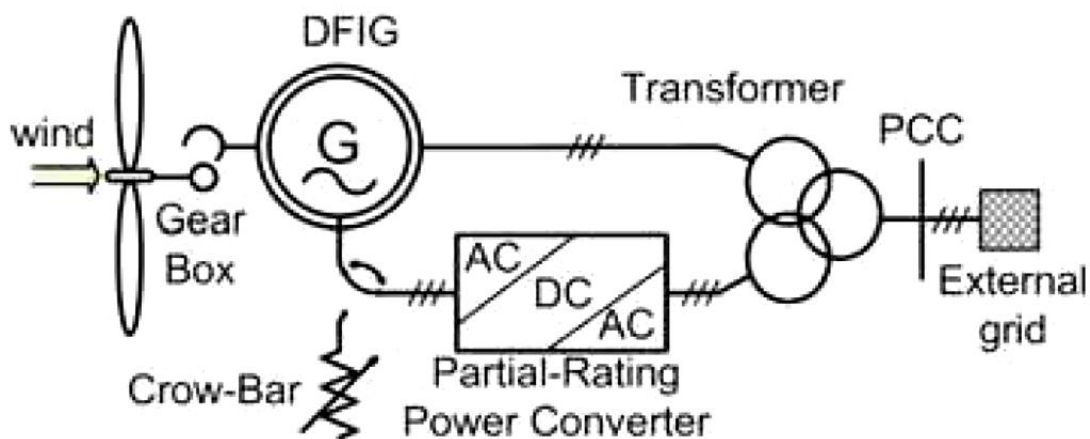


Figure 2.6 Schematic of a variable speed WT with partial-scale converter [18]

2.2.4. Variable Speed Wind Turbines with Full-scale Converter

In this configuration, the generator is connected to the grid through a full-scale power converter as shown in Figure 2.7. The gearbox is optional due to the fact that direct driven multi-pole generators may be used. The converter operates along the whole speed range smoothly and provides the necessary reactive power. The generator may be selected as permanent magnet synchronous generator (PMSG), wound rotor synchronous generator (WRSG) or squirrel cage induction generator (SCIG).

This type of WT is designed to provide maximum efficiency over a wide range of wind speed. The rotational speed of the wind turbine is matched to the wind speed

thus the ratio of the tip speed is kept constant, tracking the maximum power efficiency. The changes in wind speed are absorbed by the generator speed variations; hence, the generator torque is kept constant.

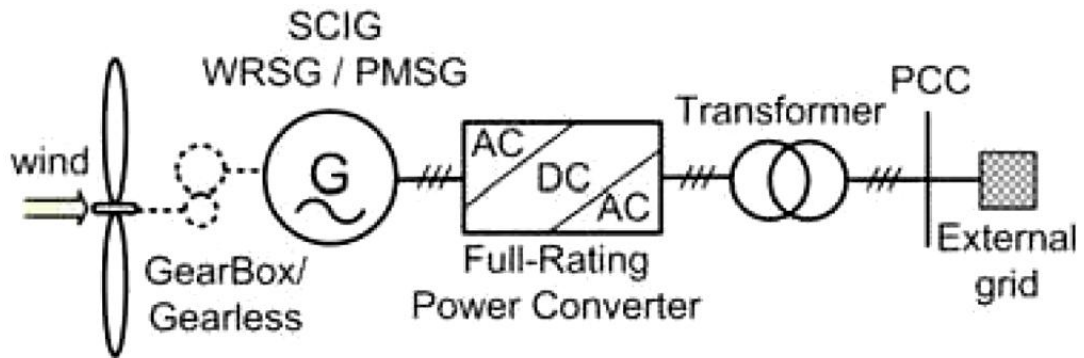


Figure 2.7 Schematic of a variable speed WT with full-scale converter [18]

The mechanical stresses on shaft and gearbox are reduced, power transferred to the grid is increased and acoustical noise is reduced by planting variable speed WTs rather than planting fixed speed WTs. The behavior of variable speed WTs with the full-scale converters during grid events are more preferable to that of variable speed WTs with partial-scale WTs. Moreover, this type of WTs can support 100% reactive power injection to the grid during faults which is required by some TSOs.

2.3. Grid Connection Requirements

The main parts of a power supply system are power generation units, grid, and loads. The energy demand imposed by the customer is met by the power supply system whose size depends on the generated, distributed, and consumed energy. Generally, the grid is divided into two parts: transmission (high-voltage) and distribution (medium- and low-voltage). The grid transmits energy from power generation plants to the distribution networks while the energy is distributed from the grid or small scale power generation plants to the end users by distribution networks.

The power generators should produce power at a cost efficient price while the transmission and distribution companies should form and specify power station requirements, plan further development of the grid, balance the requirements on different types of plants and ensure the power system properties in order to achieve reliability, quality, and safety of the power supply system at an economical price. The power system specifications must be defined to understand the abilities and characteristics in the power input for better operation and control of the power system. Therefore, various load conditions and disturbances are possible to be controlled. As it is stated, the stability of the power system and the quality of the power are main control aspects.

2.3.1. Power Quality

Power quality includes two aspects of power supply, the quality of the voltage and the reliability of the supply. Voltage quality covers various disturbances like rapid changes, flicker, unbalance, harmonics, transients, and dc components. Supply reliability; however, includes long duration faults such as interruptions, voltage dips, overvoltages, and frequency deviations.

Reliable electricity distribution with enhanced voltage quality has become a fundamental issue due to the emergence of highly sensitive loads such as computers, automation machines, and modern communication devices. The sensation of reliability for the customers has also changed in terms of the outage times per year. A reliable supply has nearly no outage times nowadays. The domestic and industrial users may be affected owing to a few cycles of interruption or a voltage drop to less than 90% [16]. The duration of voltage sags and swells and their total number in a year is getting more and more important rather than the cumulative outage times in a year.

The standard, EN 50160 [19] describes the low-voltage grid characteristics with the variations in the supply voltage. The disturbances affecting the customers can be classified according to [16] in Table 2.1 below. The origins of these disturbances and their possible consequences are also shown in the same table.

Table 2.1 Categories, typical characteristics, origins, and consequences of variations in the supply voltage

| Category | | Typical Characteristics | | | Origin | Consequences |
|---------------------------|-----------------------|-------------------------|-----------------|------------|--|--|
| | | Spectrum | Duration | Magnitude | | |
| Transients | Impulsive | 5ns-0.1ms | 50ns- > 1ms | < 6kV | Lightning strike or switching | Failure of insulation and reduced lifetime of windings |
| | Oscillatory | < 5kHz-5MHz | 5 μ s-0.3ms | 0-4 p.u. | | |
| Short duration variations | Interruptions | | 10ms – 3min. | < 1% | Direct short-circuit, disconnection, false tripping or load shedding | Disconnection of equipment |
| | Sag | | 10ms – 1min. | 1-90% | Short-circuits or start-up of large motors | Disconnection of sensitive loads |
| | Swell | | 10ms – 1min. | 110-180% | Earth fault, shut down of large loads, lightning strike or incorrect setting in sub-stations | Ageing of insulation, disconnection or damage of equipment |
| | Rapid voltage changes | | not defined | > \pm 5% | | |
| Long duration variations | Undervoltage | | >1min. | 80-90% | | |
| | Overvoltage | | >1min. | 106-120% | | |
| Voltage unbalance | | | stationary | 0.5-2% | | |
| Curve Distortion | DC offset | n = 0 | stationary | 0-0.1% | Geomagnetic disturbance, half-wave rectification, voltage setting on iron core equipment or short-circuits close to the generators | Saturation of transformer cores, heating, reduced lifetime in transformers and electrolytic erosion of grounding equipment |
| | Harmonics | n = 2-40 | stationary | 0-20% | Nonlinear loads, resonance, transformer saturation or notches | Overheating and failure of equipment |
| | Inter-harmonics | 0-6kHz | stationary | 0-2% | Static frequency converters, cycloconverters or arcing devices | Disturbance on power line carrier signaling and flicker in display devices |
| | Notches | | stationary | | | |
| | Noise | broadband | stationary | 0-1% | | |
| | Signal transmission | < 148kHz | stationary | 0.09% | | |
| Voltage fluctuations | | < 25kHz | intermittent | 0.2-7% | Arc furnaces, sawmills, welding, wind turbines, start-up of large motors | Ageing of insulation, function failure |

Table 2.1 (continued) Categories, typical characteristics, origins, and consequences of variations in the supply voltage

| Category | Typical Characteristics | | | Origin | Consequences |
|----------------------------|-------------------------|----------|-----------|--|---|
| | Spectrum | Duration | Magnitude | | |
| Power frequency variations | 50Hz | < 10s | 1% | Mismatch of dynamic balance between load and generators, faults on the transmission system, disconnection of large loads or large source of generation going offline | Failure of function in electronic equipment |

In order to define the real power quality issue, the categorized voltage variations in the above table are used. Since the nature of the load and the demand of the customer have changed recently, the TSO should be aware of these disturbances. The TSO is therefore forced to take some precautions to secure improved reliability and superior voltage quality.

Reactive power is not defined as an independent power quality constraint owing to the definition of voltage as the power quality indicator. As reactive power is directly related to the amount of losses in the power network, the size of power transformers and generators, it can be evaluated by considering the causes of large reactive power in the grid. Large voltage drops in the network due to increased reactive power leads to inferior voltage quality; hence, the voltage fluctuations can be regarded as a direct consequence of the reactive power and treated as in Table 2.1.

Having mentioned about the definition of power quality and categories of voltage disturbances, the equipment used to improve the power quality shall be stated. The equipments used on the distribution level (up to 34.5 kV in Turkey) are called Custom Power Systems (CUPS) whereas equipments used on the transmission level are called Flexible AC Transmission Systems (FACTS). These devices can be classified in three main groups:

- On/off apparatus, switches,
- Stepwise controllable apparatus,

- Continuously controllable apparatus.

On/off apparatus is used to switch the voltage between two different sources and is generally installed at industrial and commercial plants. Electromechanical switches are replaced with solid state switches such as GTOs since the time required for switching takes from 1 to 10 seconds for electromechanical switches. The sensitive devices may be affected by the voltage sags and swells due to slow response of electromechanical switches. Semiconductors are also used for fault current limiting and breaker applications where the reduction of voltage sags or the transfer between asynchronous sources is needed respectively.

Stepwise controllable apparatus is similar to Static VAR Compensator (SVC). It regulates the voltage by using an electronic controlled voltage tap changer or by using stepwise-coupled capacitor banks. Semiconductor switches are preferred instead of mechanical switches in small power systems.

Continuously controllable apparatus typically contains a VSC connected to the grid via transformers. The topology used for the converters can be shunt or series and the semiconductors used in the power block are mostly IGBTs or IGCTs. Shunt devices inject current to the grid at the Point of Common Coupling (PCC). Different types of disturbances are compensated using a variety of shunt-connected apparatus, namely: SVC, Static Synchronous Compensator (STATCOM), and Active Harmonic Filter (AHF). Series-connected devices injects voltage between the source and the load with a phase lag or lead property. Dynamic Voltage Restorers (DVRs) are the mostly used types of series-connected power quality improvement devices. Shunt devices are used for regulating the grid current, while series devices are used for compensating voltage disturbances occurring on the load.

The combination of shunt and series devices is named as Unified Power Quality Conditioner (UPQC) and used for both the regulation of grid current and load voltage at the same time.

Passive filter elements may also be connected together with the active compensators to reduce the power flow through the semiconductors and reduce the switching and

conduction losses. These types of topologies are called as hybrid compensators. If the apparatus has an energy storage device, the voltage dips and voltage fluctuations may also be compensated.

In order to define the disturbances in connection with wind turbines, measurements and indicators are needed. The influence of wind turbines on the power quality and measurement methods are described in IEC 61400-21 [20]. Measures for maximum power, reactive power, voltage fluctuations, and harmonics are covered by this standard.

By Fourier transform, the analysis of a signal can be done. The connection of a WT to the grid via power electronics converter requires a spectrum analysis on the harmonic content due to switching of the semiconductors. Ideally, complete sinusoidal current and voltage at the grid frequency (50 Hz in Turkey) are sought; however, the deviations from the ideal case are described in two different measures. These are total harmonic voltage distortion (THD_U) and weighted distortion factor (THD_W) expressed in (2.1) and (2.2) respectively. The power quality of the grid is defined using the distortion measures of the voltage.

$$THD_{U\%} = \sqrt{\sum_{h=2}^n \left(\frac{U_h}{U_1}\right)^2} \cdot 100\% \quad (2.1)$$

$$THD_W = \sqrt{\sum_{h=2}^n \left(h \cdot \frac{U_h}{U_1}\right)^2} \quad (2.2)$$

where U_h is the amplitude of the harmonics with “h” indicating the number of harmonics (i.e. 2, 3, 4...). U_{rms} denotes the rms value of the line voltage including the harmonics.

IEC 61400-21 addresses other standards related to voltage and current harmonics as well as electromagnetic compatibility (EMC). The voltage harmonics limitations are set by EN 50160 together with the characteristics of the voltage disturbances as stated previously. EN 61000-2-2 defines the EMC levels for low-voltage applications. IEC 61000-3-6 is referred so as to indicate current harmonic distortion limits whereas IEC 61000-2-2 defines the current inter-harmonic distortion limits. As the supportive standards, IEC 61000-4-7 and IEC 61000-4-30 are used for measuring methods on harmonic emissions. On the other hand, IEEE-STD-519 is a well-known standard not only for wind turbines but also for all kinds of electrical power systems addressing recommended practices and requirements regarding the harmonic control issue [21]. A general overview of the abovementioned standards related to WECS is shown elegantly in Figure 2.8.

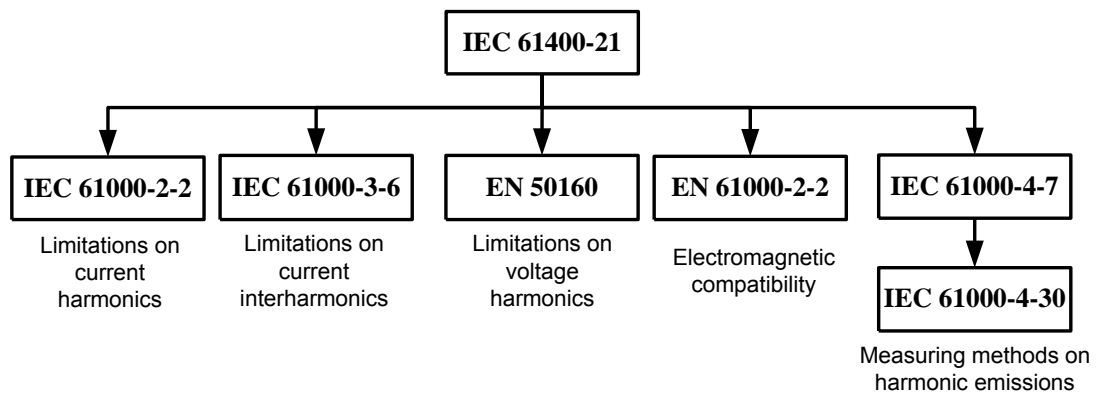


Figure 2.8 Harmonic standards for grid integration of WTs

The process of designing an appropriate power converter is a key element to comply these severe standards. Apart from the power converter, active or passive filters are required for reducing the current harmonics injected to the grid. The frequently used *LCL* filter should also be designed according to grid codes set by the TSO. The compatibility of the WECS to the current harmonic distortion limits is mainly sought in the next chapters as a performance criterion.

The voltage disturbances tabulated in Table 2.2 shall be expanded in terms of the harmonics. The following table states the individual harmonic voltage components up to 25th component.

Table 2.2 Individual harmonic voltage values at the supply terminals as percent of nominal voltage, U_n

| Odd Harmonics | | | | Even harmonics | |
|--------------------|----------------------|----------------|----------------------|----------------|----------------------|
| Not multiples of 3 | | Multiples of 3 | | | |
| Order h | Relative voltage (%) | Order h | Relative voltage (%) | Order h | Relative voltage (%) |
| 5 | 6 | 3 | 5 | 2 | 2 |
| 7 | 5 | 9 | 1.5 | 4 | 1 |
| 11 | 3.5 | 15 | 0.5 | 6...24 | 0.5 |
| 13 | 3 | 21 | 0.5 | | |
| 17 | 2 | | | | |
| 19 | 1.5 | | | | |
| 23 | 1.5 | | | | |
| 25 | 1.5 | | | | |

According to IEC61400-21, WTs directly connected to the medium-voltage (MV) network through a standard step-up transformer should have a total voltage harmonic distortion, $THD_{U\%}$ less than 5% including all harmonics up to 50th order, measured as 10 minutes average data at the HV-side of the step-up transformer. It should be noted that the harmonics below 0.1% of the value of U_l shall be neglected. Additionally, $THD_{U\%}$ value should be less than 5% on power lines below 69 kV according to IEEE-STD-519.

For variable speed wind turbines, the measurement of current harmonics is important according to IEC 61400-21. Fixed speed WTSs; on the other hand, does not contain power electronics converters. The generators are directly connected to the grid. The limits of the harmonic currents injected to the grid are given in IEC 61000-3-6.

The converters utilized in WTs are mostly of medium and high power with at least hundreds of kilowatts power rating. The switching frequency is therefore limited to

only a few kilohertz. The connection of individual wind turbines to form a wind park may cause the superposition of the harmonics. Since the operating points and the phase angles of each WT are not the same, the worst case summation of harmonic components is not likely. The value of the current THD should be less than 6-8% depending on the type of the grid. The calculation of harmonic distortion factor for a group of WTs connected in the same grid is somewhat dissimilar to the equation in (2.1) replacing the voltage, U with the current, I . Low order harmonics are more important than higher order harmonics regarding the contribution to the current distortion factor. Inter-harmonics and high frequency harmonic components are also calculated with the same equation.

The current harmonic values allowed according to IEEE-STD-519 depend on the grid type. The short-circuit ratio (SCR) is an important criterion to select the range of harmonic values correctly. For this reason, the understanding of IEEE-STD-519 is left for the oncoming sections.

2.3.2. Demands to Grid Connection

The requirements for the penetration of the wind power into the electrical network are set such that wind farms act as an ordinary power plant. These requirements are very stringent to ensure controllability, power quality, fault ride-through capability, and grid support during network disturbances [22]. In the following, some of these severe conditions are explained briefly.

WECS shall be controlled within the 20%-100% power range of its rated power by the TSO. For WECS rated up to 100 MW, the load acceptance rate of the system should not exceed 5% and the load reduction rate of the system should not be below 5%.

WECS should be able to control the active power in the PCC within their power range. The active power control is typically carried out when the system frequency is changed. The power control curve against frequency variations for Turkish Wind Turbines Network Regulation [23] is shown in Figure 2.9. Between 47.5 Hz and

50.3 Hz the WECS should be able to supply its rated power to the grid. If the grid frequency increase beyond 50.3 Hz, the power delivered to the grid is reduced.

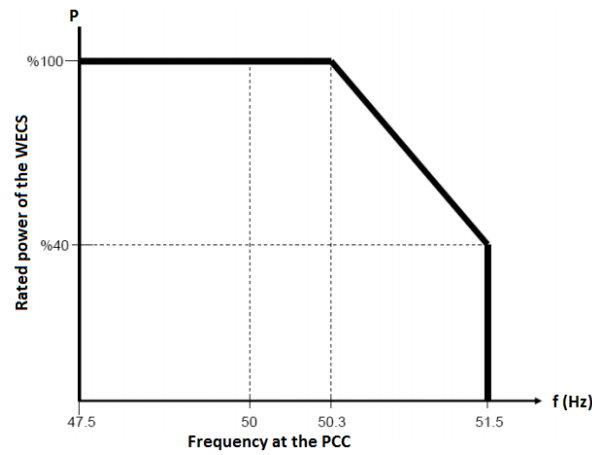


Figure 2.9 Power control characteristics of a WECS

The reactive power output of a WECS should also be controlled in a given range. The grid codes define the region of reactive power control. The rate and the level of reactive power exchange with the grid are controlled by the transmission system operator. In Figure 2.10, the graphical illustration of reactive power control in Turkey is shown. The figure on the left describes the reactive power allowed as the percentage of the active power and the figure on the right addresses the same issue based on the power factor of the WECS.

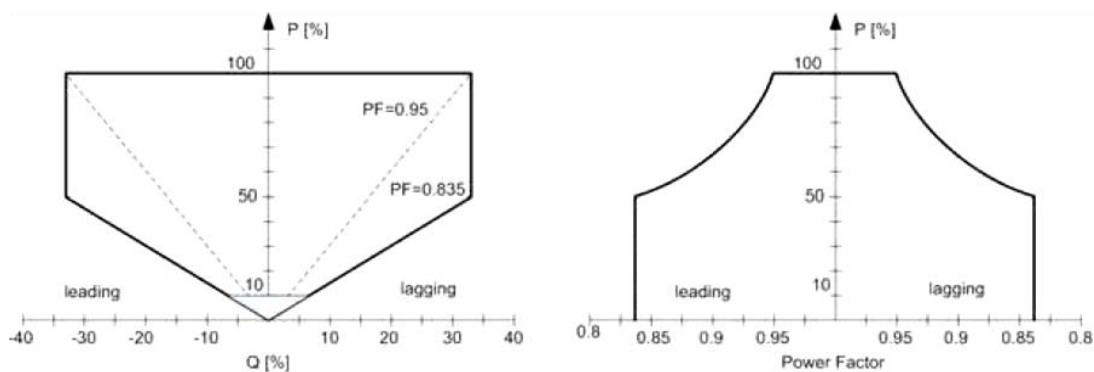


Figure 2.10 Reactive power exchange for WECS in the PCC in Turkey

The given reactive power demands shall be satisfied depending on the voltage values given in Figure 2.11 below.

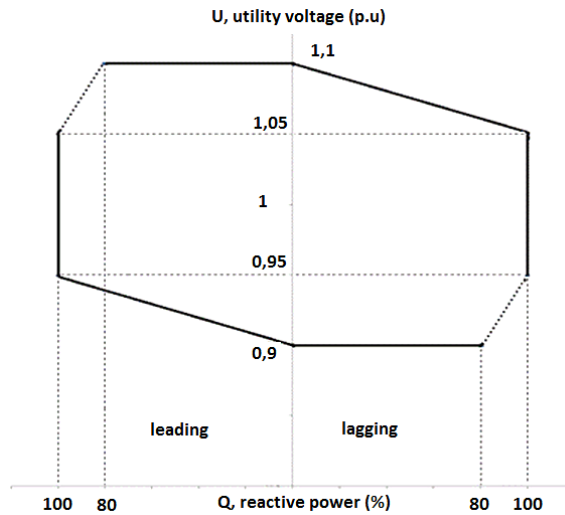


Figure 2.11 Reactive power exchange against utility voltage

The current due to reactive power flow results in voltage drop and causes power losses. If the amount of reactive current increases, it may cause voltage instability due to voltage drops in the transmission line. WTs with induction generators consume reactive power; hence, PWM converters are used to minimize power losses and to increase the voltage stability resulting from the reactive power consumption. As it is known, PWM converters can satisfy unity power factor owing to the controllability of the currents flowing through the utility.

During the normal operation of WTs, voltage dips may occur and the clearance time of the dips may be small enough that the WECS recovers the fault. Such an ability of the system is called fault ride-through capability. For the Turkish Wind Turbines Network Regulation, WTs connected to the grid should satisfy the demands given in Figure 2.12. In regions 1 and 2, WECS should stay connected to the grid as voltage dips occur in one of the phases or in all phases.

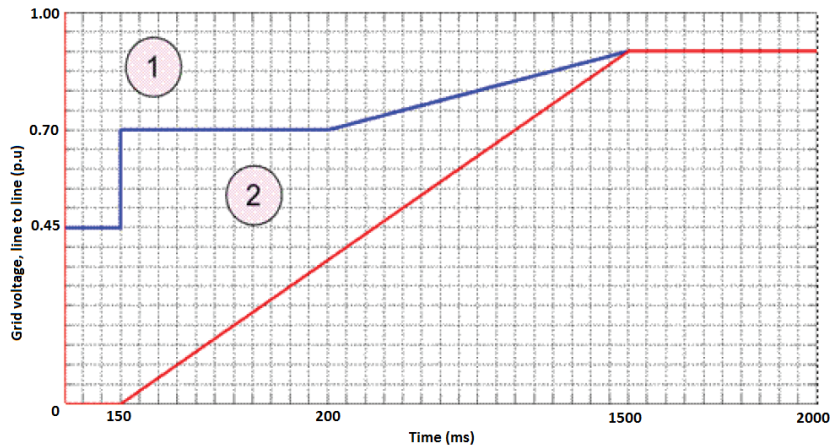


Figure 2.12 Fault ride-through capability of grid-connected WTGs [23]

After the fault is cleared, the WECS should power up to the full rating with 0.2 *p.u.* of its rated power in every second if the voltage dip is in region 1. On the other hand, the WECS should increase the delivered power to the grid with 0.05 *p.u.* of its rated power in every second if the voltage dip is region 2.

Voltage fluctuations between 0.9 *p.u.* and 1.1 *p.u.* are accepted as normal grid operation and WECS should follow the reactive power support specifications.

2.3.3. Grid Types

Voltage drops on the grid are likely to happen due to harmonic currents flowing through the grid. The disturbances resulting from the voltage drops are directly related to the short-circuit power (SCC) of the grid. Even small amounts of load change may disturb the grid voltage if the grid is not strong enough. Therefore, the strength of a grid is very important for the connection of WECS. The main measure assessing the stiffness of a grid is the short-circuit ratio (SCR) which is defined in this section.

The power network can be analyzed by approximating it as a first order circuit. A simple approximation of the grid is shown in Figure 2.13 below. SCC of the grid is calculated as in (2.3) by short circuiting the load impedance, Z_{load} . The short-circuit

grid current is calculated by dividing the grid voltage with the magnitude of the grid impedance, Z_{line} as in (2.4).

$$SCC = \sqrt{3} \cdot V_{grid} \cdot I_{sc} \quad (2.3)$$

$$I_{sc} = \frac{V_{grid}/\sqrt{3}}{|Z_{line}|} \quad (2.4)$$

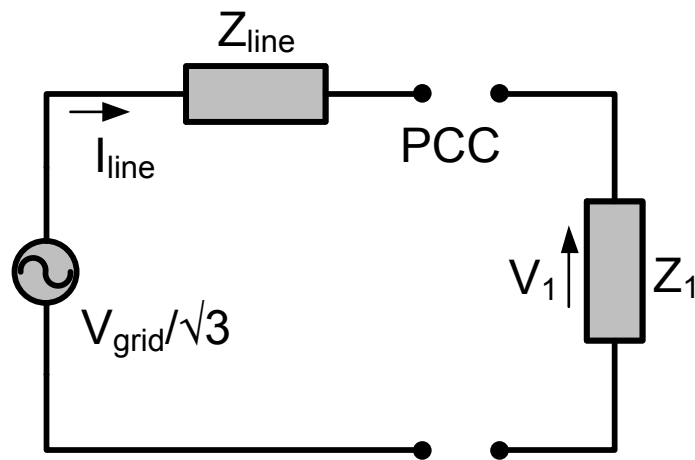


Figure 2.13 First order equivalent of the grid

The SCR of the grid is then calculated as follows;

$$SCR = \frac{SCC}{S_n} \quad (2.5)$$

where S_n is the installed capacity (apparent power) of the WECS.

Another important definition related to the grid measure is the short-circuit angle defined in [20] as

$$\psi_{grid} = \tan^{-1} \left(\frac{X_{line}}{R_{line}} \right) \quad (2.6)$$

where X_{line} and R_{line} denote the reactance and the resistance of the grid respectively.

The load voltage at the PCC can be described at steady-state conditions simply as in (2.7) with P_l is the active power production and Q_l is the reactive power consumption of the load. With this information between the grid and the load, the voltage of the PCC can be estimated to check whether it is in the limits defined by the TSO or not.

$$V_{PCC} = V_{grid} - \frac{R_{line} \cdot P_1 + X_{line} \cdot Q_1}{V_{grid}} \quad (2.7)$$

Having defined the basic properties of a grid, the various grid types are now described briefly. In addition to the short-circuit ratio and short-circuit angle, two important parameters to describe a grid are the voltage rating and the source type, i.e. AC or DC. Grids can also be classified as transmission grid, distribution grid, AC/DC grid, isolated grid, stiff grid or weak grid in terms of their featured characteristics.

The grid is considered as weak if the SCR is less than 8-10 while the grid having SCR higher than 20-25 is considered as stiff [24]. In other words, the higher the SCR, the stiffer the grid is. Grids with a few WTs are connected can be seen as stiff whereas the same grid may be characterized as weak if more WTs are attached to it. The line voltage at the PCC of a weak grid is not stable when large wind power is injected through it. Power quality devices mentioned in the previous section should be connected in this case to regulate the voltage at the PCC.

IEEE-STD-519 which is also a compilation of recommended practices serving as a guide to suppliers and consumers of electrical energy defines the current harmonics allowed using the SCR of the grid. The current limits are set depending on the size

of the consumer relative to the size of the supply. As the size of the consumer gets bigger, the regulations become more stringent.

Table 2.3 demonstrates the maximum current distortion values as a function of SCR and harmonic order. Total harmonic distortion levels are also shown in the same table. The data given in Table 2.3 is defined relative to the maximum demand load current. The distortion level is defined in terms of total demand distortion (TDD) which accounts for the load change as opposed to THD.

Table 2.3 Current distortion limits set by IEEE-STD-519 [21]

For conditions lasting more than one hour. (Shorter periods increase limit by 50%)

| Harmonic Current Limits for Non-Linear Load at the Point-of-Common-Coupling with Other Loads, for voltages 120 - 69,000 volts | | | | | | |
|---|-----|-------|-------|-------|-----|-----|
| Maximum Odd Harmonic Current Distortion in % of Fundamental Harmonic Order | | | | | | |
| ISC/IL | <11 | 11<17 | 17<23 | 23<35 | 35 | TDD |
| <20* | 4 | 2 | 1.5 | 0.6 | 0.3 | 5 |
| 20<50 | 7 | 3.5 | 2.5 | 1 | 0.5 | 8 |
| 50<100 | 10 | 4.5 | 4 | 1.5 | 0.7 | 12 |
| 100<1000 | 12 | 5.5 | 5 | 2 | 1 | 15 |
| >1000 | 15 | 7 | 6 | 2.5 | 1.4 | 20 |

Even harmonics are limited to 25% of the odd harmonic limits above.
 *All power generation equipment is limited to these values of current distortion, regardless of actual ISC/IL.
 Where ISC = Maximum short circuit current at point-of-common-coupling.
 And IL = Maximum demand load current (fundamental frequency) at point of common coupling.
 TDD = Total demand distortion (RSS) in % of maximum demand

It should be mentioned that all the individual harmonic components cannot be at the maximum limit and comply with the TDD rating at the same time.

The even harmonic limits are not shown in the above table. The limits for even harmonics are set as 25% of the limit for odd harmonics within the same range. Even harmonics are not invited as they lead to asymmetrical current waves and a DC component saturating the magnetic cores may occur.

2.4. Power Converter Topologies

Wind turbines operate at various speeds; thus, the electric generators produce power at a range of frequency. The changing frequency at the generator terminals should be decoupled from the frequency of the grid which is constant. Power converters are used to match with the grid frequency. For fixed-speed wind turbines, power electronics devices are still used for soft-start purposes. Before the clarification of some of the most important converter topologies, power electronic devices used in earlier designs and modern WECS are introduced briefly.

The developments in the semiconductor devices have led vigorous changes in power electronics. The reduction of semiconductor device prices continuously and the increase of power capacity at the same package are main reasons for the growth in power electronics mainly focusing on three important aspects: reliability, efficiency, and cost. Power electronic devices have a decreasing cost by 2-5% each year for the same output performance [25]. The historical development of power semiconductors are briefly shown in Figure 2.14 below.

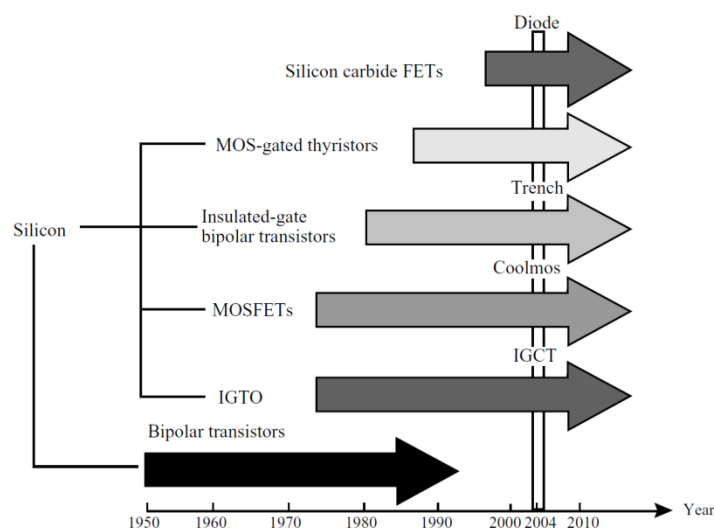


Figure 2.14 Development of power semiconductors in the past and in the future

The invention of silicon controlled rectifiers (SCRs) also known as thyristors prior to fully controlled switches was a major step in the development of power electronics. Thyristors have a controlled turn-on via gate signals while turn-off is achieved via commutation circuits. In the “on” cycle, thyristors behave as diode and the current can flow through the device only in one direction. Conversely, thyristors can block both negative and positive voltages in the “off” cycle. Later, the development of gate turn-off thyristors (GTOs) made easier to turn the device “off” by removing commutation circuits.

After the development of SCRs, bipolar junction transistors (BJTs) and metal oxide semiconductor field effect transistors (MOSFETs) are used as fully controlled switches for low power applications whereas GTOs are used for high power applications. The insulated gate bipolar transistor (IGBT) developed in 1980’s and is still popular for low to medium power applications. New emerging technologies in IGBTs surely sustain the importance of these devices in power electronic applications. In late 1990’s insulated gate controlled thyristors (IGCTs) developed for high power applications replacing GTOs.

The base material has changed recently from silicon to silicon carbide (SiC) which enables higher power density in the same package. The cost of silicon carbide devices is still not competitive with conventional silicon devices but in the near future their price would decrease.

Power converters used for WECS have various topologies. For fixed speed WTs, which are not installed nowadays soft-starters are used to limit transient currents during the connection and the disconnection to the grid. Capacitor banks are also used for power factor compensation in fixed speed WTs.

Diode rectifiers are used in old designs for the rectification of the generator’s output voltage. Since diode rectifiers can operate in only one quadrant, they cannot be used at fully controlled power conversion topologies.

Converter topologies with fully controllability of the generated voltage are preferable for modern WTs. They can be used for partial-scale power conversion as

it is stated in 2.2.3 or full-scale power conversion as in 2.2.4. Back-to-back PWM-VSIs, matrix converters, tandem converters, multilevel converters, and resonant converters are mostly implemented power converters. A short explanation of these topologies is given and a comparison of them is stated below.

2.4.1. Back-to-back PWM-VSI

The back-to-back PWM-VSI consists of two conventional PWM-VSI and a DC-link capacitor. This topology shown in Figure 2.15 provides bi-directional power flow. Two-level VSI is a proven technology and power devices used are standard as IGBTs with higher power ratings are available.

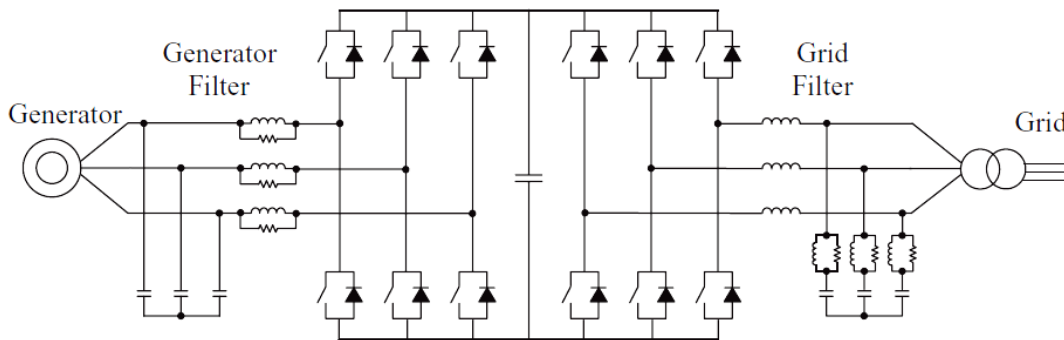


Figure 2.15 Two-level (2L) back-to-back PWM-VSI [26]

DC-link voltage is boosted to a level higher than the line-to-line voltage of the grid by the generator side converter to achieve full control of the grid current. Generator side converter adjusts the magnetization demand and the reference speed while grid side converter keeps the DC-link voltage and controls the AC currents.

Required DC-link inductance can be provided by the power cables from the generator side converter to the capacitor. Grid side converters are installed at the tower base instead of nacelle to reduce the weight at the top of the tower. This can provide enough inductance to achieve a stable DC-link. For wind parks, DC

transmission cables could be long enough to provide the needed inductance [26]. DC-link reactor is an intrinsic protector against short-circuit faults hence fault ride-through strategy of the system required by the grid code can be implemented without difficulty. It also reduces the filter size at the AC side since smaller filter components can be used against harmonics flowing through the grid. A higher level of DC-link current provides a faster dynamic response but fast transients can cause power system instabilities. DC-link current is kept smaller at lower speeds for variable speed operation of multi-megawatt applications. The output power of the WECS is regulated such that the changes are rather slow.

For higher power ratings, three-level (3L) VSIs can be implemented offering lower grid side THD, lower rating for semiconductors, and reduced semiconductor switching losses. Nevertheless, the increased complexity in hardware design and controllers and high conduction losses due to series-connected switches are the drawbacks of 3L VSIs. The back-to-back connected 3L PWM-VSI topology for wind turbine applications is shown in Figure 2.16.

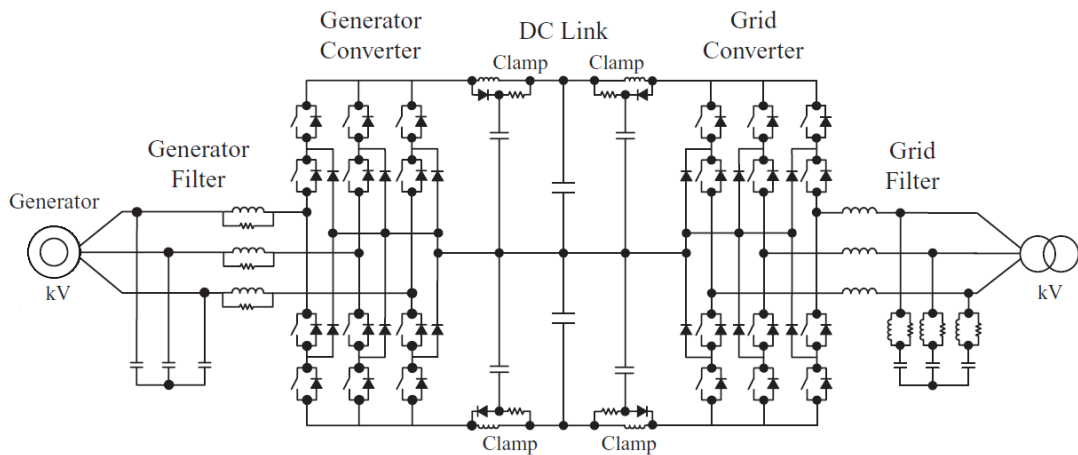


Figure 2.16 3L back-to-back PWM-VSI [26]

An alternative method to increase the power rating of the system is to use multi-cell structures in which the power converters (cells) are connected in parallel or in

cascade. The reliability of the system is increased since the system continues to operate even if one or more cells fail. The modularity of this type of connection is also advantageous for low wind conditions. The number of operating cells can be reduced for low wind power hence decreasing the power losses and enhancing the efficiency. A multi-phase machine connected to the grid via back-to-back PWM-VSIs is shown in Figure 2.17. The PWM patterns are shifted for each cell to cancel the sideband harmonics. This allows lower harmonics on the grid side thus smaller filter requirement.

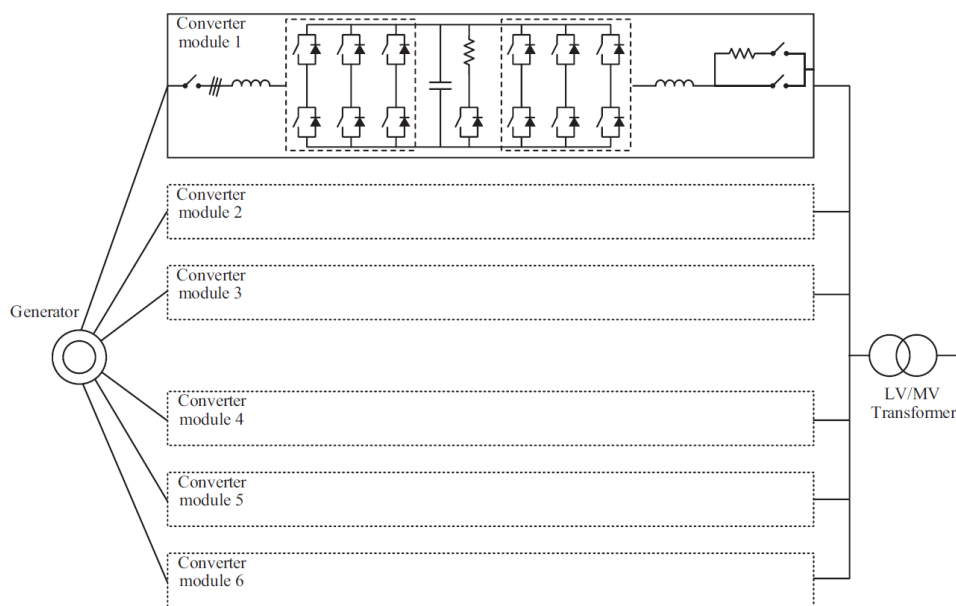


Figure 2.17 Back-to-back PWM-VSIs fed by a multi-phase machine and connected in parallel [26]

2.4.2. Tandem Converter

Tandem converter topology uses an active PWM-VSI harmonic filter for harmonic distortion compensation. This converter is fairly new and based on current source inverter (CSI). The topology of the tandem converter is shown in Figure 2.18.

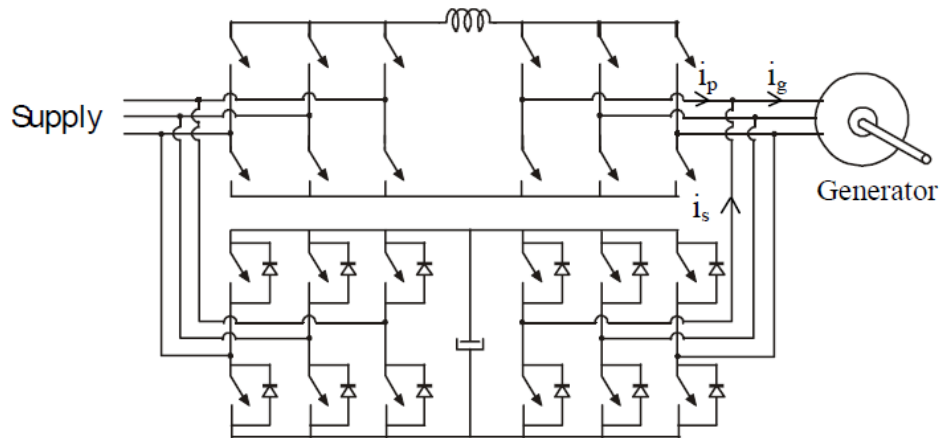


Figure 2.18 Tandem converter topology [16]

There are four distinct inverters in the topology which brings several degrees of freedom to controllers. The primary converter, the CSI is operated in square-wave mode. In this mode the switches of the CSI are turned on and off once in each fundamental cycle. The switches used in the CSI are GTOs or series-connected IGBT and diode pairs. The secondary VSI operates at high switching frequency; however, only the harmonic currents are processed by the VSI. By processing a small fraction of total load current, the rated power of the PWM-VSI is reduced and the efficiency of the system is enhanced. A well-defined control of both the main CSI and PWM-VSI are stated in the references given in [16].

2.4.3. Matrix Converter

Matrix converter is a direct energy transfer method from the generator side to the grid with no passive components in the power circuit. The power circuit is composed of semiconductor bi-directional switches. The ideal matrix converter topology and the bi-directional switch configuration are demonstrated in Figure 2.19. Matrix converters have capability to control the power flow in both directions and suppress input current harmonics. The input power factor can be fully controlled and the energy storage is kept at minimum hence the bulky and lifetime-limited capacitors are not required.

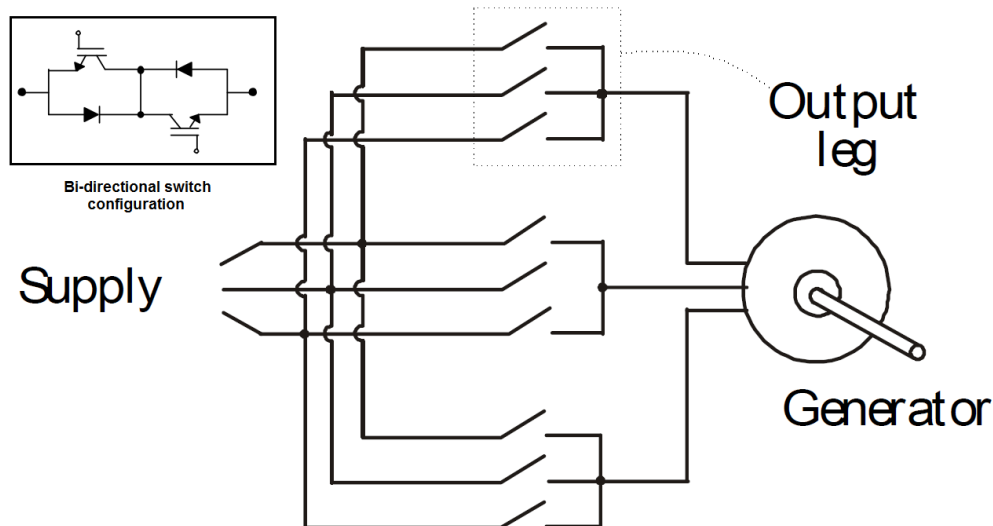


Figure 2.19 Ideal matrix converter topology [16]

The filtering requirements of the matrix converter are lower than traditional indirect AC-DC-AC energy conversion systems. The capacitive filters at the voltage-fed side and the inductive filters at the current-fed side are inversely proportional with the switching frequency of the converter.

Theoretically there are 512 combinations of switching schemes but only 27 of them are applied to protect the converter. For protection of the converter, two or three switches in the same leg are not allowed to be turned on at the same time and at least one of the switches in a leg should be turned on at any instant. However, the actual combination of switches depends on the modulation strategy applied.

2.4.4. Multilevel Converter

Since the invention of neutral point clamped (NPC) 3L converters, several multilevel converter topologies have been presented. An increasing interest on multilevel converters still continues especially for medium to high power, high-voltage WECS. The elementary operation of a multilevel converter is to use a series connection of power semiconductors with several voltage levels to convert the power by creating a

staircase voltage waveform. The voltage ratings of power semiconductors depend only on the voltages of multiple DC sources.

Multilevel converter topologies proposed up to now are plentiful and can be grouped in three major structures: cascaded H-bridge converter, diode clamped converter, and flying capacitor converter [27]. PWM strategies such as sinusoidal PWM (SPWM), space vector PWM (SVPWM), and selective harmonic elimination PWM (SHE-PWM) are developed on industrial motor drives, flexible AC transmission systems (FACTS) as well as utility interface for renewable energy systems.

The abovementioned topologies for 3L converters are demonstrated in Figure 2.20. In cascaded H-bridge topology, each DC source is connected to a single-phase full-bridge (H-bridge) inverter. Each inverter can generate positive, negative rail (DC-link) voltage or zero voltage at its output terminals. The output of each inverter is connected in series to form a synthesized output voltage. Each phase of diode clamped inverter; on the other hand, shares the common DC-link voltage and the bus voltage is subdivided by capacitors. The voltage stress across each semiconductor device is limited to the capacitor voltage level through the clamping diodes.

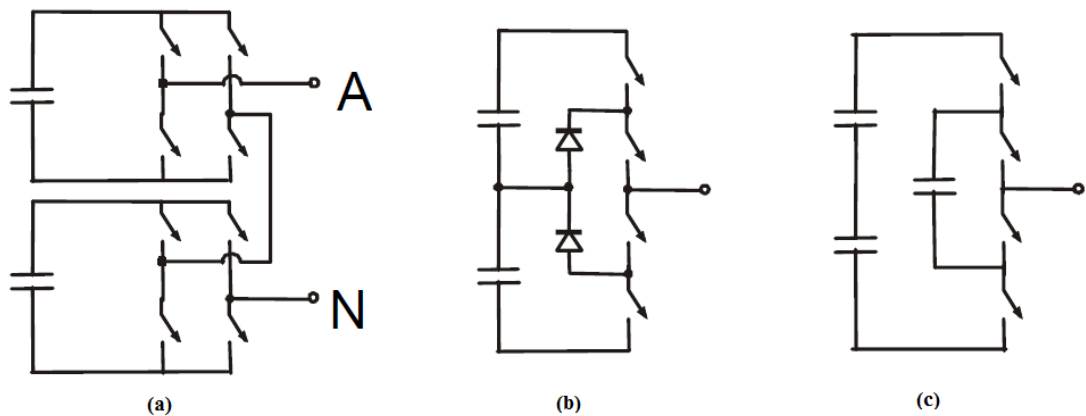


Figure 2.20 Multilevel converters topologies for 3L converter a) Cascaded H-bridge b) Diode clamped c) Flying capacitor

The flying capacitor topology is very similar to diode clamped topology except that capacitors are used instead of clamping diodes. The voltage level in each capacitor differs from the adjacent capacitor. Moreover, the redundancy of flying capacitor topology is better compared to diode clamped topology since a few switching combinations are enough to form an output voltage.

2.4.5. Resonant Converter

The efforts to minimize the switching losses of power converters have led to the proposal of various resonant converter topologies. Resonant converters are relatively complex in both hardware and control, have voltage peaks in DC-link and output voltage and high power flow through the resonant circuit.

The neutral clamped converter (NCC) topology shown in Figure 2.21; however, does not suffer from the previously discussed drawbacks. The back-to-back PWM-VSI and the resonant circuit in the middle are used. The resonance is achieved by inductive energy transfer. The DC-link voltage is boosted to control the current from the grid or supplied to the grid. The switches employed in the resonant circuit are bi-directional as the switches used in the matrix converter.

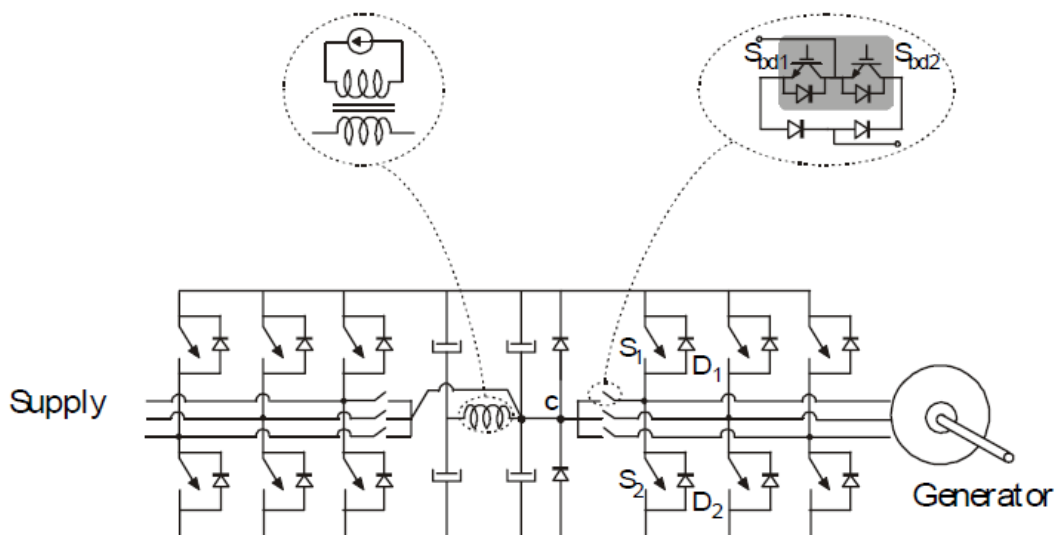


Figure 2.21 Natural clamped converter topology and the switch configuration [16]

2.4.6. Comparison of Power Converters

The AC/AC conversion discussed in various topologies can be direct and indirect. In the indirect case the DC-link connects two converters performing AC/DC and DC/AC conversions, while in the direct case the DC-link is not present. The decoupling provided by the DC-link compensates for non-symmetry and other power quality problems whereas the lifetime is reduced and the expenses are increased in the indirect energy conversion. The presence of a DC-link can be advantageous in the case of low-voltage ride-through and in the case of a need for providing some inertia in the power flow from the generator side to the grid side.

On the other hand, direct energy transfer topologies such as matrix converter does not require transitional energy storage. The thermal loads of power semiconductors decrease due to less switching losses and harmonic performance on the generator side is improved. Nevertheless, higher number of active components, more complex control, more complex grid side filter design, and non-proven technological background are the main drawbacks of direct energy transfer topologies.

In terms of the applicability of the converter topologies to WECS, it is evident that the back-to-back PWM-VSI is extremely appropriate since this topology is the one used in today's wind turbines. Moreover, the knowledge about PWM-VSIs available in the field is widespread and well-defined. Before stating the advantages and disadvantages of each topology, a general comparison regarding the components and ratings, efficiency, harmonic performance, and implementation should be given.

The back-to-back PWM-VSI includes the least number of active components but a moderate number of passive components. The matrix converter is composed of only active components and the remaining topologies have a high number of both active and passive elements. The number of auxiliary components such as transducers and gate drives are high in tandem converters and NCCs. The output transformer may be omitted in multilevel converters, which reduces the overall system cost. In the literature, the efficiency evaluation is based on the conduction and switching losses. The NCC has the highest potential efficiency level and the multilevel converter

follows it. The harmonic performance of multilevel converters is superior to other topologies since the requirements for filters are not so demanding. Considering the implementation, back-to-back PWM-VSI, and multilevel converter topologies are least troublesome since these are the most used commercial converters. The advantages and the disadvantages of each topology are given briefly in the following.

The back-to-back PWM-VSI is frequently used in the literature. For this reason, manufacturers specially design and produce components such as IGBT stacks and anti-parallel diodes to use in this type of applications. Consequently, the component costs are reduced. Besides, the decoupling provided by the DC-link capacitor allows independent control of the rectifier and the inverter parts. The boost inductance in the DC-link also has a positive effect on the protection of the converter against abnormal grid conditions and it reduces the grid side filter requirements resulting from high frequency switching harmonics. The main drawback of the back-to-back PWM-VSI is due to heavy and bulky DC-link capacitor. It also reduces the lifetime and increases the cost of the overall system. The switching losses associated with the grid side and generator side converters are considerably high and some EMI filters shall be used at the grid side due to high switching speed.

Tandem converter may reduce the switching losses by 70% compared to conventional 2L PWM-VSI due to low switching frequency of the primary converter and low level current processed by the secondary converter. The conduction losses increase due to increased number of semiconductors; however, the overall efficiency is still increased. The performance of tandem converter is better than both CSI and VSI since the magnitude of the current is controlled by the VSI and the phase shift command is controlled by the CSI. The secondary converter can also emulate a damping resistor for light load conditions other than compensating the current distortions initiated by the primary converter. The high number of semiconductors and auxiliary components bring more complexity both in hardware and software. The generator voltage is also reduced due to CSI hence only 86.6% of the grid

voltage is utilized [16]. Therefore, currents through the semiconductor devices have to be increased in order to obtain the same output power.

The matrix converter reduces the thermal design complexity for low switching frequencies compared to conventional PWM-VSI given that the semiconductors in the matrix converter are equally stressed. The absence of a DC-link capacitor both increases the efficiency and extends the lifetime of the system although six additional switches are introduced in contrast to conventional PWM-VSI. The intrinsic limitation of the output voltage to 86.6% of the input voltage is a disadvantage of the matrix converter [16]. The current through the converter should be increased by 1.15 times to give the same output power as in the case of tandem converter. The increase in the current hence leads to ascending conduction losses. The voltage unbalance or distortions at the input or unbalanced load conditions lead to distorted input current and output voltages due to absence of a DC-link. The protection of the matrix converter under faults is also troublesome which is not desired for WECS.

Multilevel converters offer reduced input and output voltage harmonics and the EMI ratings are reduced. The sizes of the filters both at the generator side and at the grid side are reduced. For the same harmonic performance, the switching losses are reduced which is another favorable property of multilevel converters. The conduction losses are more than 2L converter; however, the switching losses can be smaller by 25%. A disadvantage of multilevel converters is the unbalanced capacitor voltages. The unbalance may be due to differences of capacitance values of real capacitors, unequal dead-time compensation or unbalanced loads. This phenomenon can be solved by hardware or software by controlling the modulation. The current stress on semiconductors differs in the same leg of diode clamped and flying capacitor topologies thus a design challenge occurs.

The resonant voltage of NCC topology is limited to the value of the DC-link. The resonant circuit is not in the power part and only one resonant circuit is needed for the AC/AC conversion. Although the conduction losses of NCC is close to PWM-VSI, the switching losses are greatly reduced hence the overall efficiency is

increased. The reduced dV/dt rating provides lower EMI and lower output inductance. Different modulation strategies shall be applied to reduce the harmonics at the grid side. The design of resonant converters is more complex than PWM-VSIs and additional components are required. The unbalanced voltages between capacitors and the continuous resonant operation are other challenges regarding the NCC topology.

2.5. Review of Back-to-back WECS

Modern WTs use either partial-scale or full-scale power converters with variable speed operation. The use of full-scale power converters with back-to-back PWM-VSI topology is advantageous due to better response to deal with grid related problems [2], [3], [28], [29]. The voltage level; on the other hand, depends on the type of the generator employed. Induction generators are often designed in low-voltage (LV) range and synchronous generators can be implemented in either in LV or medium-voltage (MV). Multi-pole generator which is also a synchronous generator eliminates the use of costly and bulky gearboxes and provides a direct connection. The development of PMSGs and multi-pole generators for wind turbine applications increase the wind penetration percentage owing to the higher overall system efficiency.

Figure 2.22 demonstrates the most common WECS topologies and the control issues. The generator can be an induction generator (IG) with or without a doubly-fed terminals or a synchronous generator (SG). The gearbox is not used when the generator is designed as a multi-pole machine. Such a direct drive design decreases the overall cost of the WT. The generator side converter is selected as PWM rectifier to fully control the generator dynamics usually. For some old applications; however, diode rectifiers which are unable to control the harmonics and lacking the maximum power point tracking capability are used. The grid side converter works coherently with the generator side converter. It regulates the grid currents through a low pass filter with different filter topologies. The loads where the WECS is connected can be a large power network, a local load or a micro-grid.

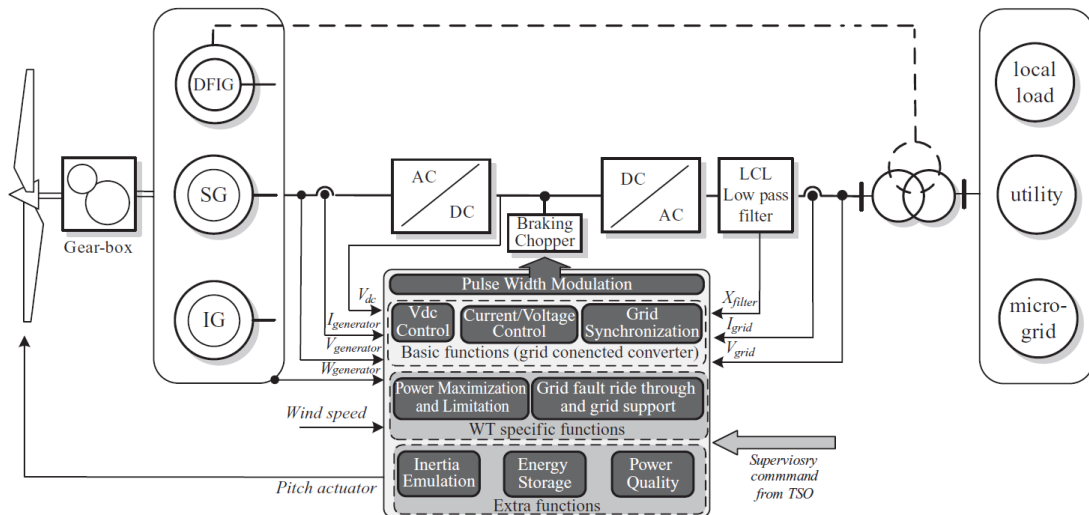


Figure 2.22 A general design schematic of a WECS [26]

The WT topology investigated in this section is the back-to-back 2L PWM-VSI with full power rating. The generator side converter is responsible for maximum power point tracking and control of the DC-link voltage by employing flux-vector control. The grid side converter on the other hand transfers the power from the DC-link to the grid by controlling the amount of active and reactive power. This topology is a four-quadrant converter; hence, the active and the reactive power can be moved from the turbine to the grid and vice versa.

2.5.1. Requirements on the Power Converter

The grid side converter has a definite number of tasks as stated in the previous section. While fulfilling the assigned tasks, the converter has to satisfy the requirements specified by the designer/investor and the TSO. The efficiency of the converter and the grid side harmonic extent are two important requirements that the converter has to deal with. The initial cost, the failure rate, and the complexity of design are other important criteria for power converters. The demands to power electronics in a WT are summarized in Figure 2.23 [28].

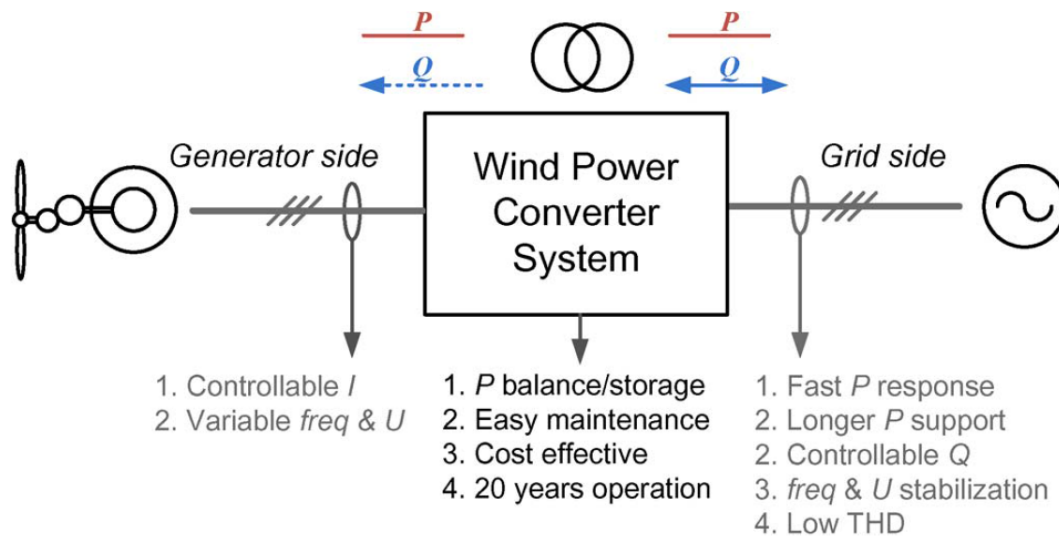


Figure 2.23 Demands to power electronics in a WT [28]

The measure of the grid side currents is the well-defined THD value which is found as the ratio of the sum of the powers of all harmonic components to the power of the fundamental frequency. Although grid codes are specified using the individual current harmonics such as 5th, 7th, 11th, etc., THD is a lot easier way of defining the harmonic extent injected to the grid. The graphical implementations are also easier to demonstrate. THD value can be reduced using passive or active filtering with additional elements or using optimized pulse patterns in the controller. A closer look on the filtering is given in the following sections.

The power conversion performance in terms of the losses produced by the converter is measured by the efficiency value. Simply the ratio of the output power of the converter to the input power gives the efficiency of the converter. Although 2L PWM converter is the most adopted topology in the wind energy market, a trend towards multilevel converters with MV connection is observed. By increasing the voltage level, the current flowing through the semiconductors and filter elements are reduced. Therefore, the efficiency level is boosted beyond 98-99%.

The initial cost of the converter depends on the price of semiconductors, passive elements, voltage/current sensors, and electronic boards. Both the engineering and

the technician's effort to combine all the distinct elements of the converter should also be included in the initial cost.

The voltage/current stresses and the reliability of the individual components are determining factors for defining the failure rate of the converter. The comparison of power semiconductors utilized in high power wind energy conversion applications is stated in [28]. IGBTs are widely used in WECS applications; however, press-pack technology offers a higher power density, enhanced cooling performance, and reliability. Press-pack IGCTs are mostly used in oil and gas industry and they are newly adopted in WECS. IGCTs offer to extend the use of 2L PWM-VSIs for high power applications. Generally, the design limitation of LV converters is around 3 MW. For applications from 3 MW to 7 MW, MV converters are adopted since current limitations on the semiconductor devices do not allow to use single-cell LV converters.

Design complexity is a relative issue addressing the controller and hardware design. As the penetration of power electronics to the WECS increases, the topologies used in the previous designs are updated or totally abandoned. Starting from thyristors-based soft-starters and rotor resistance controllers, modern WECS employ back-to-back power converters either in partial-scale or in full-scale. The most adopted topology in the best-seller range, 1.5 MW – 3 MW for a WT is 2L back-to-back PWM-VSI. The design of such converters is settled and the design complexity is minimized. For multilevel converters or matrix converters emerging as power converter solutions, the design complexity in the hardware is increased. On the other hand, the control structure of multilevel converters is more or less the same for 2L or 3L converters; however, the number of switches increase and the capacitor balancing problems arise for multilevel structures. The computational load and the number of peripheral interface for matrix converters as well as multilevel converters increase. The lower demands for the electronic boards may be an advantage for 2L converters. The software implemented on the controller boards is also easier for 2L converters.

Apart from the abovementioned issues, the grid side converter should also control the reactive power and satisfy a fast real power response. The full-scale power

converters can deliver the reactive power up to full generator's rating while partial-scale power converters used in DFIGs can deliver the reactive power only at 30% of the generator's rated power. The dynamic performance of the grid side converter for a step load change is investigated as a measure of fast real power response.

By considering the requirements on the power converter and the installed capacity of the WT, converter topologies are described. In the next section, the topology of the power converter is determined using the numerical data collected from the biggest WT manufacturers.

2.5.2. Determination of the Converter Topology

The market shares of the biggest WT manufacturers according to BTM Consult are given in Figure 2.24 below [30]. The research is based on the installed capacity of wind power and conducted in 2014.

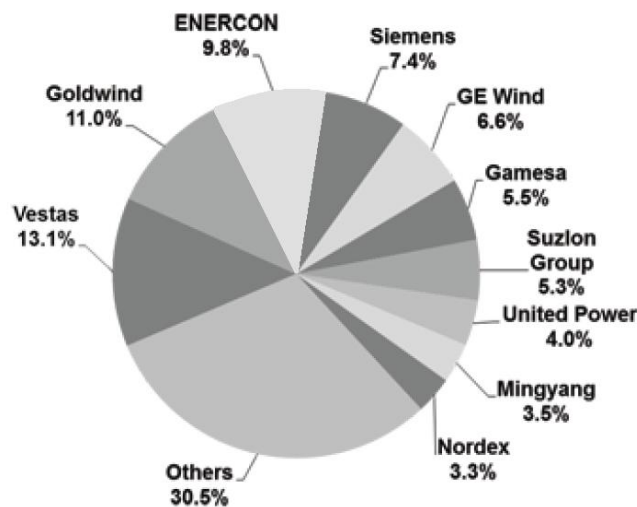


Figure 2.24 Market shares of the WT manufacturers based on the installed capacity

The market leaders adopt different WT topologies each having advantages and disadvantages. As the grid codes require full reactive power support, DFIGs have a

limited use. The implementation of variable speed WTs with full-scale converters is adopted. Enercon and Siemens use heavier and more expensive multi-pole generators (MPGs) instead of externally excited wound rotor synchronous generators (WRSGs) or permanent magnet synchronous generators (PMSGs). The benefit of using a multi-pole generator is the elimination of gearbox which costs around 12% of the overall WT's cost. The voltage for full-scale power converters can be LV with 690 V_{rms} or MV with a few kilovolts. In the near future, the voltage level may increase suitably to get directly connected to the distribution network without transformers.

The nameplate data of WTs and WT generators from various manufacturers [31]-[40] are summarized in Table 2.4. The applications both in LV and MV are considered. Among the tabulated generators, PMSG with 3 MW rating is highlighted due to high efficiency and the wide use in WTs. The voltage level of the generator is selected as 690 V_{rms} to comply with the LV specifications. The efficiency level of such machines is very high, approximately 98%.

The rated power of the WT is very important for the selection of the power converter topology. The knowledge available for 2L back-to-back PWM-VSI is extensive. Besides the robustness and the reliability of the topology is well-proven and the number of semiconductors used in the hardware are fewer. However, 2L back-to-back PWM-VSI topology suffers from switching loss phenomena as the power level increases beyond 3 MW. For LV applications, switching devices should be paralleled in order to obtain the required current level. On the other hand, switching devices should be connected in series to satisfy the voltage rating for MV applications. This, in turn, reduces the reliability and the simplicity of the converter.

Table III in [2] summarizes the commercially available WECS in the 1.5 MW – 3 MW range. The generators mostly operate at LV and the types of the generators are mainly DFIG and PMSG. The power conversion is achieved using back-to-back PWM-VSIs either in partial-scale or in full-scale depending on the generator type.

Table 2.4 Technical information on WTs and WT generators

| Manufacturer | Type Number | Generator Type | Voltage | Power level | Efficiency |
|--------------|-------------|----------------|---------------|---------------|------------|
| ABB | AMK/L | DFIG | 690-1000 V | up to 3.6 MW | 97-97.5% |
| | | | 3-6 kV | | |
| | AMG | PMSG | 690 V 4 kV | 1.5 MW-3.6 MW | 98% |
| Enercon | E | MPG | - | up to 7.5 MW | - |
| | | | | up to 12.5 MW | - |
| GE | - | PMSG | 690-14400 V | up to 12.5 MW | - |
| | | DFIG | 690-15000 V | up to 10 MW | - |
| Siemens | SWT-6.0-154 | MPG | 690 V | 6 MW | - |
| | SWT-4.0-130 | SCIG | - | 4 MW | - |
| | SWT-3.6-120 | SCIG | - | 3.6 MW | - |
| | SWT-3.3-130 | PMSG | 690 V | 3.3 MW | - |
| | SWT-3.2-113 | PMSG | 690 V | 3.2 MW | - |
| | SWT-3.0-113 | PMSG | 690 V | 3 MW | - |

Table 2.5 presents the technical data of ABB's LV full-scale wind power converters [41], [42]. The converter configuration can be either in-line or back-to-back. The efficiency level and the THD value are same for all types. Liquid cooling is preferred due to high power processed in an enclosed cabinet by the converter.

For instance, the generator is selected as 3 MW PMSG with 690 V_{rms} line-to-line voltage and the power converter shall be a 2L back-to-back PWM-VSI. The DC-link voltage of the converter is usually set as 1070 V for LV applications. The grid side converter has 6 switches each of them is constructed by paralleling two IGBTs due to current limitation of single-pack IGBTs. The maximum current rating of the commercially available IGBTs is 3600 A developed by Infineon, ABB, and Fuji. The grid side current value of a 3 MW WECS is approximately 2500 A_{rms} hence the peak current rating is above 3500 A. Single-pack IGBTs are not sufficient in terms of current rating; hence, two 2400 A IGBTs are used in parallel. The IGBTs available in the market with 1700 V voltage rating and 2400 A current rating are

listed in Table 2.6 [43]-[46]. Among them, the IGBT of Mitsubishi Electric (CM2400HCB-34N) is selected and used for the power loss analysis throughout this study.

Table 2.5 ABB's LV full-scale wind power converters

| Converter model | ACS800-77LC | ACS800-87LC | ACS880-77LC | ACS880-87LC |
|---|---|--------------|-------------|--------------|
| Converter type | Full-scale (Permanent magnet / asynchronous generators) | | | |
| Configuration | In-line | Back-to-back | In-line | Back-to-back |
| Power range | 0.6-3.3 MW | 1.5-6 MW | 0.8-4.6 MW | 1.5-8 MW |
| Cooling | Liquid cooling with totally enclosed cabinet | | | |
| Rated grid voltage | 525 to 690 V AC, 3 ph, $\pm 10\%$ | | | |
| Nominal frequency | 50 \pm 3 Hz / 60 \pm 3 Hz | | | |
| Efficiency at converter's rated point | $\geq 96.5\%$ | | | |
| Grid harmonics Total harmonic current distortion (n = 2 to 40) | Max 4% | | | |

Table 2.6 IGBT electrical characteristics

| IGBT Manufacturer | Mitsubishi | Infineon | Fuji | ABB |
|--------------------------------------|---------------|------------------|-----------------|-----------------|
| Type number | CM2400HCB-34N | FZ2400R17HP4_B9 | 1MBI2400U4D-170 | 5SNA2400E170305 |
| Collector current | 2400 A | 2400 A | 2400 A | 2400 A |
| Collector-emitter voltage | 1700 V | 1700 V | 1700 V | 1700 V |
| Collector-emitter saturation voltage | 2.1 V | 1.9 V | 2.47 V | 2.05 V |
| Base plate material | AlSiC | AlSiC | Copper | AlSiC |
| Technology | Trench gate | Trench-fieldstop | - | SPT |
| Typical gate resistance (On) | 0.8 Ω | 0.8 Ω | 1.8 Ω | 0.6 Ω |
| Typical gate resistance (Off) | 1.1 Ω | 0.4 Ω | 0.68 Ω | 0.6 Ω |

For the same 3 MW generator, 3L back-to-back converter can also be used. The IGBTs are selected as 1700 V and 2400 A with two parallel IGBTs as in the case of 2L converter. The voltage across each IGBT is reduced to $V_{dc}/2$ for 3L converter; hence, the voltage rating could be reduced down to 1200 V. Nevertheless, the reduced voltage stress on the same IGBT leads to improved life cycle. The comparison of 2L and 3L converters is presented using the same IGBTs in order not to get affected by device parameters' variation. The clamping diodes of 3L topology are selected from Mitsubishi as RM1800HE-34S with 1700 V peak repetitive voltage and 1800 A forward current ratings. The diodes are also paralleled as in the case of IGBTs due to smaller current ratings of the diodes than the nominal current rating of the converter.

The switching frequency of a 3L converter is effectively doubled at the converter's output different from a 2L converter. Due to increased switching frequency, the output filter requirements are not the same. Reduced current harmonics of 3L converter diminish the filtering requirements hence smaller filter components shall be used. Although the controller bandwidth does not change, the reduction in size of the 3L converter's output filter presents to be an attractive solution.

For higher power ratings above 3 MW, increased number of semiconductors should be paralleled or multi-cell topologies should be adopted. By increasing the converter output voltage to MV, the current rating of the converter decreases hence multilevel topologies become an apparent solution. Since the scope of this thesis does not include multilevel converters, technical analysis of multilevel converters is not covered.

2.6. Cost and Efficiency Evaluation of WECS

Recent wind turbine configurations mostly use back-to-back PWM-VSIs with full-scale power rating. Variable speed WTs allow more power integration to the grid owing to the wide range of operation starting from nearly 3 m/s up to 25 m/s wind speed. The controllability of active and reactive power together with the dynamic response offers superior advantages compared to the fix speed WTs. The reduced

power capability of the power converters employed in partial-scale WTs may become attractive; however, the design and production of a specially designed doubly-fed induction generator may be troublesome. As the cost of power converters and electric generators are very close, the benefits along with the use of DFIGs are minimal.

The cost of an induction machine (IM) and a PMSG for the same power rating are different. The rare earth magnets used in the PMSGs are relatively high in cost but the efficiency of PMSGs is about 5-7% higher for a standard 3 MW WECS. Moreover, the installation of offshore WPPs due to environmental and financial factors renders the use of maintenance-free equipments compulsory. The cost of the maintenance expenses are doubled for offshore applications compared to onshore applications. The investors therefore naturally ask for reducing the maintenance cost as much as possible. PMSGs offer cheaper maintenance and are very desirable for offshore applications.

The emerging wind energy market in China also forces the designers to develop PMSGs with higher efficiency rating. Despite the wide use of DFIGs in Europe, the new trend is to use synchronous machines with full-scale power converters. The advantages are mainly the reduced maintenance cost and the increased overall efficiency of the WECS as mentioned above. When the payback time of the system is taken into account, it is wise to employ PMSGs. Moreover, medium-voltage power conversion with reduced harmonic distortion levels is achieved seamless along with the development of multilevel converter topologies.

Since the focus of this thesis is not the economical aspects of a WT investment, a shallow knowledge on the cost and efficiency evaluation is given.

2.7. Trends in WECS

The rapid development of power electronics has led to the decrease of semiconductor devices and the increase in the power density. By reducing the volume and the weight of power electronic devices at the same power level, more

compact designs are developed recently. As the power density increase, the cooling expenses also become significant and the design of a suitable cooling method becomes substantial for safe operation of the WECS. Generally, low-voltage converters use forced air cooling while medium-voltage converters use liquid cooling.

The size and the power rating of the WTs are growing continuously over the past 35 years. The development of WTs and the utilization of power electronics capacity are shown in Figure 2.25. The most commonly used solution for WECS in the best-selling power range 1.5-3 MW is the use of back-to-back 2L PWM-VSI at both the generator side and the grid side. The biggest commercially available WT, V164-8.0 MW designed by Vestas has a power rating of 8 MW and a blade length of 80 m while other manufacturers also have WTs around 6-7 MW [47]. Samsung Heavy Industries' S7.0-171 with 7 MW rated power was the previous holder of the world's largest WT title. A European company, Enercon has also developed a 7.5 MW WT for onshore applications. 10 MW turbines, Sea Titan designed by AMSC and ST10 designed and developed by Sway having rotor diameters of 190 m and 164 m respectively are the biggest WTs which are not commercialized yet [48]. As newer designs are on the way, the power rating of the WTs tends to increase further than 10 MW in the near future.

The increased power levels beyond 3 MW nullify the use of single-cell 2L PWM-VSIs. Instead, multilevel converters with three or more levels are utilized. A newly developed five-level (5L) topology offers reduced harmonic content on the output current and transformerless DC supply [49]. The voltage level is increased up to 6kV at the converter's output to make use of high-voltage semiconductor switches. The topology is applied as back-to-back for multi-megawatt industrial motor drives. The major applications include cement, mining, metal industries, and power generation as fan or pump drive. Such a topology could also be used in WECS for a direct drive WT.

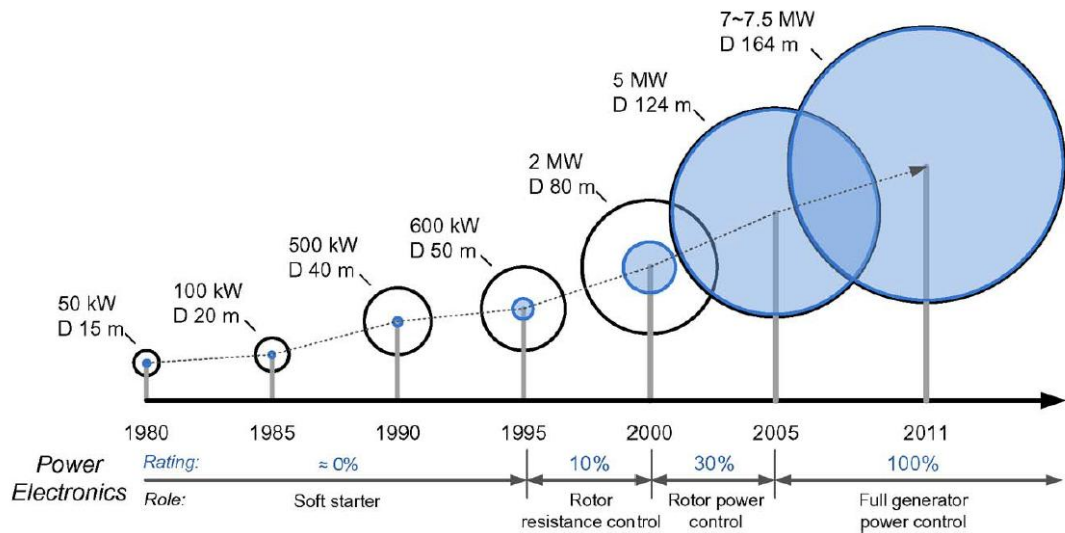


Figure 2.25 Development of wind turbines [28]

Individual WTs used in the past are replaced with MW-size WTs combined in onshore and offshore wind power plants (WPPs). The grid integration of wind power is therefore increasing continuously. The unpredicted nature of the wind power deeply affects the stability and the security of the grid. The future challenges of the WECS are mainly the integration of wind power to the existing distribution network and the regulation of the WPP as a conventional power source. As the grid connection requires that WTs stay connected to the grid in the event of a grid fault, the control of power electronics is a major issue.

The HVDC networks for the connection of large scale WPPs present a new and attracted solution delivering only DC power to a common grid. The conversion expenses of the wind power get reduced as well as the transmission expenses. The receiver of the grid power is responsible for satisfying the grid codes while the WECS are only responsible for extracting the maximum available power.

The improvements of the present designs could be estimated in the future. The development of novel semiconductor switches and the use of diverse materials for the passive elements in order to increase the power density, provide the cheapest and the most reliable solution will be the main motive.

The challenges related to technological developments are to reduce the uncertainties come up so far, to develop more optimal, reliable technology, to improve the grid stability, to build up larger and more silent WTs, to establish easily maintained hybrid systems for isolated grids in rural areas and to develop technologies allowing the integration of variable energy sources such as HVDC transmission, energy storage facilities, compensation devices used to regulate voltage, frequency, power factor, and voltage unbalance, and production forecasting.

Further research topics in power electronics for WT technology can be stated as [16]:

- Practice and analysis of switched reluctance machines and transverse flux machines for high power WTs,
- Optimization of back-to-back PWM-VSIs,
- Study and analysis of matrix converters and multilevel converters in WECS,
- Introduction and diagnosis of novel power converter topologies.

Regarding the wind power integration to the utility network, dynamic operation under normal operation and fault events, droop control strategy, energy storage systems, grid stability, and standardization of wind energy requirements may be highlighted as further research areas.

2.8. Summary

An overview of WT concepts both on recent configurations and earlier designs, grid codes required for wind power injection to the utility network, frequently used topologies on power electronic converters, cost and efficiency evaluation of WECS, and lastly future studies and trends in WT design are stated in this chapter.

The importance of variable speed WTs in capture of maximum available wind energy is stated. The advantages and the disadvantages of WTs using DFIG with partial-scale converter and full-scale back-to-back PWM-VSI are pointed out clearly.

Power quality issues with respect to the international standards (IEC 61400-21, IEEE-STD-519, etc.) are mentioned. The voltage at the PCC should have certain characteristics not to disturb sensitive loads of the consumer. The origins and the causes of these disturbances as well as the characteristics of them are summarized in a table. The devices utilized to enhance the power quality are described by considering the disturbances encountered on the utility network. Moreover, grid connection requirements set by the TSO are covered for the distribution network in Turkey. As the most important regulations, the active and reactive power control, reactive power exchange, and fault ride-through capability are highlighted. The characterization of the grid behavior is expressed using the SCR definition and current distortion limits depending on the SCR value are stated.

The topologies used as the power electronics converter from the generator side to the grid side are described briefly. Additionally, the comparison of matrix converter, tandem converter, resonant converter, multilevel converter, and state-of-the-art back-to-back PWM-VSI with advantages and drawbacks for each one is carried out. The dominant use of PWM-VSIs in WTs makes it a reference in a benchmark to the other converter topologies. The number of active and passive elements, the ease of hardware and controller design, the ratings of the semiconductors, harmonic performance, and efficiency are the aspects of the comparison.

The evaluation of the most important topologies used in recent WTs is given regarding the cost and the efficiency. Despite the initial investment cost disadvantage, long term profit of the PMSG with back-to-back PWM-VSI based power conversion topology is emphasized. The technical data of commercially available WT generators and converters are presented. The selection of semiconductors for 2L and 3L converters are stated and the technical data of various manufacturers' 1700 V 2400 A IGBTs are tabulated.

Finally, the recent improvements on the power capability of WTs and semiconductor devices are stated. As the size of WTs increase year by year, the power electronics converters handling higher power should be designed and implemented. The power density and the reliability of the converters used should be improved to reduce the

design and maintenance expenses. The challenges on the power converter topology and on the integration of large wind power to the utility are expressed. Besides, further research topics in the power electronics aspect of a WT design are stated.

CHAPTER 3

DESIGN AND CONTROL OF GRID-CONNECTED PWM-VSI

A comprehensive description of a WECS including the WT topologies, grid codes, and power converter topologies is given in Chapter 2. In this chapter, a review of hardware and controller design for a back-to-back connected WECS is given. In the hardware part, the selection of switching frequency, controller and grid side filter is given. Moreover, calculation of DC-link capacitor value and *LCL* filter parameters is explained in step by step. On the other hand, converter control structures used in the simulation studies are analyzed deeply in the controller design part. AC grid currents controller, DC-link voltage controller, and phase locked loop designs are given. Brief information on the stability assessment is also given.

The efficiency target especially for high power systems is very important. The losses are mainly converted to heat hence the cooling expenses are increased. Therefore, the efficiency criterion can be thought as the origin of the converter design. Then, the determination of the switching frequency with a suitable topology is accomplished using efficiency curves. The calculation of DC-link capacitors and appropriate *LCL* line filters to mitigate the harmonics is described in a guiding manner.

The WECS analyzed in this thesis is mainly full-scale back-to-back connected 2L PWM-VSI connected to the grid via *LCL* filter. The grid side converter and the grid interface are the focus of this thesis. The PWM-VSI is a frequently used topology as it is stated in the previous chapters. The *LCL* filter as the grid side harmonic filter has been used widely rather than standard *L* filter in recent years [3]-[6], [8], [50]-[55]. The inherent resonance problem of the *LCL* filter presents a challenge that has to be dealt with. Hardware solutions with additional passive elements or alternative

control methods are proposed in the literature to suppress the resonance effect [56]. The proper design of the *LCL* filter is important for grid current regulation. By taking the grid codes into account, *LCL* filter design is reviewed in this chapter.

3.1. System Description

This study is interested in the grid current regulation of the WECS and the generator side is not in the scope hence the wind power, the generator and the generator side converter is simply modeled as a current source as it is shown in Figure 3.1. The aerodynamic speed regulation strategies related to the wind turbine and the maximum power point traction (MPPT) algorithms dedicated for the generator side converter are omitted in this study.

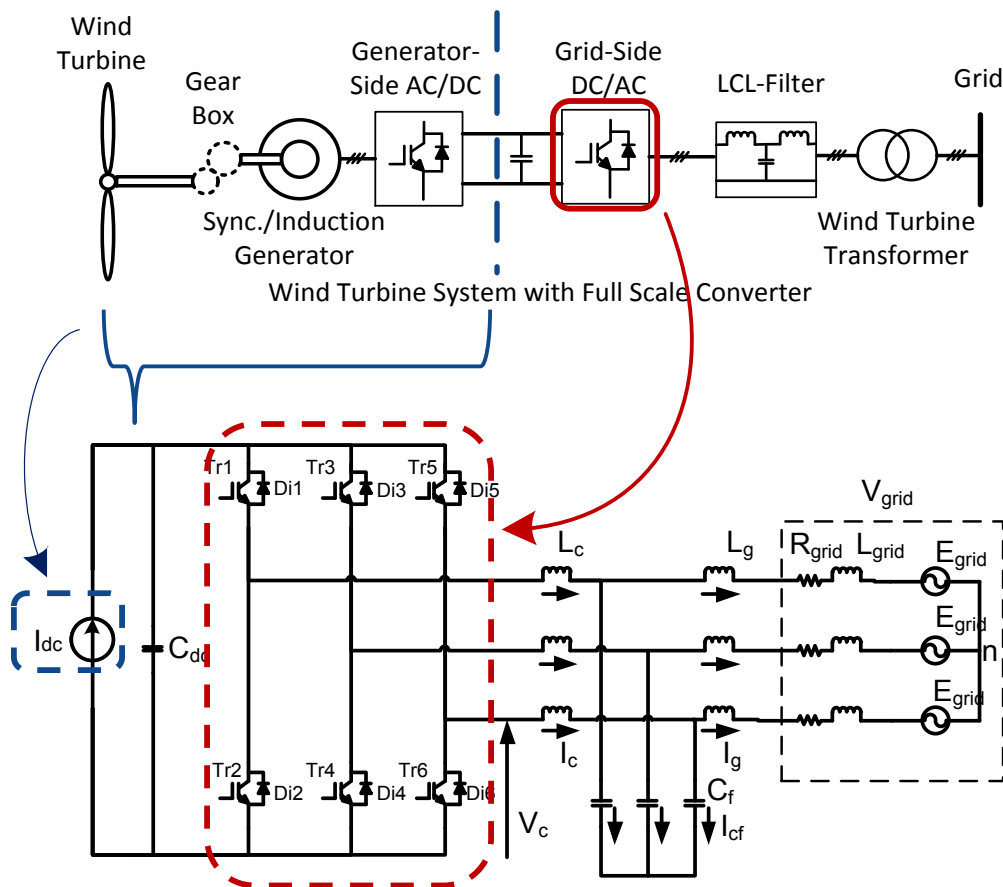


Figure 3.1 Full-scale WECS analyzed in this thesis

The grid side PWM-VSI has six semiconductor switches, a DC-link capacitor, and necessary amount of current/voltage transducers. The grid connection to the LV side of a step-up transformer is accomplished via an *LCL* filter. The ideal *LCL* filter composed of converter side inductor, L_c , grid side inductor, L_g , and the filter capacitor, C_f consumes only reactive power; nevertheless, the components designed in practice have resistive parts and filter consumes active power as well. Winding resistance and core loss of inductors together with equivalent series resistances (ESRs) of capacitors are neglected throughout this thesis, presenting a worst case scenario. The parameters of the step-up transformer are also neglected, equivalent L_{grid} and R_{grid} parameters are used to model both the grid and the transformer instead. The voltage rating of the DC-link, line-to-line voltages of the grid and depending on the control strategy, converter side currents or grid side currents are measured. With all these feedbacks, complete state space representation can be driven and the controllers can employ the proposed algorithms.

Depending on the hardware limitations and control preferences, converter current feedback (CCF) or grid current feedback (GCF) methods can be adopted [5], [6], [51], [52]. Moreover, a trade-off between resonance damping property of the controller and the dynamic response of the system occurs regarding the selection of feedback variable. For industrial applications, currents sensors may be embedded in the hardware at the converter side for protection purposes or the grid may not be reached easily to place the sensors. Such limitations guide the designer to use CCF rather than GCF. On the other hand, WECS should provide unity power factor operation which may not be possible due to the phase shift property of the grid side harmonic filter. GCF obviously provides an advantage on power factor since the controlled variable and the output of the system are the same. All in all, the requirements of the design determines the control type yet designs involving both the grid side and the converter side current sensors are available in the literature. The controller design in this study applies GCF; nevertheless, CCF is also applied to distinguish the differences between two methods where necessary. A comprehensive research on this subject is conducted in [56].

3.1.1. Determination of the Switching Frequency

Having selected the converter topology, DC-link voltage value, and semiconductor devices, now the switching frequency of the converter shall be decided. The efficiency target is the primary source of selecting a suitable switching frequency. In this section, a variety of switching frequencies is applied on the 3 MW PWM-VSI to demonstrate the effect on the efficiency.

The switching frequency is determined together with the modulation strategy. High power inverters have a limited frequency bandwidth due to low frequency switching and the output current distortion levels are excessive. Therefore, optimized pulse patterns to eliminate specific harmonics such as 5th or 7th can be used to reduce the grid side filter size. However, carrier based modulation strategies are utilized often. Recently, space vector modulation (SVM) techniques are more preferred to conventional sinusoidal PWM (SPWM). Two commonly utilized SVM techniques, namely space vector pulse-width modulation (SVPWM) and discontinuous PWM1 (DPWM1) methods are compared in terms of efficiency via visual aids.

An exemplary WECS topology determined on the previous section was 2L PWM-VSI with 690 V_{rms} grid voltage and 1070 V DC-link voltage. The study is narrowed down to a specific problem to present a complete illustration. In Figure 3.2, efficiency curves when SPWM, SVPWM, and DPWM1 methods are applied on the proposed PWM-VSI are seen for a variety of switching frequencies. The conduction and the switching losses of the semiconductors and grid side filter losses are considered through the efficiency analysis demonstrated in Figure 3.2. Semiconductor losses are calculated using Melcosim, developed by Mitsubishi Electric Corporation.

Obviously, DPWM1 is superior to both SPWM and SVPWM in term of efficiency according to Figure 3.2. The difference in efficiency ratings of SPWM and SVPWM is so small that two curves are seen on top of each other. As the voltage modulation index is constant, the benefits of SVPWM are not revealed. For overmodulation region (i.e. voltage modulation index is greater than “1”), SVPWM is advantageous

over SPWM but the grid voltage is fixed and the inverter does not enter overmodulation region. Selecting the switching frequency as 1.2 kHz with DPWM1 technique gives the efficiency close to 99% by considering the grid side filter losses.

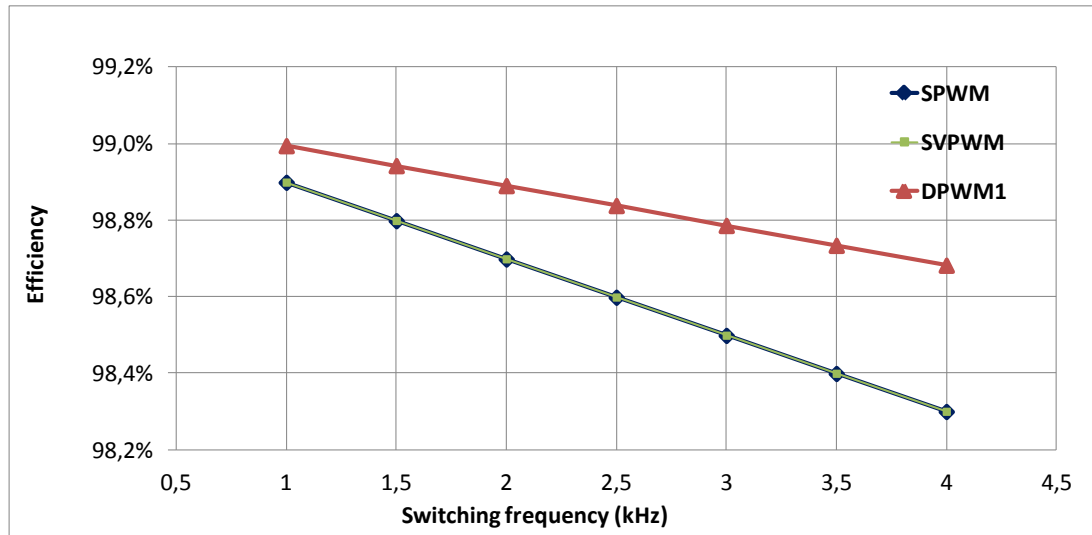


Figure 3.2 Efficiency analysis of 3 MW 2L PWM-VSI for SPWM, SVPWM, and DPWM1 methods

3.1.2. Determination of the Controller

The controller type is also an important part of the converter design process. Two subsystems, namely the electrical and mechanical ones composing the WECS are specified by different control goals but the main aim is to control the power injected to the grid. Direct torque control (DTC) with a very fast response is generally applied in the generator side converter. Grid side converter; on the other hand, employs synchronous frame PI regulators.

Grid side converter controls the current and voltage harmonics strictly limited by the grid codes for multi-megawatt WTs. The modulation technique is a determining factor for the harmonic levels at the grid side as discussed in the previous section. Grid currents can be regulated using voltage oriented control or adaptive band

hysteresis current control. Detailed information on voltage oriented control is given in this chapter. Adaptive band hysteresis current control provides a very fast response current loop [57]. The varying frequency due to fixed hysteresis band makes the design of the grid side filter hard. With the adaptive hysteresis band implementation, the problem is solved. DC-link voltage control is similar to voltage oriented control algorithm and the controller operates in synchronous reference frame as well.

Due to implementation easiness on 2L PWM-VSIs, synchronous reference frame voltage oriented control is chosen. The control of the grid side converter needs a number of voltage/current sensors. A voltage sensor across the DC-link capacitor, at least two voltage sensors between the successive grid phase terminals, at least two current sensors on the phase lines and at least one current sensor on the DC-link lines for the protection of the DC-link is needed. DC-link voltage controller utilize the voltage across the DC-link as the feedback while PLL block requires at least two phase voltages to obtain the phase angle. Grid side currents or converter side currents are measured as the main feedback variable for current controller. A detailed discussion on the grid current feedback (GCF) and converter current feedback (CCF) is also given in this chapter.

3.1.3. Determination of the Grid Side Filter

The role of grid side filters for VSI based converters is twofold. First, the grid side filter provides a dominant inductive behavior to guarantee the proper operation when connected to the utility. Second, PWM carrier and sideband harmonics generated by the converter are removed not to affect sensitive loads connected to the same network. A simple L filter provides these two requirements; however, the application of L filters is very limited for modern WECS.

Current harmonic levels at the grid side can be a problematic issue especially for high power systems. The attenuation of current harmonics is provided by passive filters. The reduction in the switching frequency and high grid currents make the design of the grid side filter very difficult. The realization of the L filter with high

inductance to meet the demands of standards and grid codes is quite expensive. The dynamic response of the system also becomes poorer.

At the system level, disturbances created by some specific harmonics can be deteriorated by employing a bank of tuned LC trap filters. Nevertheless, low-pass filter attenuation is required due to the fact that grid codes are very stringent for frequencies above a defined threshold. A higher order LCL filter could replace standard L filter in terms of harmonic attenuation capability and LC trap filters in terms of grid code compliance. The schematic of LCL filter and bank of LC trap filters are shown in Figure 3.3.

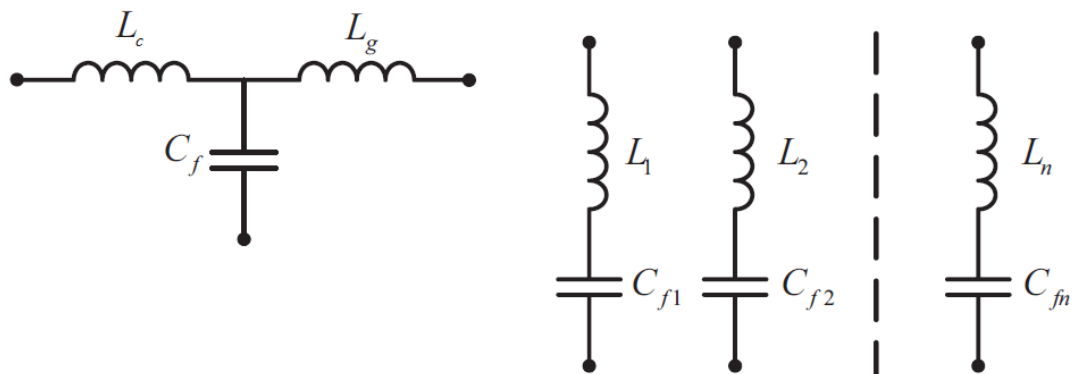


Figure 3.3 LCL Filter and bank of LC trap filters

If the converter's switching frequency is at hundreds of Hz, the tuning of LCL filter is very difficult that LC trap filters are used. Unlike tuned LC filters, LCL filters act on the whole frequency spectrum. The general design process of LCL filter is given in the following section. Solutions to inherent resonance problem of the LCL filter are given in Chapter 4 and these methods are verified with simulation results on a 3 MW WECS in Chapter 5.

Before going into detail on the design and the control aspects, the models of the standard L and the LCL filters are presented. Then cascaded control structure in dq -frame synchronous to the grid frequency is stated. Two main issues related to the

control of the PWM-VSI are stated: the control of the DC-link voltage and the control of the AC currents flowing to/from the grid.

3.1.4. Mathematical Model of the L Filter

When the converter is connected to the grid via L filter, the following equation is used to state the grid current which is the main control parameter.

$$V_c(t) = E_{grid}(t) + R_{grid}i(t) + (L_{grid} + L) \frac{d}{dt} i(t) \quad (3.1)$$

$$\frac{d}{dt} i(t) = \frac{1}{L_{grid} + L} [-R_{grid}i(t) - E_{grid}(t) + V_c(t)] \quad (3.2)$$

The output voltage of the converter, V_c , the grid voltage, E_{grid} , and the inverter's output current, i are the space vector parameters in (3.1). The state-space form of the equation is given in (3.2).

$$Y_L(s) = \frac{I(s)}{V_c(s)} = \frac{1}{sL} \quad (3.3)$$

The L filter whose transfer function is shown in (3.3) is a first order filter, having no cut-off frequency and the harmonic elimination performance of the filter is limited. For a certain frequency, the harmonic attenuation capability of the filter can only be increased by increasing the inductance value. In order to obtain a pure sinusoidal output waveform, the inductance value should be arranged such that the undesired harmonic components occurring in the frequency spectrum are at higher frequencies than the L filter's gain crossover frequency (frequency occurring at 0 dB). The fundamental current component and its multiples can be controlled using the current regulators; however, high frequency harmonics due to switching of the semiconductor switches are not directly controlled by the current regulators.

Although there are different modulation techniques producing a reduced amount of harmonics, current regulators are designed in the low frequency domain (grid frequency) and are not responsible for eliminating the switching harmonics.

3.1.5. Mathematical Model of the *LCL* Filter

For the current control analysis, it is necessary to state the model of the *LCL* filter. The outer DC voltage control loop also needs the current loop model. Accordingly, the continuous (s-domain) model of the *LCL* filter applying Kirchhoff's laws can be obtained. Time domain equations to find the s-domain model are shown in (3.4).

$$\begin{aligned}\frac{d}{dt} i_g(t) &= \frac{1}{L_{grid} + L_g} \left(V_{C_f}(t) - E_{grid}(t) - R_{grid} i_g(t) \right) \\ \frac{d}{dt} i_c(t) &= \frac{1}{L_c} \left(V_c(t) - V_{C_f}(t) \right) \\ \frac{d}{dt} V_{C_f}(t) &= \frac{1}{C_f} \left(i_c(t) - i_g(t) \right)\end{aligned}\tag{3.4}$$

With the state space vector defined as $x = [i_g \ i_c \ V_{C_f}]^T$, the simplified state space representation of the *LCL* filter is given below as

$$\begin{aligned}\dot{x}(t) &= A * x(t) + B * V_c(t) \\ y &= i_g(t) = C * x(t)\end{aligned}\tag{3.5}$$

with *A*, *B*, and *C* matrices defined below.

$$A = \begin{bmatrix} 0 & 0 & \frac{1}{L_g} \\ 0 & 0 & -\frac{1}{L_c} \\ -\frac{1}{C_f} & \frac{1}{C_f} & 0 \end{bmatrix} \quad B = \begin{bmatrix} 0 \\ \frac{1}{L_c} \\ 0 \end{bmatrix} \quad C = [1 \quad 0 \quad 0]$$

The state space representation in dq -plane is also demonstrated for better understanding of the current controller after the presentation of space vector transformations. For ideal grid conditions (i.e. grid impedance is omitted), the grid side is assumed to be short-circuit as shown in Figure 3.4. The s-domain transfer function of the LCL filter is simply derived from the state space representation as in (3.6) from the output variable, i_g to the input variable, V_c .

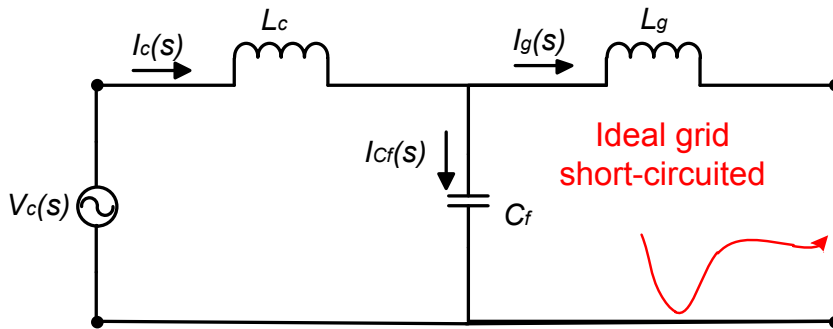


Figure 3.4 The basic LCL filter configuration with short-circuited grid side

$$Y_{LCL}(s) = \frac{I_g(s)}{V_c(s)} = \frac{1}{s^3 C_f L_c L_g + s(L_c + L_g)} \quad (3.6)$$

3.1.6. Frequency Characteristics of the LCL Filter

By observing the transfer functions (3.3) and (3.6) as “s” approaches to “0”, it can be said that the LCL filter converges to L filter for low frequencies. The capacitance has a negligible impedance at low frequencies (i.e. grid frequency) hence the LCL filter

is equivalent to L_c+L_g . Above the resonant frequency shown in Figure 3.5, the capacitor impedance decreases further and the harmonic attenuation capability of the filter rises from 20dB/dec to 60dB/dec. The resonant frequency defined in (3.7) is the minimum impedance point of the LCL filter. The filter has zero impedance ideally; however, ESRs of the capacitors and the winding resistances of the inductors prevent this. These non-zero impedance paths favor the resonance suppression yet create power losses. The values of the filter's intrinsic resistors are not sufficient to damp the resonance hence the harmonics produced by the PWM-VSI or grid originated harmonics around the resonant frequency are amplified through the LCL filter.

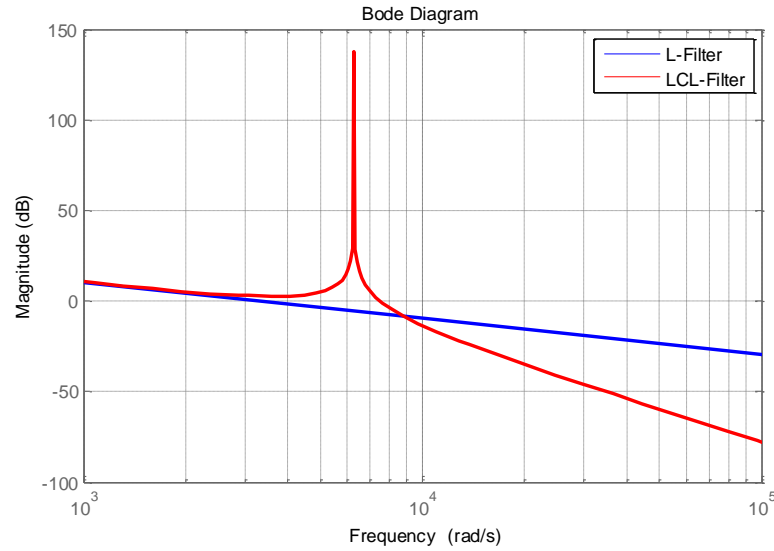


Figure 3.5 The frequency characteristics of the L filter and the LCL filter

$$\omega_{res} = 2\pi f_{res} = \sqrt{\frac{L_c + L_g}{L_c L_g C_f}} \quad (3.7)$$

The harmonics generated by the converter constitute a resonance problem, the result of which is shown on the grid side current in Figure 3.6 below. The excessive

amount of harmonics seen on the line current leads to current stresses on the semiconductors. The voltage across the filter capacitor contains harmonics as well. The voltage level shown in Figure 3.7 exceeds the DC-link voltage and the rated voltage of the semiconductor switches. These overvoltages as well as the overcurrents are harmful for the semiconductors and leads to the failure of the overall system eventually. In order to prevent the resonant harmonics, active or passive damping measures should be taken.

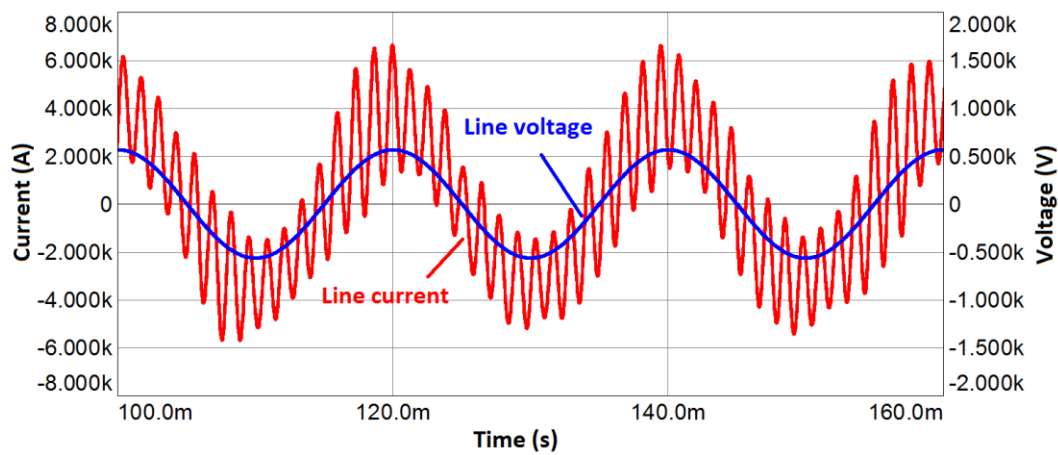


Figure 3.6 Grid side voltage and current waveforms of the insufficiently damped *LCL* filter

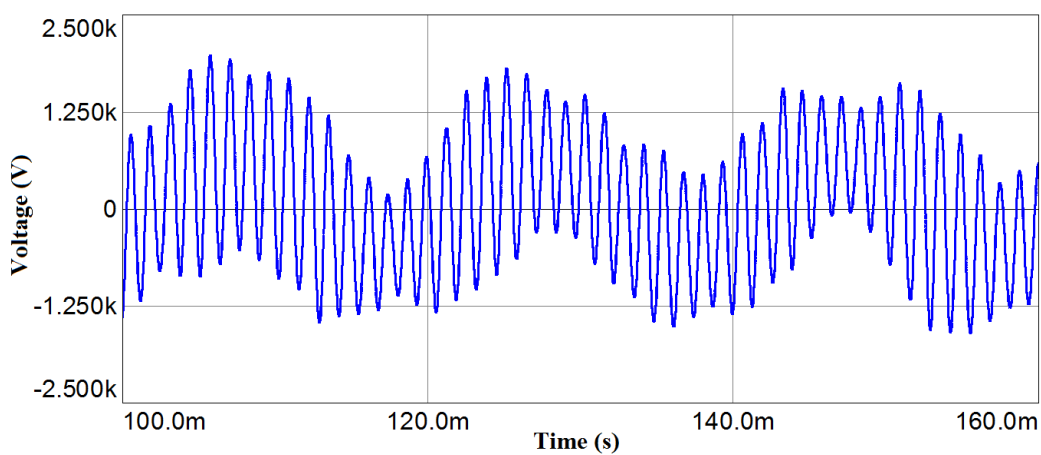


Figure 3.7 Capacitor voltage waveform of the insufficiently damped *LCL* filter

As the easiest way of providing the necessary damping, a non-zero impedance path is created for the current components creating the resonance. This can be achieved by simply adding a resistor in series with the filter capacitor. There are many alternative ways to provide damping which are discussed with all details in Chapter 4. The additional resistor is called the damping resistors, R_d and the schematic of this basic configuration is shown in Figure 3.8.

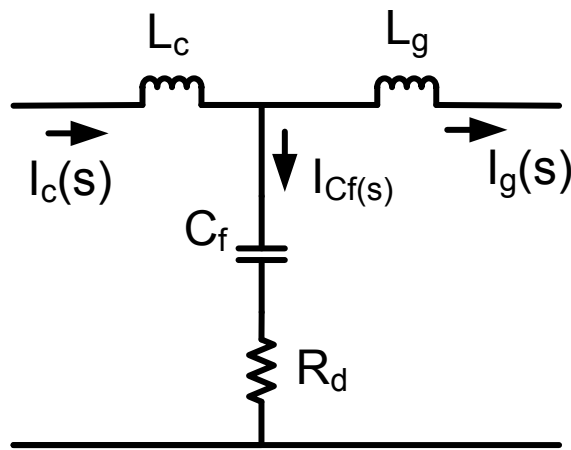


Figure 3.8 The simple passive damping schematic

The simple passive damping solves the inherent resonance problem of the *LCL* filter at the expense of resistive power loss. After the implementation of passive damping (PD), the line currents are regulated and the undesirable effects due to the resonant harmonics are eliminated as it is proven in Figure 3.9.

The ESR of the filter capacitor has a positive effect on the suppression of resonance since it is also in series with the filter capacitor. Intentionally, inserting filter capacitances with high ESRs may seem to be an option; however, the temperature rise on the capacitors due to the conversion of electrical energy into heat on the internal resistances is not desired. Additional cooling expense may come up to reduce the heat on the capacitors since commercially available capacitors generally operate up to 70 °C.

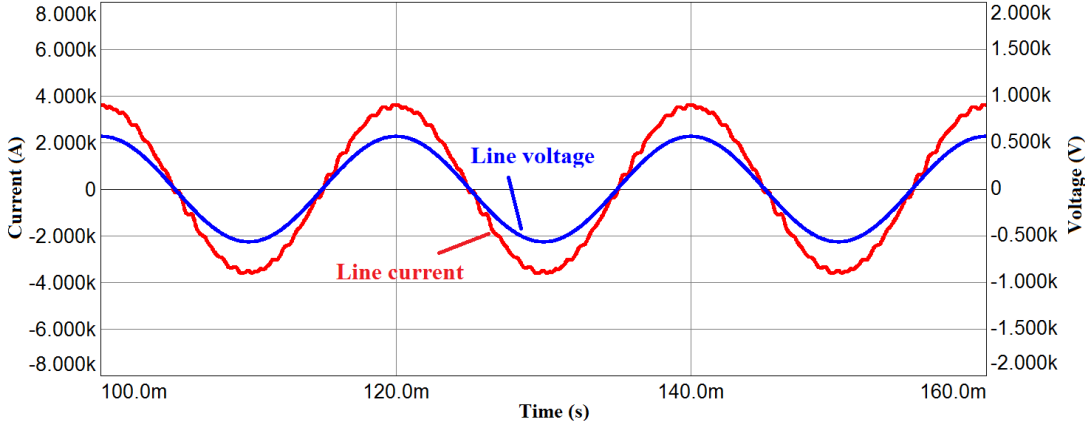


Figure 3.9 The extinction of resonant harmonics after the implementation of simple passive damping

The modified transfer function of the LCL filter including the series damping resistor is found as

$$Y'_{LCL}(s) = \frac{I_g(s)}{V_c(s)} = \frac{sC_f R_d + 1}{s^3 C_f L_c L_g + s^2 C_f R_d (L_c + L_g) + s(L_c + L_g)} \quad (3.8)$$

As it is observed from the above transfer function, the presence of the term with s in the numerator leads to noticeable degradation in the filter performance. The 3rd order characteristic of the filter now decays down to 2nd order at high frequency range. Nevertheless the term with s^2 in the denominator provides the necessary damping physically. The damping coefficient of the filter is also found as

$$\zeta = \frac{C_f \omega_{res} R_d}{2} \quad (3.9)$$

A deeper analysis on the passive damping is given in Chapter 4 together with advanced passive damping methods.

3.2. Hardware Design Review

In this section, the selection of DC-link capacitor and the design of *LCL* filter using the classical approach are given. DC-link capacitor design is not in the scope of this study; however, the basics of DC-link capacitor selection are reviewed to present a top to bottom design example.

3.2.1. DC-link Capacitor Design Review

DC-link capacitor is selected by considering the current drawn from the capacitor due to PWM operation of the grid side converter and the DC-link voltage rating. The capacitor bank shall provide the necessary power exchange from the generator side to the grid side and vice versa. The equation in (3.10) can be used for the calculation of DC-link capacitor value [58]. The peak-to-peak voltage ripple, V_{ripple} shall be defined first and the switching frequency of the PWM rectifier is needed.

$$C_{dc} = \frac{P_{rated}}{V_{ripple}V_{dc}f_{sw}} \quad (3.10)$$

With the assumption of grid side and generator side converters having the same switching frequency around 1.2 kHz, the DC-link capacitance is found as 11 mF for 10% peak ripple. The voltage rating of the DC-link is set as 1070 V throughout this study.

A suitable capacitor bank is formed using the rms current through the capacitor, I_{cap} information given in (3.11). The current through the capacitor is found approximately as 6250A using the abovementioned data.

$$I_{cap} = \frac{V_{ripple}C_{dc}\pi f_{sw}}{\sqrt{2}} \quad (3.11)$$

Table 3.1 presents the technical information of suitable DC-link capacitors from AVX and Electronicon [59]. Film capacitors have higher power density than electrolytic capacitors. The capacitance values are four times higher and the reliability of film capacitors is superior to electrolytic ones. Besides, the voltage handling capability of film capacitors is two times the rated voltage. Therefore, electrolytic capacitors are replaced by film capacitors in the industrial market.

Table 3.1 Technical information of suitable DC-link capacitors

| Type number | E50.M13-184NT7 | FFLC6U1757K-- |
|-------------------------------------|----------------|---------------|
| Capacitance value (μF) | 175 | 1750 |
| Tolerance on capacitance (%) | 10 | 10 |
| Rated voltage (V) | 1300 | 1200 |
| Max rms current (A) | 60 | 300 |
| ESR ($\text{m}\Omega$) | 1.2 | 0.41 |
| Stray inductance (nH) | 40 | 35 |

The number of parallel and series capacitors is selected using the rated capacitor voltage and capacitance value. The selection of Electronicon DC-link capacitors leads to parallel connection of roughly 63 capacitors whereas only 6 capacitors are needed when AVX DC-link capacitors are used. The current rating supported by the capacitor bank formed using Electronicon capacitors goes up to 3800 A_{rms} while the bank of AVX capacitors can give 1800 A_{rms} . These two ratings are below the necessary value of I_{cap} found above but the number of parallel capacitors can be increased further. As the DC-link capacitance is selected bigger, the voltage ripple on the capacitor tends to decrease. It should be noted that the value of the capacitor is limited by the cost, encumbrance and safety considerations.

3.2.2. LCL Filter Design Review

The grid side filter has two functions: one of them is to provide an inductive behavior to secure the proper operation of the PWM-VSI when connected to voltage

source loads such as the grid and the other one is to prevent the PWM voltage harmonics to flow into the grid as harmonic current which may disturb other loads connected to the same point of common coupling (PCC). The excessive amount of PWM harmonics also creates power losses on the semiconductor devices and the filter equipments. The simplest way of introducing a grid side filter is to use inductors; however, the harmonic attenuation capability of the standard L filters is very limited.

For high power applications as WECS, the switching frequency is very low and the size of the filter to meet the demands of the TSO and to comply with the grid codes is very large. It will also be quite expensive and bulky to realize higher value filter inductors. Additionally, the dynamic performance of the system may also become deteriorated. Tuned LC trap filter may also be used to limit the values of harmonics at certain frequencies but the stringent requirements of the grid codes recommend using low-pass filter structures due to limitations in magnitude for frequencies above a certain threshold. The use of high-order low-pass filters as the LCL filter provides an advantage to comply with the grid codes.

The design of a proper LCL filter requires very much attention. The movement of designed filter parameters from their origin due to aging, stray inductances/capacitances of the system or parasitic components may lead to instability of the system [4]. Such a case should be treated carefully and regarded as an important part of the WECS design.

Several design methods are presented in [3], [4] and an improved design method including the stability and controllability of the system is discussed in [56]. An overview of the conventional design algorithm should be stated at this point to complete the design process of the simulated systems. The selection of filter parameters is referred for better understanding of the difficulties in the design.

As the general design methodology is iterative and the parameters are adjusted such that certain equations or rule of thumbs are satisfied. Since the controller design is a latter design step, the filter parameters are selected so as to leave enough phase

margin for the controllers. The resonant frequency is selected away from the switching frequency in order not to cause any resonance due to controllers. Also, the harmonic attenuation of the filter increases as the resonant frequency is selected further away from the switching frequency. In such a case, the effectiveness of the filter or the controllers can be discussed. In [56], the selection of the control technique (GCF or CCF) is a prerequisite for the *LCL* filter design.

The conventional *LCL* filter design procedure is summarized step by step with the following initial design inputs:

- Rated power of the grid side PWM-VSI, P_n
- Frequency of the grid, f_g
- Voltage of the grid, V_g
- DC-link voltage, V_{dc}
- Switching frequency, f_{sw}

1st Step: Grid side and converter side filter inductances and the filter capacitance are expressed as the percentage of the base impedance, Z_b and the base capacitance values which are defined in (3.12) and (3.13) respectively.

$$Z_b = \frac{V_g^2}{P_n} \quad (3.12)$$

$$C_b = \frac{1}{Z_b \omega_g} \quad (3.13)$$

where $\omega_g = 2\pi f_g$.

2nd Step: Filter capacitance value is determined as the percentage of the base capacitor value. In general, C_f is selected in the range of 1% to 5% of the C_b to meet 0.95 to 1.00 power factor (PF) at the PCC [3]. This percentage, x is defined as the reactive power absorption ratio of the filter.

$$C_f = x C_b \quad (3.14)$$

The reactive power flow on the filter capacitor increases if x is selected higher than 5%. Consequently, the current drawn from the DC-link capacitor increases and it leads higher semiconductor and filter losses. Since the design process is iterative, the capacitance of the filter capacitor is changed several times during the design process. The amount of ripple passing from the converter side to the grid side is adjusted by varying the capacitance value.

3rd Step: By selecting the desired peak-to-peak current ripple, Δi_{max} on the converter side inductor in the range of 10% to 25%, the stresses on the semiconductors are limited. It should also be noted that the total inductance value should be less than 0.1 *p.u.* to limit the AC voltage drop on the inductances. Moreover, a higher value of DC-link voltage may be needed to guarantee the controllability of the current. For high power systems it may not be possible due to low switching frequency hence higher current ripple on the converter side in. The value of L_c can be found using the equation (3.15).

$$L_c = \frac{V_{dc}}{12f_{sw}\Delta i_{max}} \quad (3.15)$$

where Δi_{max} is expressed as 0.1 or 0.25 times the peak output current, \hat{I} .

The correlation parameter, r between L_c and L_g is defined so as to select the grid side inductance. In order to minimize the filter energy hence the filter size [3], [4], [6] r is usually selected equal to 1.

$$L_g = r L_c \quad (3.16)$$

4th Step: The current ripple attenuation given in (3.17) is calculated neglecting the losses on the filter and the damping of the filter. By considering (3.14) and (3.16) the equation can be written as

$$\frac{i_g(h_{sw})}{i_c(h_{sw})} = \frac{1}{|1 + r(1 - L_c C_b \omega_{sw}^2 x)|} \quad (3.17)$$

where ω_{sw} is the switching frequency in rad/sec.

Selecting a ripple attenuation of 20% often provides a good filtering performance and compliance with the grid codes. The r value can be increased beyond 1 but the disadvantages occurring such as the filter size, cost, and instability of the current regulators does not worth the further decrease of the current ripple on the grid side.

The ripple attenuation rate for an arbitrary LCL filter is obtained in Figure 3.10 by varying r value. The current ripple permitted to pass to the grid side can be chosen just by selecting the value of r from the related graphic.

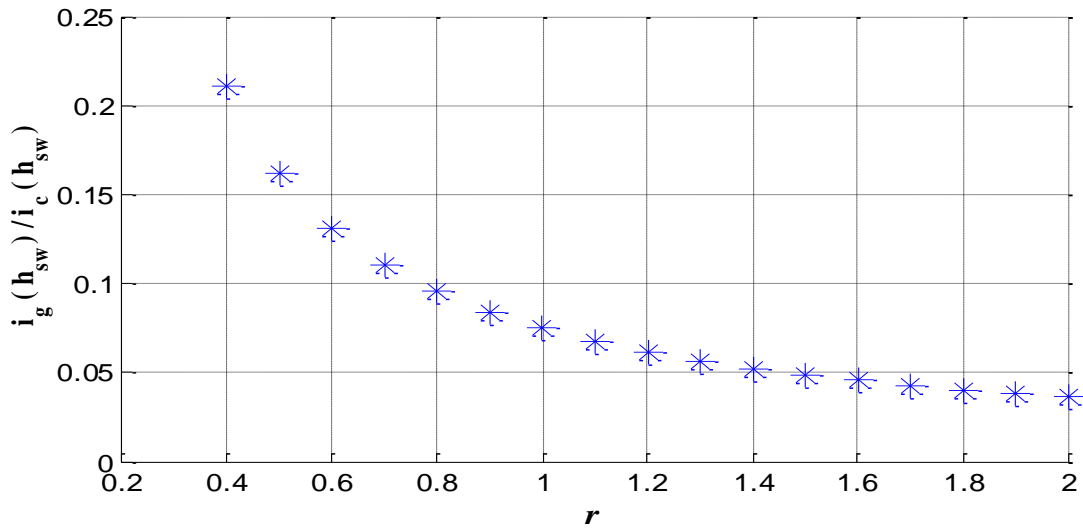


Figure 3.10 Ripple attenuation rate against r

5th Step: The resonant frequency is calculated using (3.18) and verified that the resonant frequency is in the range between ten times the grid frequency and one-half of the switching frequency as shown in (3.19).

$$\omega_{res} = 2\pi f_{res} = \sqrt{\frac{L_c + L_g}{L_c L_g C_f}} \quad (3.18)$$

$$10f_g < f_{res} < 0.5f_{sw} \quad (3.19)$$

If (3.19) fails to satisfy, the process goes back to 2nd step to update the reactive power absorption ratio (to change x) or to 3rd step to update the correlation factor between the grid side and converter side inductance (to change r value). Due to the reason stated in 3rd step, updating r value is not adopted as the first choice to comply with the requirements. As an alternative, reactive power absorption ratio can be updated assuming that the switching frequency is fixed prior to the design of the *LCL* filter.

6th Step: A necessary amount of damping should be provided to avoid oscillations. As the simplest solution to provide damping is to use damping resistors, the minimum value of the damping resistors minimizing the resistive power losses is calculated as

$$R_d = \frac{1}{3\omega_{res}C_f} \quad (3.20)$$

Although the value of the damping resistors are selected equal to the one third of the filter capacitor's impedance at the resonant frequency for low power converters [7], [60], it is not the same for medium to high power converters of several hundreds of kilowatts. It usually results for a higher damping resistor value hence higher power losses. The optimum value of damping resistors is selected using (3.21) such that the damping factor, ζ is 0.707; however, adopting the damping factor around 0.5 both provides the necessary damping and eliminates the excessive power losses on the resistors.

$$\zeta = \frac{C_f \omega_{res} R_d}{2} \quad (3.21)$$

3.3. Control Overview and Controller Design

Stabilization is regarded as the main target of the controller design procedure throughout this study. Besides, damping extent of the resonance poles are investigated and correlated with high frequency oscillations occurring at the transient periods. The stability of the controller is depicted using MATLAB[®] outputs.

The control scheme of grid-connected, *LCL* filtered PWM-VSI is shown in Figure 3.11 below. DC voltage control, power control, and grid management blocks are the main parts of the controller. Power control is simply the control of converter's output current and grid management deals with the extraction of grid phase angle.

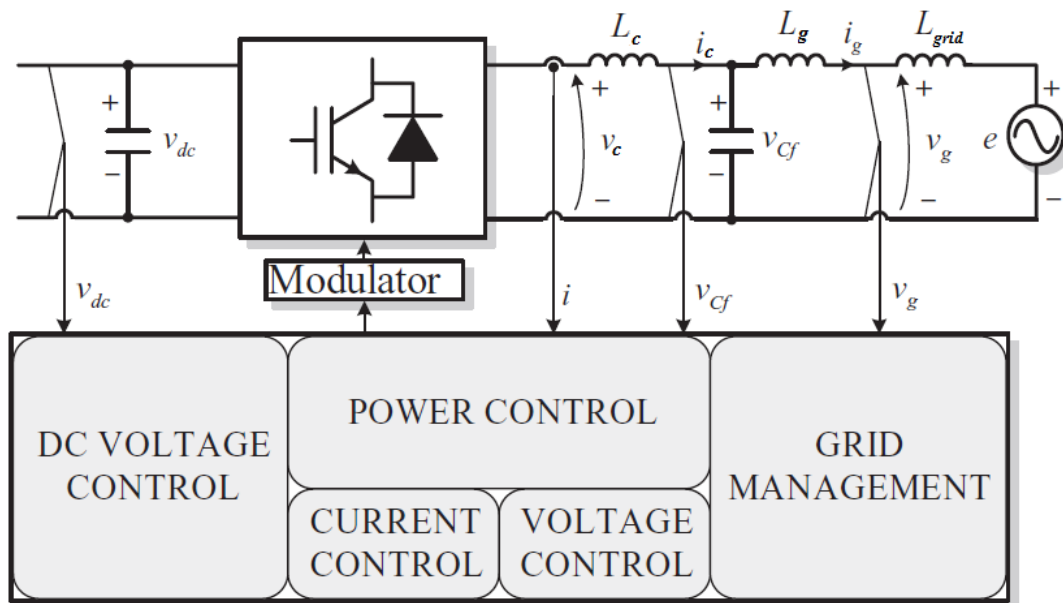


Figure 3.11 Overall control scheme of grid-connected, *LCL* filtered PWM-VSI

In this study, dq -frame controllers synchronous to the grid frequency are used. As it is shown in the control structure of the PWM-VSI in Figure 3.12, two-phase DC signals are controlled instead of three-phase AC signals by employing space vector transformations. Control of DC signals is more useful than AC signals due to well-known benefits of linear control techniques. The controllers successfully track the reference values with zero steady-state error value as the control signals are nothing but DC signals. The number of the controllers is also reduced from three to two by employing dq -frame controllers.

Figure 3.12 shows the two loop cascaded control structure of a three-phase PWM-VSI. DC-link voltage, V_{dc} is regulated by the outer control loop with the reference input V_{dc}^* . The output of the voltage control loop is the reference value of the inner current control loop. The active and the reactive components of the current feedback variable are regulated by the inner control loop. Hence, this multi loop control structure can be named as “voltage oriented current control”. Both the outer and the inner loops regulate the feedback variables in synchronous reference frame locked directly to the grid voltage vector as demonstrated in Figure 3.12.

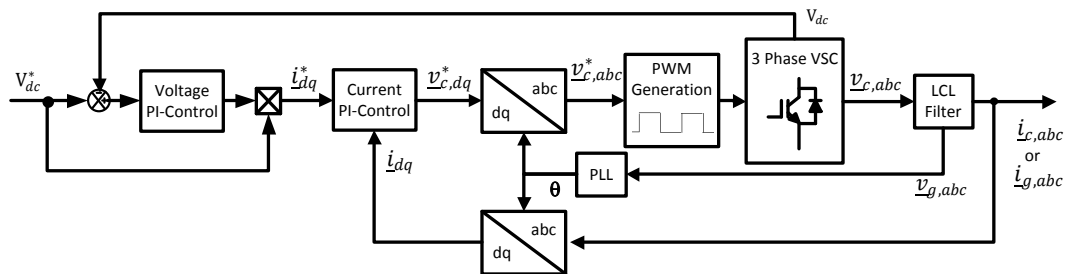


Figure 3.12 Two loop cascaded control structure

The output of the outer DC-link voltage control loop is the dq current reference vector, \underline{i}_{dq}^* for the inner current control loop. Then, \underline{i}_{dq}^* is compared with the actual value of the current feedback variable, \underline{i}_{dq} transformed into the dq -frame and the output of the inner current control loop then determines the reference value for the

dq -frame VSC output voltage vector $\underline{v}_{c,dq}^*$. Afterward, this reference voltage value is back-transformed into the stationary abc -reference frame. Finally, the three-phase voltage vector is employed to generate PWM signals for the switching of the VSC. The phase angle of line voltage vectors are obtained using phase-locked loop (PLL) algorithm stated in [61], [62]. Either GCF or CCF can be adopted as the current feedback method as shown in Figure 3.12. It should be noted that the transfer function of the LCL filter is different for each method.

The internal current loop is designed such that the settling time is short and the response of the controller is fast. The outer voltage loop on the other hand aims optimum regulation and stability. The voltage loop therefore can be designed to be slower. With different bandwidths, these two loops can be considered decoupled, and so the current feedbacks measured from either converter side or grid side are considered equal to their reference values when designing the outer DC voltage controller. The control problem is linearized with this assumption.

Voltage oriented control is generally implemented in the synchronous frame (rotating, dq -frame) with two cascaded loops as shown in Figure 3.12. Moreover, active/reactive power feed-forward terms plus the rotating frame controllers offer fast dynamic response. Since the three-phase current information is converted to two DC signals rotating in synchronous with the grid frequency, ω_g , the performance of the PI controllers increase due to the reference tracking capability of controllers with zero error in steady-state. Hence, the reliability and the simplicity of the controller are ensured. Furthermore, the decomposition of the three-phase currents into two axes makes the decoupled control of active and reactive power available.

In addition to voltage oriented controller approach with PI controller, direct power controller approach is also used in WECS designs [26]. Alternatively, stationary frame ($\alpha\beta$ -frame) voltage oriented control designs can be used leading to an indirect control. Resonant controllers; on the other hand; offer both simplicity and high performance and they are working in the stationary frame as well. Although they are not frequently used in industrial applications, adaptive band hysteresis current

control and synchronous virtual flux oriented control with PI controller can be named as other control strategies.

The transformation of coordinate system is achieved using PLL. The control structure includes the control of DC-link voltage and the AC currents in the d -axis. The reactive power and the reactive component of the current are controlled in the q -axis. The control algorithm also comprises the output filter inductance in order to achieve a high accuracy current tracking. Thus, the voltage drops on the output filter inductances are compensated by the current controllers.

An important notice on the performance of the controllers is that the accuracy of the PLL estimating the grid voltage angle is very crucial. The current controllers are easily affected by the power quality problems described in Chapter 2. For unbalanced grid condition and voltage sag or swell events, improved PLL structures are presented in [62].

Transformation of three-phase signals to two-phase synchronous signals is stated in the next section before the detailed explanation of two cascaded loops.

3.3.1. Space Vector Transformations of Three-phase Systems

A three-phase electrical system consists of a set of three voltages and three currents interacting with each other to deliver electrical power. However, a practical three-phase system cannot be considered as the simple addition of three independent single-phase subsystems. Actually, particular relations exist between the phase variables of a three-phase system, which invite the application of certain space vector transformations to obtain a more elegant and meaningful representation of its variables. Generally, the control system of a power converter connected to a three-phase system is based on these transformed variables.

Let i_a , i_b , and i_c be a set of equally spaced three-phase current vectors in abc sequence (clockwise direction) with grid frequency in the stationary abc reference frame as shown below in (3.22).

$$\begin{bmatrix} i_a \\ i_b \\ i_c \end{bmatrix} = \begin{bmatrix} \hat{I} \cos(\omega t) \\ \hat{I} \cos(\omega t - 2\pi/3) \\ \hat{I} \cos(\omega t + 2\pi/3) \end{bmatrix} \quad (3.22)$$

Firstly, these vectors are transformed into two-phase stationary $\alpha\beta$ reference frame as shown in Figure 3.13. The transformed current waveforms in $\alpha\beta$ reference frame are represented with i_α and i_β and they are also in clockwise direction.

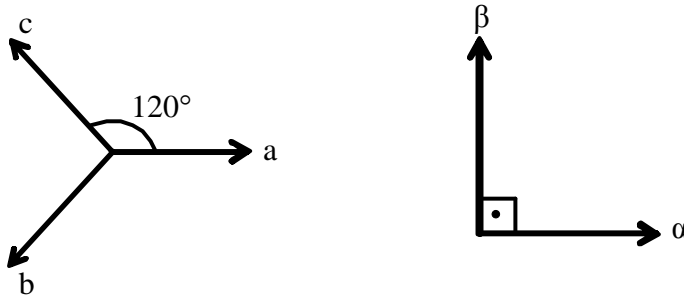


Figure 3.13 Stationary abc -frame and stationary $\alpha\beta$ -frame

By decomposing abc phase vectors on α and β axes, three equations with three unknowns are obtained as shown in (3.23). The magnitude of each component in $\alpha\beta$ -frame is represented with N_2 ; whereas, N_3 is used for the components in abc -frame.

$$\begin{aligned} N_2 i_\alpha &= N_3 i_a + N_3 i_b \cos\left(\frac{4\pi}{3}\right) + N_3 i_c \cos\left(\frac{2\pi}{3}\right) \\ N_2 i_\beta &= 0 + N_3 i_b \sin\left(\frac{4\pi}{3}\right) + N_3 i_c \sin\left(\frac{2\pi}{3}\right) \\ N_2 i_0 &= kN_3 i_a + kN_3 i_b + kN_3 i_c \end{aligned} \quad (3.23)$$

Then, these three equations in (3.23) are organized in matrix notation in (3.24).

$$\begin{bmatrix} i_0 \\ i_\alpha \\ i_\beta \end{bmatrix} = \frac{N_3}{N_2} \underbrace{\begin{bmatrix} k & k & k \\ 1 & -1/2 & -1/2 \\ 0 & -\sqrt{3}/2 & -\sqrt{3}/2 \end{bmatrix}}_{[T_{\alpha\beta 0}]} \begin{bmatrix} i_a \\ i_b \\ i_c \end{bmatrix} \quad (3.24)$$

By using the orthogonality condition, $[T_{\alpha\beta 0}]^T [T_{\alpha\beta 0}] = I_{3 \times 3}$, the transformation matrix, $[T_{\alpha\beta 0}]$ and N_3/N_2 ratio are found as in (4.13) where $[T_{\alpha\beta 0}]^T$ is the transpose of $[T_{\alpha\beta 0}]$ and $I_{3 \times 3}$ is 3x3 identity matrix.

$$\begin{bmatrix} i_0 \\ i_\alpha \\ i_\beta \end{bmatrix} = \frac{1}{\sqrt{3}} \begin{bmatrix} \sqrt{2} & 1/\sqrt{2} & 1/\sqrt{2} \\ 1 & -1/2 & -1/2 \\ 0 & \sqrt{3}/2 & -\sqrt{3}/2 \end{bmatrix} \begin{bmatrix} i_a \\ i_b \\ i_c \end{bmatrix} \quad (3.25)$$

The transformation given in (3.25) is known as famous Clarke transformation. The norms of the vectors in both frames are the same since the transformation is normalized using (3.23). This results in the following equation:

$$i_\alpha^2 + i_\beta^2 + i_0^2 = i_a^2 + i_b^2 + i_c^2 \quad (3.26)$$

Zero sequence component is not be utilized for the rest of the transformation analysis. Thus, for simplicity, it is omitted and the reduced matrix is shown in (3.27).

$$\begin{bmatrix} i_\alpha \\ i_\beta \end{bmatrix} = \frac{1}{\sqrt{3}} \begin{bmatrix} 1 & -1/2 & -1/2 \\ 0 & \sqrt{3}/2 & -\sqrt{3}/2 \end{bmatrix} \begin{bmatrix} i_a \\ i_b \\ i_c \end{bmatrix} \quad (3.27)$$

As the next step, the transformed vectors in the stationary $\alpha\beta$ -frame are referred to the rotating dq -frame shown in Figure 3.14. The current vectors in dq -frame are expressed as i_d and i_q . The frequency of rotation in dq -frame is the grid frequency, ω_g . Using the information given in Figure 3.14, stationary $\alpha\beta$ -frame variables can be represented as in (3.28). The stationary reference frame variables in (3.27) can be transformed into synchronous frame using (3.29) where the displacement angle, θ varies between 0 - 2π radians in clockwise direction.

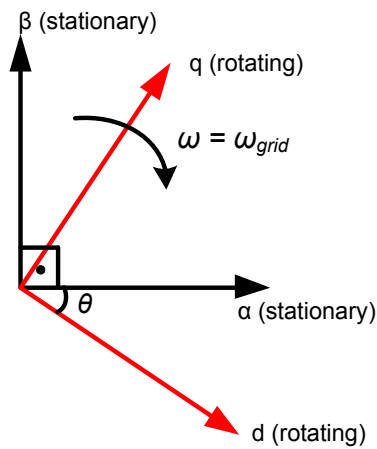


Figure 3.14 Vector diagram of PWM-VSC control structure.

$$\underline{i}_{\alpha\beta} = i_{\alpha} + j i_{\beta} \quad (3.28)$$

$$\underline{i}_{dq} = \underline{i}_{\alpha\beta} e^{j\theta} \quad \theta = \int \omega dt \quad (3.29)$$

Transforming $\alpha\beta$ vectors using (3.27), (3.28), and (3.29) along two orthogonal dq -axes results in two equations with two unknowns shown in (3.30). Using the transformation matrix, $[T_{dq}]$, the equations can be represented as in (3.31).

$$\begin{aligned} i_d &= i_{\alpha} \cos\theta + i_{\beta} \sin\theta \\ i_q &= -i_{\alpha} \sin\theta + i_{\beta} \cos\theta \end{aligned} \quad (3.30)$$

$$\begin{bmatrix} i_d \\ i_q \end{bmatrix} = \underbrace{\begin{bmatrix} \cos \theta & -\sin \theta \\ \sin \theta & \cos \theta \end{bmatrix}}_{[T_{dq}]} \begin{bmatrix} i_\alpha \\ i_\beta \end{bmatrix} \quad (3.31)$$

$[T_{dq}]$ satisfies the orthogonality condition i.e. $[T_{dq}]^T [T_{dq}] = I_{2 \times 2}$; where $[T_{dq}]^T$ is transpose of $[T_{dq}]$ and $I_{2 \times 2}$ is 2×2 identity matrix. The transformation represented in (3.31) with the additional “0” sequence component is known as Park transformation.

The normalized transformation from $\alpha\beta$ -frame to dq -frame allows the norm of the current vector to be same in both reference frames; hence

$$i_\alpha^2 + i_\beta^2 = i_d^2 + i_q^2 \quad (3.32)$$

By modifying (3.4) and using the transformations given above, the mathematical model of the *LCL* filter can be expressed in dq -frame as

$$\begin{aligned} \frac{d}{dt} \underline{i}_{g,dq} &= \frac{1}{L_{grid} + L_g} \left(\underline{V}_{C_f,dq} - \underline{E}_{grid,dq} - R_{grid} \underline{i}_{g,dq} - j\omega(L_{grid} + L_g) \underline{i}_{g,dq} \right) \\ \frac{d}{dt} \underline{i}_{c,dq} &= \frac{1}{L_c} \left(\underline{V}_{c,dq} - \underline{V}_{C_f,dq} - j\omega L_c \underline{i}_{c,dq} \right) \\ \frac{d}{dt} \underline{V}_{C_f,dq} &= \frac{1}{C_f} \left(\underline{i}_{c,dq} - \underline{i}_{g,dq} - j\omega C_f \underline{V}_{C_f,dq} \right) \end{aligned} \quad (3.33)$$

As the current controllers operate in dq -frame, the transformation of the mathematical model into the same reference is reasonable. The grid voltage vector, the converter output voltage vector and the filter capacitor current vector are all denoted in dq -frame as $\underline{V}_{g,dq}$, $\underline{V}_{c,dq}$, and $\underline{V}_{C_f,dq}$ respectively. In addition, $\underline{i}_{g,dq}$ is the grid current vector and $\underline{i}_{c,dq}$ is the converter current vector. The decoupling terms with $j\omega$

are resulting from the space vector transformations. The controllers may or may not include this terms.

3.3.2. Phase Locked Loop

PLL is a phase tracking algorithm mainly applied in communication technology. The algorithm provides an output signal synchronized with its reference input in both frequency and phase.

In power electronics, PLL is a widely accepted method to determine the phase angle of the grid voltages [18], [26], [61], [62]. The conventional synchronous reference frame PLL transforms the three-phase voltage vector from abc reference frame to the rotating dq reference frame by using Clarke and Park transformations as shown in Figure 3.15. The angular position, θ is controlled by a feedback loop regulating the q -axis component to zero. After the integration of the grid frequency, the angular position of the grid fed back in the Clarke and Park transformations is obtained.

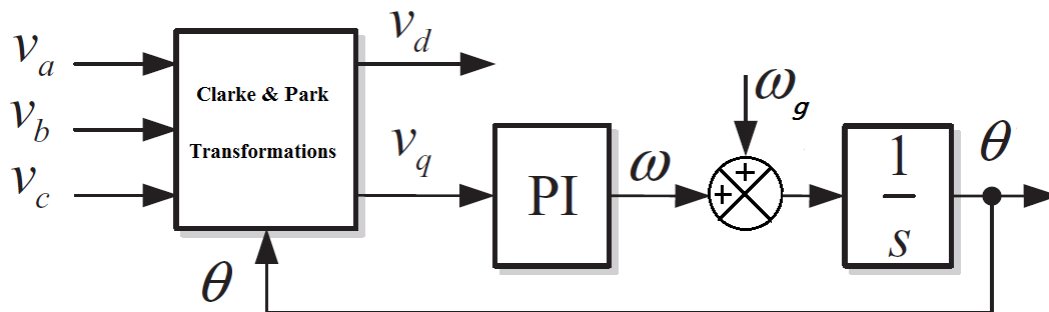


Figure 3.15 Phase locked loop in synchronous reference frame

The transfer function of the PLL can be shown as

$$G_{PLL}(s) = \frac{sK_p + \frac{K_p}{T_i}}{s^2 + sK_p + \frac{K_p}{T_i}} \quad (3.34)$$

By modifying the transfer function (3.34), a standard second order transfer function could be obtained

$$G_{PLL}(s) = \frac{2\zeta\omega_n s + \omega_n^2}{s^2 + 2\zeta\omega_n s + \omega_n^2} \quad (3.35)$$

where K_p and T_i are defined below by assuming that settling time, T_{set} is $3.9/\zeta\omega_n$

$$K_p = \frac{7.8}{T_{set}} \quad (3.36)$$

$$T_i = \frac{T_{set}\zeta^2}{1.95}$$

Selecting the damping ratio, ζ as 0.707 provides an overshoot under 5% and the settling time, T_{set} as 0.04, PI parameters can be calculated using (3.36).

When the grid voltage is not distorted, a high bandwidth for the PLL can be set and it yields a fast and precise detection of the phase angle. On the other hand, the effect of distorting components can be attenuated by reducing the PLL bandwidth. A detailed investigation on the bandwidth and performance relationship of the PLL analyzing the effect of voltage unbalance and voltage sag is given in [26]. An additional second order low-pass filter with a cutoff frequency of 20 Hz could be used to obtain the average voltage of the d -axis component, V_d . Then, the reconstruction of the voltage is needed.

For severe disturbances such as asymmetrical components in the voltage or variations in the supply frequency, more complex PLL structures including adaptive filters and estimators shall be used. Double synchronous reference frame PLL, synchronous reference frame PLL with positive sequence filter, synchronous reference frame PLL with sinusoidal signal integrator and double second order generalized integrator PLL are alternative PLL techniques used for utility applications of power electronics.

3.3.3. Current Control

Different current control approaches are presented in the literature. Using only proportional controllers cause steady-state errors. An integrator is placed in the loop to achieve zero steady-state error. A further improvement is accomplished by replacing the integrator with a PI controller. The tracking performance even for slow system poles is improved due to the zero of the PI controller. The parameters of the PI controller are the proportional gain K_p and the integrator time constant T_i . The transfer function of the PI controller is given as

$$G_{PI}(s) = K_p \frac{sT_i + 1}{sT_i} \quad (3.37)$$

The filter capacitor, C_f is neglected for the control design since the current controller operates at the grid frequency [3], [52], [63]. The effect of C_f becomes noticeable for higher frequencies. With this acceptance, the grid side current, $i_{c,dq}$ and the converter side current, $i_{q,dq}$ becomes identical as in the case of simple L filter. Therefore, the equations given in (3.33) can be simplified as

$$\underline{V}_{c,dq} = R_{grid}\underline{i}_{c,dq} + (L_c + L_g + L_{grid})\frac{d}{dt}\underline{i}_{c,dq} + \underline{E}_{grid,dq} \quad (3.38)$$

The current controllers are designed in dq -frame hence the decomposition of the above equation along d and q axes is shown in (3.39) with the decoupling terms.

$$V_{c,d} = R_{grid}i_{c,d} + (L_c + L_g + L_{grid})\frac{d}{dt}i_{c,d} + E_{grid,d} - \omega_g(L_c + L_g + L_{grid})i_{c,q} \quad (3.39)$$

$$V_{c,q} = R_{grid}i_{c,q} + (L_c + L_g + L_{grid})\frac{d}{dt}i_{c,q} + E_{grid,q} + \omega_g(L_c + L_g + L_{grid})i_{c,d}$$

Current controller employs either CCF or GCF. The illustration of these two methods is shown in Figure 3.16 (a) and (b) respectively. Apart from the feedback

variable, the only difference is that the q-axis reference input of the CCF is not zero as in the case of GCF. Due to the presence of filter capacitance, the phase information taken from the converter side does not match with the grid phase angle. The q -axis reference is therefore set as $\omega_g C_f V_{g,d}$ in order to compensate the phase difference. For light loads, the unity factor operation is guaranteed via nonzero reference value while the unity power factor at the grid terminals is achieved even if the reference value is set to zero in the case of CCF.

The tuning of PI controller parameters are done in the same way for both methods since the filter capacitance is neglected while designing the controller as mentioned above. The tuning method is based on the symmetrical optimum [9], [52] owing to decoupled d and q axis components. It should be noted that the decoupling terms are found using (3.39). The feedforward terms, $V_{g,d}$ and $V_{g,q}$ are added to the controllers to compensate for the grid voltage [54] as shown in Figure 3.16.

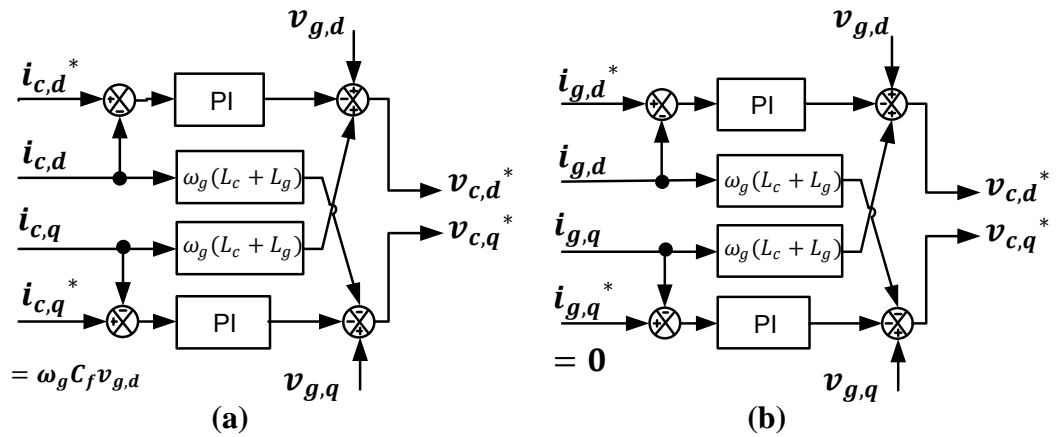


Figure 3.16 Current control using (a) converter current feedback (CCF) and (b) grid current feedback (GCF)

The L filter approximation gives K_p and T_i values of the PI controller as follows

$$K_p = \frac{L_c + L_g}{\alpha_i T_{samp}} \quad (3.40)$$

$$T_i = \alpha_i^2 T_{samp}$$

where α_i is the proportion of T_i to T_{eq} . The relationship between α_i and the phase margin of the controller, ψ can be expressed as

$$\alpha_i = \frac{1 + \cos \psi}{\sin \psi} \quad (3.41)$$

A satisfactory amount of disturbance rejection with an acceptable level of overshoot as the response to the step change of the reference can be satisfied by maximizing the phase margin (i.e. $\psi \geq 45^\circ$). If $\psi \geq 45^\circ$ substituted in (3.41), α_i is found approximately as 2.4. However, it is stated that selecting α_i as 3 yields an overshoot of approximately 4% and the settling time of 3-4 control periods [5].

Emerging technological developments in digital processors are adopted by power electronics designs as well. Increased computational capability and faster analog to digital conversion time of microprocessors, digital signal processors (DSPs), and field programmable gate arrays (FPGAs) have led to advanced control techniques with reduced delays. However, the transformation of the signals from analog domain to digital domain is done by sampling and it has a certain delay which cannot be ignored. The most adopted sampling methods are single-update with sampling at the start of the switching period, single-update with sampling in the middle of the switching period and double update with sampling twice in each switching period [64].

At the k^{th} instant the controller is able to set the PWM duty depending on the modulation index, m_i value updated in the previous control cycle. Therefore the PWM is adjustment is always one control cycle behind the real currents measured from the system. This issue is addressed as sampling delay or PWM transport delay

in PWM power electronics converters [3], [8], [52], [65], [66]. Figure 3.17 and Figure 3.18 demonstrate three PWM update methods by emphasizing the differences between these methods.

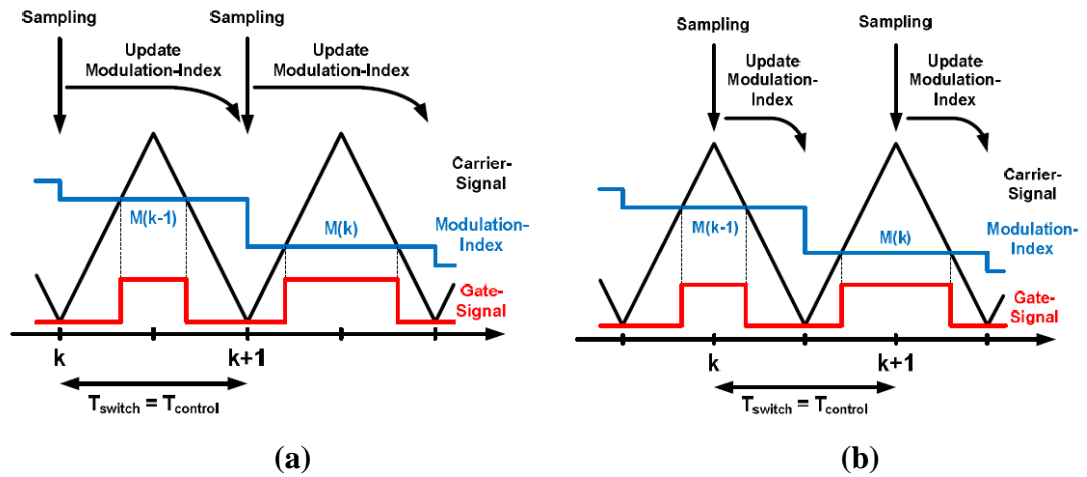


Figure 3.17 PWM update methods (a) single-update with sampling at the start (b) single-update with sampling in the middle [64]

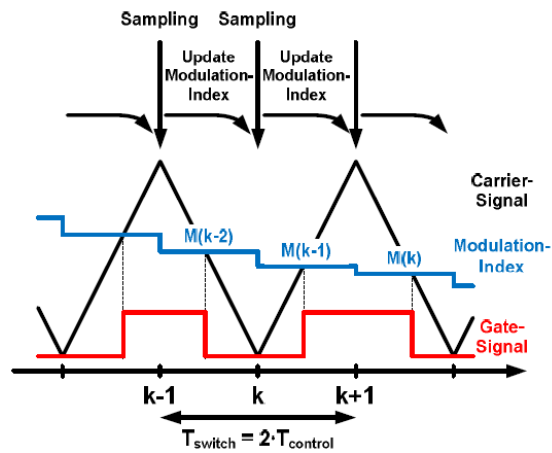


Figure 3.18 Double update PWM method

In Figure 3.17 (a) the sampling and the update of the modulation index are done simultaneously. The modulation index value does not change during any sampling

period as the updates are done at the beginning of each PWM switching period. The comparison of the voltage set value and the triangular carrier wave are done twice in each PWM switching period.

Apart from the first method, Figure 3.17 (b) describes the single-update method with sampling in the middle of the switching period. The sampling is done in the middle of the switching frequency while the update of modulation index is carried out at the end of the switching period. The modulation index is updated during the control (sampling) period but the comparison of the voltage reference value and the triangular wave is done using the previous value of the modulation index as in the first method. The time difference between the sampling and the update of the modulation index is reduced hence a more accurate result is obtained. The actual values of the currents are sampled a half switching period before the update of the modulation index.

Double update PWM method shown in Figure 3.18 leads to asymmetrical PWM signals unlike single-update PWM methods in which the PWM signals are symmetrical. This may lead to undesired current harmonics at the grid side. Nevertheless, the bandwidth of the controller is doubled using double update method. As the controller bandwidth is doubled, the phase margin of the controller decreases which may lead to higher overshoots. The sampling and the update of the modulation index are done simultaneously and the modulation index is updated during the sampling period. For the next sampling period, the modulation index is updated again hence two different modulation index values are used while generating the PWM signal.

The PWM update method utilized in the current controller design process is double update. The sampling frequency, f_{smp} of the current controllers is set as the twice of the switching frequency, f_{sw} . For high power applications with limited switching frequencies around a few kilohertz, this method extends the bandwidth of the controllers.

In digital control of modern power electronics devices, significant delays occur in the control loop such as processing delay (analog to digital conversion, computation etc.) and PWM transport delay as stated above. Generally, processing delay is taken as one sample delay while PWM transport is deemed as one half sample delay. By reducing the *LCL* filter to a first order delay element [64], the single-phase representation of the current control loop is given in Figure 3.19.

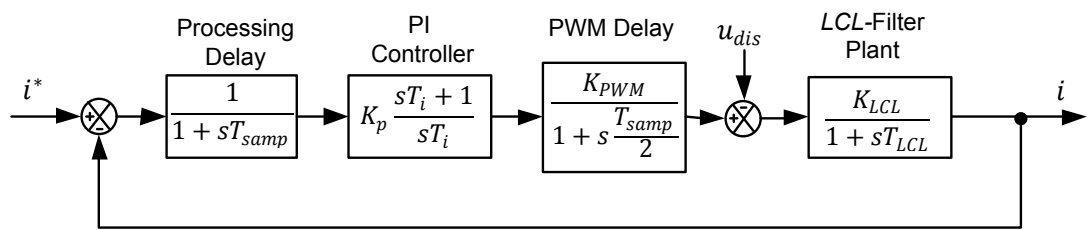


Figure 3.19 Single-phase block diagram of current control loop

where T_{smp} is the sampling time, u_{dis} is the disturbance voltage modeling the impact of variations in the grid voltage. K_{PWM} is proportional gain constant of the PWM block, K_{LCL} is proportional gain constant of the *LCL*-filter plant, and T_{LCL} is time constant of the *LCL*-filter plant.

The delay elements can be combined to simplify the current control structure. The equivalent delay time, T_{eq} is taken as $1.5T_{smp}$ and the block diagram is shown in Figure 3.20.

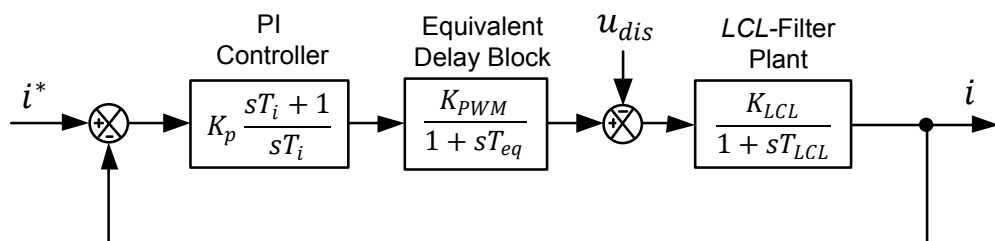


Figure 3.20 Simplified single-phase block diagram of current control loop

The controller design can also be carried out in the discrete domain by importing the PWM and sampling delays as in [55], [64], [66]; however, continuous domain design of the controllers is widely accepted and utilized method in the literature [3], [5], [6], [9], [50].

Generating PWM signals is also an important part of the current controller design. There are numerous PWM methods presented in the literature. A survey on the modulation strategies widely used in power electronics converters are presented in [67]. A guideline for PWM in power conversion with space vector definition is given in [68]. Both carrier-based and carrierless PWM techniques applied on open-loop and closed-loop control are also given.

Space vector modulation (SVM) algorithms replacing sinusoidal pulse-width modulation (SPWM) have become popular with the wide use of voltage source converters. The methods are developed for a specific number of levels and the complexity of the methods increase as the number of the levels increase. The computational effort and the complexity are reduced with the application of space vectors for the switching of power semiconductors. The space vectors resulting from a balanced three-phase system are shown in Figure 3.21.

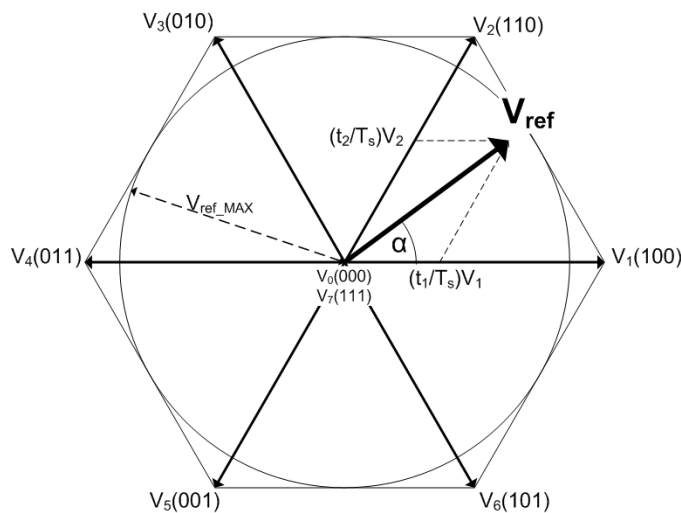


Figure 3.21 Eight possible space vectors for a three-phase PWM-VSI

The reference voltage vector formed by space vector transformations is synthesized with two adjacent vectors and one or both of the zero vectors. Various SVM algorithms can be applied by changing the sequence of vectors and the selection of zero vectors. The differences mainly occur in THD, switching losses, harmonic spectrum, dynamic performance, and torque ripple for motor drives.

The generation of PWM signals does not require trigonometric functions, look-up tables or coordinate system transformations; it is carried out using simple equations. The reduced computational effort makes the application of online calculated PWM possible. Most frequently used SVM techniques are space vector pulse-width modulation (SVPWM) and discontinuous pulse-width modulation (DPWM) shown in Figure 3.22 (a) and (b) respectively. Depending on the modulator phase angle, various DPWM techniques are derived. A commonly used one is DPWM1 with the modulator phase angle of 30° .

In Figure 3.22, zero-sequence signals of SVPWM and DPWM1 derived from the reference three-phase signals are shown. Phase-A reference signal is purely sinusoidal and the modulation signal which is the sum of the zero-sequence signal and the phase-A reference signal is modified sinusoidal.

Apart from the abovementioned SVM techniques, active zero state PWM (AZSPWM), near state PWM (NSPWM), third harmonic injection PWM (THIPPWM), and remote state PWM (RSPWM) are other techniques reported in the literature [69], [70]. SVPWM and DPWM1 are applied as PWM generating techniques in this study. SVPWM is superior to DPWM1 in the low modulation index range. As the modulation index increases, the SVPWM performance degrades and DPWM1 becomes more effective in the high modulation index range [67].

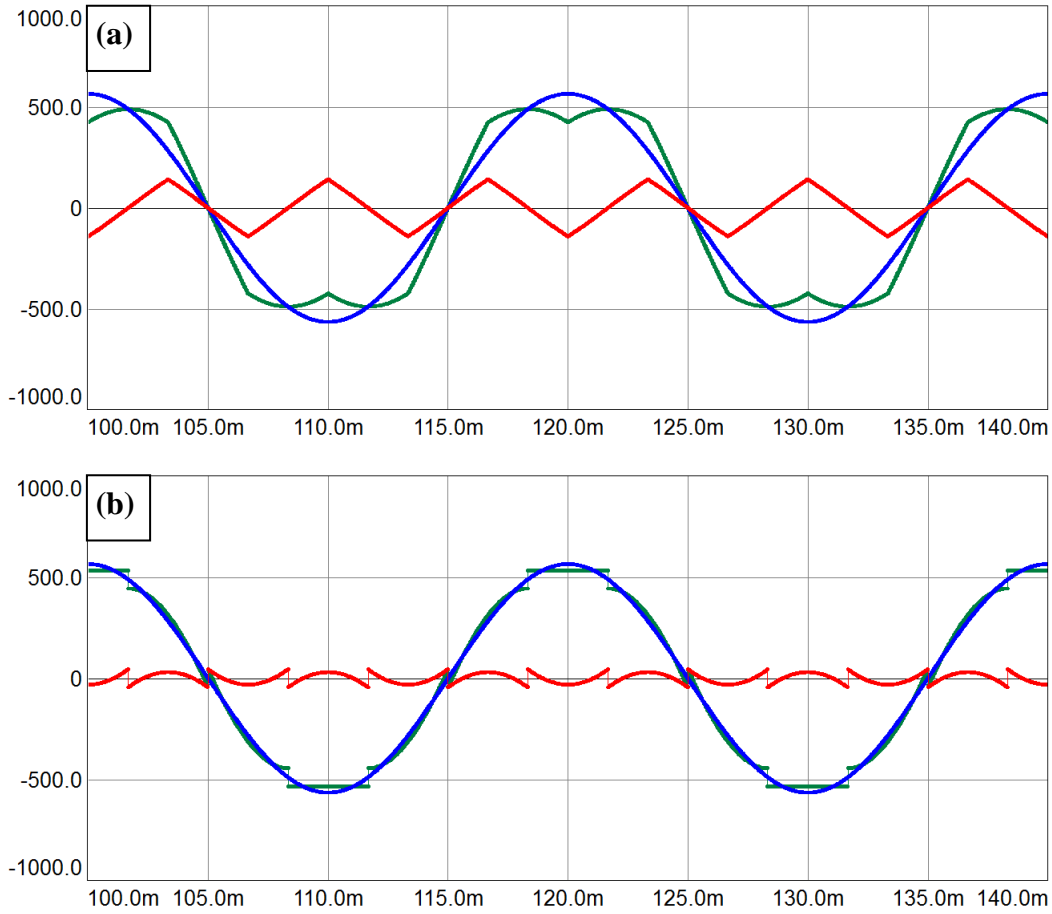


Figure 3.22 Modulation waveforms of (a) SVPWM and (b) DPWM1

3.3.4. DC Voltage Control

The power exchange between the load and the source is balanced by the control of DC-link voltage. The set value of the d -axis current component is adjusted by the DC-link voltage controller. The dynamics of the DC-link voltage can be stated in (3.42) [3], [52], [71]. Here C_{DC} is the DC-link capacitor, i_{DC} is the source current, and i_{source} is the injected current to the VSC.

$$C_{DC} \frac{dV_{DC}}{dt} = i_{source} - i_{DC} = i_{source} - \frac{3}{2} \frac{i_{g,d} V_{g,d}}{v_{DC}} \quad (3.42)$$

The voltage control loop is designed 5-20 times slower than the current control loop [9]. The difference between the bandwidths of these two loops provides the necessary decoupling of controllers. The inner current loop is simplified as a delay element with four sample time ($T_{inner} = 4T_{samp}$) for the design of the outer DC-link voltage control loop. The block diagram of the DC-link voltage controller is demonstrated using (3.42) in Figure 3.23 below.

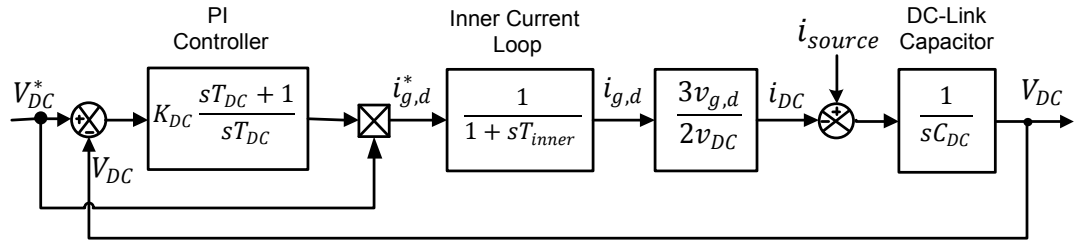


Figure 3.23 Block diagram of DC-link voltage control loop

The symmetrical optimum method is also valid for the determination of DC-link voltage controller's proportional gain constant, K_{DC} and integral time constant, T_{DC} . These parameters are found using

$$K_{DC} = \frac{2}{3} \frac{V_{DC}^* C_{DC}}{\alpha_{DC} T_{inner} v_{grid,d}} \quad (3.43)$$

$$T_{DC} = \alpha_{DC}^2 T_{inner}$$

Where α_{DC} is suggested as 3 in [52] and the bandwidth of the voltage controller is 9 times narrower than the bandwidth of the current controller.

3.4. Stability Assessment

The stability of the cascaded control loop system in the literature is based on the stability of the inner current loop. Therefore, the DC-link voltage control loop could

be ignored and modeled as a DC voltage supply without investigating the stability of it [3], [5], [6], [8]-[10]. As an alternative common approach in the literature, discrete z-domain analysis in conjunction with root locus of the open-loop system's transfer function is generally applied in stability analysis due to the discrete nature of the control algorithm [5], [9], [52], [64].

The stability analysis is carried out using bode diagrams and pole-zero diagrams of the investigated systems via MATLAB[®]. For this purpose, open-loop and closed-loop transfer functions of the system with *LCL* filter under different damping approaches are derived in the next chapter. However, a brief knowledge on the stability issue is given here.

The admittance transfer function of the *LCL* filter is given in (3.6). The resonance problem of the undamped *LCL* filter is suppressed using simple passive damping. The transfer function regarding the passive damping is given in (3.8). Using these s-domain transfer functions, the bode diagram of the undamped and damped *LCL* filter can be sketched as in Figure 3.24. The resonant peak is smoothed using simple passive damping approach.

Using the pole-zero map of the same transfer functions with continuous time analysis, Figure 3.25 is obtained. The undamped transfer function does not have any zero. Three poles, one at the origin and two conjugate symmetric on the imaginary axis are seen. The poles concerning the resonance are placed on the imaginary axis. These poles disturb the stability of the system and shall be moved to the left hand side of the imaginary axis. With the application of passive damping, the resonant poles are pushed to the left hand side of the y-axis satisfying the stability. Due to passive damping, an additional zero occurs on the x-axis. As it is seen from the pole-zero map, the low frequency pole location does not change, meaning that the dynamic response of the system is not affected by the introduction of passive damping. This can be verified using Figure 3.24 as well. The low frequency behavior of the filter is not affected when the filter is passively damped.

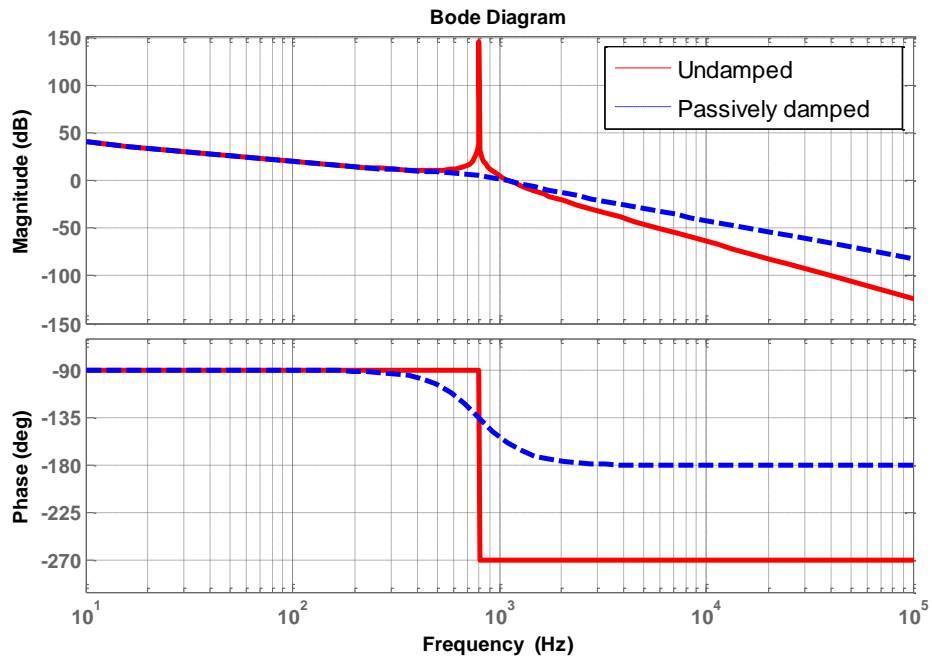


Figure 3.24 Bode diagram of the undamped and passively damped *LCL* filter

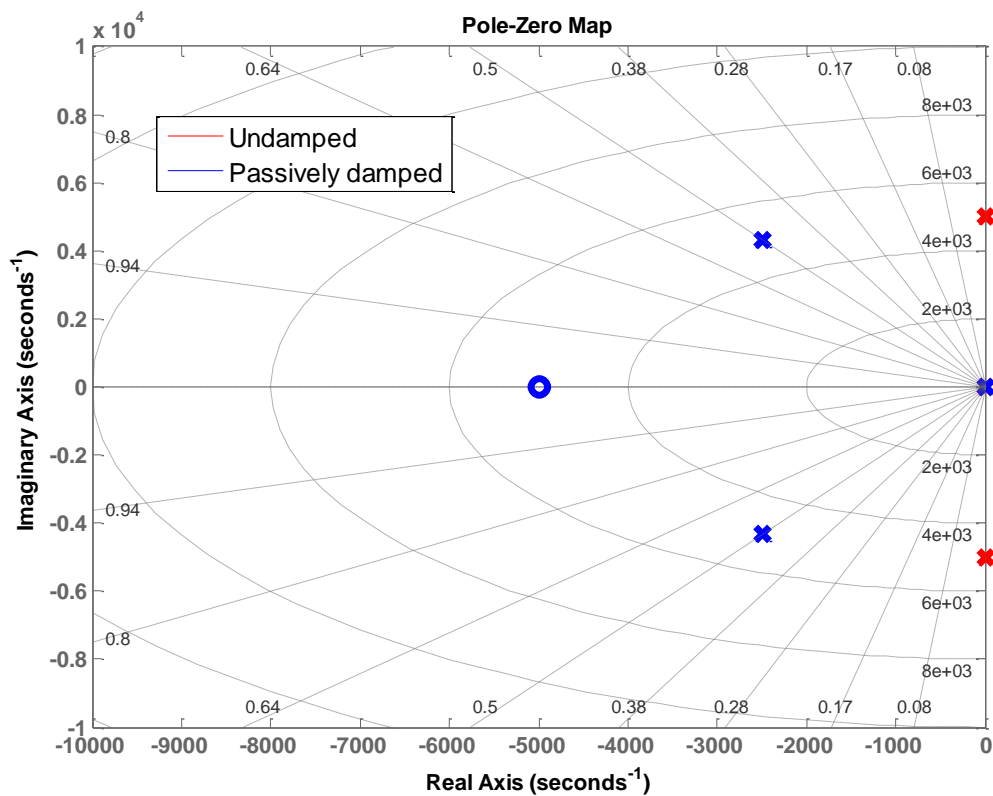


Figure 3.25 Pole-zero diagram of the undamped and passively damped *LCL* filter

3.5. Summary and Conclusion

This chapter presents a design and control overview for a WECS. Based on the knowledge stated in Chapter 2, the converter type is selected. DC-link voltage and capacitance value, switching frequency, pulse-width modulation technique, and grid side filter are chosen. Moreover, the theoretical analysis on the PWM-VSI with *LCL* filter is conducted in this chapter. Starting from the mathematical model and frequency analysis of simple *L* filter and *LCL* filter, the control of a PWM-VSI together with a grid side *LCL* filter is presented. The conventional design process of an *LCL* filter is described step by step. The controller design is analyzed deeply by specifying three-phase space vector transformations, phase locked loop algorithm, digital sampling of feedback variables, current controller, and DC-link voltage controller. An introduction to PWM methods is also stated. At the end of the chapter, stability analysis of the undamped and passively damped *LCL* filter is carried out.

The requirements on the grid side converter define the converter topology. To comply with the grid codes with reduced complexity and reduced switch count, 2L back-to-back PWM-VSI is chosen. Due to 690 V_{rms} line-to-line voltage of the selected generator, the converter is also designed in LV and the DC-link voltage is set as 1070 V. The power semiconductors are selected with 1700 V and 2400 A rated values. Paralleling of two IGBTs is required to satisfy the current flow through the converter. DC-link capacitor value is proposed and the number of capacitors is defined for the selected high density film capacitor.

The switching frequency together with the modulation technique is analyzed briefly using the efficiency curve obtained for SPWM, SVPWM, and DPWM1 techniques. The apparent advantage of DPWM1 over SPWM and SVPWM is presented. The switching frequency is also defined as 1.2 kHz leading to the overall efficiency close to 99%.

The control method generally applied for 2L back-to-back PWM-VSI is synchronous frame voltage oriented control. This method is chosen due to easiness

in implementation. The grid side harmonic filter is proposed as *LCL* filter. The advantages of *LCL* filters over tuned *LC* trap filters are stated. The design of *LCL* filter for high power systems is reviewed and sub-blocks of the controller are presented.

After the presentation of individual control loops, the combination of the control structure and the hardware demonstration is given in Figure 3.26.

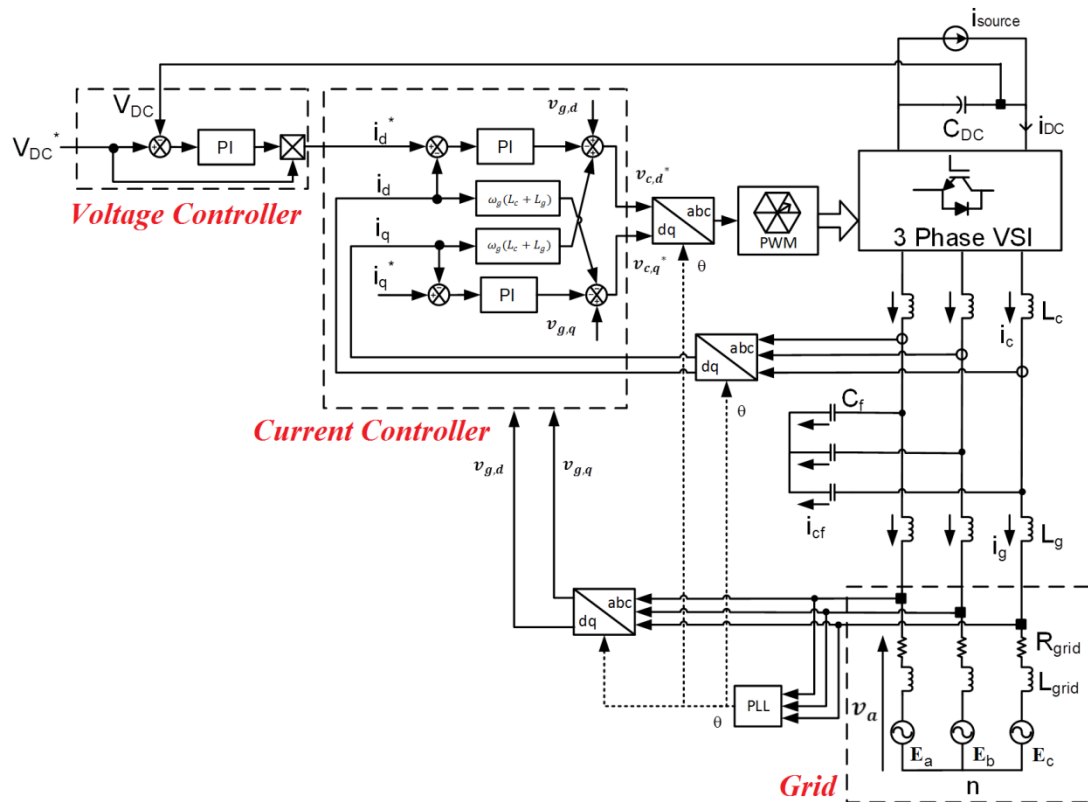


Figure 3.26 Voltage oriented current control of a three-phase PWM-VSI with *LCL* filter

Both the DC-link voltage and the current control are utilized with PI controllers with the transformation of three-phase currents into *dq*-frame. The reference tracking capability of the controllers increase as the signals are transformed into DC values. The decoupling terms are used in the current controllers to eliminate the effect of each axis component on the other one. The PWM strategy used in the design is

based on space vector modulation; mainly DPWM1 and SVPWM are used. The current feedback is measured from the grid side for better control of the grid currents. The resonance damping is basically provided by passive damping techniques for high power systems. However, AD methods could also be used for small or medium power systems up to a few hundreds of kilowatts.

CHAPTER 4

RESONANCE DAMPING METHODS

Resonance damping methods or simply, damping methods for *LCL* filters are introduced in this chapter. Due to the inherent resonance problem of 3rd order *LCL* filter, the harmonics produced by the PWM-VSI or grid originated harmonics could be amplified by the filter and cause the instability of the WECS hence the whole system could be destroyed. As the solution to the inherent resonance phenomena stated in the literature, passive or active damping methods are utilized. In addition to active and passive damping methods, advanced passive damping methods especially for high power systems are reviewed in this chapter. Moreover, two novel damping methods based on switch mode converters are presented.

In the literature, various active and passive damping methods are proposed in order to deal with the resonance issue of *LCL* filters [4]-[10], [51], [65], [72]. With the development of active damping (AD) methods, the use of passive damping (PD) methods has declined due to power losses associated with the damping resistors. AD methods modify the reference voltage signal of the controller whereas PD methods physically insert passive elements with the *LCL* filter not to excite resonant harmonics. The frequency characteristics of AD and PD methods are reflected in Figure 4.1. The suppression of resonant peak and the phase transition at the resonant frequency differ in each case. The behavior of the filter at frequencies higher than the resonant frequency is also a distinctive point to be noted that PD reduces the filtering performance while AD maintains the same characteristics with the undamped *LCL* filter throughout the whole frequency spectrum.

The resonant frequency of the *LCL* filter is selected usually below the half of the inverter's switching frequency. For high power inverters, the resonant frequency is

unfortunately very close to the switching frequency by design limitations. Further decrease of the resonant frequency leads to bulky and costly filter elements. Moreover, the voltage drop on the filter inductors increase and the system may not be controlled. On the other hand, further increase of the resonant frequency leads to smaller filter elements; hence, the output line current THD (typically below 4%) cannot be satisfied. As a result, an optimized multi-megawatt inverter has very close switching and resonant frequencies and passive damping of the system is inevitable.

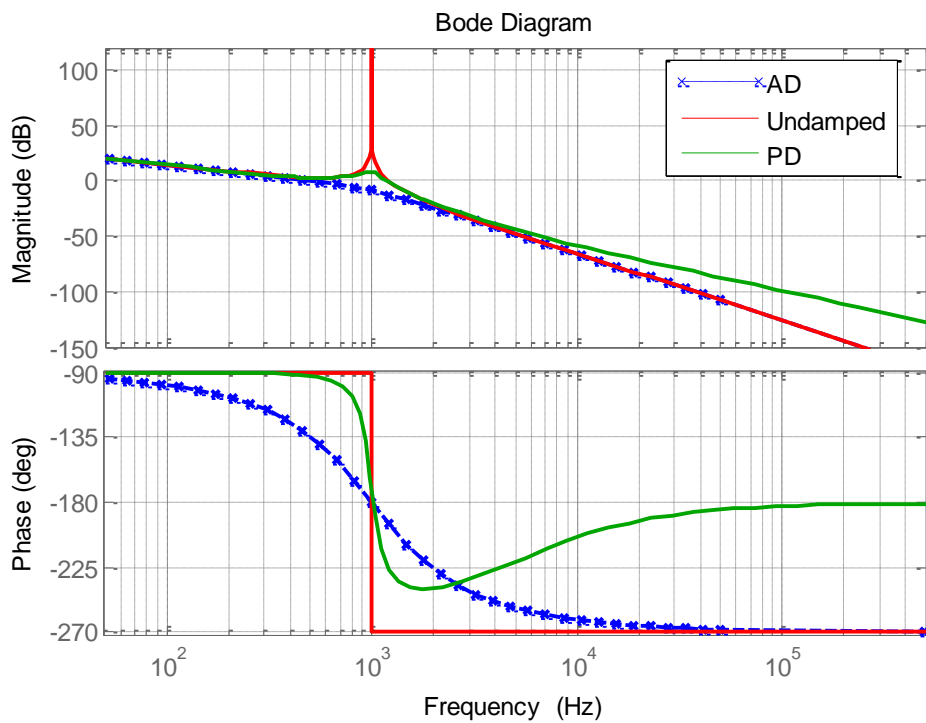


Figure 4.1 Bode diagrams of undamped, passively damped and actively damped *LCL* filter

As mentioned above, passive damping losses are not acceptable for high power inverters and losses should be minimized to reduce the cooling expenses and the mechanical dimensions of the system. The proposed switch mode converter based damping (SMCD) methods suppress the resonant harmonics by emulating resistors in series with the filter capacitors. The name of the proposed topologies, SAF

compensated *LCL* filter is originated from the idea of emulating series resistors. The details are given in the following sections.

Passive and active damping methods as well as natural damping which is the realization of the inherent damping property of the controller are described in detail at the beginning of the chapter. The limitations of each method are stated as well as the advantages. Since the focus of this study is high power inverters, passive damping methods are analyzed with various topologies namely, advanced passive damping methods. The power dissipation on passive damping elements is found above the acceptable limits; therefore, the efficiency rating of the system cannot reach the predefined efficiency target. A wise approach by emulating series resistors via switch mode power converters is utilized to reduce the power losses associated with the passive damping elements.

4.1. Natural Damping

Conventionally, the current feedback is measured from the grid side but the converter current can alternatively be measured for the feedback control. The q -axis current (phase component) should be set to $\omega_g C_f V_{g,q}$ instead of zero in order to perform with unity power factor, as the grid side current is not controlled directly. Natural damping (ND); on the other hand, is not a damping method itself. It is the understanding of inherent resonance damping capability of the current control loop when converter current feedback (CCF) is applied.

The converter side current feedback has an inherent damping term which is explained comprehensively in [9]. The location of the resonant frequency with respect to the critical resonant frequency, ω_{crit} in the frequency spectrum defines the regions of damping. ω_{crit} is defined as

$$\omega_{crit} = \frac{\pi}{3T_{samp}} \quad (4.1)$$

where T_{samp} is the sampling frequency as discussed in the previous chapter.

The application of converter side feedback is limited to power converters of several tens of kilowatts whose resonant frequencies are below ω_{crit} . As the power rating of the converter increases, the positions of these two frequencies interchange to provide an optimum design in terms of LCL parameters. Hence, the natural damping approach becomes invalid for high power rating inverters. The block diagram of CCF control method can be shown as in Figure 4.2 [6].

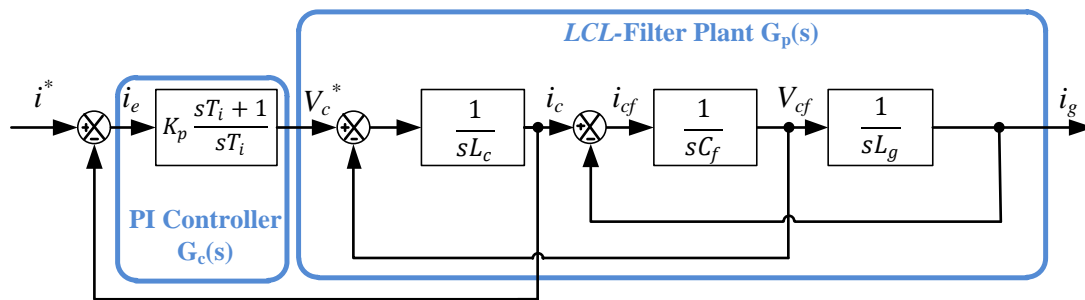


Figure 4.2 Block diagram of CCF control

The equivalency of CCF to GCF except for an additional i_{cf} term is shown in Figure 4.3 using block diagram transformations. The inherent damping term is explicitly shown such that the resonance damping effect is enforced by this term [6]. From the open-loop transfer function shown in (4.2) it can also be deduced that damping factor is adjusted by the current controller gain, K_p .

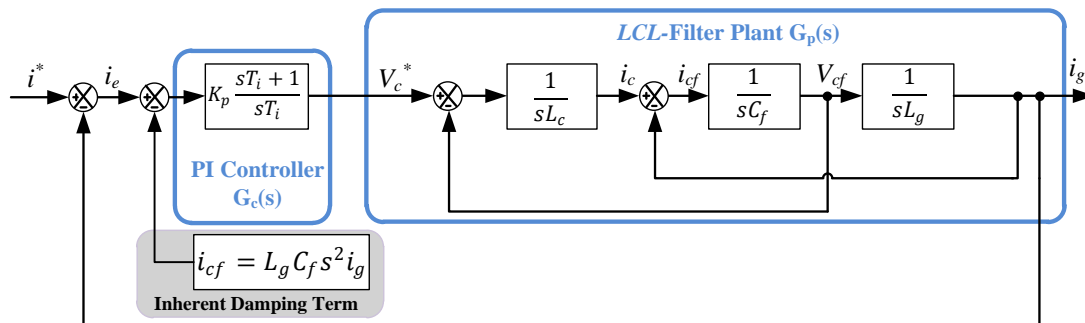


Figure 4.3 Modified block diagram of CCF control

$$\frac{I_g(s)}{I_e(s)} = \frac{K_p(s + 1/T_i)}{s^4 C_f L_c L_g + s^3 K_p C_f L_g + s^2 (K_p C_f L_g / T_i + L_c + L_g)} \quad (4.2)$$

The inherent damping does not exist when the grid current is measured as the current feedback, hence CCF could be deemed as more stable than GCF where applicable. The deviation of *LCL* filter parameters due to aging, temperature variation, and system uncertainty is a challenging task for optimum design of the controller using GCF without additional damping. If only the inherent damping characteristic of CCF is relied on, the system may not achieve stability. However, a tuning of the damping factor is proposed in [6] at the expense of a deteriorated transient response.

4.2. Passive Damping

The easiest way to remove the resonant peak of the *LCL* filter is to add damping resistors as proposed in [4], [7]. However, the power losses in conjunction with the damping resistors create a major problem; so that, the method producing the minimal losses, adding a resistor in series with the filter capacitor, C_f is selected. The application of simple PD structure is shown in Figure 4.4. Without passive damping, the *LCL* filter transfer function is 3rd order but it reduces to 2nd order when passive damping is applied. The 2nd order characteristic of the filter when passive damping applied is clearly seen in (3.8).

Any change in the resonant frequency owing to the aging, stray inductance/capacitance in the system, or large tolerance in the components does not affect the stability of the system since there is always nonzero impedance at the filter capacitor branch eliminating the resonance [4]. Hence, PD guarantees the stable and long-lasting operation of the system. Besides, unlike AD methods, there is no need to use additional voltage and/or current sensors in PD methods. On the contrary, dynamic response of the system diminishes with the addition of damping resistors to the *LCL* filter

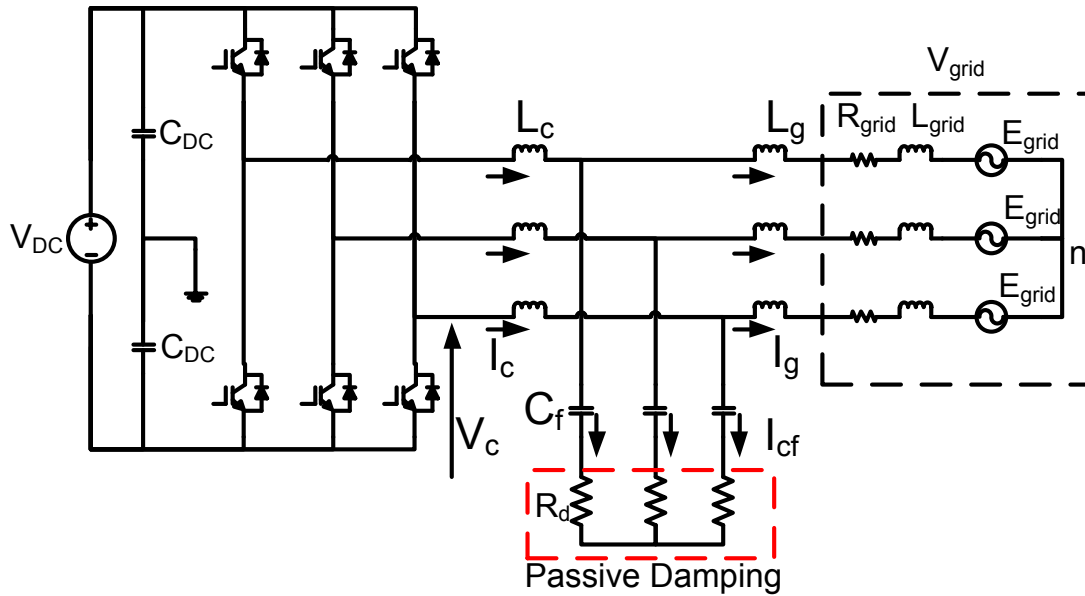


Figure 4.4 Simple PD structure applied on a 2L PWM-VSI

A non-zero impedance path for the undesired current harmonics is created by inserting passive components to the *LCL* filter. In this way, the stabilization of the system is achieved while the harmonics transferred to the grid are reduced. For 4% overshoot, the damping ratio should be 0.707; hence, the damping resistor should be selected in accordance. Moreover, the minimum value of the damping resistor is approximated as 20% of the capacitor's impedance at $\omega = \omega_{res}$ [7].

The single-phase representation of *LCL* filter with damping resistors connected in series with the filter capacitor and the block diagram representation are shown in Figure 4.5 (a) and (b) respectively. Equation (3.8) can also be verified using the block diagram representation.

At low frequencies, the impedance of the capacitor is dominant with respect to the damping resistor while the impedance of the damping resistor is much higher at higher frequencies. Since the impedance of the capacitor is low enough to attract high frequency switching harmonics, a non-zero impedance shall be placed for those harmonics creating the resonance problem.

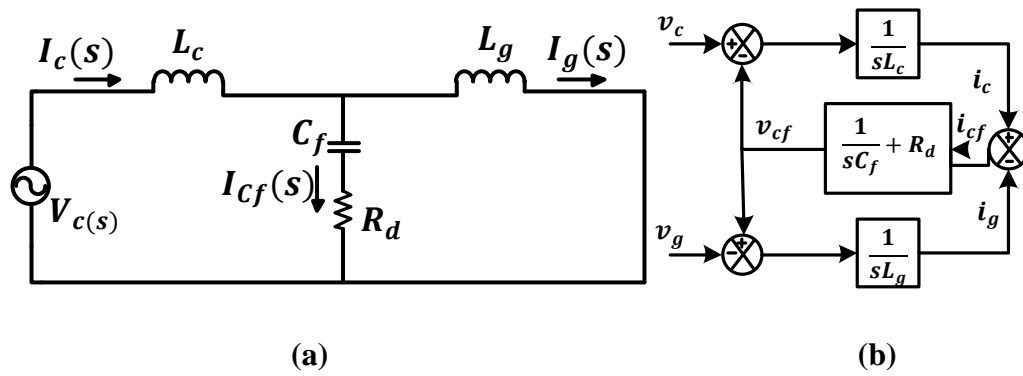


Figure 4.5 Simple passive damping with *LCL* filter (a) Single-phase representation
(b) Block diagram representation

Apart from the series-connected damping resistor approach, complex damping methods can be applied with the addition of reactive components to the *LCL* filter; however, the cost and size of such damping methods cannot be ignored. The power losses related to complex damping methods are reduced to one fourth of the simplest case [7]; nevertheless, it is still very high for multi-megawatt inverters.

For small power applications up to tens of kilowatts, damping resistance does not create significant reduction in the efficiency. For medium power converters up to hundreds of kilowatts and high power converters with several megawatts rating; on the other hand, the power losses are extremely high leading to additional cooling cost of the WECS.

Since the efficiency target of the multi-megawatt systems are around 99%, the switching frequency is reduced down to a few kilohertz. The current harmonics; however, increase in magnitude due to low switching frequency. Hence, the components of the *LCL* filter are selected such that the grid codes specified by the TSO are satisfied. If only gigantic filter inductors are selected, the resonant frequency is placed away from the switching frequency [13]. Nonetheless, bulky and costly inductors are not allowed in WECS. Moreover, high inductance in the grid connection reduces the dynamic behavior of the system. As a result, necessary

damping shall be provided using PD for high power systems not to be affected by the switching harmonics of the PWM-VSI [4].

With the additional damping resistor, the current harmonics injected to the grid increase as the filter attenuation is reduced. A tradeoff between the stability of the WECS and low current THD value is adjusted by the selection of damping resistor. The bode plot and the pole-zero map obtained via MATLAB[®] are given in Figure 4.6 and Figure 4.7 respectively. The figures demonstrate the effect of damping resistor value on the characteristic of the *LCL* filter. As the damping resistor increases, the stability of the system gets harder to achieve. The zero location along the x-axis moves towards left, meaning that the settling time of the system increases.

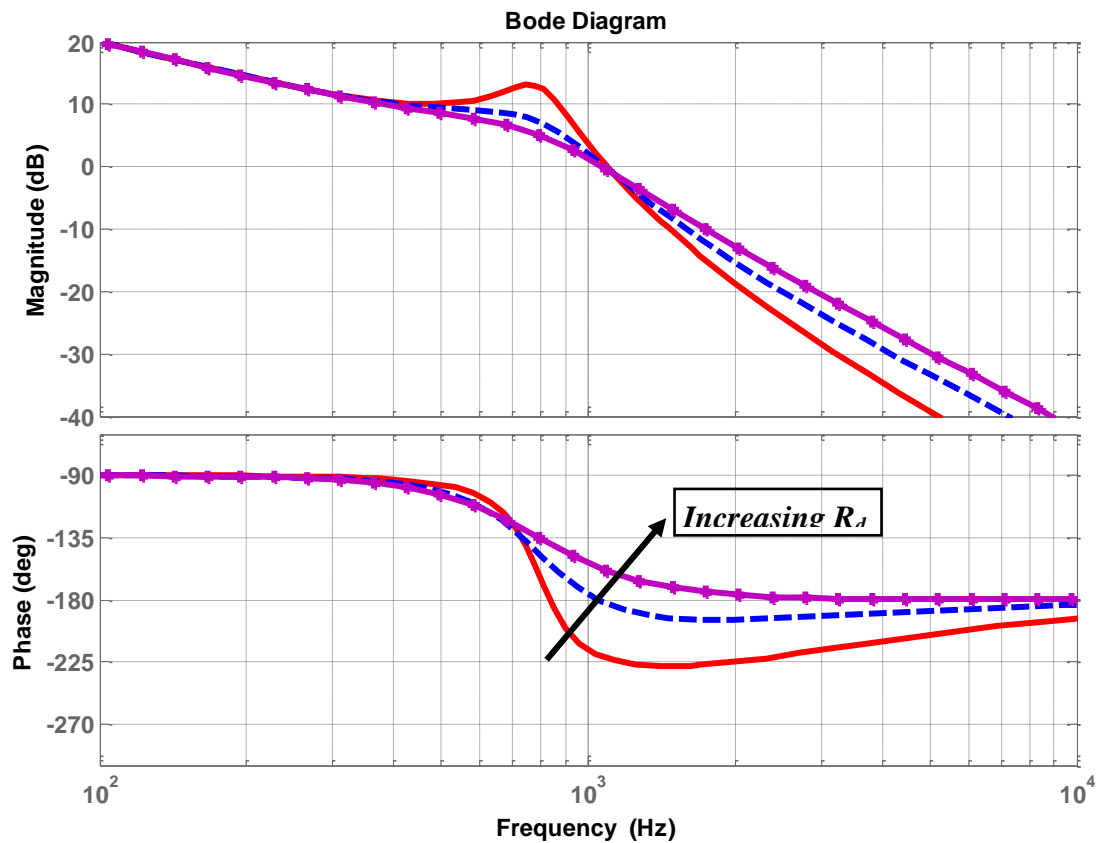


Figure 4.6 Bode plots of the passively damped *LCL* filter for various R_d .

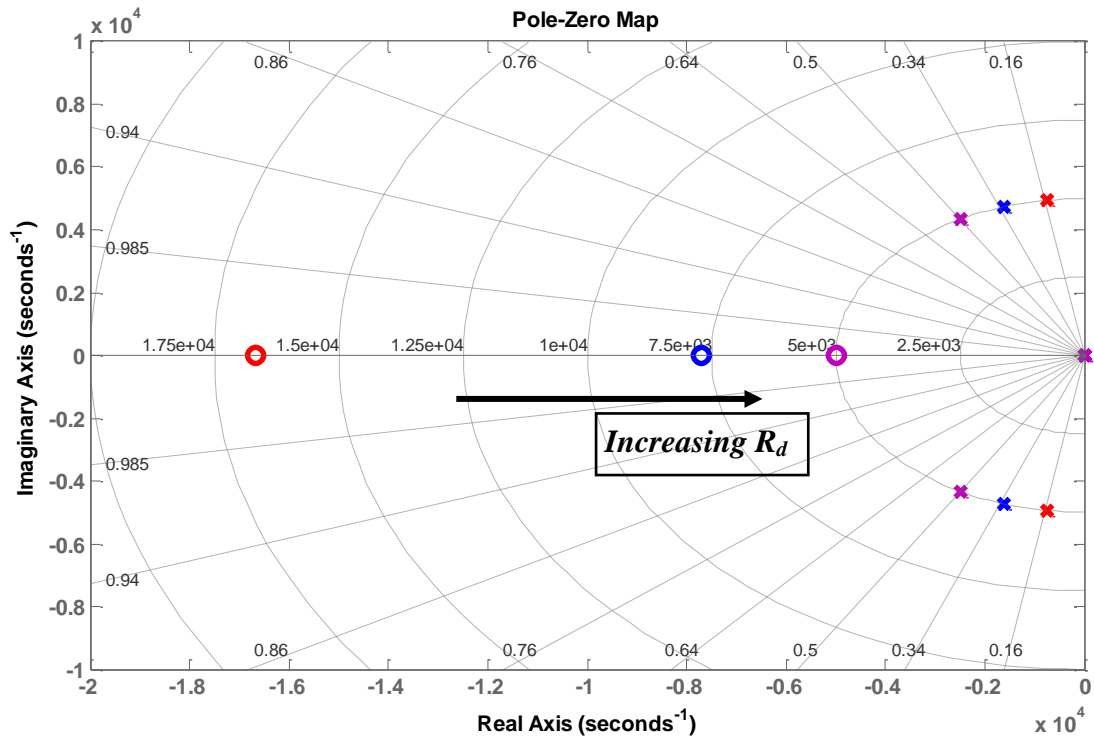


Figure 4.7 Pole-zero diagram of the passively damped *LCL* filter for various R_d

4.3. Active Damping

Active damping (AD) methods utilize extra sensors to sense the filter capacitor current/voltage or complex state observers to modify the reference voltage generated by the controllers [5]. The current through or the voltage across the filter capacitor is sensed and added to the reference voltages through proportional or derivative controllers depending on the sensed parameter. In this way, the controller does not allow any resonant harmonics to be amplified by the inverter.

Filter based active damping methods by changing the reference voltages of the controller are also used without any state feedback via controllers. The verification of active damping has been done by various researches [5], [8], [9]; however, the limitation of the controller bandwidth is a major issue for high power inverters [4]. The sensitivity of active damping to parameter variations is another drawback of this method.

In this study, filter capacitor current, i_{cf} information is used in order to achieve AD in the current control loop. If the voltage across the capacitor, V_{Cf} is used, the AD loop employs a derivative controller which may disturb the stability of the system. In real life applications, derivative controllers are not favored due to the amplification of high frequency and noise by the controller.

The additional AD loop together with the LCL filter plant, $G_p(s)$ is shown in Figure 4.8 below. The controller used in the AD loop is simply a proportional controller with the gain K_d .

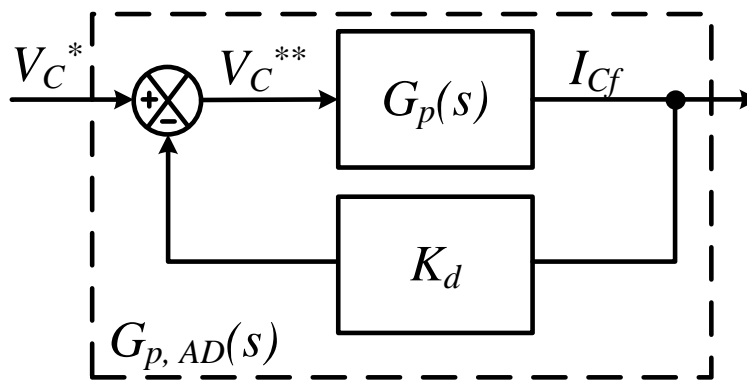


Figure 4.8 Block diagram of AD loop with the LCL plant

For the above representation $G_p(s)$ is defined as

$$G_p(s) = \frac{I_{cf}(s)}{V_c(s)} = \frac{1}{L_c} \frac{s}{s^2 + \omega_{res}^2} \quad (4.3)$$

Hence, the closed-loop transfer function having an s^2 term is shown in (4.4). The damping is provided by this term. A virtual resistance is added to the control loop while the physical structure of the filter is not changed at all.

$$G_{p,AD}(s) = \frac{G_p(s)}{1 + G_p(s)K_d} = \frac{1}{L_c} \frac{s}{s^2 + s \frac{K_d}{L_c} + \omega_{res}^2} \quad (4.4)$$

AD can be applied either on GCF or CCF. Figure 4.9 shows the application of AD using the filter capacitor current on GCF method. The open-loop characteristic should include the damping term to eliminate instability. Stability analysis using the pole-zero map is also conducted with open-loop transfer function in (4.5).

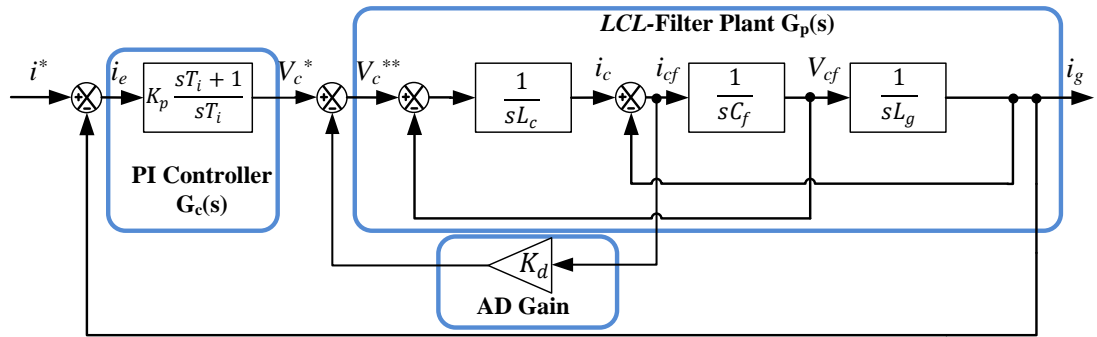


Figure 4.9 Block diagram of GCF with AD loop

$$\frac{I_g(s)}{I_e(s)} = \frac{K_p(s + 1/T_i)}{s^4 C_f L_c L_g + s^3 K_d C_f L_g + s^2 (L_c + L_g)} \quad (4.5)$$

The degree of damping is adjusted by changing AD controller gain, K_d . The sizes of filter components are also effective when adjusting the damping degree. For optimum damping with 5% overshoot, the damping ratio, ζ should be set as 0.707 [6], [9]. Therefore, K_d can be found using (4.6).

$$K_d = 2\zeta \sqrt{\frac{L_c^2 + L_c L_g}{L_g C_f}} \quad (4.6)$$

If AD is applied on CCF, Figure 4.10 is obtained using the modified block diagram of CCF. The open-loop transfer function as in GCF case is derived in (4.7). It can be understood that the current controller gain, K_p and the AD gain, K_d has the same influence on the damping extent of the system.

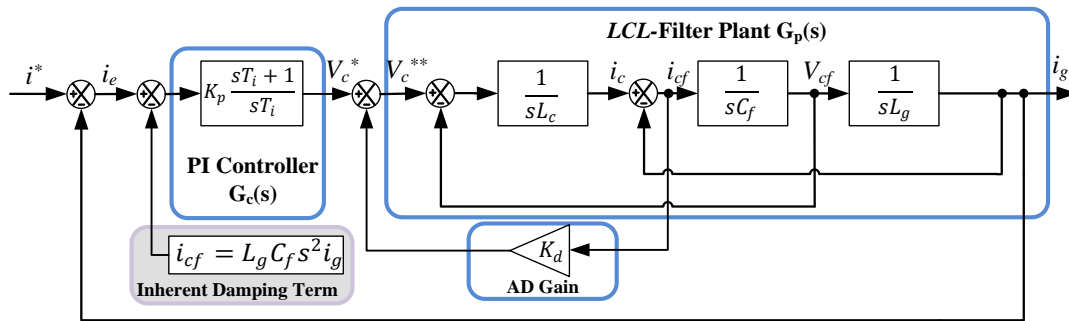


Figure 4.10 Block diagram of CCF with AD loop

$$\frac{I_g(s)}{I_e(s)} = \frac{K_p(s + 1/T_i)}{s^4 C_f L_c L_g + s^3 (K_p + K_d) C_f L_g + s^2 (K_p C_f L_g / T_i + L_c + L_g)} \quad (4.7)$$

Similar to the previous case, the current controller gain and the AD gain are adjusted as shown in (4.8). It should be noted that the effect of AD on the stability of the WECS using CCF is limited due to the presence of an inherent damping term yielding the very same effect.

$$K_p + K_d = 2\zeta \sqrt{\frac{L_c^2 + L_c L_g}{L_g C_f}} \quad (4.8)$$

The pole-zero diagram shown in Figure 4.11 demonstrates the behavior of closed-loop poles. Without AD, GCF does not achieve stability as it is discussed previously. The conjugate symmetric poles of the undamped system are pushed to the left hand side by applying AD on GCF. On the contrary, CCF satisfies a stable system without AD. With the addition of AD gain, the closed-loop poles of CCF method only moves within the stable region. This fact supports the finding derived in (4.7). The damping coefficient inherent to CCF is summed with the AD gain, K_d and

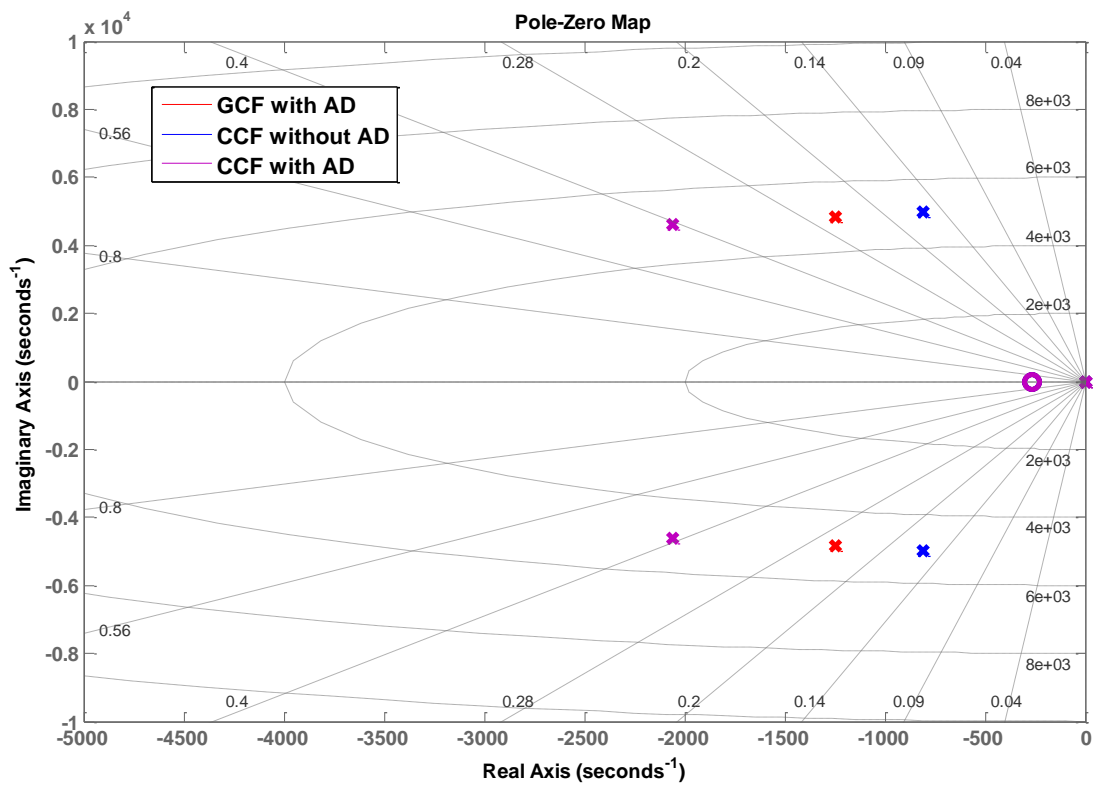


Figure 4.11 Pole and zero locations under GCF with AD, CCF with and without AD

4.4. Advanced Passive Damping

PD is an unproblematic solution to the resonance issue of the *LCL* filter as stated in the previous section; however, the losses caused by PD are extremely high especially for high power WECS. The resistive losses may increase up to 2% of the WECS's rated power and the efficiency of the overall system decreases severely. Advanced passive damping methods could be used instead of simple passive damping only with resistors.

The topologies analyzed in this study are proposed in [7]. The calculation of resistive losses is stated but the frequency characteristics are not given. The damping extent and the suppression of the resonant peak are very important for the optimum design of *LCL* filter as well as the overall efficiency of the design.

In the following, four different *LCL* filter topologies combined with reactive components are presented. In each case, inductors of the *LCL* filter on the grid side and on the converter side are assumed the same as it is stated in the design process in Chapter 3.

4.4.1. Design of Advanced Passive Damping Methods

Figure 4.12 below shows advanced passive damping methods. Reactive elements are connected in series or parallel with the damping resistors in order to provide a suitable impedance path for the resonant harmonics.

An additional damping inductor is connected in parallel with the damping resistor in Figure 4.12 (a), Type 1. At the fundamental frequency $\omega = \omega_g$ the inductor in parallel with the resistor should provide a low impedance so that the resistive losses are minimized. At the resonant frequency $\omega = \omega_{res}$ the resistor must accept the dominant part of the current flow through itself for a suitable damping performance.

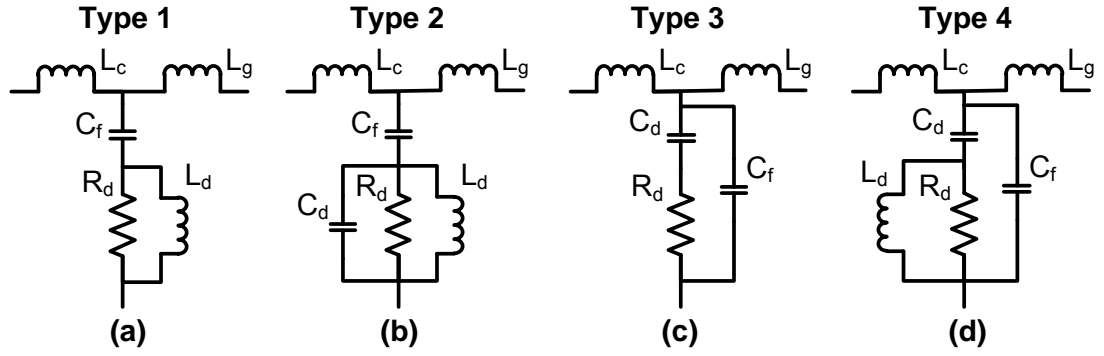


Figure 4.12 Advanced passive damping methods (a) Type 1, (b) Type 2, (c) Type 3, and (d) Type 4

Transfer function of the abovementioned damping schematic is given in equation (4.9). The characteristics of the advanced damping method shown in Figure 4.12 (a) is similar to the simple passive damping case as the transfer function is in the order of two. The damping inductor value is calculated using the equation (4.10). The impedance ratios of R_d and L_d at the fundamental frequency and resonant frequency are kept equal for keeping a proper balance.

$$Y_{Type\ 1}(s) = \frac{I_g(s)}{V_c(s)} = \frac{s^2 C_f L_d R_d + s L_d + R_d}{b_4 s^4 + b_3 s^3 + b_2 s^2 + b_1 s}$$

$$b_4 = C_f L_c L_g L_d$$

$$b_3 = C_f R_d (L_c L_g + L_c L_d + L_g L_d) \quad (4.9)$$

$$b_2 = L_d (L_c + L_g)$$

$$b_1 = R_d (L_c + L_g)$$

$$\frac{R_d}{L_d \omega_g} = \frac{L_d \omega_{res}}{R_d} \quad (4.10)$$

In Figure 4.12 (b), Type2, a damping capacitor is added in parallel with the inductor and resistor for reducing the losses with regard to switching frequency harmonic. A very small impedance path is created by inserting the damping capacitor. At $\omega = \omega_{sw}$ the dominant current flow path is through the capacitor while the resistor is the only effective element at $\omega = \omega_{res}$. As the switching frequency and the resonant frequency are very close for high power inverters, it would be risky to create a small impedance path. The resonance may be triggered by harmonics at the sideband of the resonance even if they are very small. In the frequency characteristics, it is seen more clearly.

Transfer function related to Figure 4.12 (b) is derived in equation (4.11). The third order transfer function may provide an advantage for removing the switching harmonics. The value of damping capacitor is calculated using (4.12).

$$Y_{Type\ 2}(s) = \frac{I_g(s)}{V_c(s)} = \frac{s^2(C_f L_d R_d + C_d L_d R_d) + s L_d + R_d}{b_5 s^5 + b_4 s^4 + b_3 s^3 + b_2 s^2 + b_1 s}$$

$$b_5 = C_f L_c L_g R_d L_d C_d$$

$$b_4 = C_f L_c L_g L_d \tag{4.11}$$

$$b_3 = R_d(C_f L_c L_g + C_f L_c L_d + C_f L_g L_d + C_d L_c L_d + C_d L_g L_d)$$

$$b_2 = L_d(L_c + L_g)$$

$$b_1 = R_d(L_c + L_g)$$

$$\frac{1/C_d \omega_{res}}{R_d} = \frac{R_d}{1/C_d \omega_{sw}} \tag{4.12}$$

Most of the current harmonics at the switching frequency are bypassed through the filter capacitor, C_f in Figure 4.12 (c), Type 3. The resistive losses are eliminated while the damping performance of the filter is kept satisfactory. The value of the damping capacitor is the same as in Type 2.

Transfer function of the filter shown in Figure 4.12 (c) is derived in the equation (4.13) below. The third order characteristic of the filter is maintained as the indicator of superior performance for removing the high frequency switching harmonics.

$$Y_{Type\ 3}(s) = \frac{I_g(s)}{V_c(s)} = \frac{sC_d R_d + 1}{b_4 s^4 + b_3 s^3 + b_2 s^2 + b_1 s}$$

$$b_4 = C_f L_c L_g R_d C_d$$

$$b_3 = L_c L_g (C_f + C_d)$$

$$b_2 = C_d R_d (L_c + L_g)$$

$$b_1 = L_c + L_g$$
(4.13)

Lastly, a more advanced topology is shown in Figure 4.12 (d), Type 4. The damping inductor is connected in parallel with the damping resistor as the difference from Type 3. The resistive losses at the fundamental frequency are reduced while the damping performance is not affected by the insertion of reactive elements.

Equation (4.14) demonstrates the transfer function of the filter in Figure 4.12 (d). The third order characteristic of the filter reflects the good filtering performance as in the case of Type 2 and Type 3.

$$Y_{Type\ 4}(s) = \frac{I_g(s)}{V_c(s)} = \frac{s^2 L_d C_d R_d + s L_d + R_d}{b_5 s^5 + b_4 s^4 + b_3 s^3 + b_2 s^2 + b_1 s}$$

$$b_5 = C_f L_c L_g R_d L_d C_d$$

$$b_4 = L_c L_g L_d (C_f + C_d)$$

$$b_3 = R_d (C_f L_c L_g + C_d L_c L_g + C_d L_c L_d + C_d L_d L_g)$$

$$b_2 = L_d (L_c + L_g)$$

$$b_1 = R_d (L_c + L_g)$$
(4.14)

4.4.2. Frequency Characteristics of Advanced Passive Damping Methods

Using the transfer functions given in equations (3.6), (3.8), (4.9), (4.11), (4.13), and (4.14) the frequency characteristics of the filters are demonstrated. As it can be seen in Figure 4.13, the undamped case causes an infinite gain at the resonant frequency which should be smoothed. Simple passive damping provides the necessary damping effect at the expense of resistive losses.

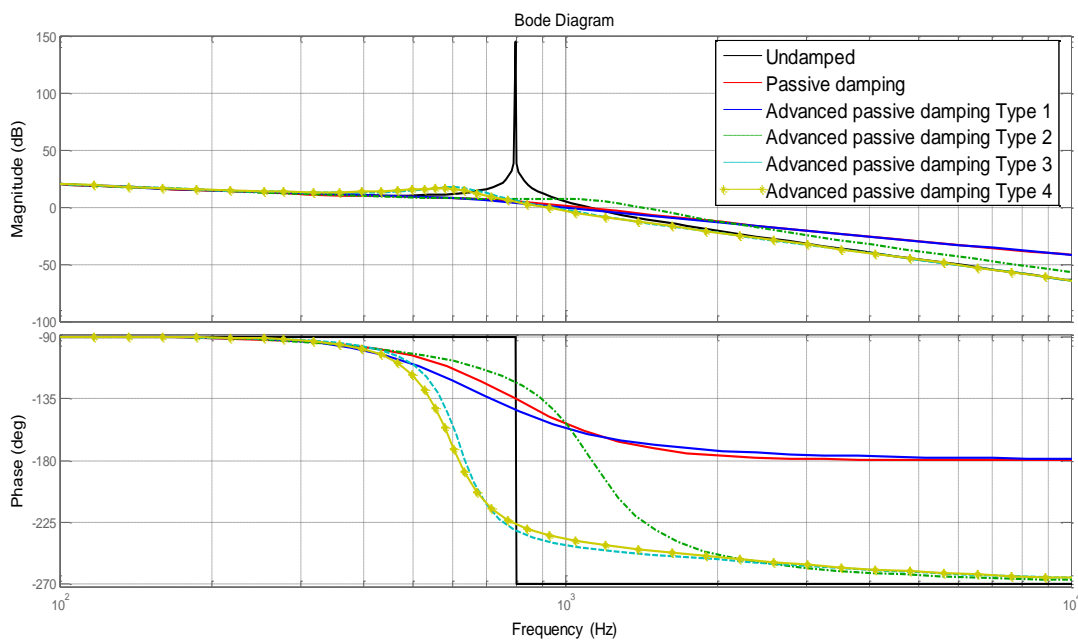


Figure 4.13 Bode plots of investigated advanced passive damping methods

Advanced damping method Type 1 is very similar to the simple passive damping in terms of both the magnitude response and the phase response. -40dB/dec slope in the magnitude response beyond the resonant frequency is maintained. The phase margin is almost the same as the phase crossover frequencies are very close to each other.

The magnitude response of advanced passive damping Type 2 is somehow different as a resonant peak occurs at a frequency very close to the switching frequency. There is a high risk of resonance for this case. The phase crossover frequency is

shifted to the right side of the undamped case, leaving no phase margin at all. The filter should be tuned not to create undesired oscillations.

The responses of the advanced passive damping Type 3 and Type 4 are found to be similar despite the addition of a damping inductor, L_d . There is a slight difference in terms of phase crossover frequency. The latter method provides a higher phase margin and hence a more stable system.

As the resonance problem may be triggered due to a non-zero gain of Type 2 around the switching frequency, the filter is tuned according to the results obtained from Figure 4.14. The damping capacitor value is varied from 200 μF to 1200 μF . 200 μF is found to be more suitable since the resonant peak is diminished although the phase crossing frequency is shifted towards 1100 Hz. A further decrease of the damping capacitor value does not make a significant effect on removing the resonant peak. Moreover, the phase crossover frequency gets closer to the switching frequency. Hence, 200 μF is selected.

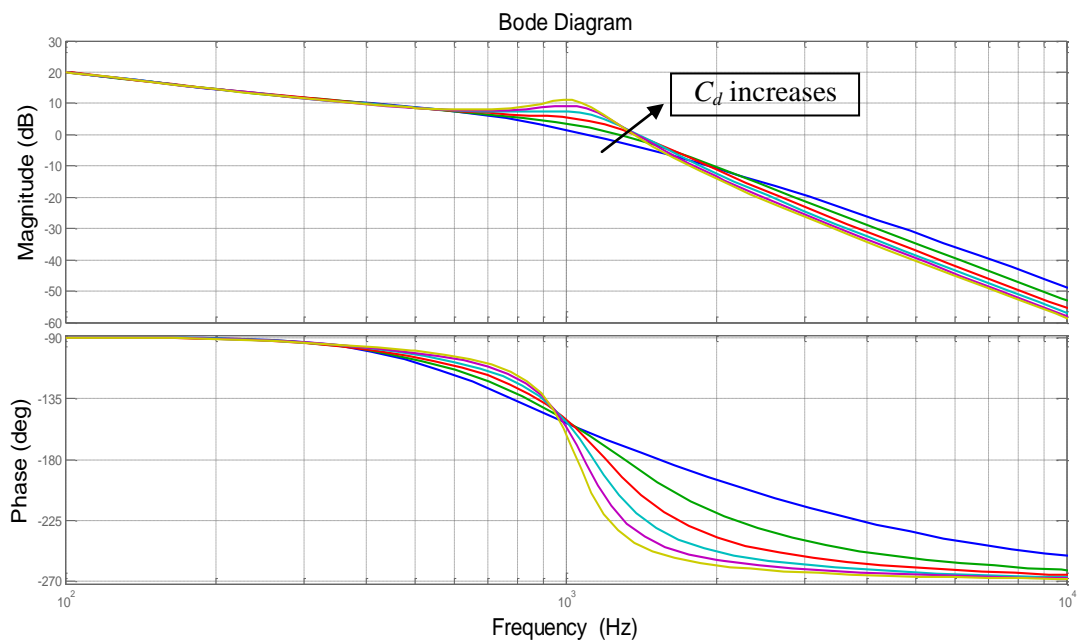


Figure 4.14 Tuning of the damping capacitor value for Type 2

The overall comparison of bode plots with Type 2 tuned is shown in Figure 4.15.

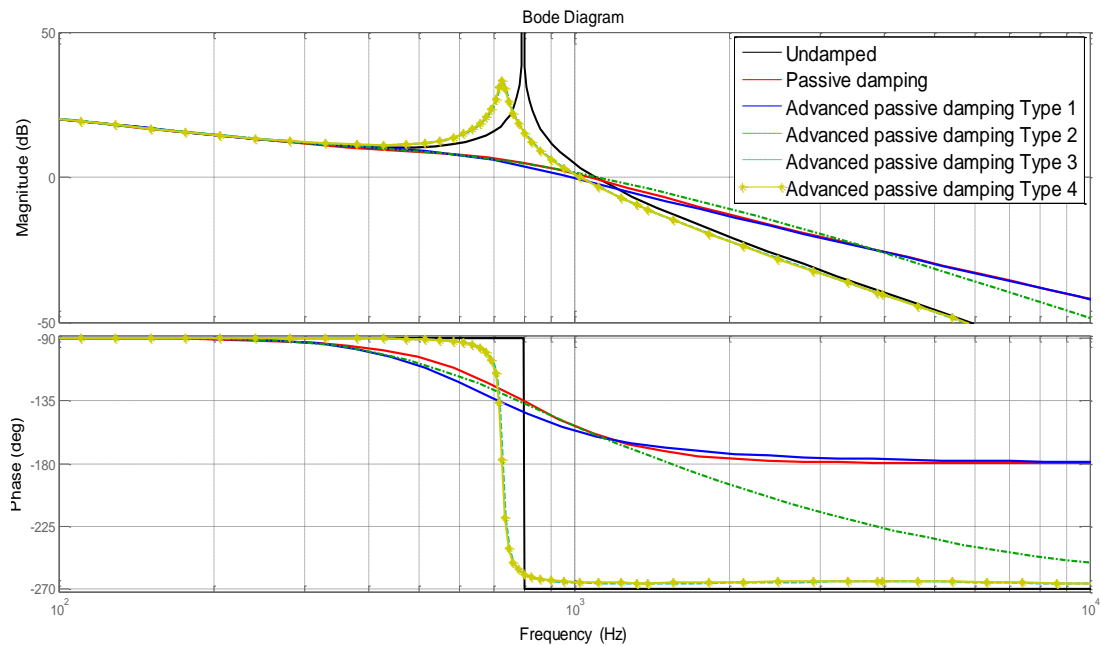


Figure 4.15 Bode plots of advanced passive damping methods, Type 2 tuned

4.5. Switch Mode Converter Based Damping

The proposed SAF compensated systems are investigated under two distinct topologies: transformer-coupled SAF (TC-SAF) and directly-connected SAF (DC-SAF) both acting as equivalent series damping resistors.

TC-SAF has three auxiliary single-phase PWM converters connected to a common DC-bus and each of the auxiliary converters has its own current regulator. The outputs of the auxiliary converters are shifted by 120° to reconstruct the desired voltage and current waveforms on the three-phase *LCL* filter. On the contrary, DC-SAF has a common auxiliary three-phase PWM converter connected to the *LCL* filter via ac coupling inductors. The first topology is thoroughly analyzed in [11] but an overview is still presented in [12]. Proposed in [12], the second approach; however, eliminates the coupling transformers and halves the number of auxiliary

converter switches. The common aspects of these methods are stated via schematics below.

SAF algorithm is applied to a selected frequency bandwidth in which the resonant frequency exists while passive damping provides a constant damping ratio along the whole bandwidth. Simplified circuit diagrams at the fundamental frequency and resonant frequency are demonstrated in Figure 4.16 and Figure 4.17 respectively.

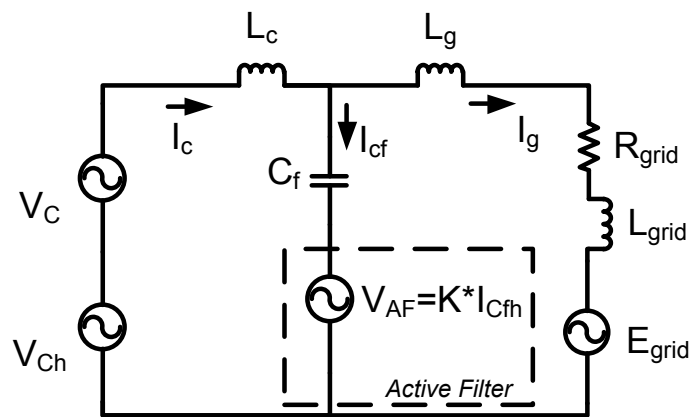


Figure 4.16 Single-phase equivalent circuit of SAF compensated system

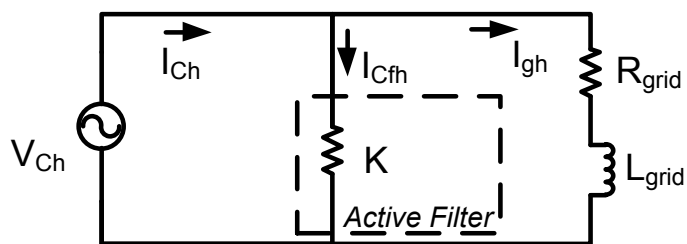


Figure 4.17 Single-phase equivalent circuit of SAF compensated system at the resonant frequency

The subscript “h” denotes the resonant harmonic component of the currents and voltages. The effect of passive damping is directly applied by an active sub-system yet a major difference occurs in the efficiency rating of the inverter. The resistive

losses of PD are transformed to switching and conduction losses of semiconductors in SMCD.

4.5.1. Design of SMCD Methods

4.5.1.1. Design of Transformer-coupled SAF Based Damping

The proposed transformer-coupled method offers a suitable solution to suppress the resonant harmonics appearing in the system for high power inverters operating at very low switching frequencies. A three-phase 2L PWM-VSI is shown in Figure 4.18 together with 3 auxiliary full-bridge converters. The VSI is connected to the grid via an *LCL* filter and current feedback for the closed-loop controller is taken from the grid side.

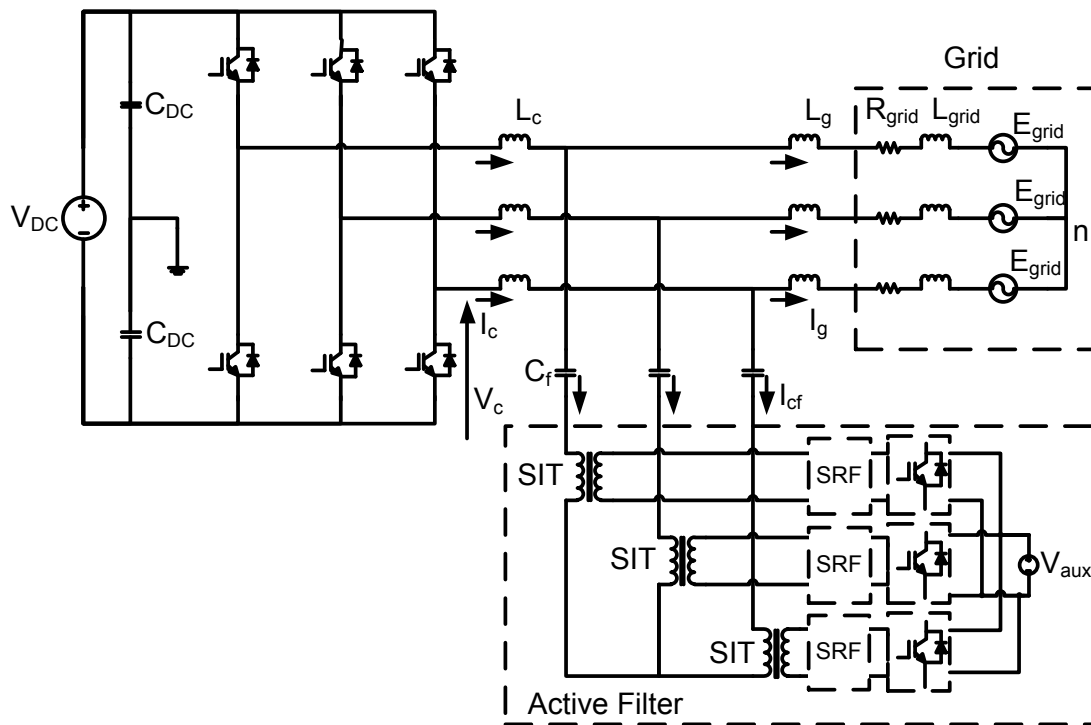


Figure 4.18 Grid-connected 2L three-phase VSI with TC-SAF based damping

The main inverter cannot be stabilized by active damping due to very low switching frequency of the inverter. The resonant frequency; on the other hand, has to be smaller than the switching frequency in order to satisfy the grid harmonics regulation. The designer should place appropriate *LCL* filter components in *p.u.* to provide suitable harmonic attenuation ratio at the switching frequency and its multiples. In contrast, the excessive sizes of line and converter side inductors create a significant voltage drop on the passive components, which should be kept small (4% typically) by the designer.

The single-phase representation of TC-SAF compensated system is shown in Figure 4.19. Single-phase full-bridge VSI, series injection transformer (SIT) and switching ripple filter (SRF) are the main parts of the TC-SAF compensated system.

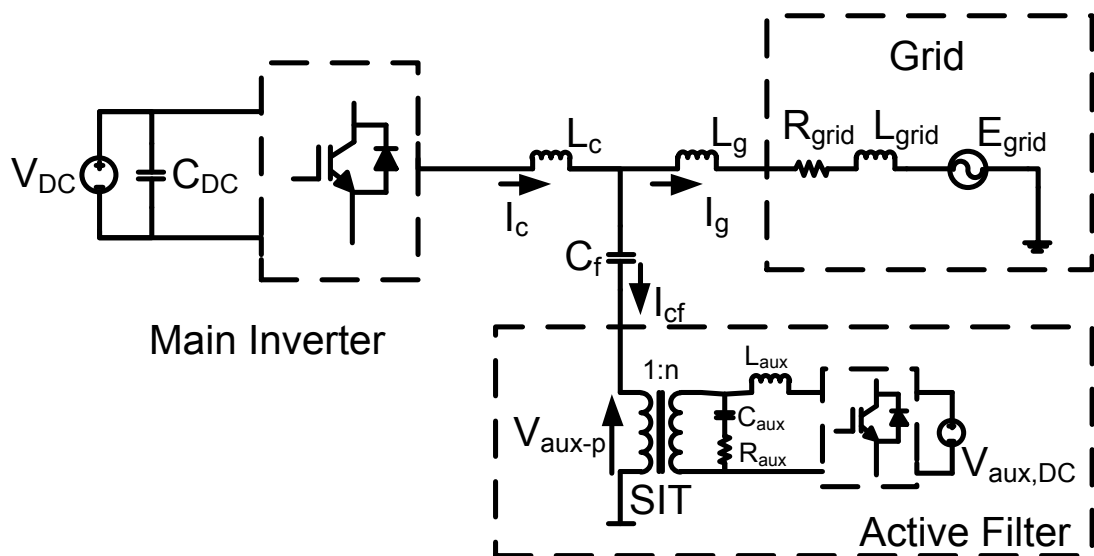


Figure 4.19 Single-phase representation of TC-SAF compensated system

SIT provides galvanic isolation between the main and auxiliary inverters. The turns ratio matches the voltage magnitudes of primary and secondary sides such that the desired voltage in series with the filter capacitor is maintained. The SIT should have low leakage inductance to keep the voltage drop on it low. Moreover, the harmonic

voltage applied to SIT should not cause overheating. The flux density of it must also be high in order to prevent magnetic saturation issues.

SRF is a low-pass filter composed of an inductor, a capacitor, and a resistor in the form of connection shown in Figure 4.19. The high frequency PWM ripple of the auxiliary VSI's output voltage is filtered out by the SRF. The required damping of the second order LC filter is provided by R_{aux} . The cut-off frequency of the filter is adjusted such that the harmonic attenuation ratio is satisfactory while the filter size is kept minimum.

The bode plots of the TC-SAF compensated and undamped LCL filters are given in Figure 4.20. A better harmonic attenuation performance at the switching frequency and its multiples is offered by the TC-SAF compensated LCL filter compared to passively damped LCL filter. Nevertheless, the resonant peak is still present on the bode plot but with a smaller magnitude.

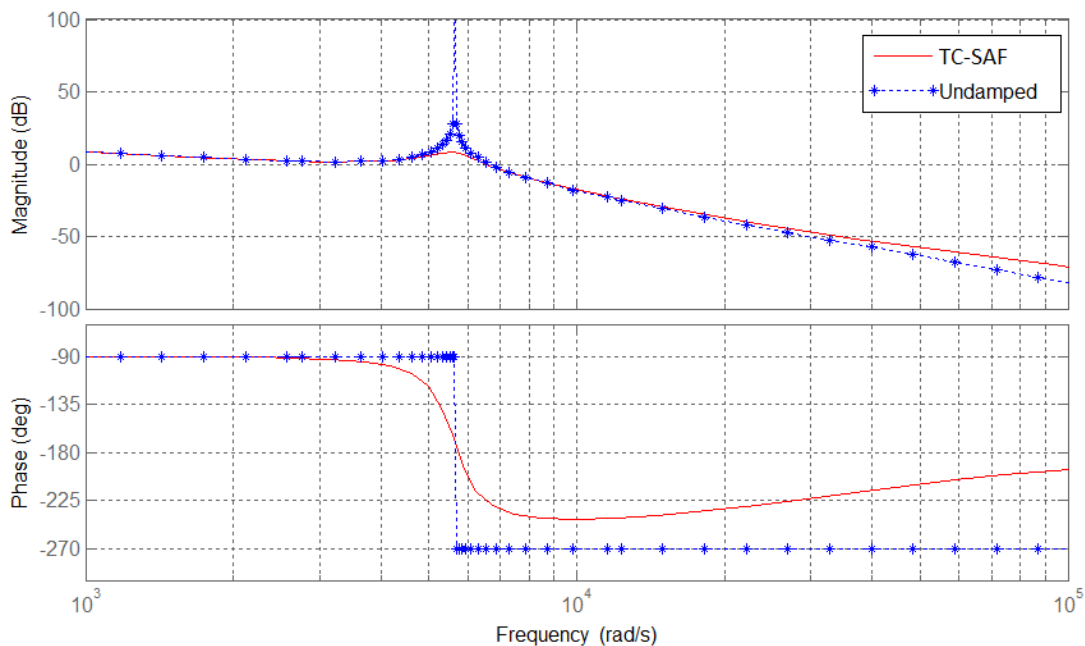


Figure 4.20 Bode plots of TC-SAF compensated and undamped LCL filters

4.5.1.2. Design of Directly-connected SAF Based Damping

The proposed DC-SAF topology together with 2L PWM-VSI connected to the grid is shown in Figure 4.21. Single-phase representation of DC-SAF based topology is also shown in Figure 4.22. DC-SAF components are a three-phase PWM inverter and a three-phase AC-link inductor, L_{aux} . The active filter is connected in series with C_f through L_{aux} .

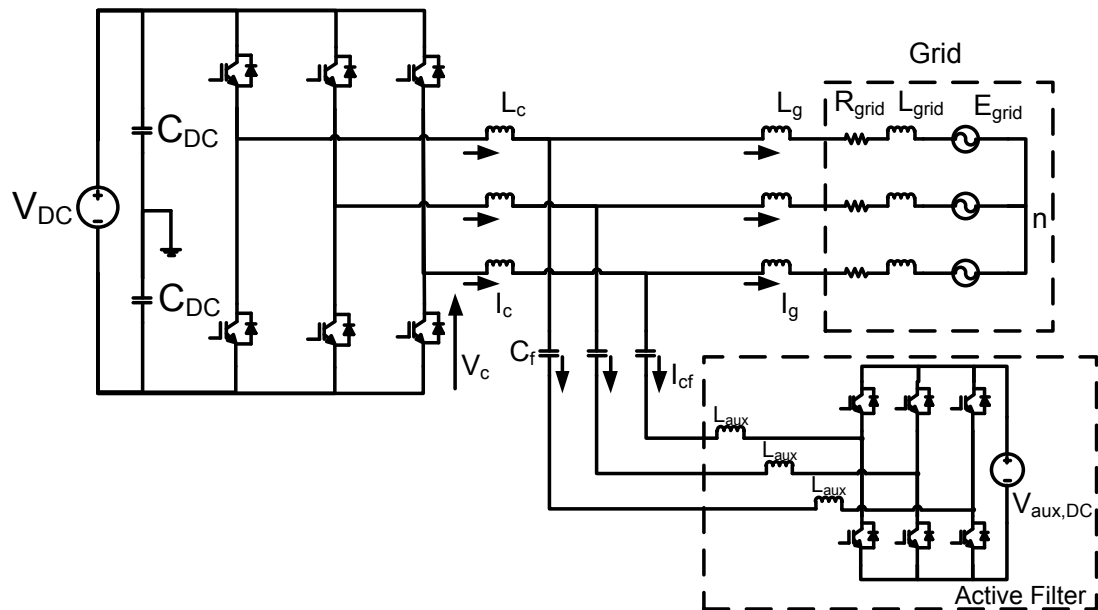


Figure 4.21 Grid-connected 2L three-phase VSI with DC-SAF based damping

The voltage at the auxiliary DC-bus is used to implement the selective resonant harmonics elimination algorithm. Due to high current and low-voltage on the auxiliary inverter, the semiconductors can be selected as MOSFET instead of IGBT. The smaller voltage drop on MOSFETs when the device is conducting is very attractive.

The bode plots of DC-SAF compensated and undamped LCL filters are given in Figure 4.23. DC-SAF has blunted the resonant peak more effectively than TC-SAF. The gain at this frequency is below 0 dB, refusing any harmonics to pass to the grid

side. At higher frequencies, the filtering performance is limited due to first-order characteristics of the DC-SAF compensated *LCL* filter. Poor filtering performance of the filter may result in a higher THD rating especially for switching frequencies of a few kilohertz.

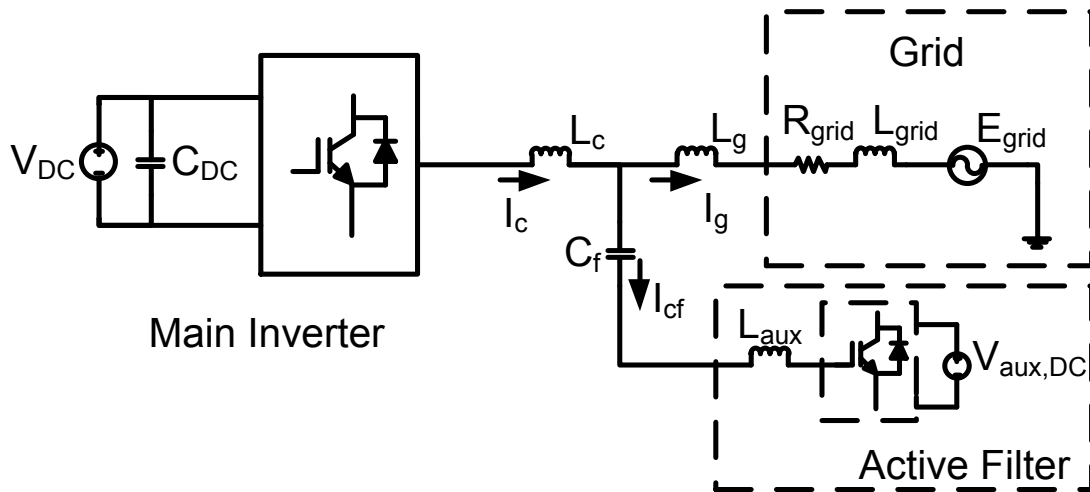


Figure 4.22 Single-phase representation of DC-SAF compensated system

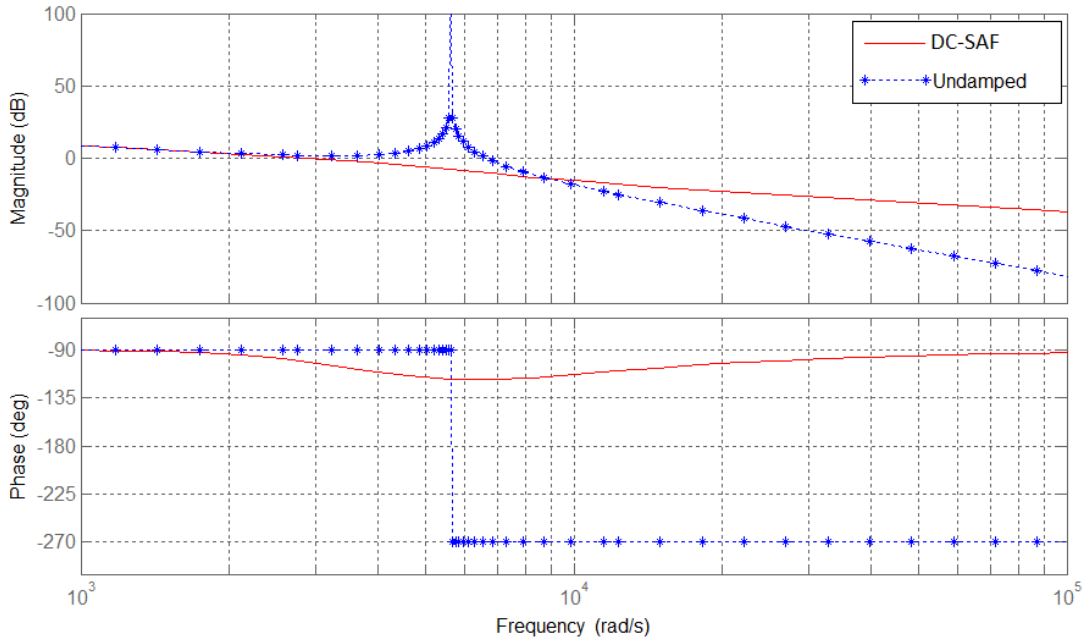


Figure 4.23 Bode plots of DC-SAF compensated and undamped *LCL* filters

4.5.2. Control of SMCD Methods

4.5.2.1. Control of Transformer-coupled SAF Based Damping

The current through the filter capacitor, I_{cf} is measured and processed by the current regulators of the auxiliary converters. The current harmonics around the resonant frequency are obtained from the measured current information via a band-pass filter and reproduced by the auxiliary converters. The high frequency ripple content of the auxiliary converters is limited by additional $L_{aux}-C_{aux}$ filters. Hence, a controlled voltage in the same phase with the resonant current is applied across the SIT terminals, in series with the filter capacitor. Consequently, the effect of a damping resistor is applied on the LCL filter through a series transformer. Proposed algorithm also provides a long-lasting operation for the system.

The control block diagram of the general system is demonstrated in Figure 4.24.

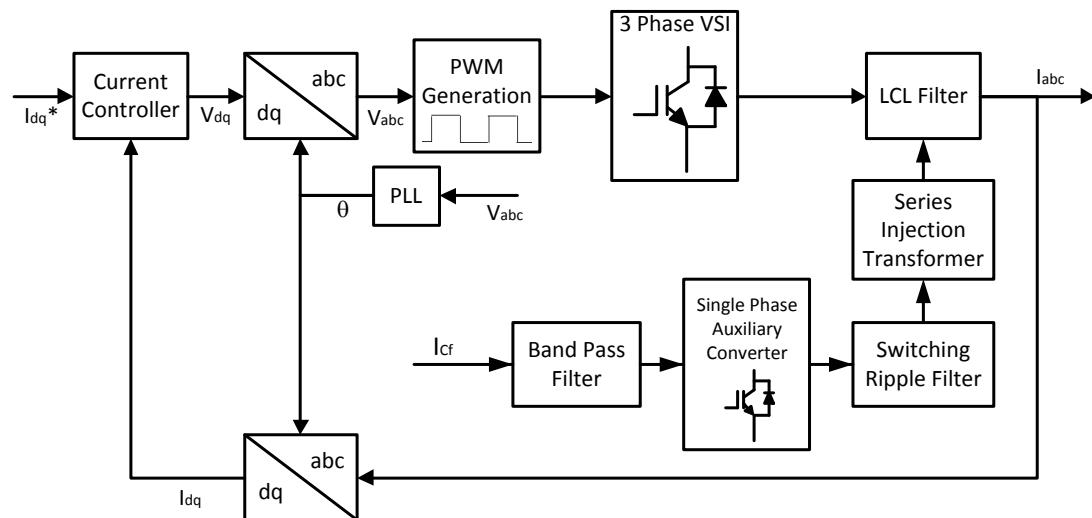


Figure 4.24 Block diagram of PWM-VSI with TC-SAF

SIT provides coupling between the LCL filter side and the auxiliary converter side. It also leads to reduced semiconductor losses in the auxiliary converters. Low-voltage,

high current at the *LCL* side is transformed to high-voltage, low current at the auxiliary converter side; therefore, semiconductor losses decrease noticeably. DC-bus voltage of the auxiliary converters is set to 600V so as to reproduce the resonant harmonics without entering the over-modulation region.

Proportional controller is applied to filter capacitor resonant harmonic current, I_{Cfh} to emulate a resistor by means of creating a voltage, V_{aux} at the output of the auxiliary VSI. The voltage reference driven by the controller is given in equation (4.15).

$$V_{aux} = K * i_{cfh} \quad (4.15)$$

Auxiliary converters work only for $s = j\omega_{res}$ and the transfer function stated in (3.8) is recalculated as follows;

$$Y_{TC-SAF}(s) = \frac{I_g(s)}{V_c(s)} = \frac{sC_f K + 1}{s^3 C_f L_c L_g + s^2 C_f K (L_c + L_g) + s(L_c + L_g)} \quad (4.16)$$

It is clear that the passive damping and SAF methods produce the same transfer function for $\omega = \omega_{res}$. The auxiliary converter gain, K is replacing the damping resistor, R_d term in (3.8) and emulates the damping resistor. Passive damping provides a constant gain along the whole bandwidth while SAF produces a controlled voltage only at the resonant frequency. The controllable auxiliary system; thus, increases the overall efficiency of the system.

4.5.2.2. Control of Directly-connected SAF Based Damping

The controller of DC-SAF compensated system is a proportional controller using the grid side current information, I_g as the feedback. The measured current is

transformed into synchronous dq reference frame and a band-pass filter is applied to select the harmonic components around the resonant frequency. The filtered current information is then multiplied by the P controller gain. The control block diagram is shown in Figure 4.25.

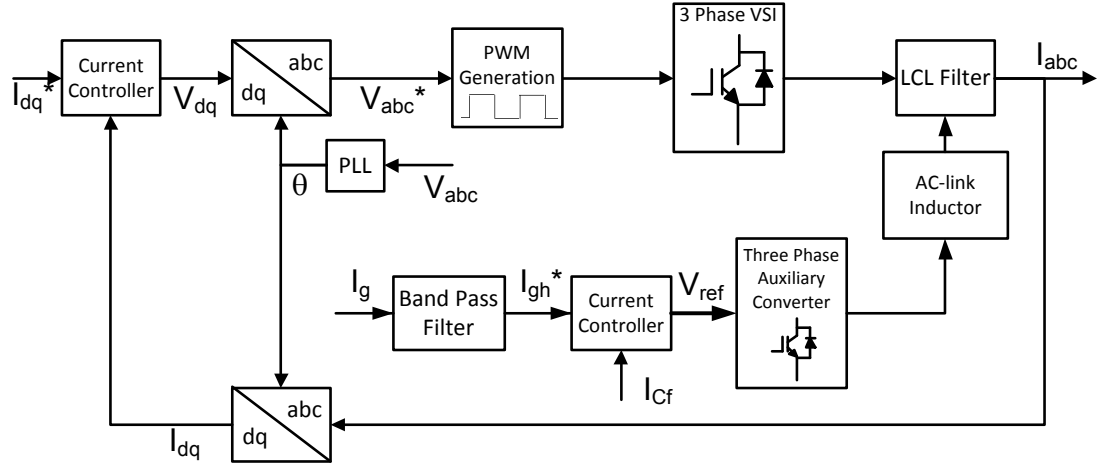


Figure 4.25 Block diagram of PWM-VSI with DC-SAF

The transfer function of the DC-SAF compensated LCL filter is given in (4.17).

$$Y_{DC-SAF}(s) = \frac{I_g(s)}{V_c(s)} = \frac{s^2 C_f L_{aux} + s C_f K + 1}{b_3 s^3 + b_2 s^2 + b_1 s}$$

$$b_3 = C_f (L_{aux} L_c + L_{aux} L_g + L_g L_c) \quad (4.17)$$

$$b_2 = K C_f (L_c + L_g)$$

$$b_1 = L_c + L_g$$

where K is the gain of the auxiliary three-phase PWM inverter.

4.6. Summary and Conclusion

ND, PD, and AD methods are analyzed in this chapter. The theoretical analyses and the simulations of all three systems are given. For high power applications such as 3 MW, the application of ND and AD is not possible due to limited controller bandwidth. PD seems to be the only option for multi-megawatt WECS. The resistive losses due to PD are not desired; hence, alternative damping structures are validated through bode plots and simulations as well.

Advanced passive damping methods are also valid options to remove the resonance as simple passive damping. The current flow path is modified by placing damping inductors and capacitors connected in series or parallel with the damping resistor. The losses with regard to the damping resistor are reduced down to 1/3 of the simple passive damping case. The resistive losses are still too high for multi-megawatt applications since the damping resistors cause power loss about 2% of the inverter's rated power. For a 3 MW application, the power loss due to PD is around 60 kW and it can only be reduced to 20 kW via advanced PD in the cause of increased complexity and cost. At this point, the advantages of SMCD methods come into discussion. The reduced power loss by utilizing SAF based topologies is very much desired since the long term benefits are worth to implement.

The advantages of DC-SAF compensated system over TC-SAF compensated system shall be stated. DC-bus voltage rating of the auxiliary converter is reduced from 600V to 200V; hence, high-voltage IGBTs shall be replaced by cheaper MOSFETs having lower forward voltage drop. The reduced voltages also mitigate radiated and/or conducted EMI emissions. Moreover, direct connection of the active filter part eliminates the usage of heavy SITs, limiting the dynamic performance of the system and having saturation problems. A possible disadvantage; on the other hand, is the increase of the auxiliary converter's current rating.

CHAPTER 5

VERIFICATION OF DAMPING METHODS

In this chapter, resonance damping methods which are stated in the literature but lacking the proof on multi-megawatt WECS are verified for a 3 MW WECS by means of computer simulations. The simulation studies are carried out via Ansoft – SIMPLORER[®]. Moreover, 3 MW PWM-VSI is simulated with different damping methods. The steady-state waveforms of the proposed damping methods are demonstrated as well as the load dynamic responses.

Simulation model in SIMULINK[®] is presented in Figure 5.1. Separate blocks of PWM-VSI, LCL filter, grid, and control blocks are seen clearly. The control blocks are presented as sub blocks; PLL, current regulator, active damping, DC-bus voltage regulator, and PWM.

The parameters of the simulated system are given in Table 5.1.

Table 5.1 Parameters of the simulated 3 MW PWM-VSI

| | Symbol | Quantity | Value |
|----------------------|---------------|---------------------------|--------------|
| Main Inverter | P_{rated} | Rated power | 3 MW |
| | f_{sw} | Switching frequency | 1.2 kHz |
| | f_{samp} | Sampling frequency | 2.4 kHz |
| | V_{dc} | DC-link voltage | 1070 V |
| | V_g | Grid voltage | 690 V |
| | f_g | Grid frequency | 50 Hz |
| | L_g | Grid side inductance | 80 μ H |
| | L_c | Converter side inductance | 80 μ H |
| | C_f | Filter capacitance | 1000 μ F |
| | R_d | Damping resistance | 0.2 Ω |
| | L_d | Damping inductance | 160 μ H |
| | C_d | Damping capacitance | 814 μ F |

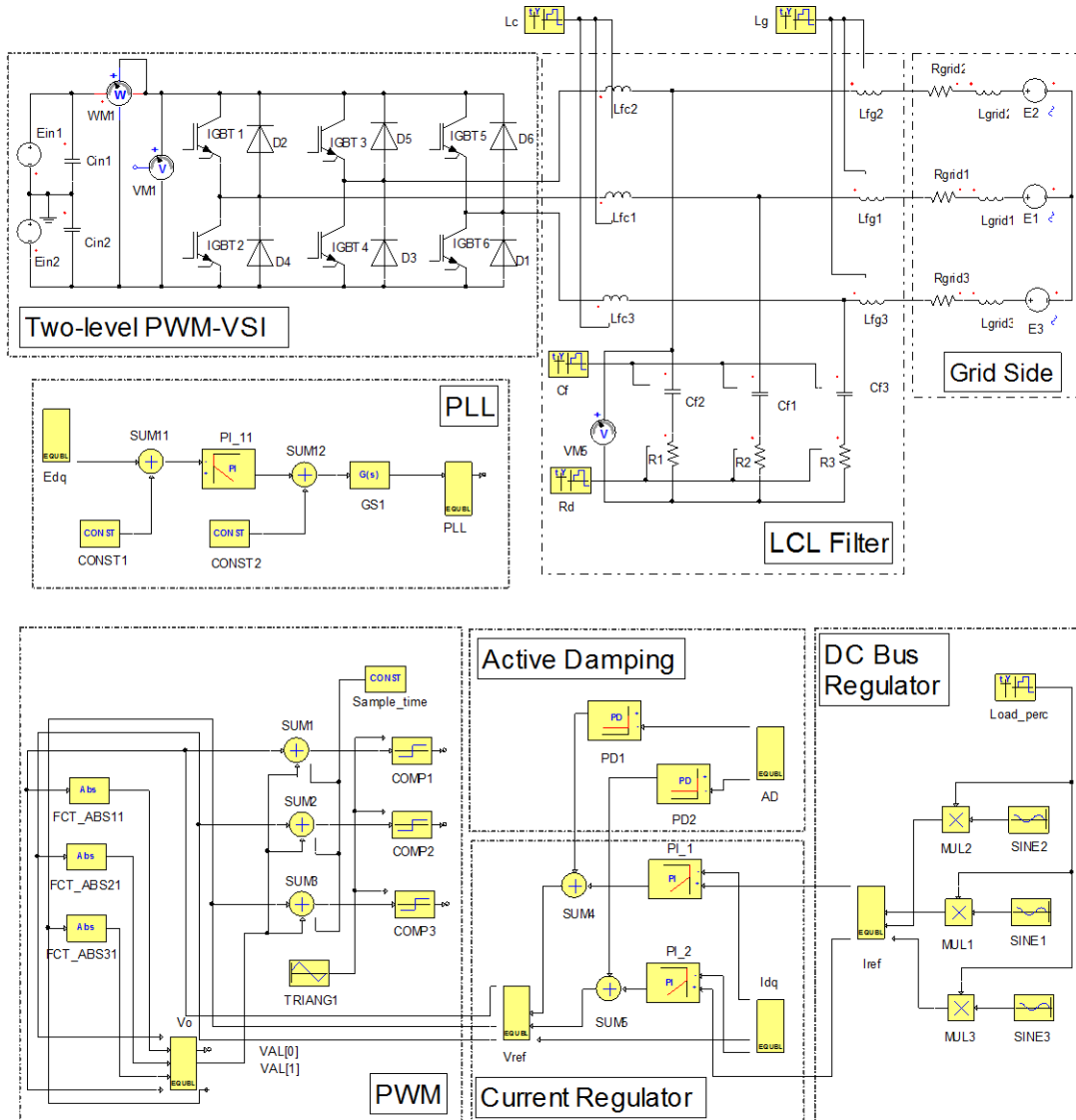


Figure 5.1 2L PWM-VSI simulation model in SIMPLORER

Although ND would provide a stable system without additional damping, it cannot be relied on practical applications such as high power grid side PWM-VSI of WECS. Thus, ND presents a solution only in theory. AD is not feasible for 3 MW system since the controller has inadequate bandwidth. Therefore, the simulation studies are not applied for ND and AD due to limited phase margins of the controllers. Instead, they are applied on 1 MW system which has a wider bandwidth due to increased switching frequency. The comparison of ND and AD methods are conducted in Chapter 6.

5.1. Simulation Results of Passive Damping

Figure 5.26 shows the simulated waveforms obtained from passively damped system. The converter side, grid side, and filter capacitor current waveforms are shown during two fundamental period of time at the steady-state.

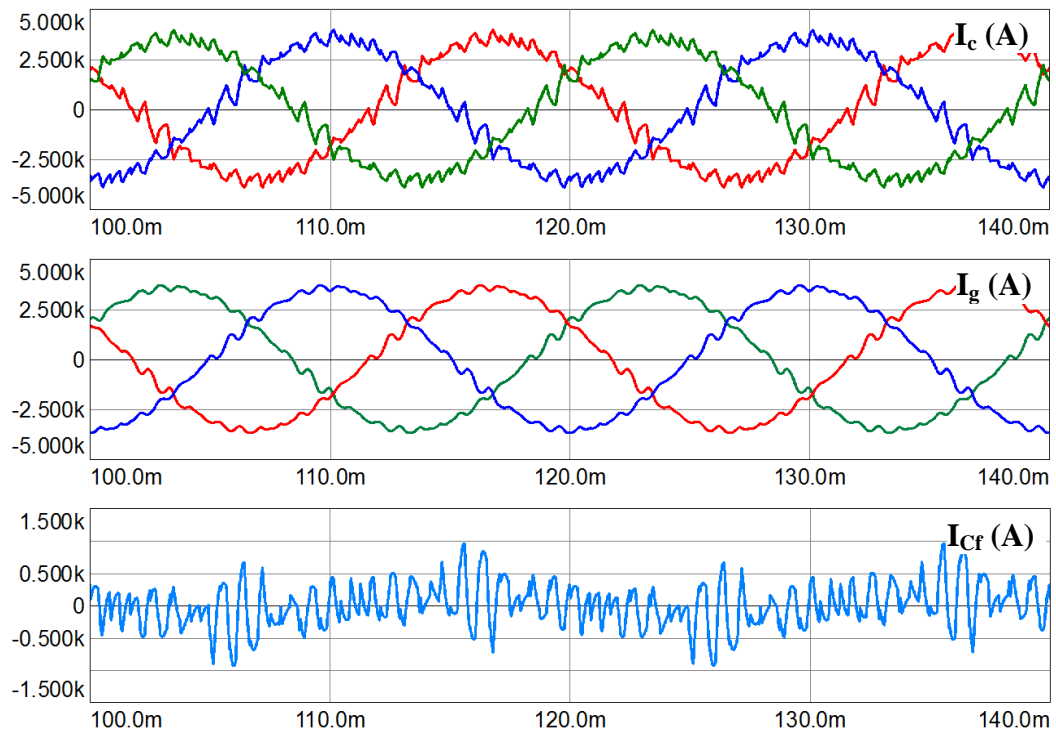


Figure 5.2 Passively damped system steady-state waveforms

In Figure 5.3, passively damped system is enabled at $t=100\text{ms}$ when the system operate with no damping. Then, PD is disabled at $t=160\text{ms}$ to demonstrate that the oscillations start again at the resonant frequency. When PD is disabled, the magnitude of the oscillations grows as time passes.

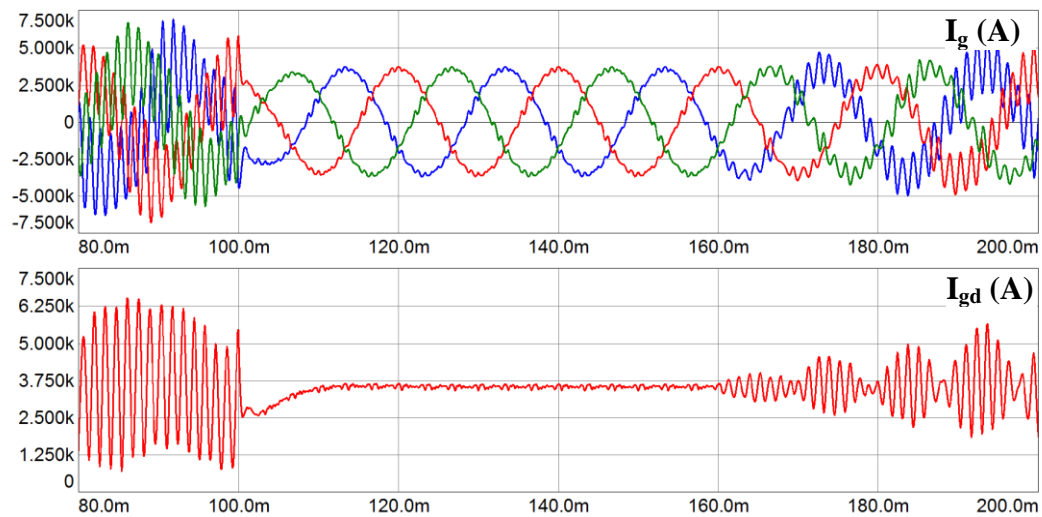


Figure 5.3 Activation of PD from undamped condition

In Figure 5.4, the converter side current, the grid side current, and the filter capacitor current are demonstrated both at the transition from undamped to passively damped condition and at steady-state. The high harmonic content in the converter side current is removed using LCL filter. The enormous magnitude of the filter capacitor current for the undamped case is controlled via PD. Otherwise; the capacitors would not withstand such current oscillations.

Dynamic response of PD is shown in Figure 5.5. Both the transition from light load (20%) to full load (100%) and vice versa are shown in the same figure. The d -axis current, I_{gd} also shown in Figure 5.5 explains the dynamic behavior of passively damped system. Due to large LCL inductors, the transition from rated load to light load takes a longer time.

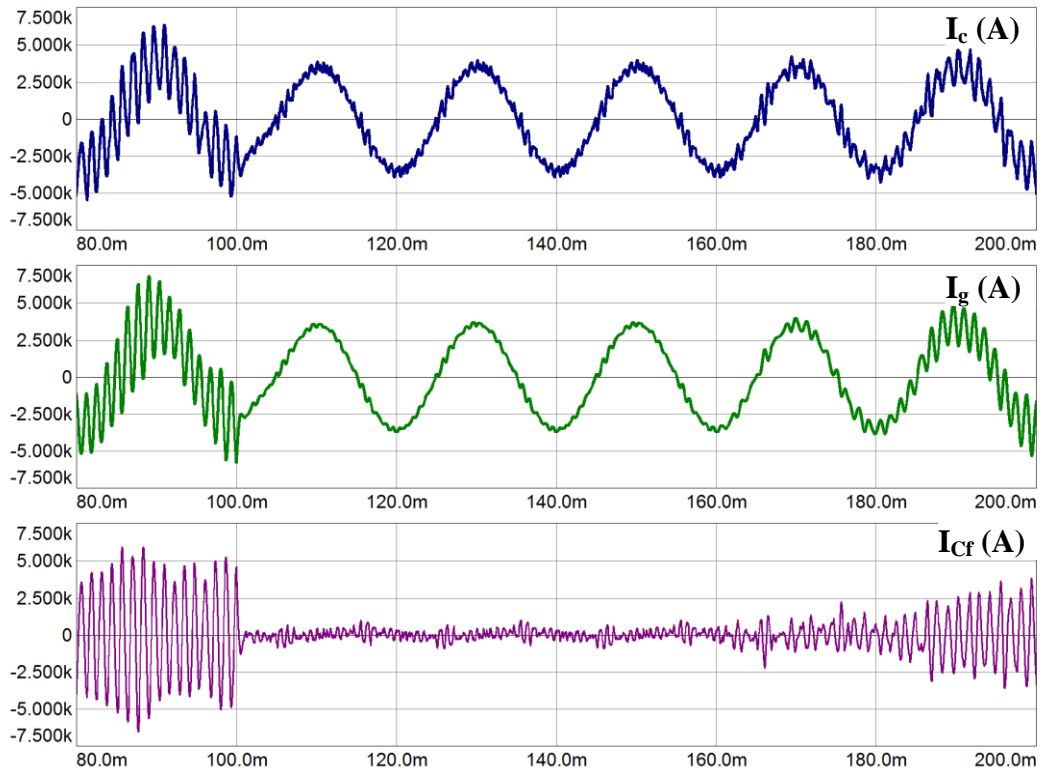


Figure 5.4 Current and voltage waveforms during the transition from undamped to passively damped condition and vice versa

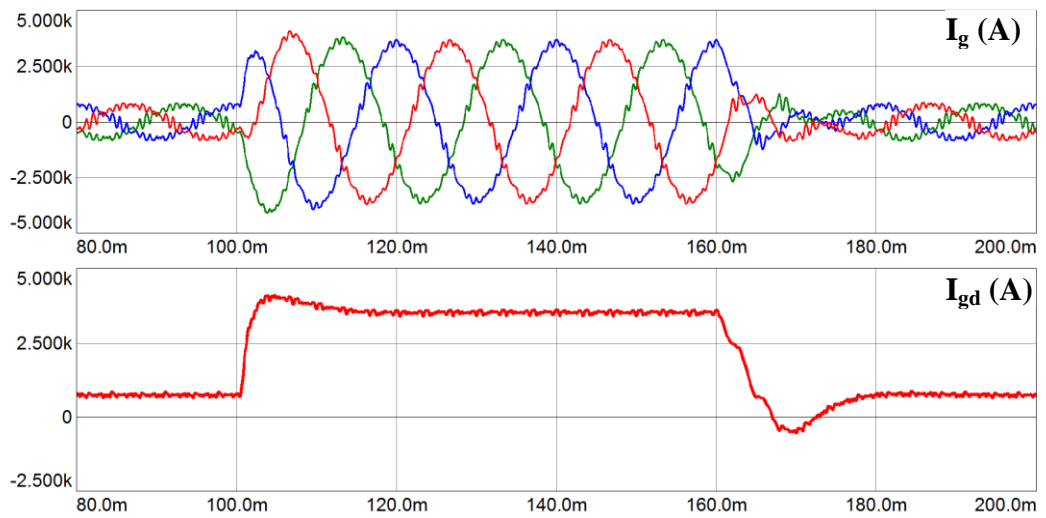


Figure 5.5 Load dynamic response of passively damped system from 20% load to rated load then to 20% load again

The FFT result of the grid side current is shown in Figure 5.6. In the frequency spectrum, low frequency harmonic components (up to 500 Hz) and resonant frequency harmonics at the sidebands of 900 Hz mixed with the switching frequency harmonics at the sidebands of 1.2 kHz are evident. The switching frequency harmonics around 2.4 kHz are not removed due to the deteriorated filtering capability of the passively damped *LCL* filter. For the higher multiples of the switching frequency, the *LCL* filter is suitable enough such that no harmonics seen beyond 3 kHz.

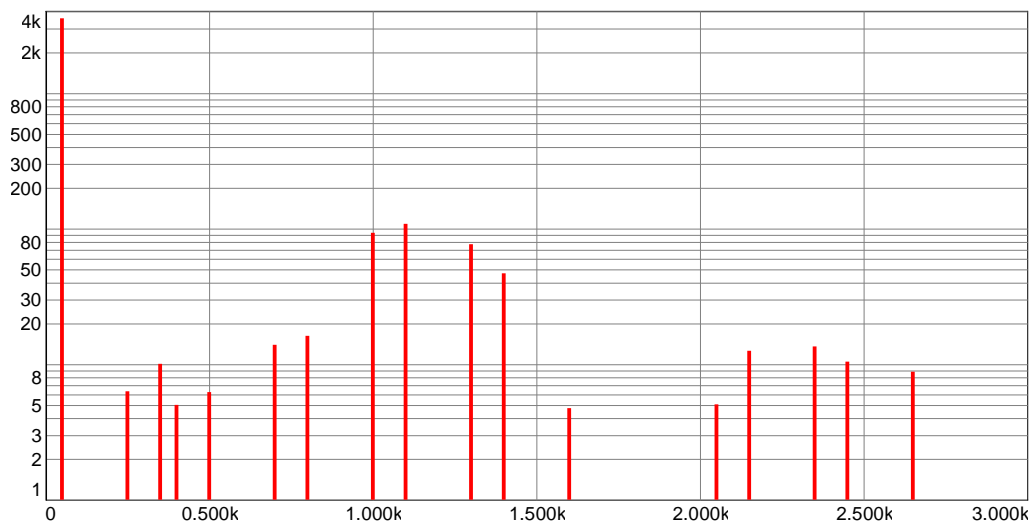


Figure 5.6 FFT analysis on grid current of passively damped system

5.2. Simulation Results of Advanced Passive Damping Methods

The steady-state waveforms of the advanced damping methods are given in this part of the chapter. The current waveforms at the grid side and the converter side together with the current waveforms through the damping resistors and inductors/capacitors are demonstrated for Type 1 to Type 4 in Figure 5.7, Figure 5.8, Figure 5.9, and Figure 5.10 respectively.

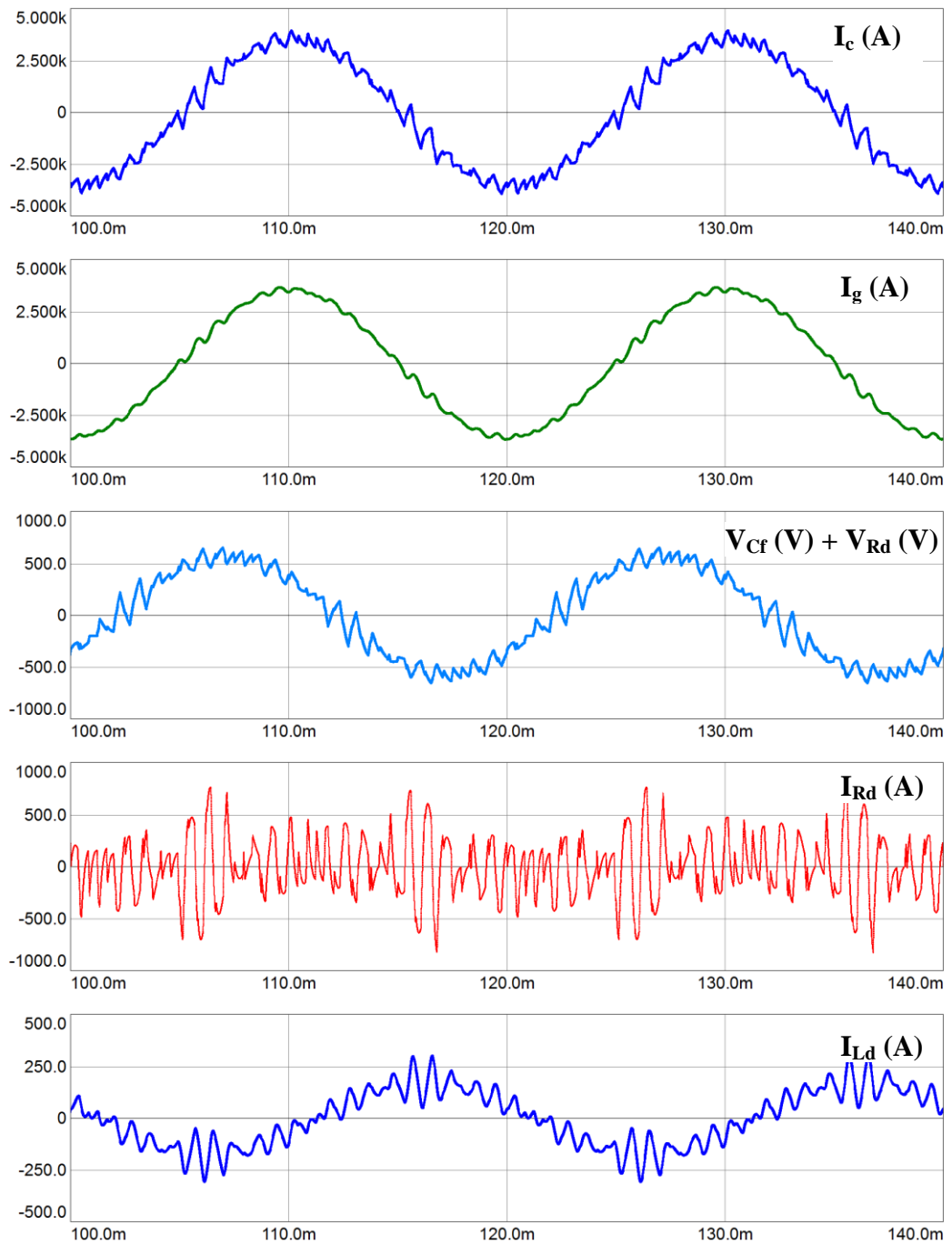


Figure 5.7 Steady-state waveforms of advanced passive damping Type 1

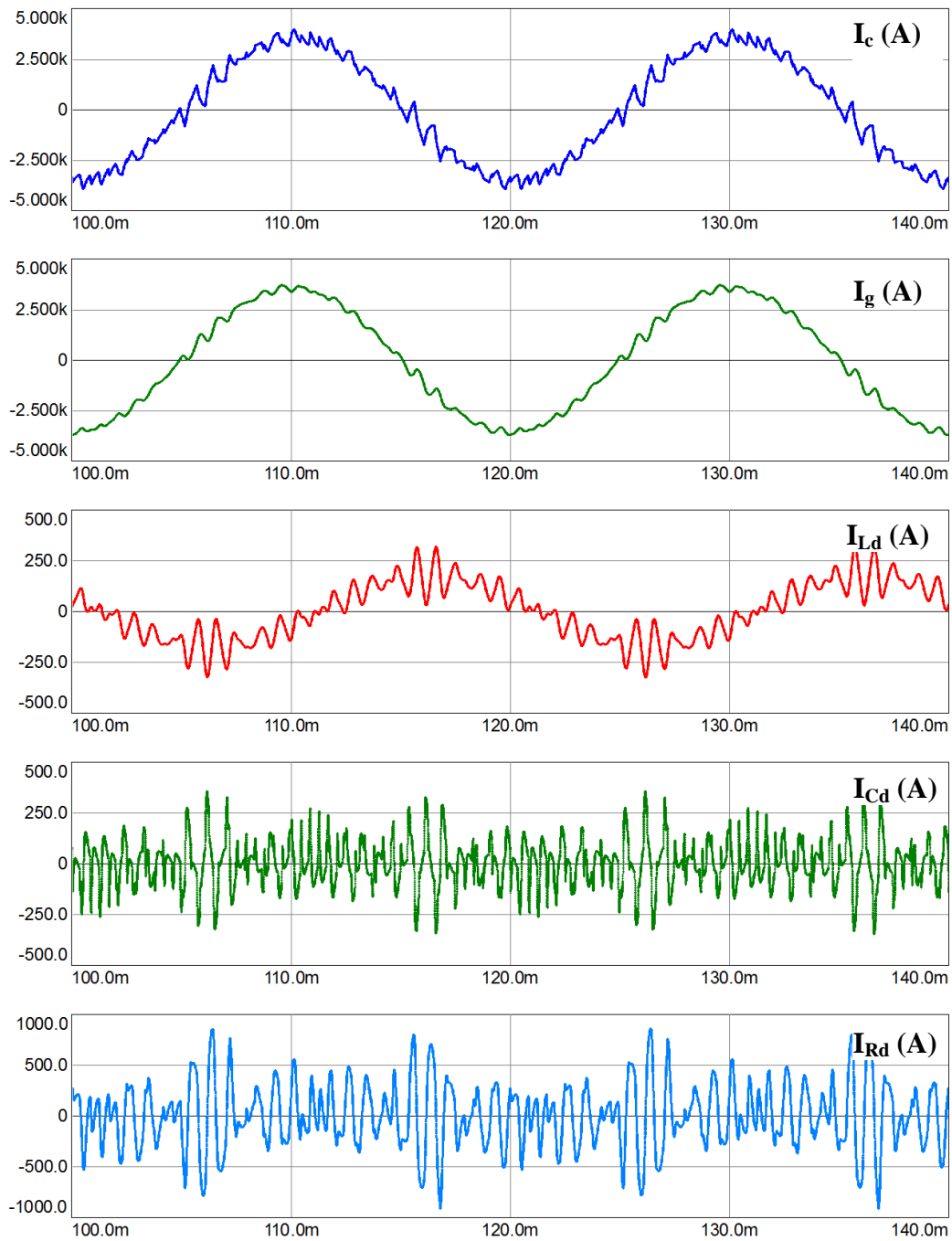


Figure 5.8 Steady-state waveforms of advanced passive damping Type 2

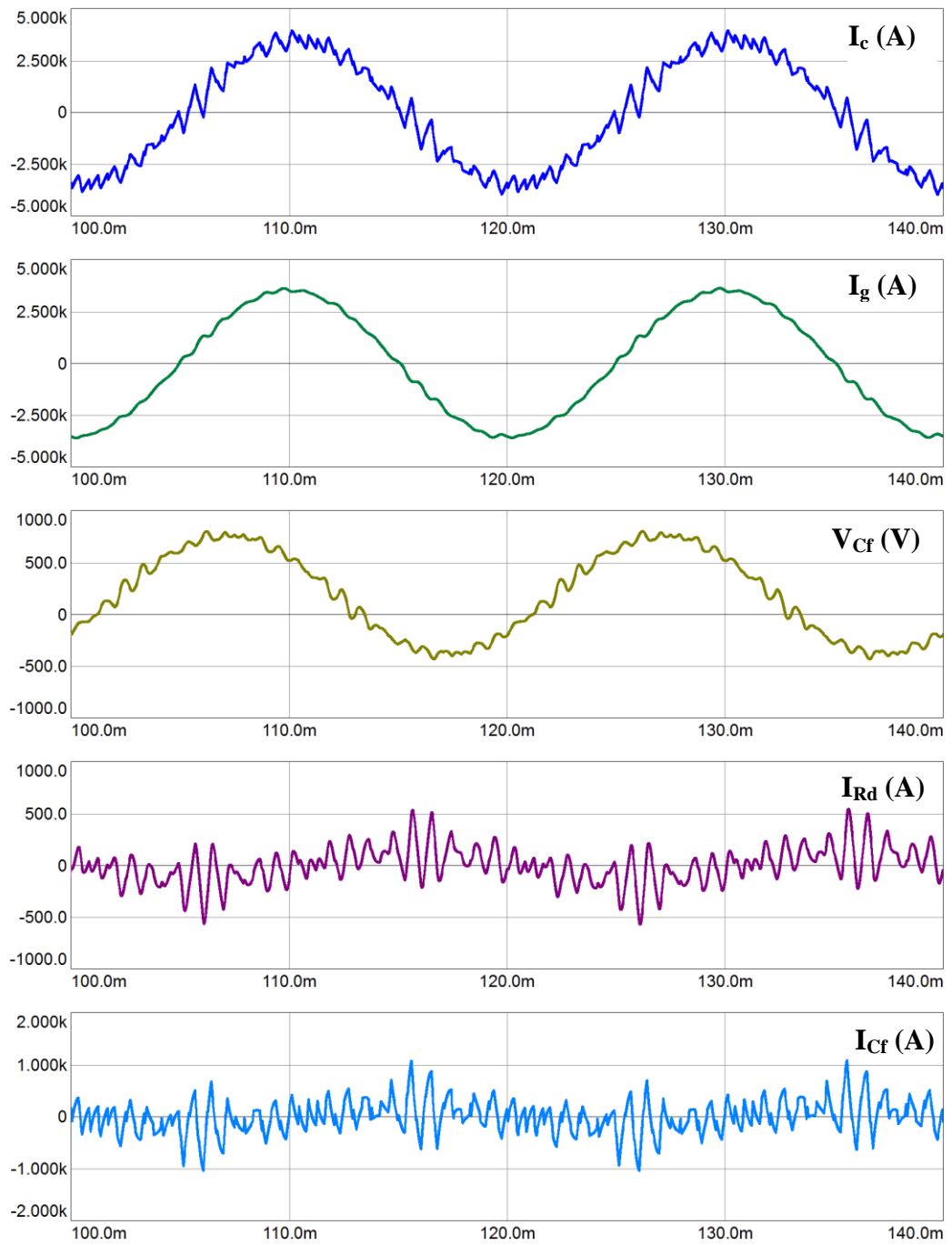


Figure 5.9 Steady-state waveforms of advanced passive damping Type 3

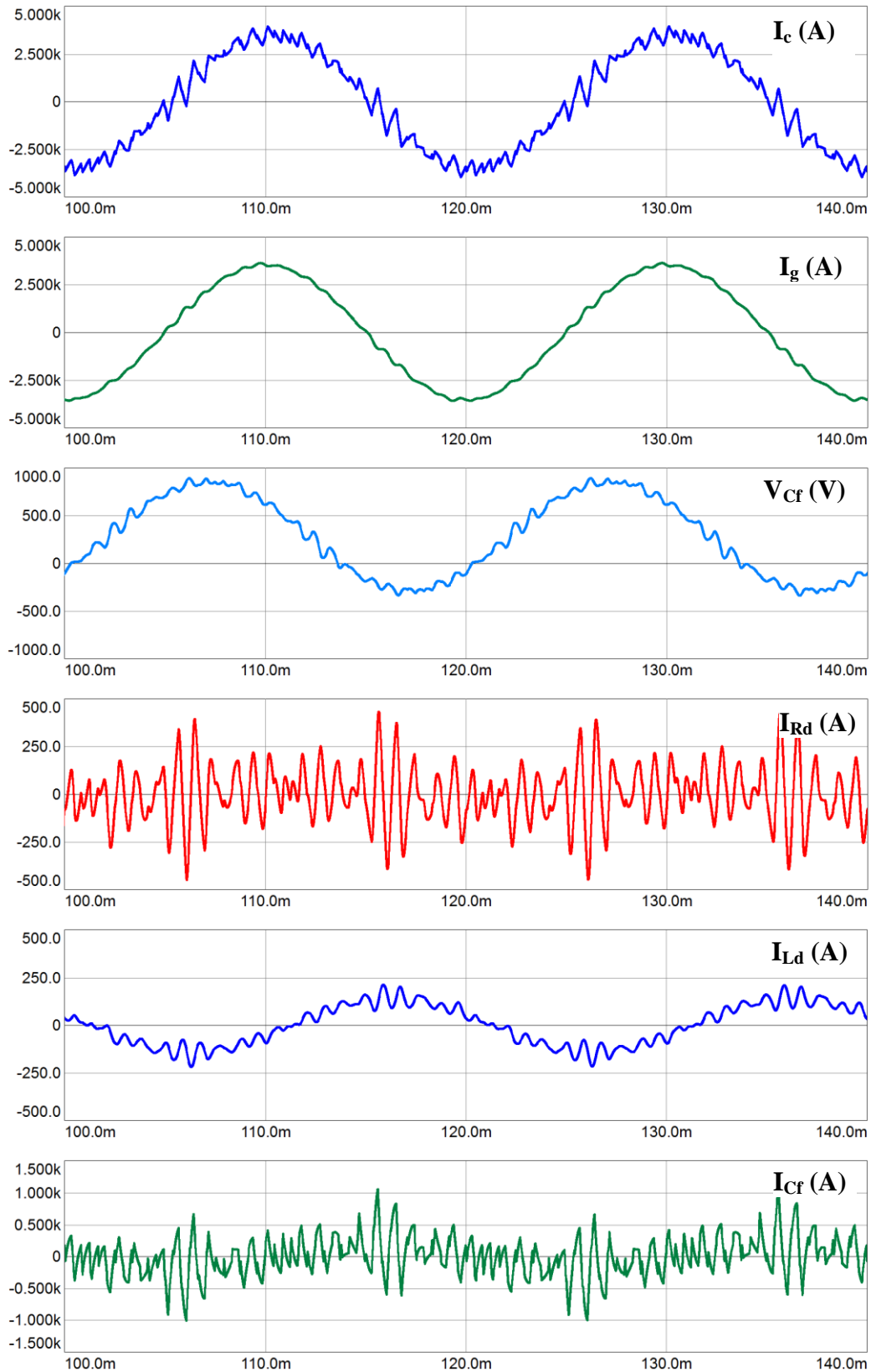


Figure 5.10 Steady-state waveforms of advanced passive damping Type 4

Dynamic load responses of advanced passive damping methods on the grid side current from 0.2 *p.u.* load to 1 *p.u.* load at $t=100\text{ms}$ and back to 0.2 *p.u.* load at $t=160\text{ms}$ are shown in Figure 5.11 to Figure 5.14 in the ascending order. The direct-axis current is also shown to demonstrate the settling times at the instants of both increased and decreased load conditions.

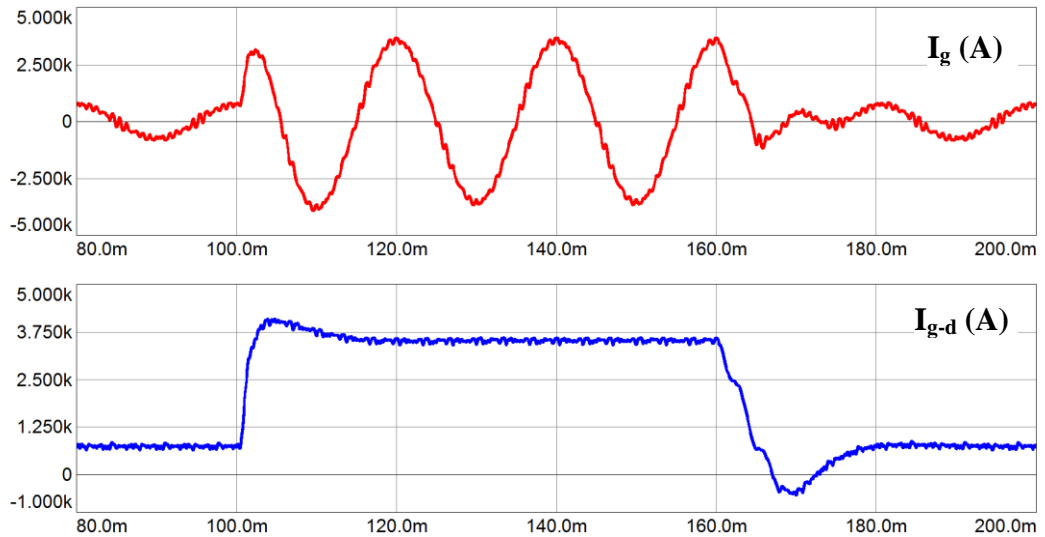


Figure 5.11 Dynamic load response of advanced passive damping Type 1

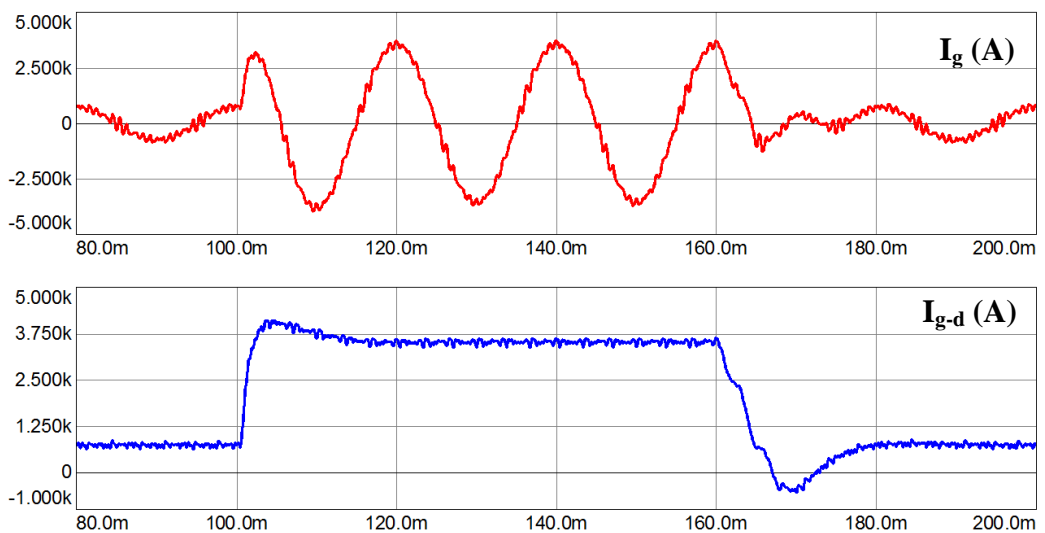


Figure 5.12 Dynamic load response of advanced passive damping Type 2

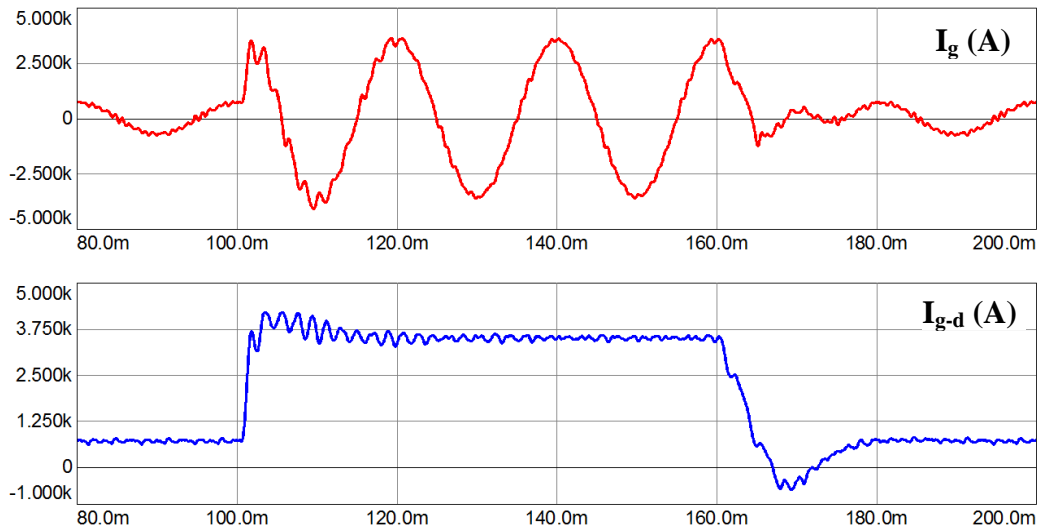


Figure 5.13 Dynamic load response of advanced passive damping Type 3

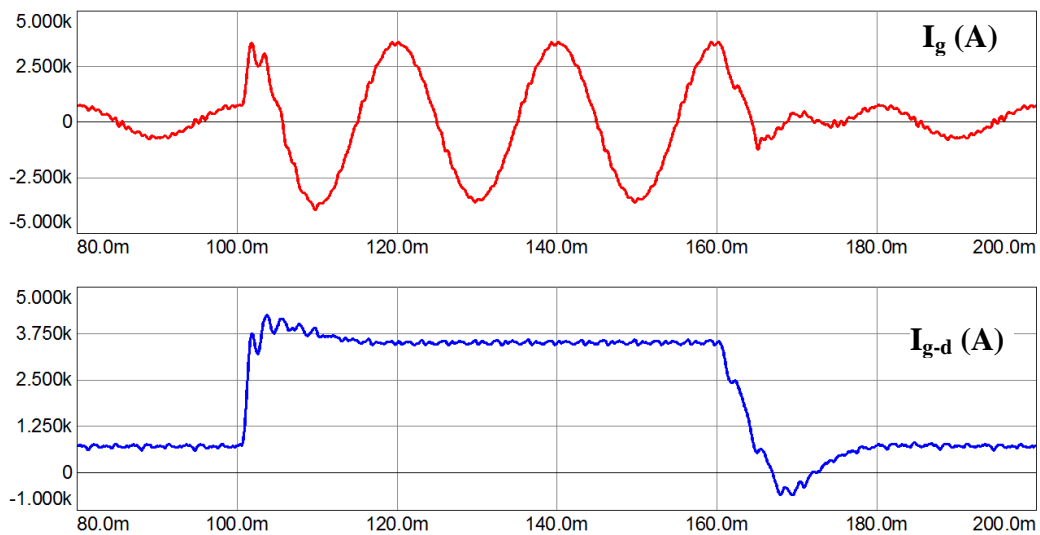


Figure 5.14 Dynamic load response of advanced passive damping Type 4

The verification of the advanced damping methods can be easily demonstrated by activating the filter in the presence of a resonance. On the following figure, Figure 5.15, advanced passive damping methods are activated at $t=100\text{ms}$ and deactivated at $t=160\text{ms}$ and the grid side currents are shown. Resonant harmonics are definitely

removed in less than half of the fundamental period time in most of the cases at the activation and they immediately start to pollute the grid at the deactivation.

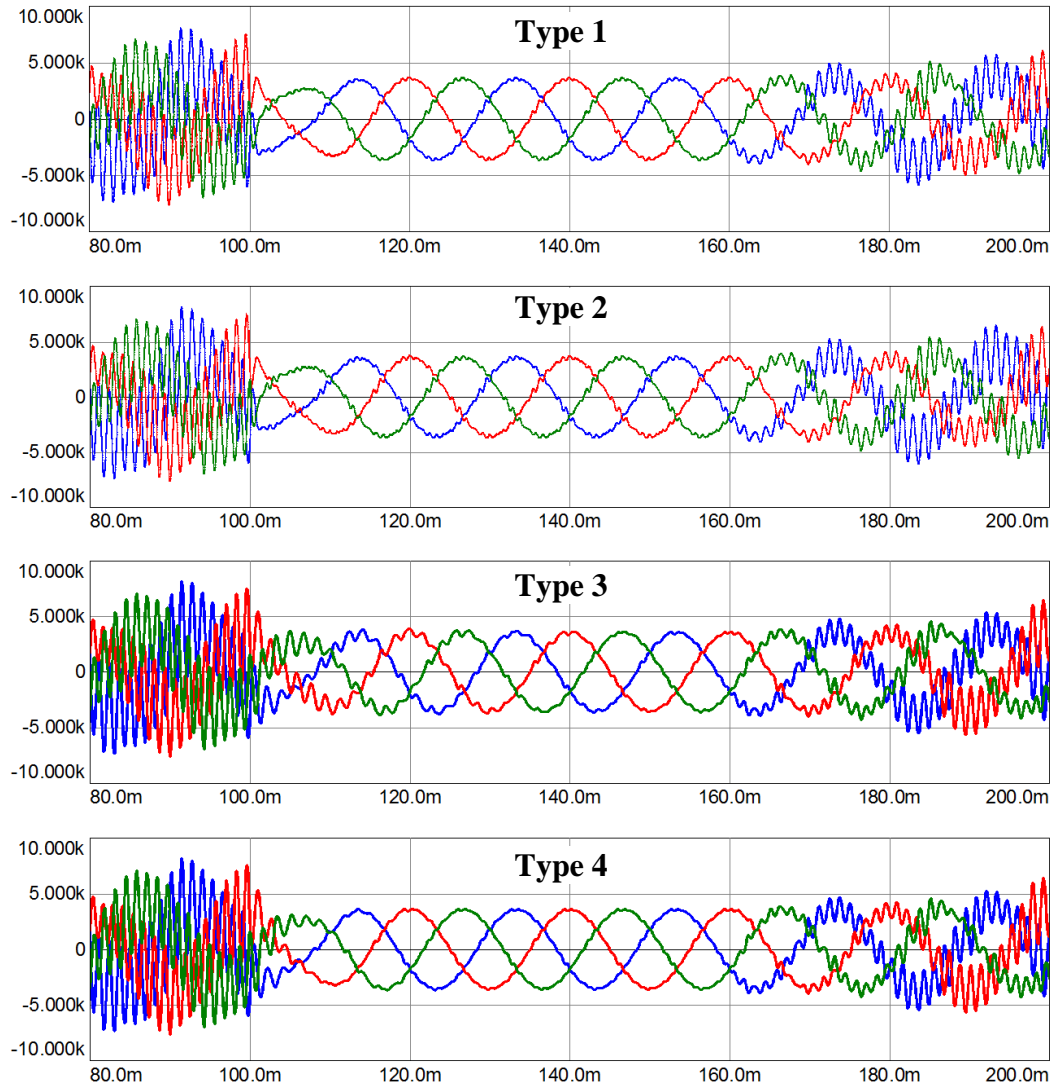


Figure 5.15 Activation and deactivation of the advanced passive damping methods in the presence of resonance

The grid side current THD value is an important element to see the effectiveness of the filter. Advanced passive damping methods aim to reduce the passive damping losses related with the damping resistor; however, THD performances should also be

compared and contrasted. In order to evaluate the steady-state performances, Figure 5.16 is demonstrated. At various load conditions, THD values are captured from the simulation software.

THD values of all advanced damping methods are superior to simple passive damping except Type 2. At the rated load (i.e. 1 *p.u.* load), all damping methods except Type 2 have THD values less than 5%.

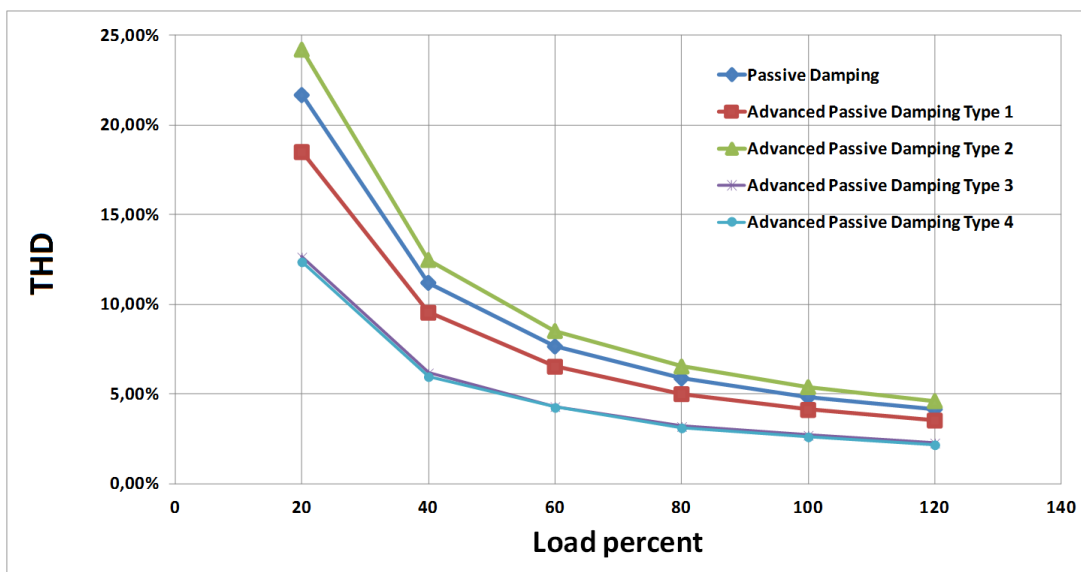


Figure 5.16 THD performances of passive damping methods

5.3. Power Loss and Efficiency Analyses of Passive Damping Methods

Advanced passive damping methods provide better efficiency for the overall system. Unlike simple passive damping, the insertion of reactive components into the filter allows new current paths for the harmonics at the switching frequency and the fundamental current component. In the following analysis, IGBT losses due to conduction and switching and the resistive filter losses are considered. The ESRs of the reactive components are neglected. Advanced and simple passive damping methods are simulated with a 3 MW 2L PWM-VSI. The power losses are calculated

for various load percentages and shown in Figure 5.17. The efficiency of each method is also shown in Figure 5.18. Type 3 and Type 4 are the most effective solutions while Type 1 and Type 2 are not worth to apply.

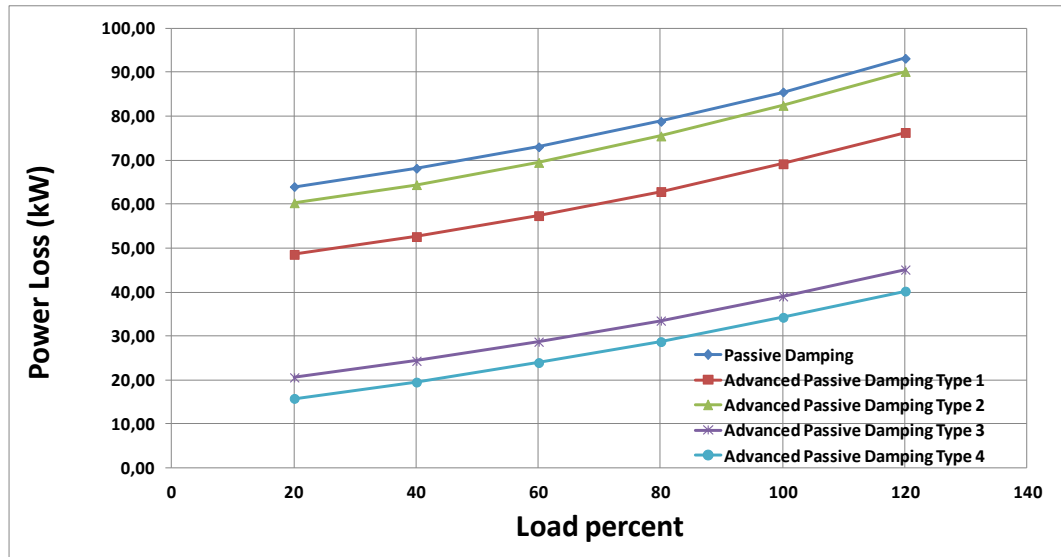


Figure 5.17 Power Losses of passive damping methods for various load percentages

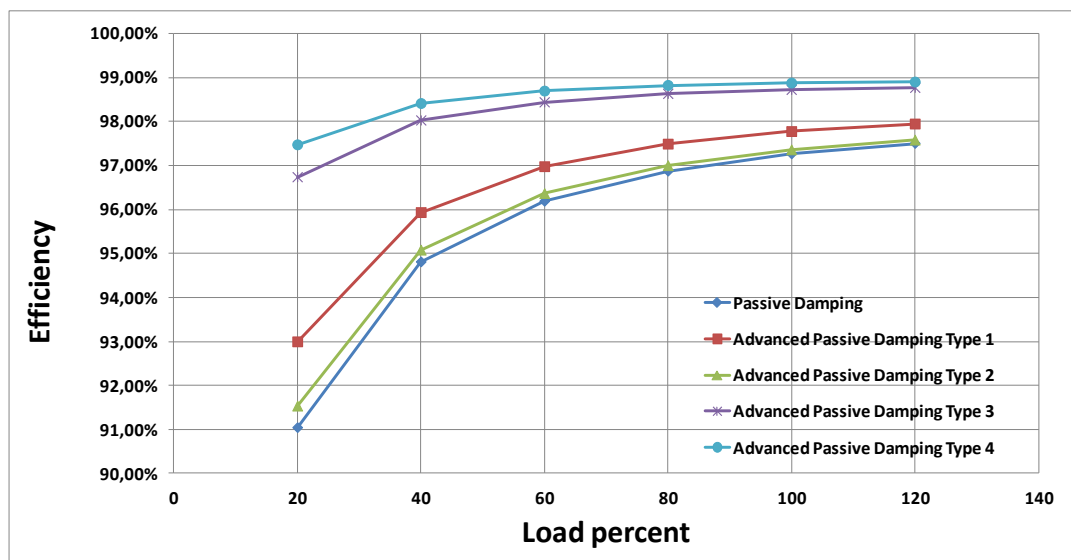


Figure 5.18 Efficiencies of passively damped systems for various load percentages

5.4. Simulation Results of SMCD Methods

The effectiveness of the analyses is supported by the simulation results via ANSOFT software. 3 MW VSIs with TC-SAF and DC-SAF compensation are investigated. The switches of the main inverter are selected as 1700V IGBTs with the current through a leg is shared by two devices. The steady-state waveforms of the proposed systems are demonstrated to verify the operation of SAF compensated systems. The load dynamic responses are considered for the selection of suitable controller parameters. The activation of SAF compensated systems when the system is undamped shows the necessary time for the system to stabilize. Efficiency and THD analyses show the advantages of the proposed methods over PD.

The simulation models for the proposed SMCD methods are shown in Figure 5.19 and Figure 5.20.

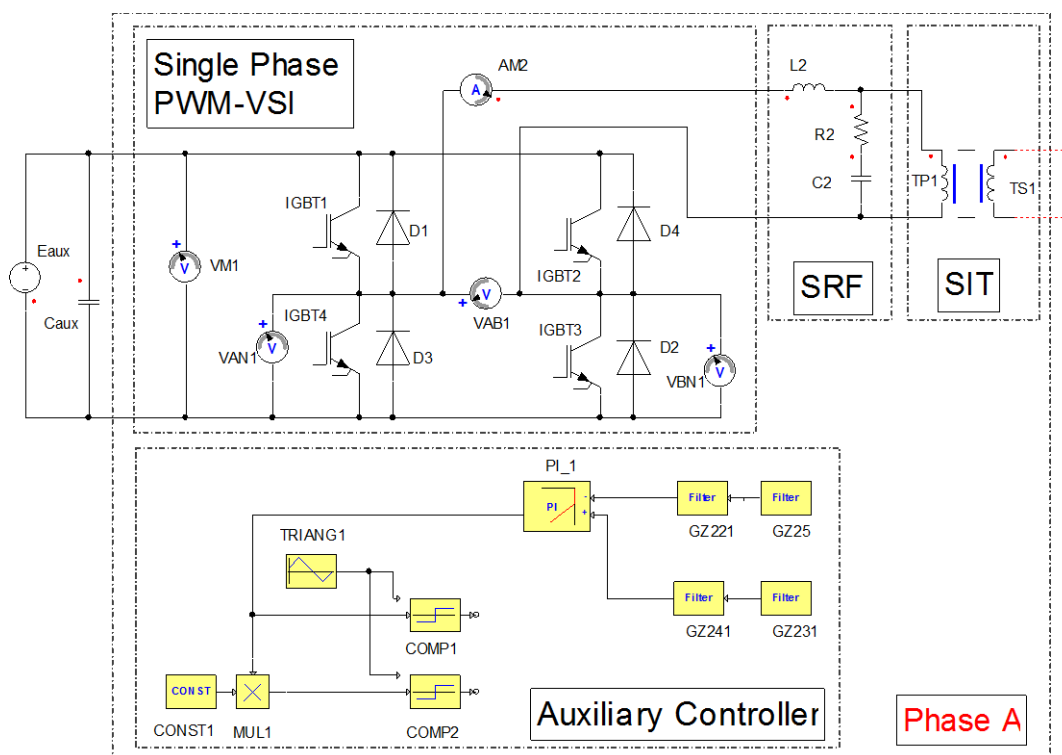


Figure 5.19 One phase of TC-SAF simulation model

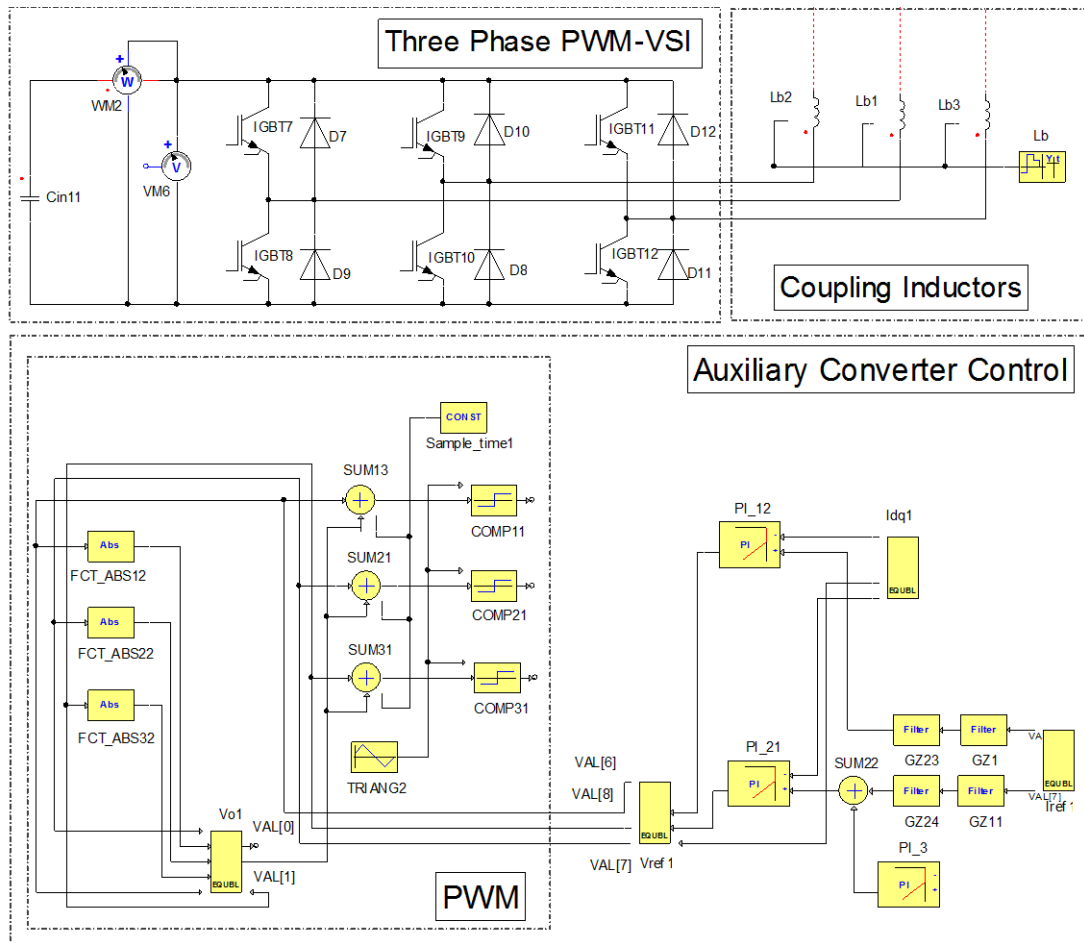


Figure 5.20 DC-SAF simulation model

The parameters of the simulated SAF compensated systems are given in Table 5.2. The main inverter has the same parameters with the passively damped case. The voltage and current ratings of the semiconductors utilized in the simulation are selected according to the table. The current through the filter capacitor is known from the simulation results of previous section. The current in the auxiliary circuit is reduced using the SIT with a turns ratio of 5 in TC-SAF while the current through the filter capacitor is directly processed in DC-SAF.

Table 5.2 Simulation parameters for TC-SAF and DC-SAF compensated 3 MW PWM-VSI

| | Symbol | Quantity | Value | |
|----------------------------|----------------|---------------------------|---------------|---------------|
| Main Inverter | P_{rated} | Rated power | 3 MW | |
| | f_{sw} | Switching frequency | 1.2 kHz | |
| | f_{samp} | Sampling frequency | 2.4 kHz | |
| | V_{dc} | DC-link voltage | 1070 V | |
| | V_g | Grid voltage | 690 V | |
| | f_g | Grid frequency | 50 Hz | |
| | L_g | Grid side inductance | 80 μ H | |
| | L_c | Converter side inductance | 80 μ H | |
| | C_f | Filter capacitance | 1000 μ F | |
| | | | TC-SAF | DC-SAF |
| Auxiliary Converter | $V_{aux,dc}$ | DC-bus voltage | 600 V | 200 V |
| | f_{sw-aux} | Switching frequency | 10 kHz | 10 kHz |
| | $f_{samp-aux}$ | Sampling frequency | 20 kHz | 20 kHz |
| | N | SIT turns ratio | 5 | - |
| | L_{aux} | SRF inductance | 5 μ H | 20 μ H |
| | C_{aux} | SRF capacitance | 1000 μ F | - |
| | R_{aux} | SRF resistance | 10 Ω | - |

5.4.1. Stability Analysis of SMCD Methods

In Figure 5.21, TC-SAF compensated system is enabled at $t=100$ ms when the system operate with no damping. Then, the TC-SAF starts to operate as damping resistors. After that, the TC-SAF is disabled at $t=160$ ms to demonstrate that the oscillations start again at the resonant frequency. The response of TC-SAF compensated system at the activation is very rapid due to an active algorithm applied on auxiliary VSIs. When the TC-SAF compensated system is disabled, the oscillations immediately start and the magnitude of the oscillations grow as time passes.

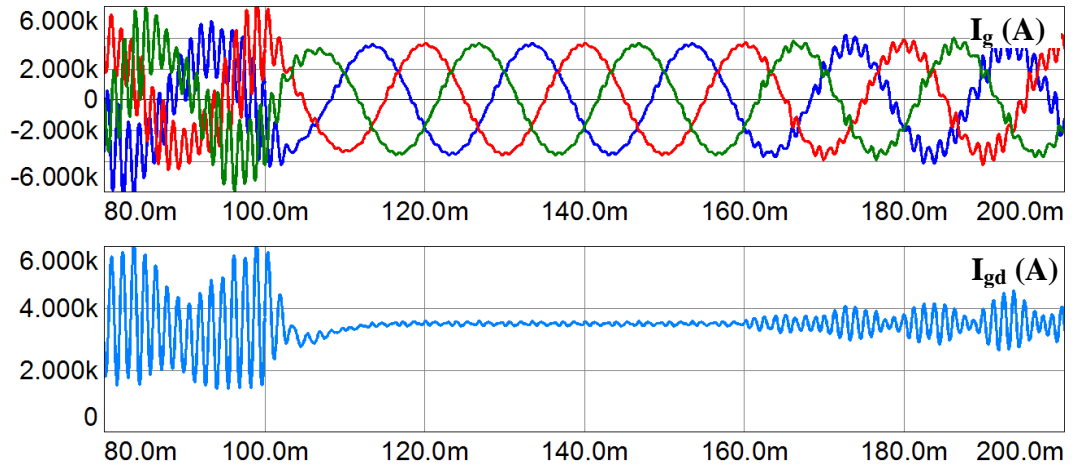


Figure 5.21 Activation of TC-SAF Based System from undamped condition

In Figure 5.22, DC-SAF compensated system is enabled at $t=100\text{ms}$ when the system operate with no damping. Then, the DC-SAF is disabled at $t=160\text{ms}$ showing that the oscillations start again at the resonant frequency. Owing to an active algorithm applied on auxiliary VSIs, the response of DC-SAF compensated system at the activation is very fast. The oscillations immediately start again when the DC-SAF compensated system is disabled.

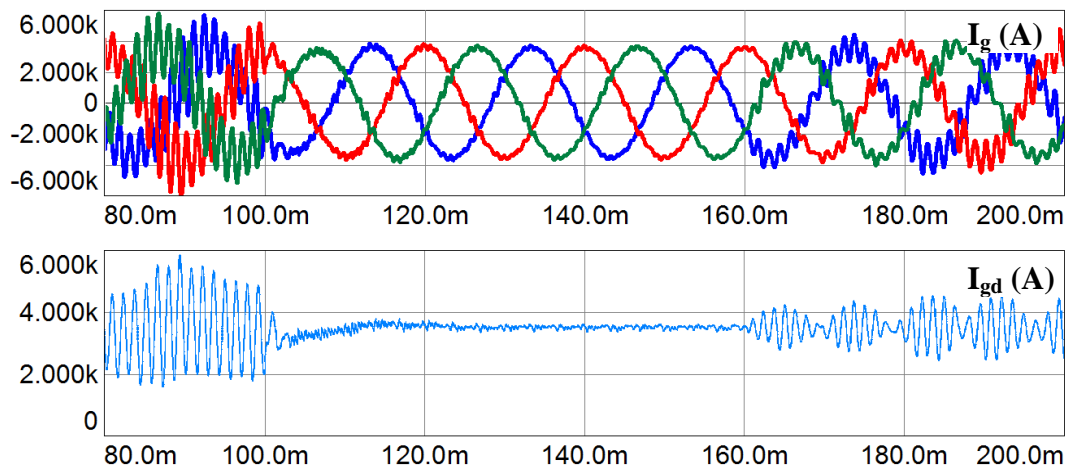


Figure 5.22 Activation of DC-SAF Based System from undamped condition

Figure 5.23 shows the simulated waveforms obtained from TC-SAF system. The steady-state waveforms of the converter side current, grid side current and filter capacitor current are shown during two fundamental period of time. Additionally, the voltage at the primary and secondary sides of the SIT, and the current at the secondary side of the SIT are shown in Figure 5.24.

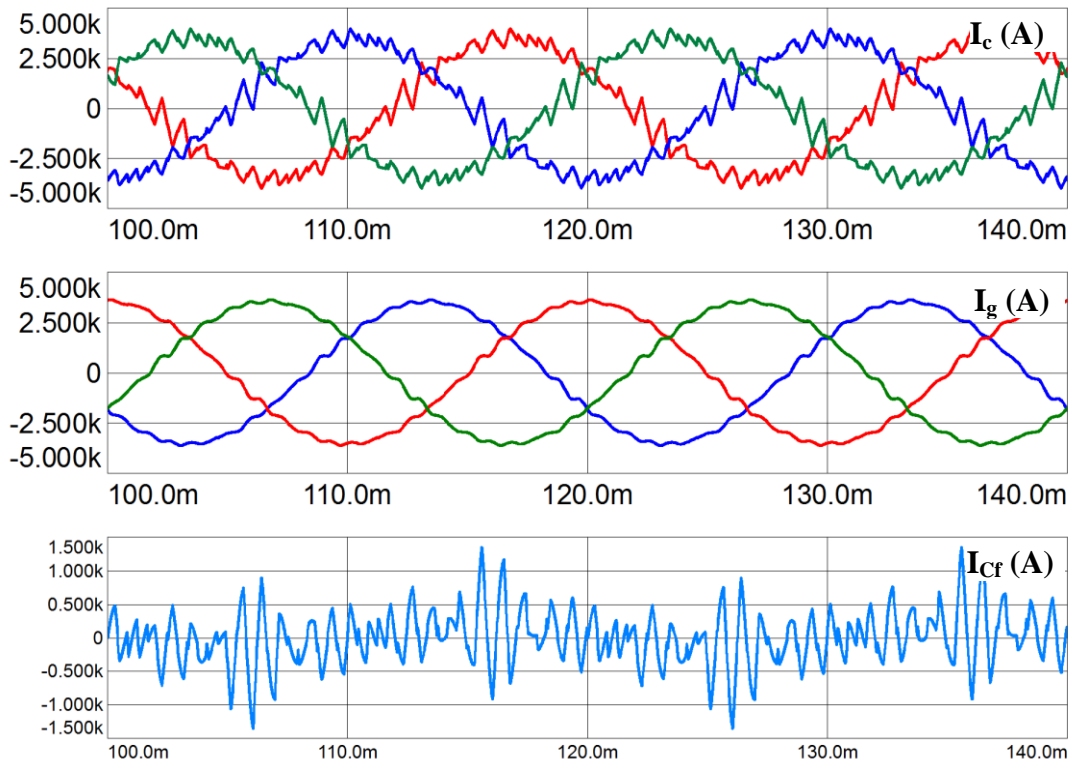


Figure 5.23 TC-SAF compensated system steady-state waveforms

The auxiliary converter output current and voltage before the SRF are shown in Figure 5.25. The SRF attenuates the high frequency switching ripples at 10 kHz and its multiples.

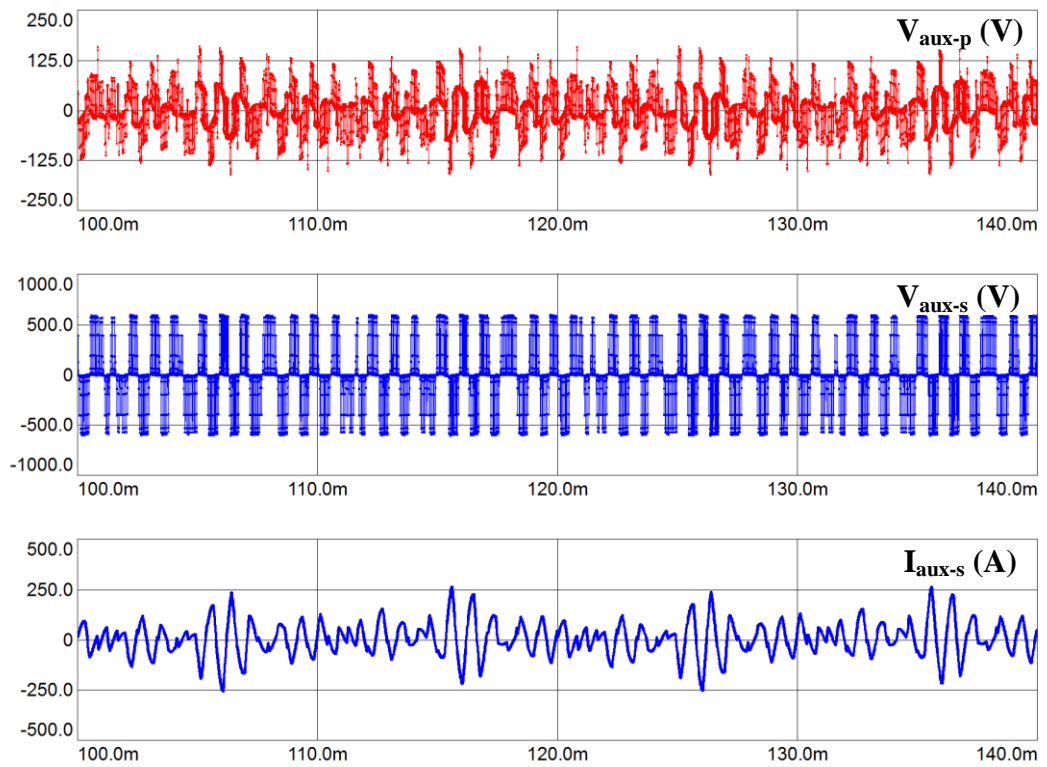


Figure 5.24 SIT waveforms at steady-state

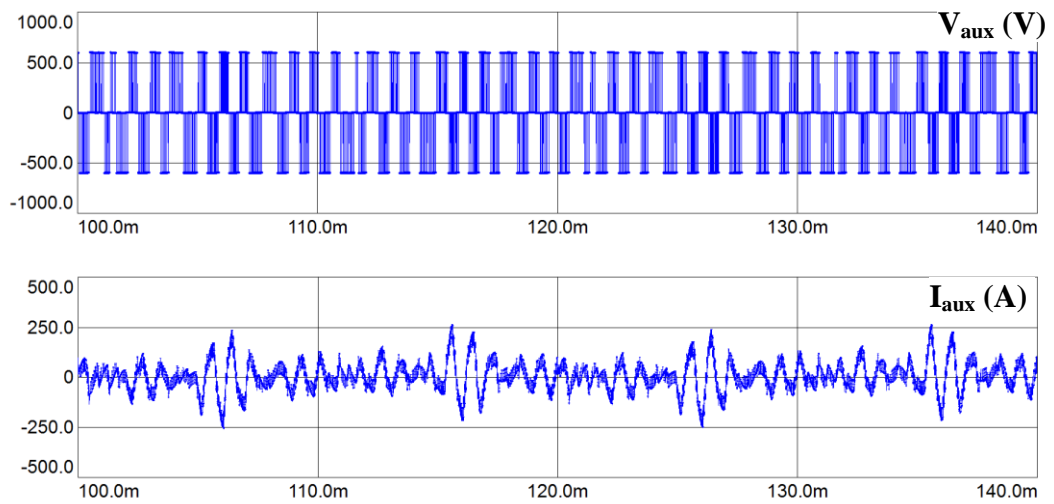


Figure 5.25 Auxiliary converter output waveforms at steady-state

Figure 5.26 shows the simulated waveforms obtained from DC-SAF system. The converter side, grid side, and filter capacitor current waveforms are shown during two fundamental period of time at the steady-state.

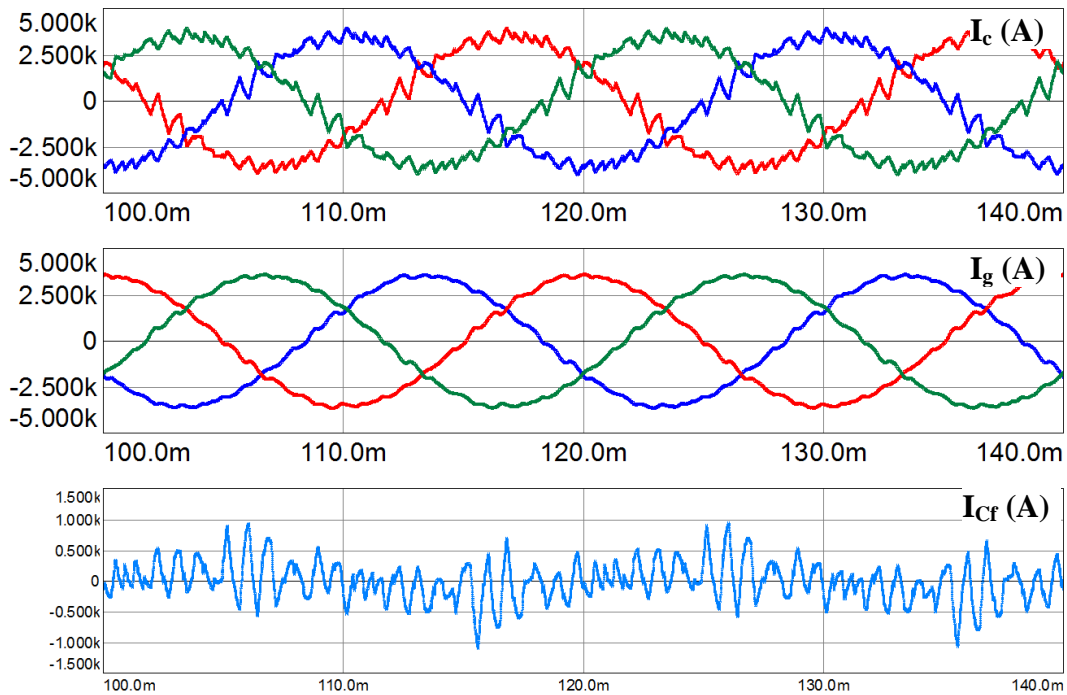


Figure 5.26 DC-SAF compensated system steady-state waveforms

The auxiliary converter output voltage before the auxiliary coupling inductor is shown in Figure 5.27. The auxiliary DC-bus voltage waveforms during the initial start-up and at the steady-state are both shown in Figure 5.28. As it can be seen, the voltage is stabilized around 200V thanks to the additional voltage control loop.

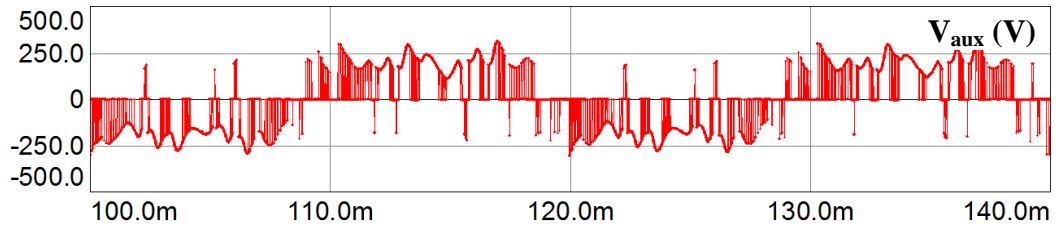


Figure 5.27 Auxiliary converter output voltage at steady-state

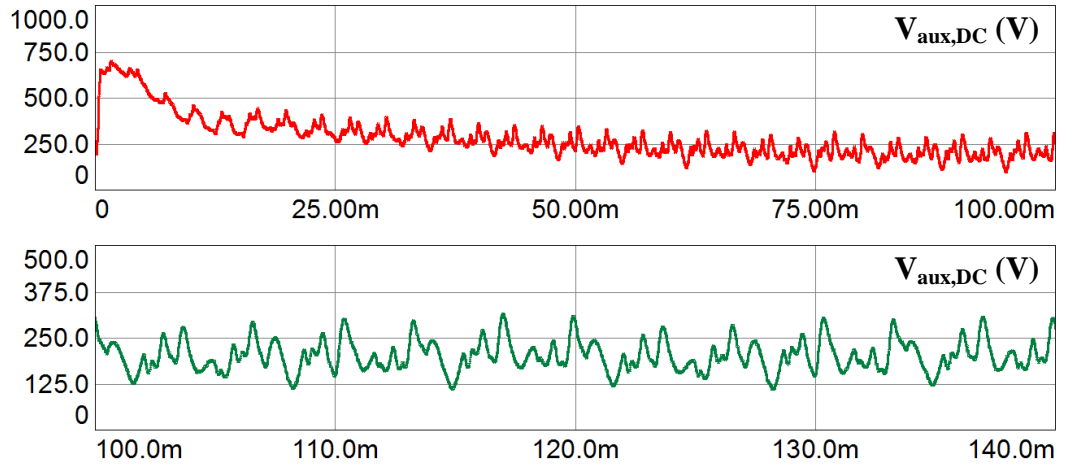


Figure 5.28 Auxiliary DC-bus voltage waveform

5.4.2. Dynamic Load Analysis of SMCD Methods

Figure 5.29 demonstrates the dynamic response of TC-SAF compensated system. The transitions from light load (20%) to full load (100%) and vice versa are both demonstrated in the same figure. The d -axis current, I_{gd} shown in Figure 5.29 explains the dynamic behavior of the system under investigation. Especially during the transition from full load to light load, recovery times are considerable due to large filter inductors.

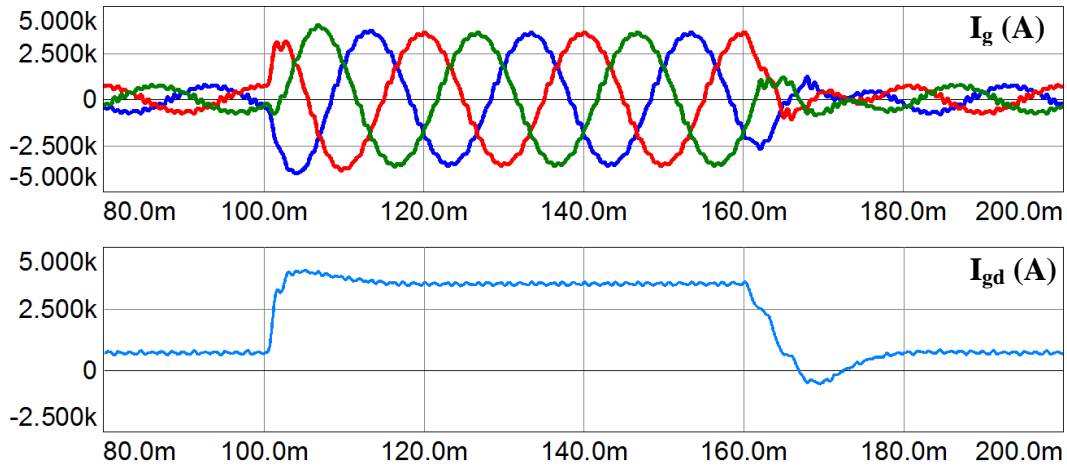


Figure 5.29 Load dynamic response of TC-SAF compensated system from 20% load to rated load then 20% load again

Dynamic response of DC-SAF compensated system is shown in Figure 5.30. Both the transition from light load (20%) to full load (100%) and vice versa are shown in the same figure. The d -axis current, I_{gd} also shown in Figure 5.30 explains the dynamic behavior of the system under investigation. Due to large LCL inductors, the transition from rated load to light load takes a longer time.

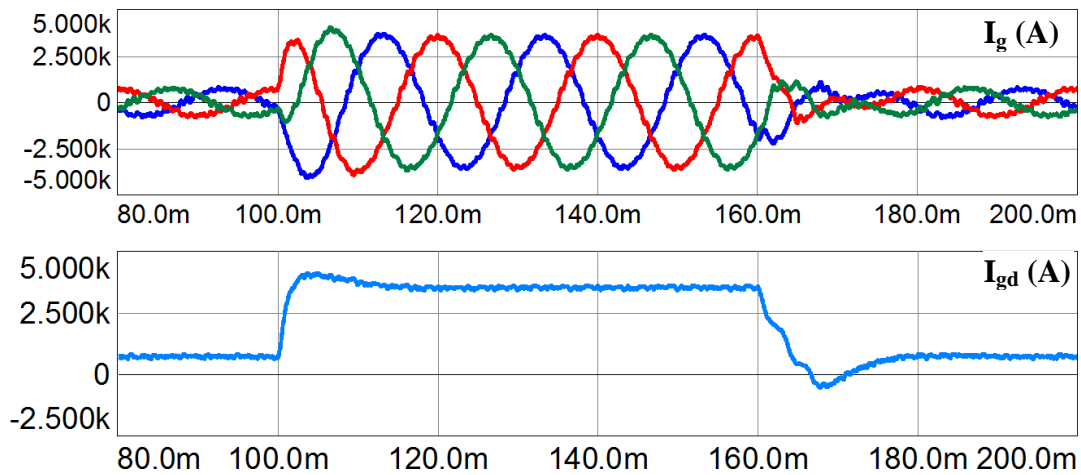


Figure 5.30 Load dynamic response of DC-SAF compensated system from 20% load to rated load then 20% load again

5.4.3. Grid Current THD Analysis of SMCD Methods

The FFT result of the grid side current is shown in Figure 5.31. In the frequency spectrum, 5th harmonic component and resonant frequency harmonics at the sidebands of 900 Hz mixed with the switching frequency harmonics at the sidebands of 1.2 kHz are evident. The multiples of the switching frequency are attenuated due to enhanced attenuation capability demonstrated in Figure 4.20.

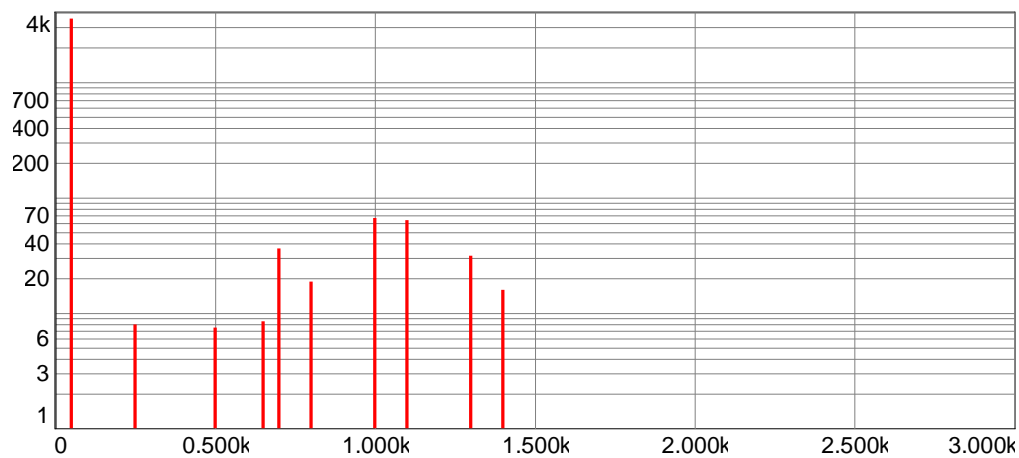


Figure 5.31 FFT analysis of TC-SAF grid current

The FFT of the grid side current is shown in Figure 5.32. Low frequency harmonic component such as 5th, 7th and 11th are very dominant. Resonant frequency harmonics at the sidebands of 900 Hz mixed with the switching frequency harmonics at the sidebands of 1.2 kHz are also seen in the frequency spectrum. The harmonics at twice the switching frequency reflects that DC-SAF is worse than TC-SAF regarding the filtering performance.

Figure 5.33 shows THD ratings of TC-SAF and DC-SAF compensated systems against load percent. A slightly better THD performance of TC-SAF compensated system over DC-SAF compensated system is seen as it is also discussed in Chapter

4. Moreover, TC-SAF and DC-SAF compensated systems stay below the THD limit of 4% at the rated load.

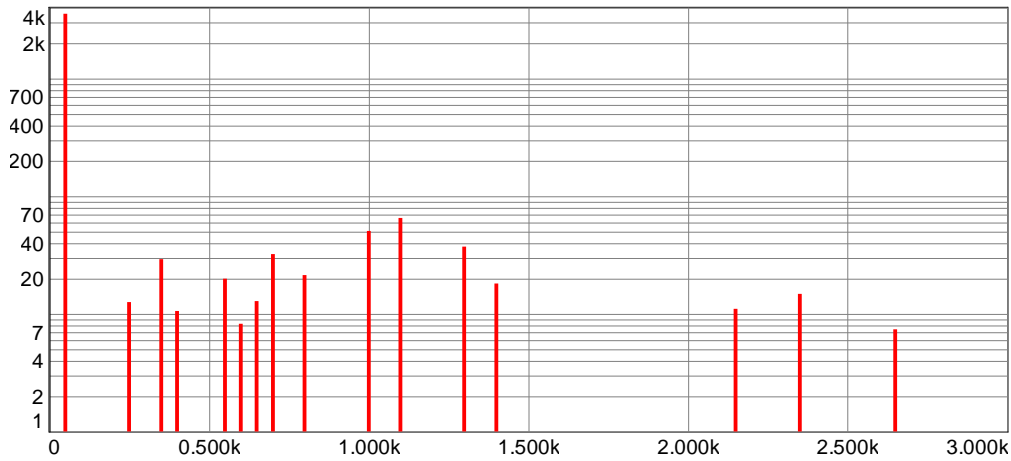


Figure 5.32 FFT analysis of DC-SAF grid current

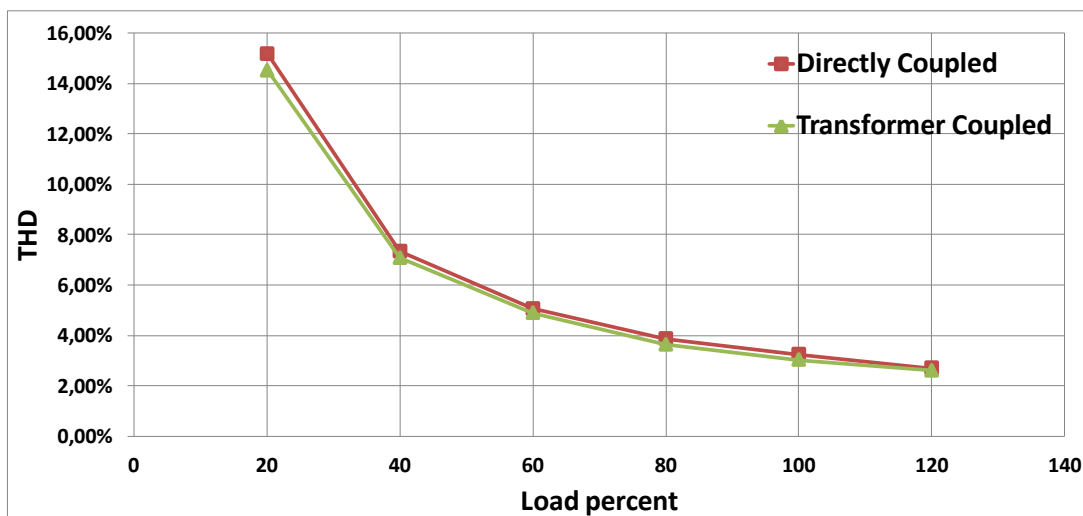


Figure 5.33 THD ratings of TC-SAF compensated and DC-SAF compensated systems under various load conditions

5.4.4. Efficiency Analysis of SMCD Methods

Efficiencies of TC-SAF and DC-SAF compensated systems at various load conditions are analyzed and the results are shown in Figure 5.34. SAF compensated systems have an efficiency rating higher than 99% at the rated load. The difference between efficiencies gets bigger as the load percent decreases. Due to less number of switches, elimination of SIT, and lower DC-bus voltage, the DC-SAF outclasses the TC-SAF in terms of the efficiency.

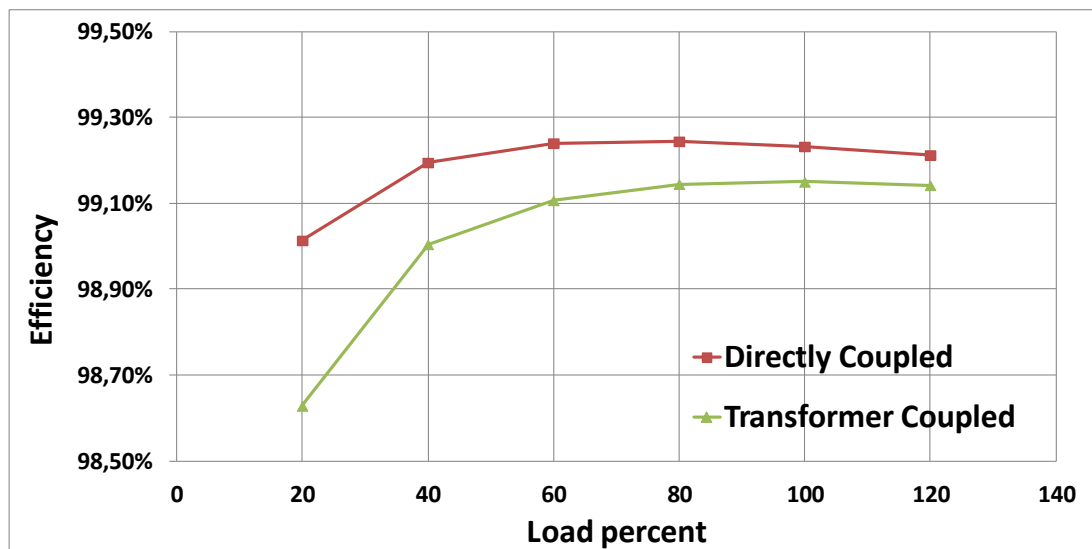


Figure 5.34 Efficiency ratings of TC-SAF and DC-SAF compensated systems under various load conditions

5.5. Verification of SMCD Methods for 3L PWM-VSI

Although SMCD methods are verified on a 2L 3 MW PWM-VSI, the proof of concept is also completed on a 3L 3 MW PWM-VSI. TC-SAF and DC-SAF based systems are investigated in this section. As the comparison of two novel damping methods shows, DC-SAF compensated system has better efficiency results and reduced number of components. Therefore, DC-SAF compensated system can be accepted as an improved solution to inherent resonance problem of the *LCL* filter.

Although the verifications in this section are mainly done using DC-SAF, TC-SAF is applied on a 3L PWM-VSI to demonstrate the feasibility of both methods.

The simulation model of 3L PWM-VSI is given in Figure 5.35. The output frequency of 3L PWM-VSI is effectively doubled compared to 2L. Due to higher switching frequency at the output, the ripple magnitudes are lower. Therefore, keeping the *LCL* filter parameters the same as 2L case yields lower grid current THD. In order to compensate this effect, the *LCL* filter is recalculated according to the selected switching frequency.

The switching frequency applied on 2L PWM-VSI was 1.2 kHz as stated in Table 5.2. 3L PWM-VSI has increased number of semiconductors in the current flow paths hence the conduction losses are increased. To obtain a better efficiency rating, the switching frequency has to be reduced. By keeping the *LCL* filter parameters constant and halving the switching frequency, grid side current THD results are obtained similar with 2L PWM-VSI. However, 600 Hz is very low to effectively apply carrier based PWM. The switching frequency; therefore, set as 800 Hz for 3L case and *LCL* filter parameters are adjusted. The parameters of the PI controllers are also adjusted due to decreased switching frequency. The grid side and the converter side inductors are set as 60 μH while filter capacitor is kept same as 1000 μF for the simulations of 3L PWM-VSI.

Apart from the *LCL* filter and controller parameters' change, the power module including IGBTs and diodes is changed. The grid model, current and voltage controllers are kept same. The voltage source is also kept same due to the fact that a fictitious ground is placed in both 2L and 3L models.

PWM generation is different in 3L due to increased number of semiconductor switches. The number of switching combinations for 3L PWM-VSI is 27 while 2L PWM-VSI has only 8 switching combinations. To compare the switching states of one leg in both 2L and 3L, Table 5.3 and Table 5.4 are given. P, N, and 0 states for positive, negative, and zero DC-link voltage respectively.

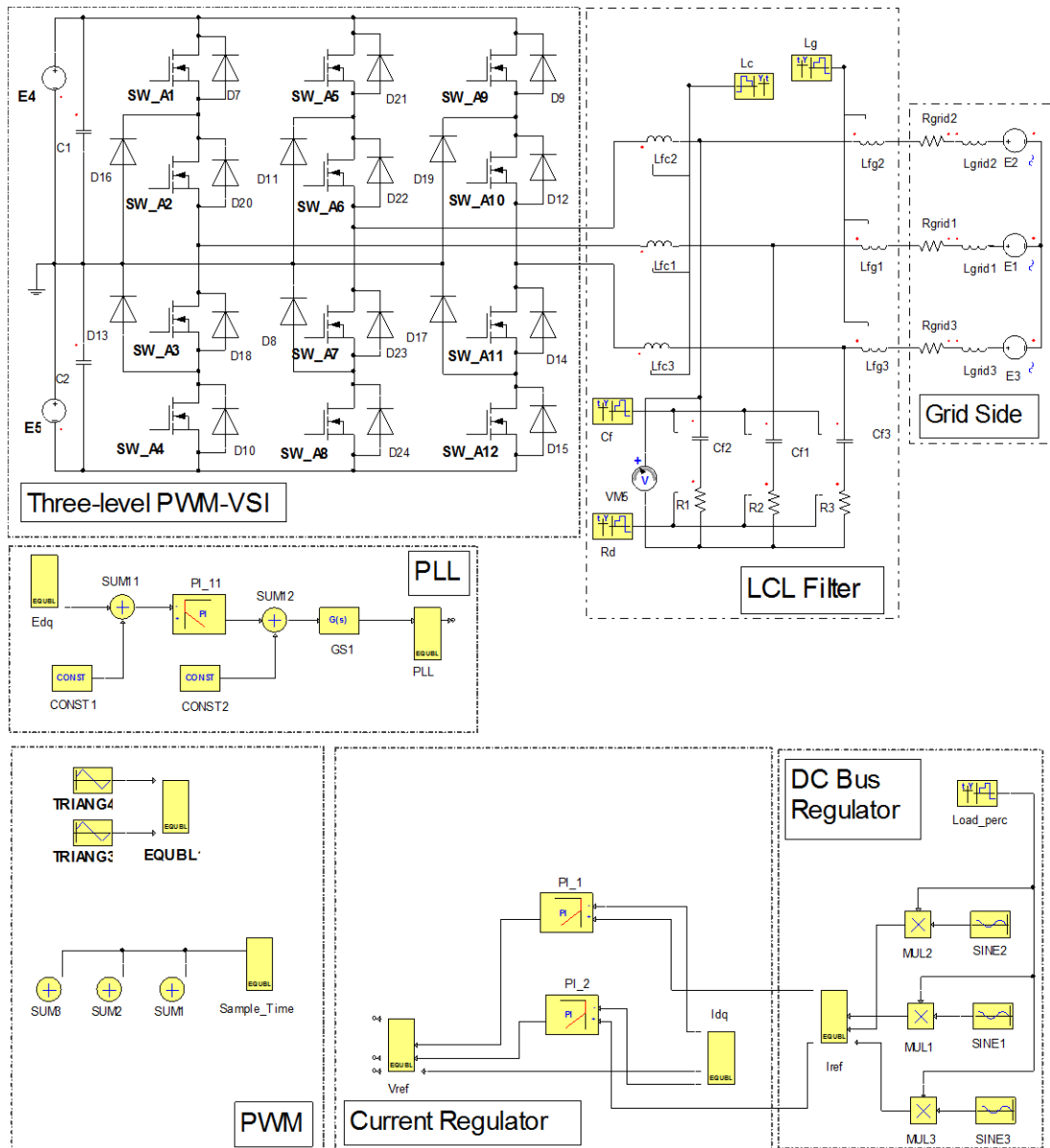


Figure 5.35 3L PWM-VSI simulation model in SIMPLORER

Table 5.3 Switching states for 2L PWM-VSI

| Switching State | Gate - (x) | | V(x) [Output voltage] |
|-----------------|------------|-----------|--------------------------|
| | Tr_{1x} | Tr_{2x} | |
| P | ON | OFF | $+V_{dc}/2$ |
| N | OFF | ON | $-V_{dc}/2$ |

Table 5.4 Switching states for 3L PWM-VSI

| Switching State | Gate - (x) | | | | V(x) [Output voltage] |
|-----------------|------------------|------------------|------------------|------------------|--------------------------|
| | Tr _{1x} | Tr _{2x} | Tr _{3x} | Tr _{4x} | |
| P | ON | ON | OFF | OFF | $+V_{dc}/2$ |
| 0 | OFF | ON | ON | OFF | 0 |
| N | OFF | OFF | ON | ON | $-V_{dc}/2$ |

5.5.1. 3L 3 MW TC-SAF Compensated System under GCF

Using the same parameter set given in Table 5.2 except the *LCL* filter parameters and switching frequency, 3L 3 MW system with TC-SAF is simulated. *LCL* filter inductors are reduced to 60 μH and the switching frequency is reduced down to 800 Hz. Therefore, the sampling frequency is reduced to 1600 Hz. The transition from undamped to TC-SAF compensated case is investigated.

Although the 3L system is stable without additional damping, TC-SAF is enabled at $t=100\text{ms}$ and disabled at $t=160\text{ms}$ to observe the effect of TC-SAF. Three-phase grid currents and the *d*-axis component are shown in Figure 5.36. Between 100ms and 160ms, the ripple magnitude on the grid side currents is reduced slightly. It can be deduced that the system is stable without additional damping and any damping method has a negligible effect on the system.

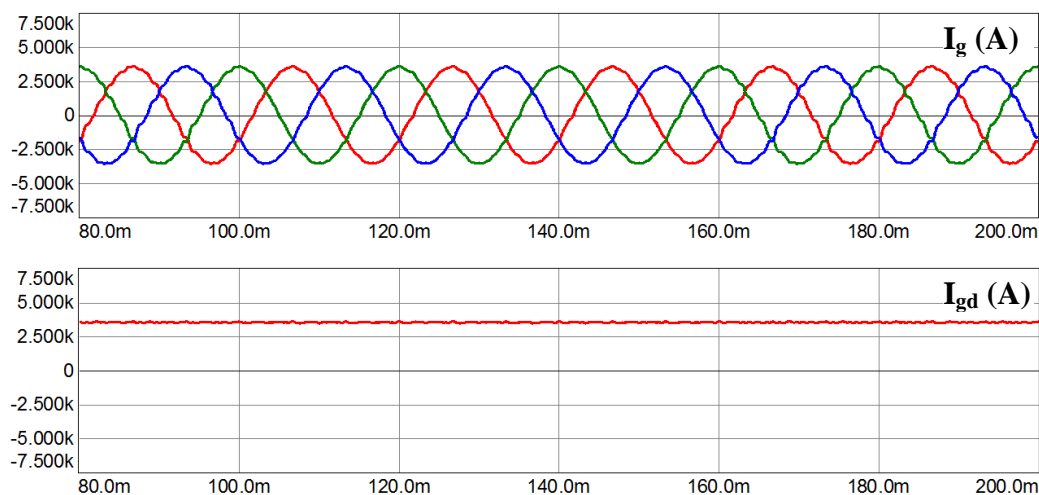


Figure 5.36 Activation of TC-SAF on 3L PWM-VSI under GCF

Figure 5.37 shows the converter side, grid side, and filter capacitor currents at steady-state and during the transition from undamped to TC-SAF compensated case. The filter capacitor current's peak-to-peak rating declines when TC-SAF is activated. The control of I_{cf} in the algorithm of TC-SAF provides the reduction of the magnitude. The filter capacitor current flowing through TC-SAF is also shown in Figure 5.37 reflecting that the system is active.

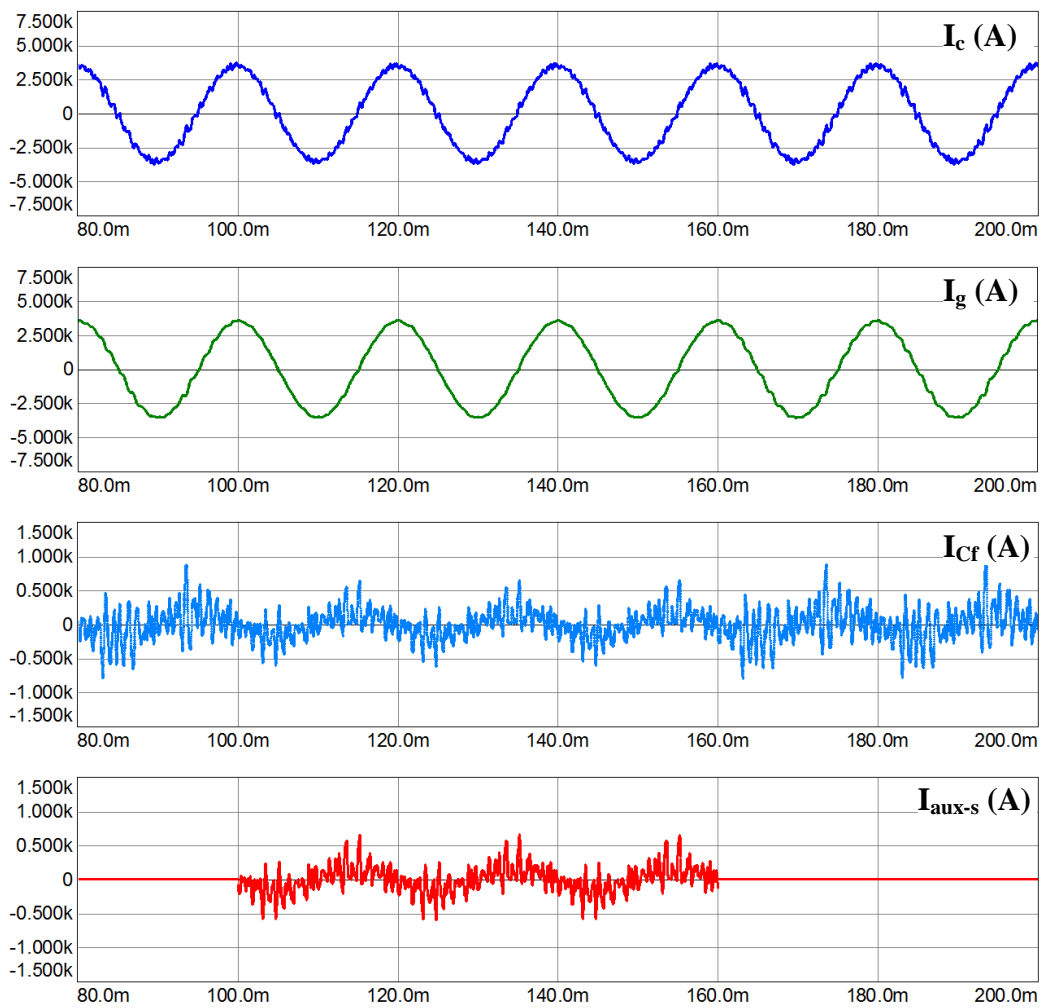


Figure 5.37 Steady-state waveforms of TC-SAF compensated 3L PWM-VSI under GCF

5.5.2. 3L 3 MW TC-SAF Compensated System under CCF

With the same set of parameters used in the previous case, TC-SAF compensated system is activated at $t=100\text{ms}$ and deactivated at $t=160\text{ms}$. This time the main feedback variable is measured from the converter side. Unlike GCF, the resonant harmonics occur in the system as the simulation time starts. In order not to lose the stability of the system for the undamped case, non-zero damping resistors are placed in the model. Although the presence of a non-zero path for the current harmonics, the resonance level seen in Figure 5.38 is very high. The resonant harmonics are suppressed as soon as TC-SAF is activated. The grid side currents return to their original values as well as the d -axis component.

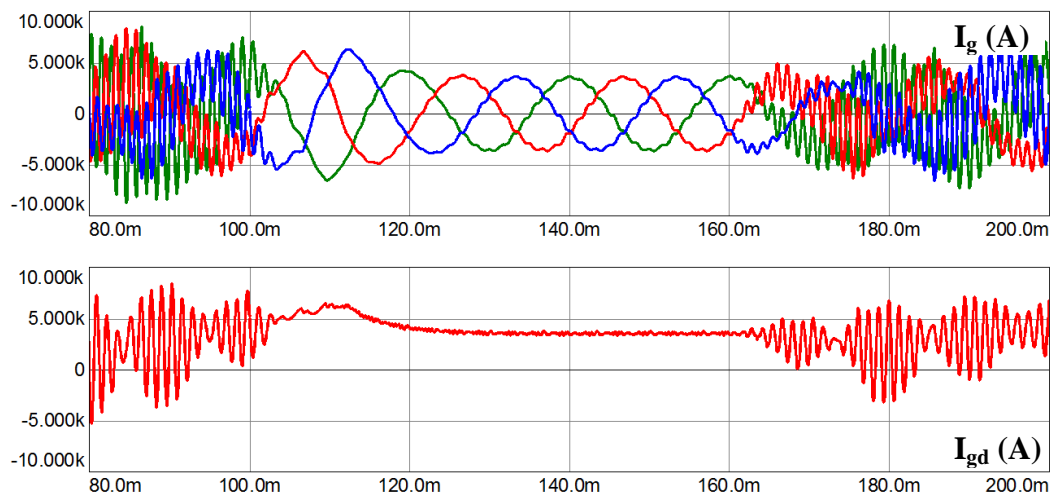


Figure 5.38 Activation of TC-SAF on 3L PWM-VSI under CCF

Steady-state waveforms when TC-SAF is activated are shown in Figure 5.39. The converter side current contains switching ripples while the grid side current does not. The filter capacitor current contains the switching ripples due to low-pass characteristics of the filter. The resonant harmonics in the grid side current can reach up to twice of the rated current value. The current flowing through TC-SAF, I_{aux-s} shows the verification of the proposed system on 3L PWM-VSI. After the activation

of TC-SAF, resonant harmonics are removed during half of the fundamental cycle. The resonant harmonics starts to oscillate again when TC-SAF is deactivated. The peak value of the filter capacitor current attains more than ten times of the rated value due to resonance. The stability of the system cannot be achieved using only the current controllers of the PWM-VSI. Additional damping measures such as TC-SAF are sought.

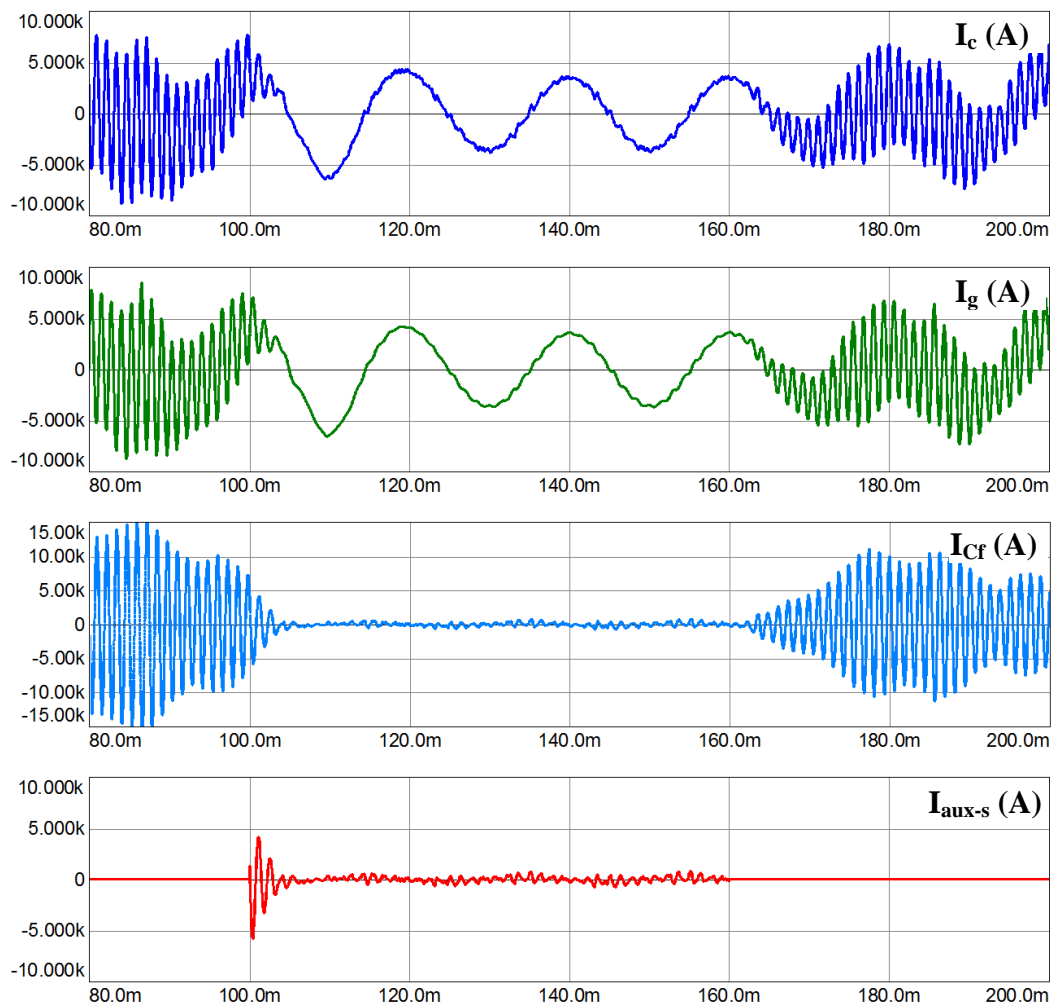


Figure 5.39 Steady-state waveforms of TC-SAF compensated 3L PWM-VSI under CCF

5.5.3. 3L 3 MW DC-SAF Compensated System under GCF

In this case, DC-SAF compensated 3L 3 MW system is investigated. For the undamped case, GCF is sufficient to provide damping like in the case of TC-SAF compensated system. Tuning of the PI controllers based on symmetrical optimum is not valid. A manual tuning approach is adopted.

DC-SAF is enabled at $t=100\text{ms}$ and disabled at $t=160\text{ms}$ to observe the effect of DC-SAF on the system. Three-phase grid currents and the d -axis component are shown in Figure 5.40Figure 5.36.

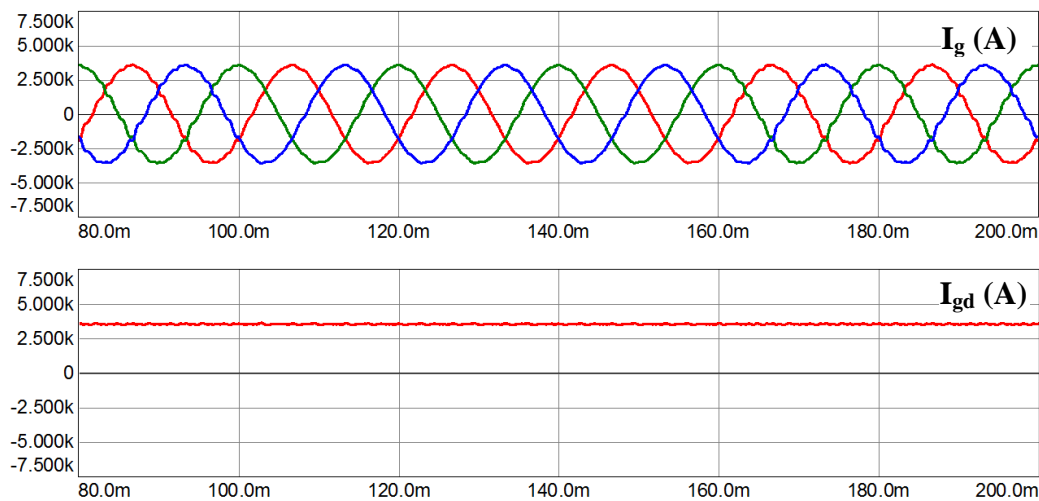


Figure 5.40 Activation of DC-SAF on 3L PWM-VSI under GCF

Converter side, grid side, and filter capacitor currents at steady-state and during the transition from undamped to DC-SAF compensated case are shown in Figure 5.41. The filter capacitor current's peak rating decreases from 1000 V to 500 V when DC-SAF is activated. The filter capacitor current flowing through auxiliary PWM-VSI of DC-SAF is shown in the same figure.

The ripple magnitude in grid side currents tends to decrease as DC-SAF is activated. Since the algorithm applies a band-pass filter around the resonant frequency, the

harmonics around this frequency are also processed by the DC-SAF and attenuated through the filter.

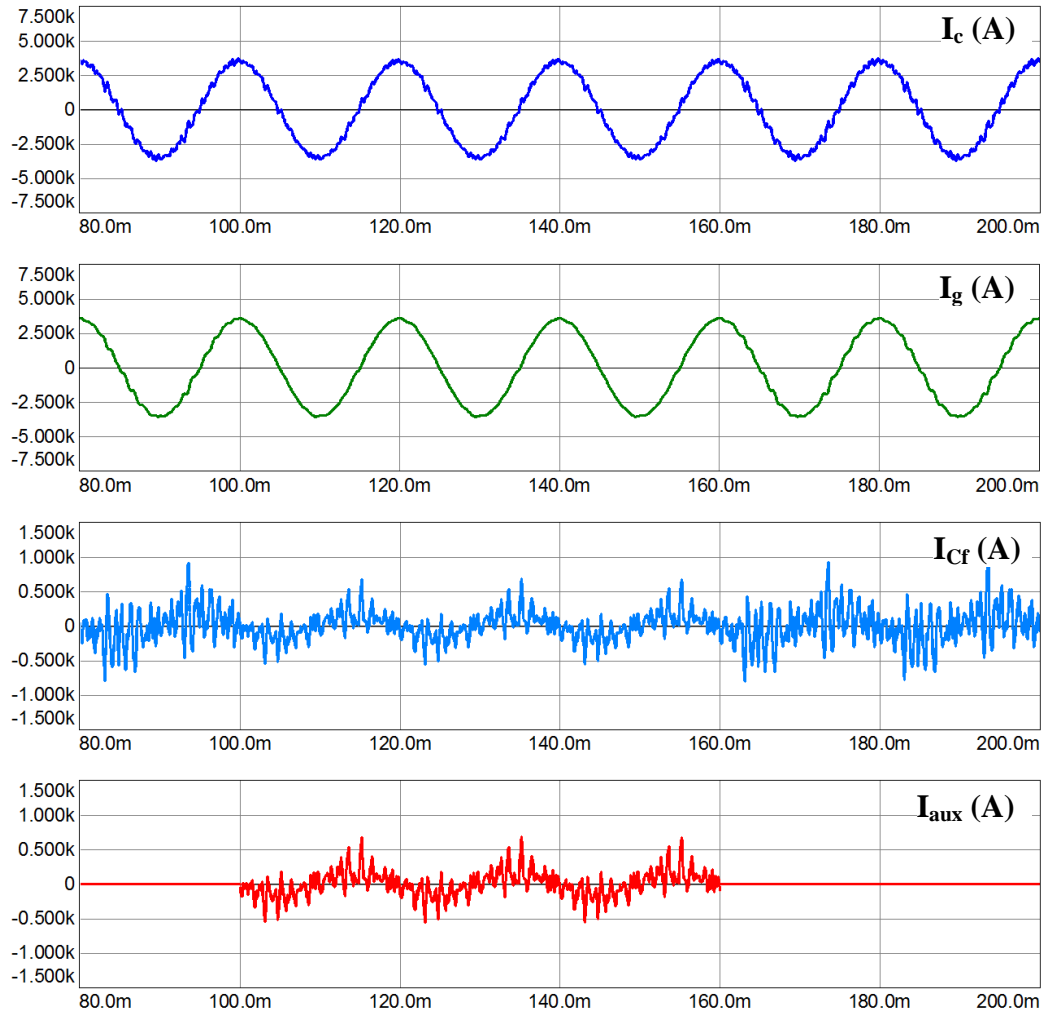


Figure 5.41 Steady-state waveforms of DC-SAF compensated 3L PWM-VSI under GCF

The controller bandwidth is intentionally reduced to half of the 2L PWM-VSI by decreasing the switching frequency. When f_{sw} is set as 600Hz, the system becomes hard to stabilize. Using GCF and adjusting PI parameters again for the new switching frequency, the verification of DC-SAF is accomplished for a very low switching frequency. Resonant harmonics occur this time unlike the previous case.

The grid currents and d -axis component are shown in Figure 5.42. DC-SAF output currents are higher than the previous case. The resonant harmonics are controlled between $t=100\text{ms}$ and $t=160\text{ms}$ by DC-SAF and eliminated immediately. The stability of the system is preserved during the activation of DC-SAF even in a low controller bandwidth.

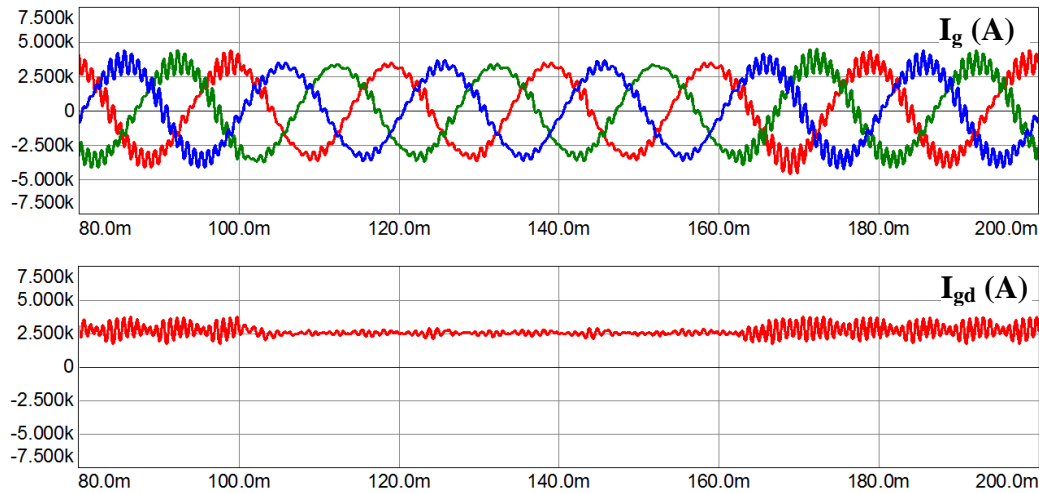


Figure 5.42 Activation of DC-SAF on 3L PWM-VSI under GCF for $f_{sw}=600$ Hz

5.5.4. 3L 3 MW DC-SAF Compensated System under CCF

CCF is not sufficient for resonance damping of the LCL filter. Additional damping must be used. DC-SAF is used to control the resonant harmonics in order to provide stability. The unstable characteristic of the system is controlled by adding non-zero resistors in series with the filter capacitors for the undamped case.

The grid currents and d -axis component are shown in Figure 5.43 below. DC-SAF is activated at $t=100\text{ms}$ and deactivated at $t=160\text{ms}$. DC-SAF has an immediate effect on the system. The resonance is damped within a fundamental cycle completely.

Figure 5.44 shows the converter side, grid side, filter capacitor, and DC-SAF output currents under GCF on 3L PWM-VSI. Before the activation of DC-SAF, the grid

side currents increase up to 10 kA which is not desired due to the fact that high current stresses can damage the power semiconductors. The filter capacitor current is also at a dangerous level such that the filter capacitors cannot withstand high repetitive currents flowing through them. As soon as DC-SAF is enabled, resonant is eliminated and the stability of the system is preserved.

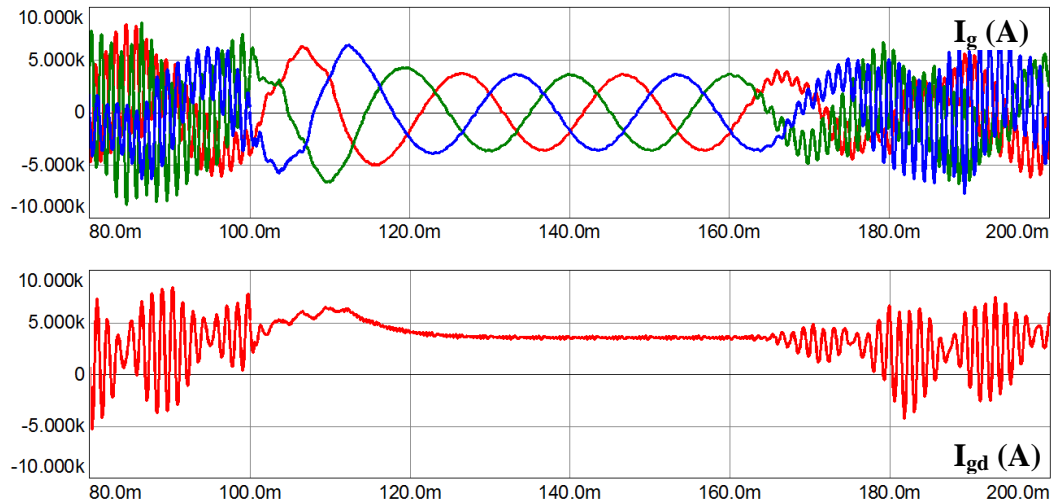


Figure 5.43 Activation of DC-SAF on 3L PWM-VSI under CCF

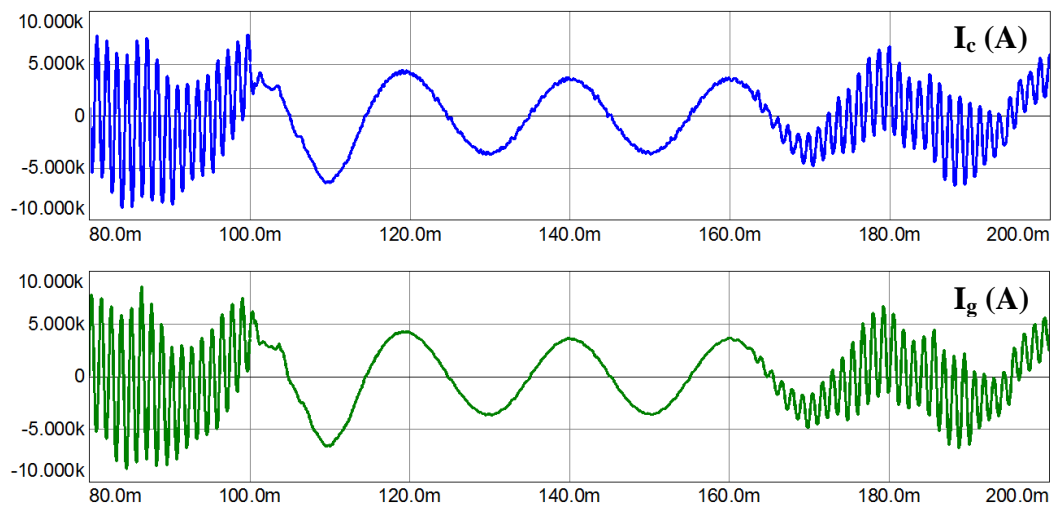


Figure 5.44 Steady-state waveforms of DC-SAF compensated 3L PWM-VSI under CCF

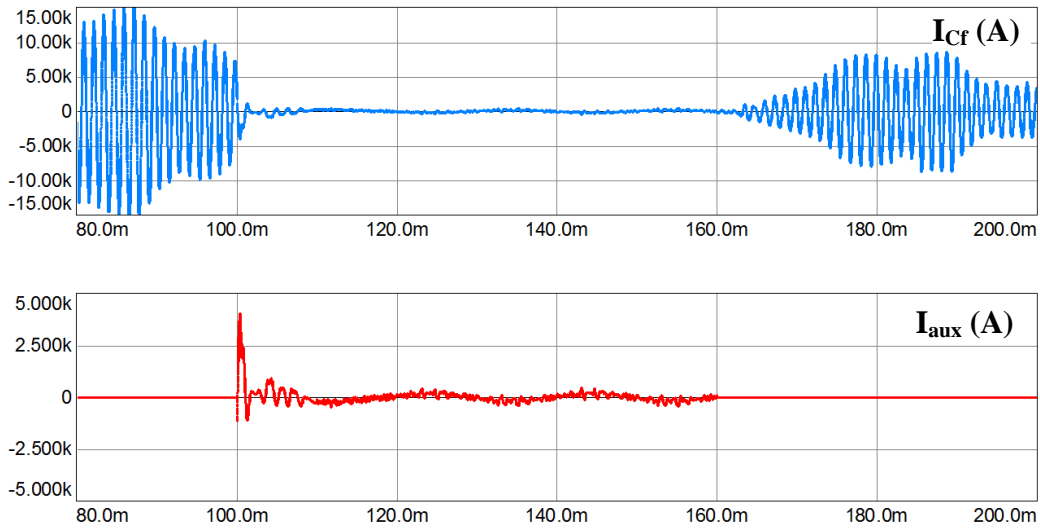


Figure 5.44 (continued) Steady-state waveforms of DC-SAF compensated 3L PWM-VSI under CCF

5.5.5. 3L 3 MW DC-SAF Compensated System under Grid Harmonic Distortion

In order to simulate the grid distortion, harmonic components given in Figure 5.45 are added to the grid voltage. These harmonics are obtained when a diode rectifier (V-type load) is connected to the same grid.

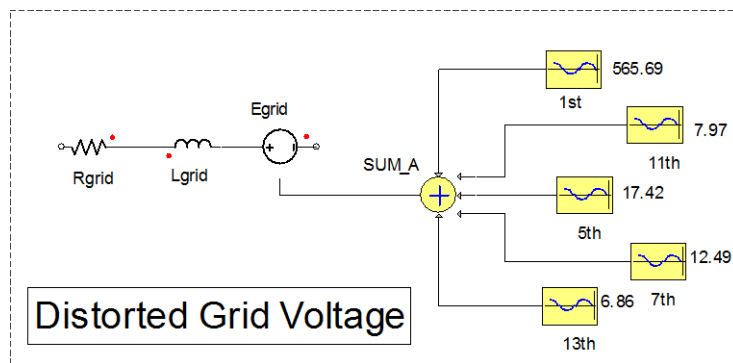


Figure 5.45 Simulation model of harmonic injection to grid voltage

5th, 7th, 11th and 13th voltage harmonic components as percentage to the fundamental voltage component (3.08%, 2.21%, 1.41% and 1.21%, respectively) are used.

The grid currents and d -axis component are shown in Figure 5.46 during the transition from undamped case to DC-SAF compensated case and at steady-state. The distorted voltage waveform at the grid side is also demonstrated below. The d -axis component is not constant even at steady-state due to distorted grid conditions. The reference voltage generated by the controller is directly affected by the low frequency harmonics injected to the grid. The stability of the system is not affected due to distorted grid; it only depends on the extent of damping. For the undamped (or insufficiently damped) case before $t=100\text{ms}$ and after $t=160\text{ms}$, stability is not accomplished whereas the activation of DC-SAF provides the necessary damping.

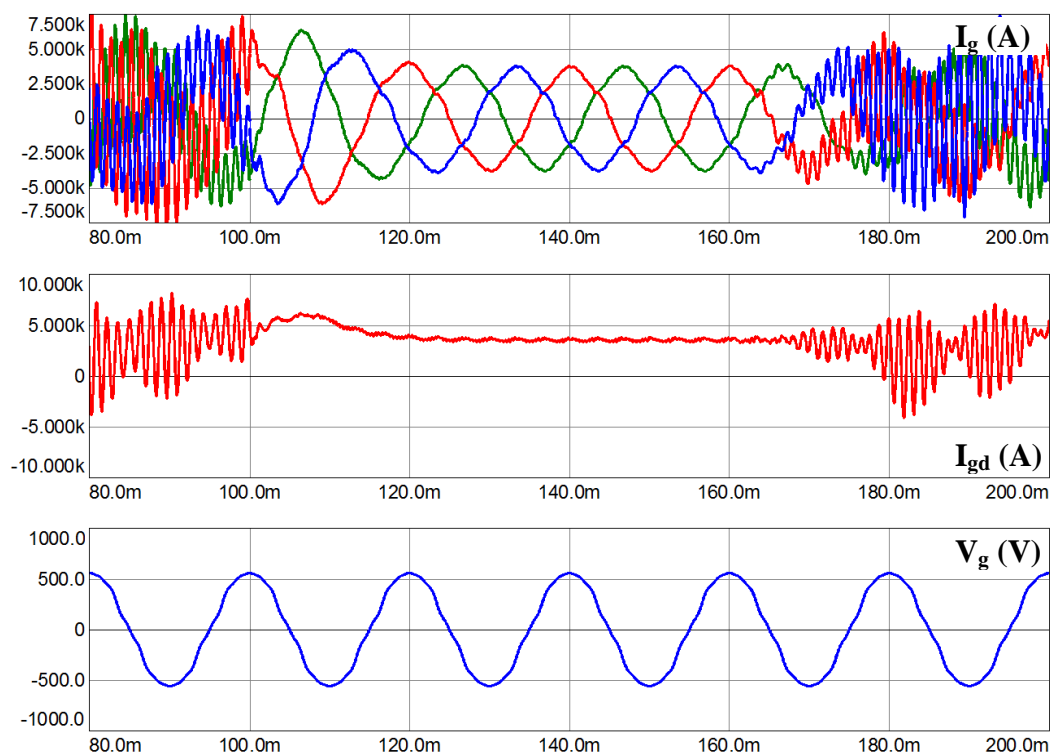


Figure 5.46 Activation of DC-SAF on 3L PWM-VSI under distorted grid condition

A closer look on the grid voltage (5x) and the grid current (1x) is given in Figure 5.47. Although the current is distorted, the power factor is kept at unity. The harmonic distortion level at the grid current is found as 6.42% which is above the previously defined limits.

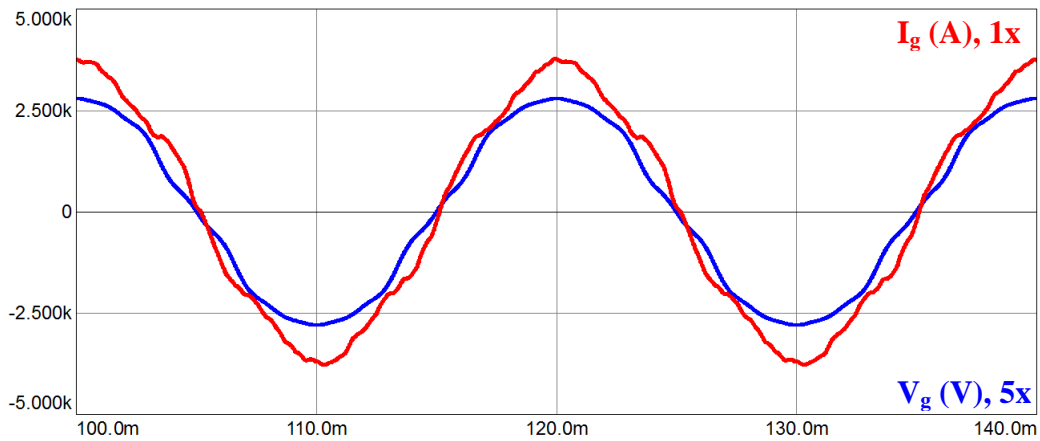


Figure 5.47 Grid current and voltage of 3L 3 MW DC-SAF compensated system with CCF under distorted grid condition

The normalized value of the phase angle at the output of PLL block is shown in Figure 5.48 below.

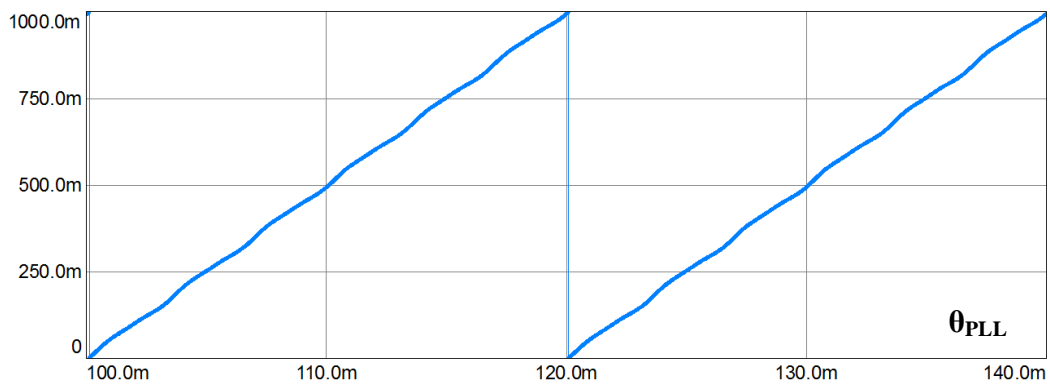


Figure 5.48 PLL angle waveform under distorted grid condition

5.5.6. 3L 3 MW DC-SAF Compensated System under Grid Unbalance

In the grid unbalance case, the voltage drop applied on Phase A is 35% of the rated phase voltage. The current and voltage waveforms are provided to reveal the behavior of the simulated 3 MW 3L system with DC-SAF compensation.

Between $t=60\text{ms}$ and $t=200\text{ms}$, DC-SAF is activated and in this interval between $t=100\text{ms}$ and $t=160\text{ms}$ Phase A is faulted intentionally. The simulated grid voltages, grid currents and d -axis component are shown below in Figure 5.49.

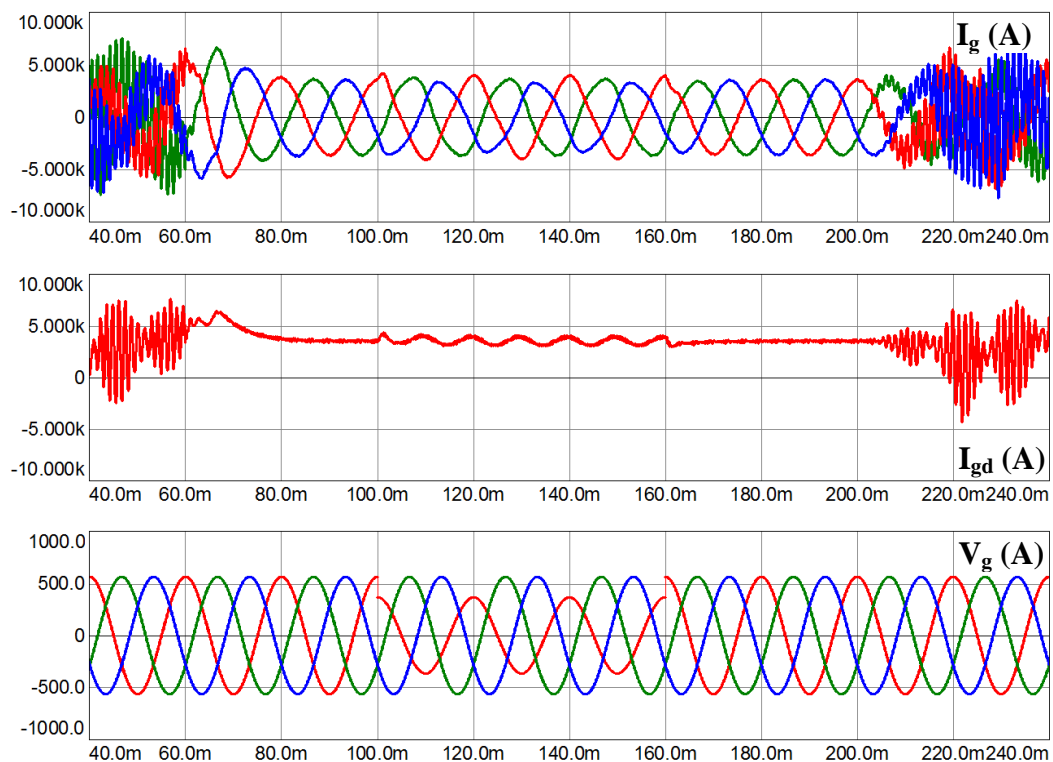


Figure 5.49 Activation of DC-SAF on 3L PWM-VSI under voltage unbalance condition

It is seen that the voltage drop on Phase A leads to increase of line current in the same phase and distortion in all three phases. The d -axis component oscillates at 100Hz as it can be seen clearly in Figure 5.49. The increased grid currents cause the

saturation of the PWM-VSI hence low order harmonics which disturb the quality of grid power.

The performance of DC-SAF compensated 3L system under voltage unbalance is also shown using grid voltage and current of Phase A on top of each other as in Figure 5.50. THD level is found as 6.45% at rated load condition. The power factor is also close to unity. The proposed DC-SAF works properly under unbalanced grid condition. Resonant harmonics are suppressed properly and the stability of the system is maintained.

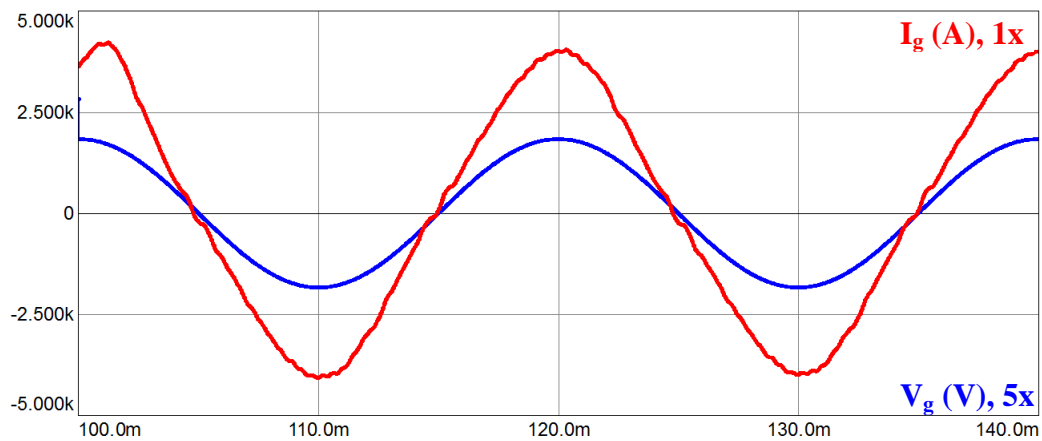


Figure 5.50 Grid current and voltage of 3L 3 MW DC-SAF compensated system with CCF under distorted grid condition under voltage unbalance condition

The normalized value of the phase angle at the output of PLL block is shown in Figure 5.51 below. The sawtooth waveform under normal grid condition is distorted by the voltage drop on Phase A. The waveform also shows that a small amount of phase shift occurs leading to mismatch of grid current and voltage.

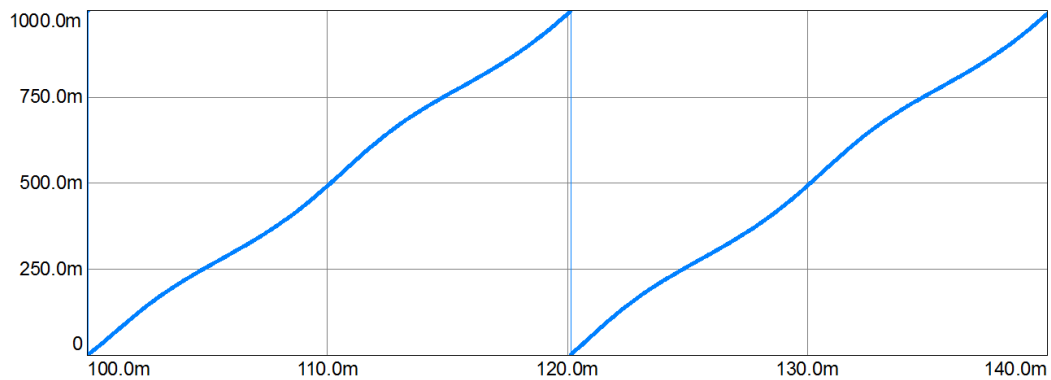


Figure 5.51 PLL angle waveform under voltage unbalance condition

5.6. Summary and Conclusion

In this chapter, detailed simulation results of passive damping methods and SMCD methods are given. The simulation models and simulation parameters for each case is given. The simulations are carried out on a 3 MW system.

At the beginning of the chapter, simple passive damping case is analyzed on 2L system. Steady-state waveforms, load dynamic responses and grid current FFT results are given. Transition from undamped case to passively case and vice versa are also shown to prove the viability of PD on multi-megawatt systems.

Advanced passive damping methods reducing the damping losses compared to simple passive damping are simulated on the same PWM-VSI. The same analysis with PD is conducted for advanced passive damping methods. The comparison of simple and advanced passive damping methods in terms of power loss, grid current THD rating and system efficiency is given.

Two novel damping methods based on SAF algorithm are evaluated and their performances are compared. The stability analysis, load dynamic responses, steady-state waveforms, grid current FFT results, grid current THD ratings and efficiency ratings of TC-SAF and DC-SAF compensated 2L 3 MW PWM-VSIs are provided.

As it can be seen from Table 5.5, DC-SAF is more advantageous than TC-SAF with regard to power rating, efficiency, size, and cost. Computer simulation and theoretical analysis have proven that SMCD methods are useful solutions to inherent resonance problem of *LCL* filters. In particular, DC-SAF is a very compact solution that can be applied to multi-megawatt inverters.

Table 5.5 The summary of proposed series active filters

| | TC-SAF | DC-SAF |
|---------------------------|---------------|---------------|
| DC Input | 600 V | 200 V |
| Rated Power | 3 x 22 kVA | 39 kVA |
| Max Output Current | 268 A | 1085 A |
| Line Current THD | 3.03 % | 3.24 % |
| Efficiency | 99.15 % | 99.23 % |

The proposed systems are also verified on 3L 3 MW systems. The main feedback variable is taken both from the grid side and the converter side. TC-SAF and DC-SAF systems are both simulated under these two conditions. Lastly, the verification of DC-SAF system which is more valuable as stated above is verified under grid distortion and grid unbalance conditions. The stability of the system is clearly demonstrated using steady-state and transient waveforms.

By changing the power module topology from 2L to 3L, the switching frequency is decreased and the filter size is reduced. Therefore, 3L PWM-VSI offers reduced semiconductor losses hence higher efficiency rating. Since the controller bandwidth is reduced and the resonant frequency of the *LCL* filter is further increased by smaller inductors, the implementation of AD is not possible as in the case of 2L PWM-VSI.

CHAPTER 6

PERFORMANCE AND COST EVALUATION OF DAMPING METHODS

6.1. Introduction

Damping methods stated in Chapter 4 are the most adopted techniques to extinguish the oscillations resulting from the inherent resonance phenomena of *LCL* filter. Active damping methods using state feedback and inherent damping using converter side current feedback are not valid for 3 MW PWM-VSI. Depending on the switching frequency, these methods can be applied to multi-MW applications; however, the efficiency criterion puts a limit to the switching frequency of the converter as discussed in Chapter 2.

Due to lack of satisfactory controller bandwidth, passive damping methods must be adopted not to excite resonance. Extreme PD losses; however, create a significant drop on the overall efficiency of the system. For this reason, advanced passive damping methods are applied reducing the resistive losses due to PD. Although PD losses are reduced to one third of the simple PD case, they are still very high as the WECS's rated power is 3 MW. SMCD methods are proposed so as to reduce the damping losses. The application of SMCD methods is independent of the switching frequency of the main PWM-VSI.

For a fair comparison of ND, AD, simple PD, and SMCD methods, the simulated system is now 1 MW with an increased switching frequency of 2 kHz. The parameters of the simulated 1 MW system are tabulated below.

Table 6.1 Parameters of the simulated 1 MW PWM-VSI

| | Symbol | Quantity | Value | |
|----------------------------|----------------|---------------------------|---------------|---------------|
| Main Inverter | P_{rated} | Rated power | 1 MW | |
| | f_{sw} | Switching frequency | 2 kHz | |
| | f_{samp} | Sampling frequency | 4 kHz | |
| | V_{dc} | DC-link voltage | 1070 V | |
| | V_g | Grid voltage | 690 V | |
| | f_g | Grid frequency | 50 Hz | |
| | L_g | Grid side inductance | 190 μ H | |
| | L_c | Converter side inductance | 190 μ H | |
| | C_f | Filter capacitance | 332 μ F | |
| | R_d | Damping resistor | 0.5 Ω | |
| | | | TC-SAF | DC-SAF |
| Auxiliary Converter | $V_{aux,dc}$ | DC-bus voltage | 600 V | 100 V |
| | f_{sw-aux} | Switching frequency | 10 kHz | 10 kHz |
| | $f_{samp-aux}$ | Sampling frequency | 20 kHz | 20 kHz |
| | N | SIT turns ratio | 3 | - |
| | L_{aux} | SRF inductance | 5 μ H | 5.7 μ H |
| | C_{aux} | SRF capacitance | 1000 μ F | - |
| | R_{aux} | SRF resistance | 10 Ω | - |

6.2. Dynamic Performance Comparison

Figure 6.1 demonstrates the dynamic response of naturally damped system. The transitions from light load (20%) to full load (100%) and vice versa are both demonstrated in the same figure. The d -axis current, I_{gd} also shown in Figure 6.1 explains the dynamic behavior of the system under investigation.

Figure 6.2 demonstrates the dynamic response of actively damped system using capacitor current feedback. The transitions from light load (20%) to full load (100%) and vice versa are both demonstrated in the same figure. The d -axis current, I_{gd} also shown in Figure 6.2 explains the dynamic behavior of the system under investigation.

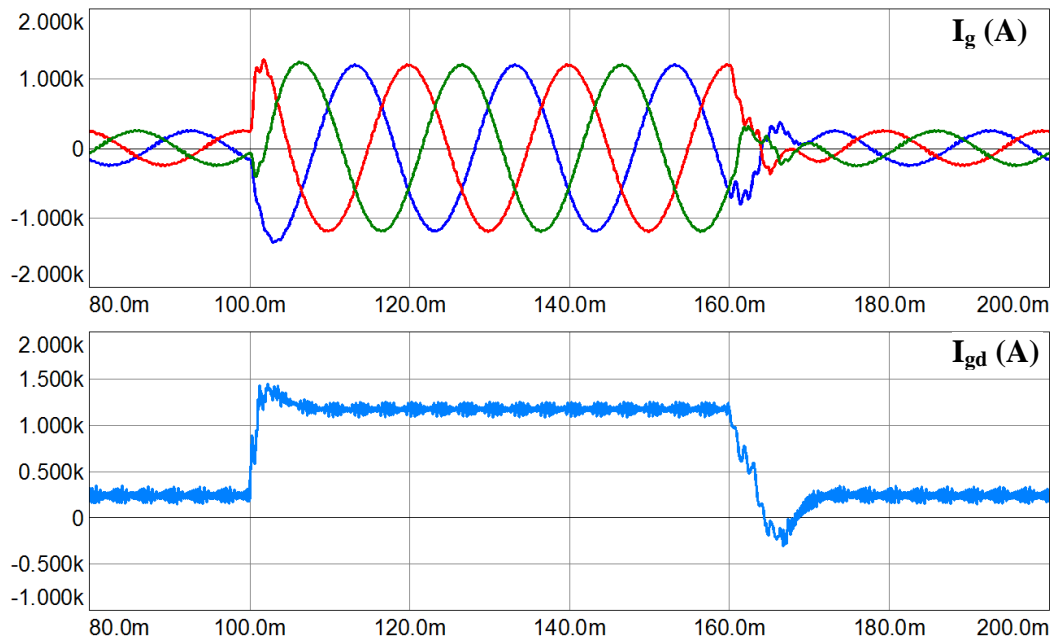


Figure 6.1 Load dynamic response of naturally damped system from 20% load to rated load then to 20% load again

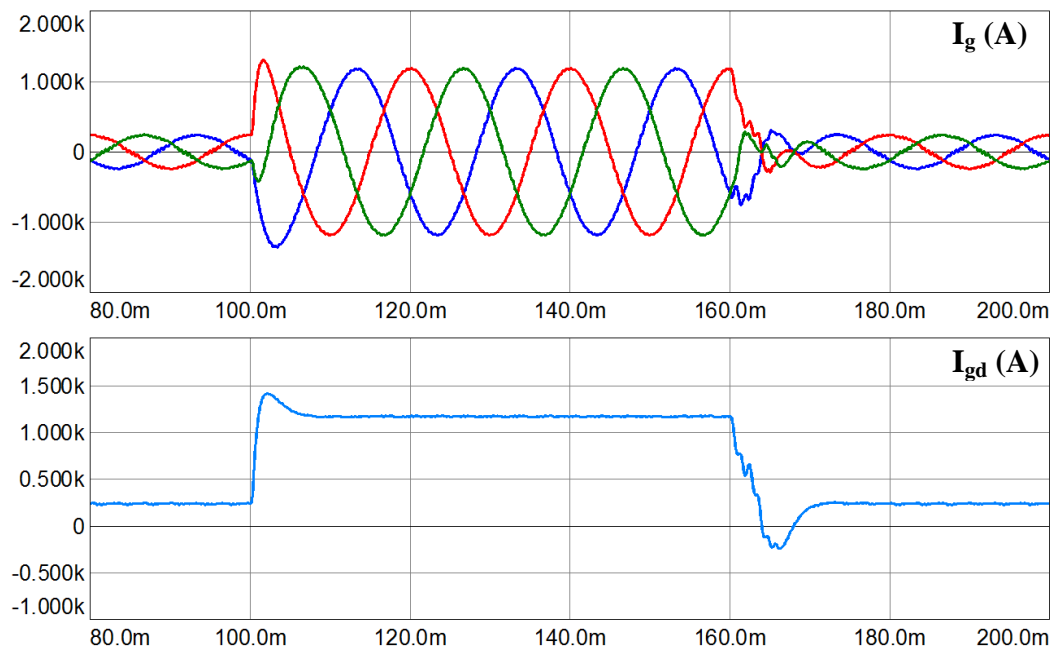


Figure 6.2 Load dynamic response of actively damped system from 20% load to rated load then to 20% load again

Figure 6.3 demonstrates the dynamic response of passively damped system using capacitor current feedback. The transitions from light load (20%) to full load (100%) and vice versa are both demonstrated in the same figure. The d -axis current, I_{gd} also shown in Figure 6.3 explains the dynamic behavior of the system under investigation.

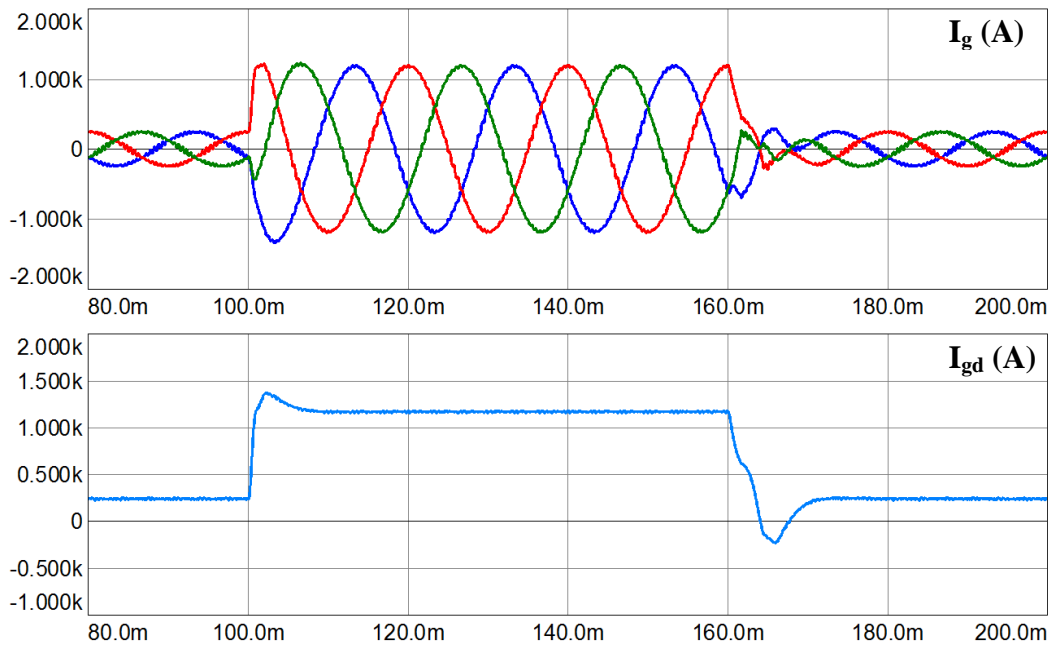


Figure 6.3 Load dynamic response of passively damped system from 20% load to rated load then to 20% load again

Figure 6.4 demonstrates the dynamic response of TC-SAF based system using capacitor current feedback. The transitions from light load (20%) to full load (100%) and vice versa are both demonstrated in the same figure. The d -axis current, I_{gd} also shown in Figure 6.4 explains the dynamic behavior of the system under investigation.

Figure 6.5 demonstrates the dynamic response of DC-SAF based system using capacitor current feedback. The transitions from light load (20%) to full load (100%) and vice versa are both demonstrated in the same figure. The d -axis current, I_{gd} also

shown in Figure 6.5 explains the dynamic behavior of the system under investigation.

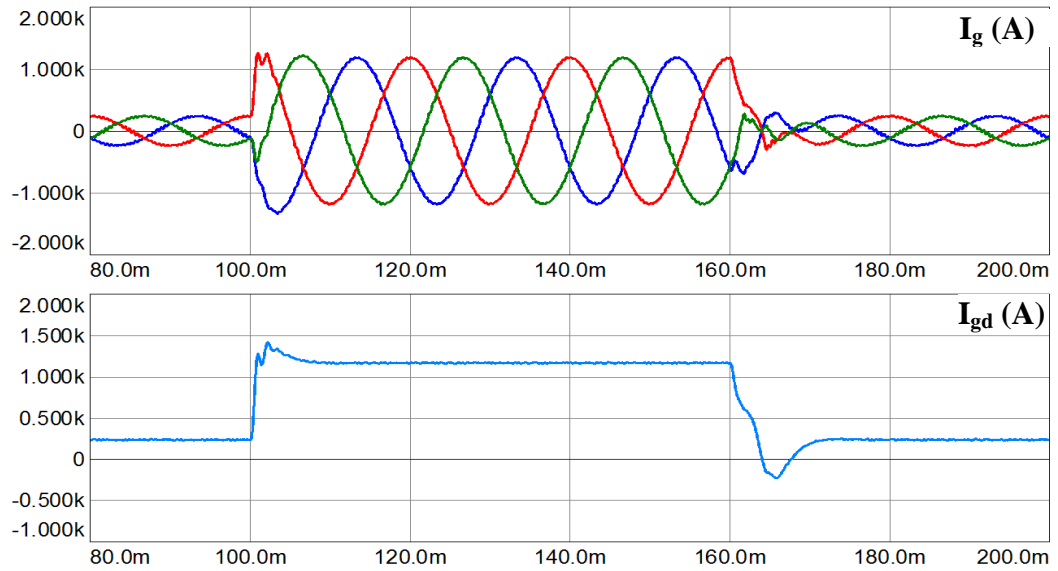


Figure 6.4 Load dynamic response of TC-SAF compensated system from 20% load to rated load then 20% load again

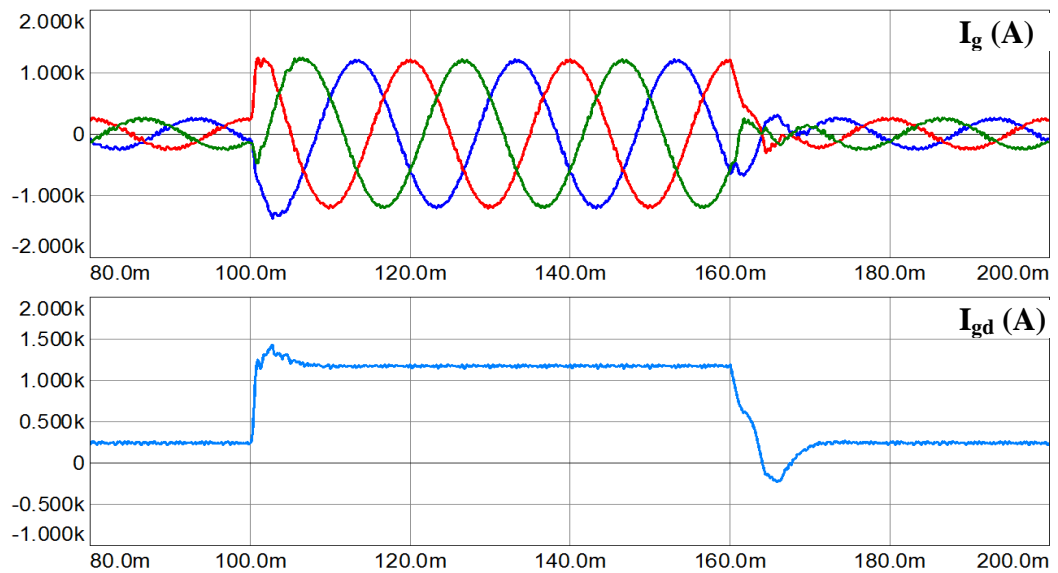


Figure 6.5 Load dynamic response of DC-SAF compensated system from 20% load to rated load then 20% load again

6.3. Grid Current THD Comparison

Grid current FFT result of naturally damped system is shown in Figure 6.6. In the frequency spectrum, switching frequency harmonics at the sidebands of 2 kHz are evident. The multiples of the switching frequency are attenuated due to enhanced attenuation capability of the *LCL* filter.

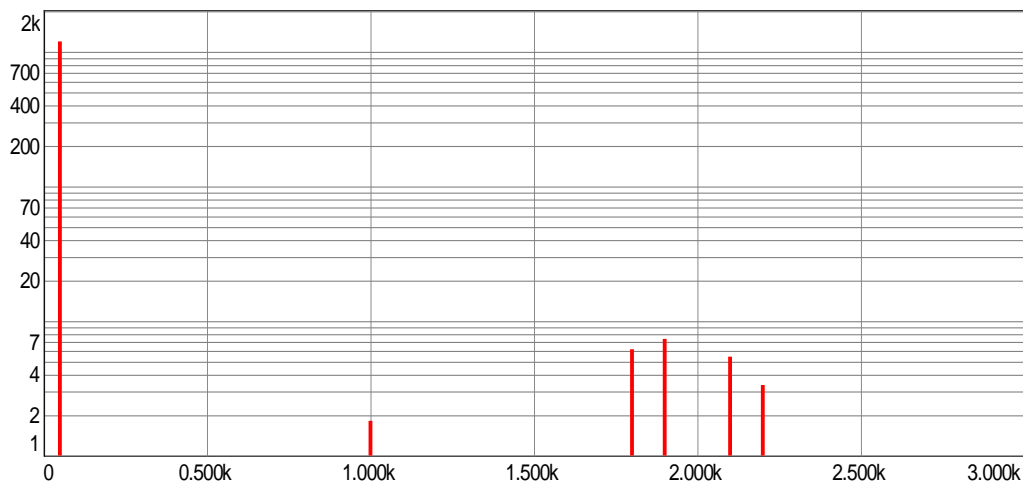


Figure 6.6 Grid current FFT result of naturally damped system

Grid current FFT result of actively damped system is shown in Figure 6.7. In the frequency spectrum, 5th, 7th, and 11th harmonic components and switching frequency harmonics at the sidebands of 2 kHz are seen. The multiples of the switching frequency are attenuated due to enhanced attenuation capability of the *LCL* filter.

Grid current FFT result of passively damped system is shown in Figure 6.8. In the frequency spectrum, only switching frequency harmonics at the sidebands of 2 kHz are observed. The multiples of the switching frequency are attenuated due to enhanced attenuation capability of the *LCL* filter.

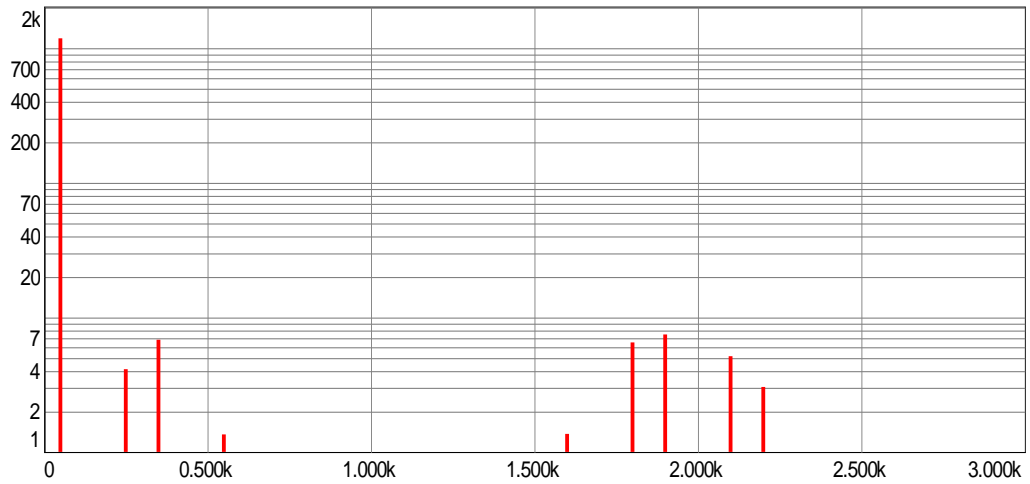


Figure 6.7 Grid current FFT result of actively damped system

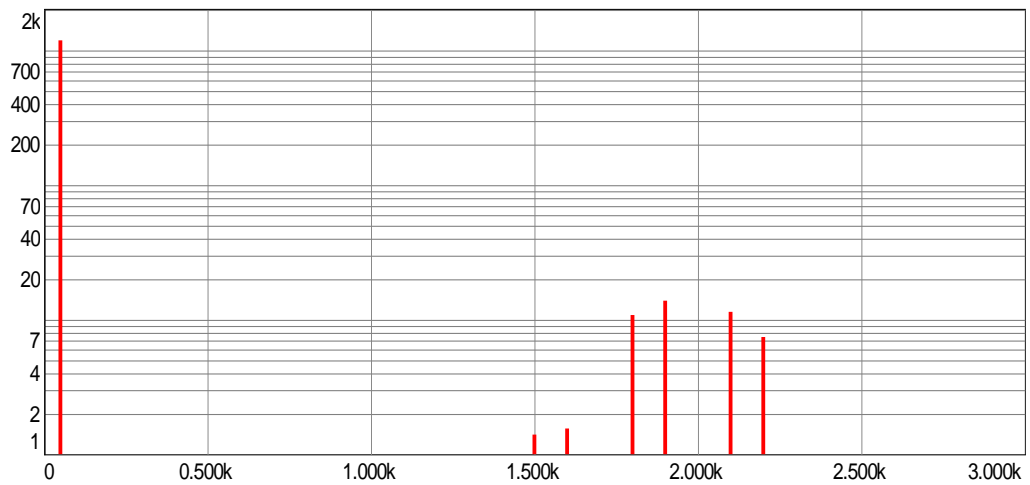


Figure 6.8 Grid current FFT result of passively damped system

Grid current FFT result of TC-SAF compensated system is shown in Figure 6.9. In the frequency spectrum, a small 5th harmonic component and switching frequency harmonics at the sidebands of 2 kHz are seen. The multiples of the switching frequency are attenuated due to enhanced attenuation capability of the *LCL* filter.

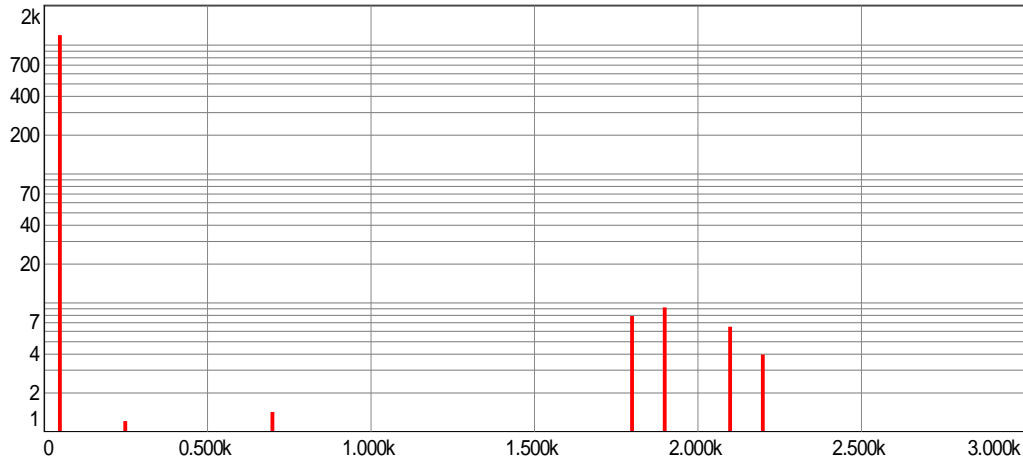


Figure 6.9 Grid current FFT result of TC-SAF compensated system

Grid current FFT result of DC-SAF compensated system is shown in Figure 6.10. Low frequency harmonic component such as 7th, 11th, and 13th are seen. Resonant frequency harmonics at the sidebands of 900 Hz and switching frequency harmonics at the sidebands of 2 kHz are also observed in the frequency spectrum. The harmonic content of DC-SAF is worse than TC-SAF due to decayed filtering performance.

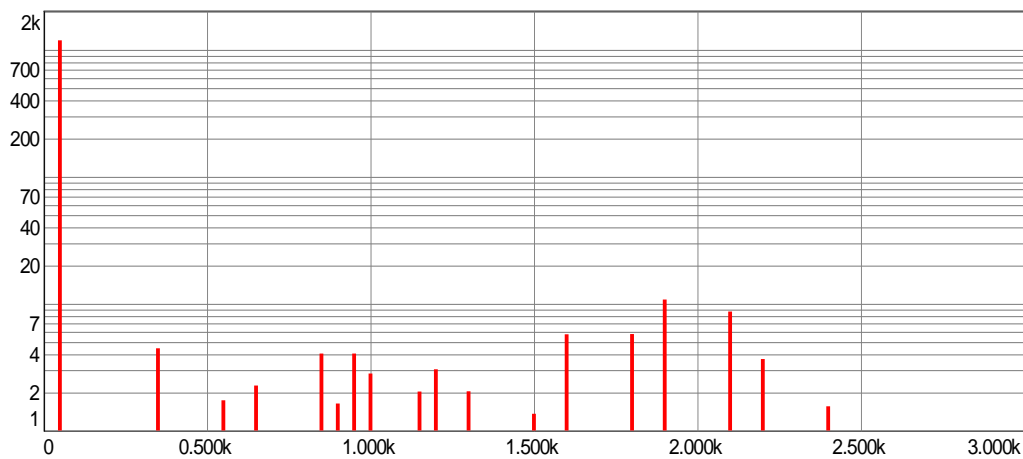


Figure 6.10 Grid current FFT result of DC-SAF compensated system

Figure 6.11 shows THD ratings of ND, AD, PD, TC-SAF compensated, and DC-SAF compensated systems against various load. PD has the worst THD result while THD performance of TC-SAF compensated system is better than DC-SAF compensated system as it is seen from Figure 6.11. All damping methods stay below the THD limit of 4% at the rated load.

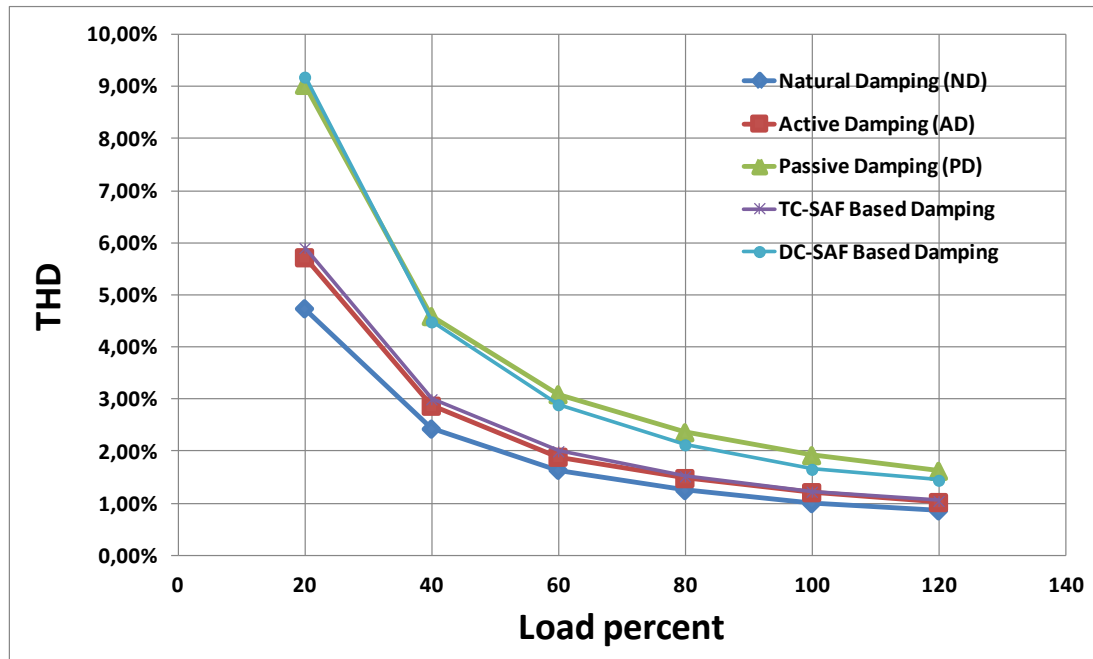


Figure 6.11 THD comparison of damping methods under various load conditions

6.4. Comparison of Power Losses

Power losses of ND, AD, PD, TC-SAF compensated, and DC-SAF compensated systems at various load conditions are analyzed and the results are shown in Figure 6.12. The losses are due to semiconductor losses and auxiliary losses such as additional semiconductor losses of SAF compensated systems and damping losses. Parasitic losses of *LCL* filter elements are ignored in this analysis. Since the damping losses of AD and ND methods are zero, the losses are kept at minimum. The power losses of these two system are almost the same for all load conditions.

SAF compensated systems have additional semiconductor losses which is a bit higher for TC-SAF. Auxiliary transformer losses and increased number of semiconductors for TC-SAF compensated system have an adverse effect on the total power loss. PD has the highest power loss due to damping resistors inserted in the *LCL* filter. The variation of losses is not proportional with the load percent but a linearly increasing curve is obtained in Figure 6.12.

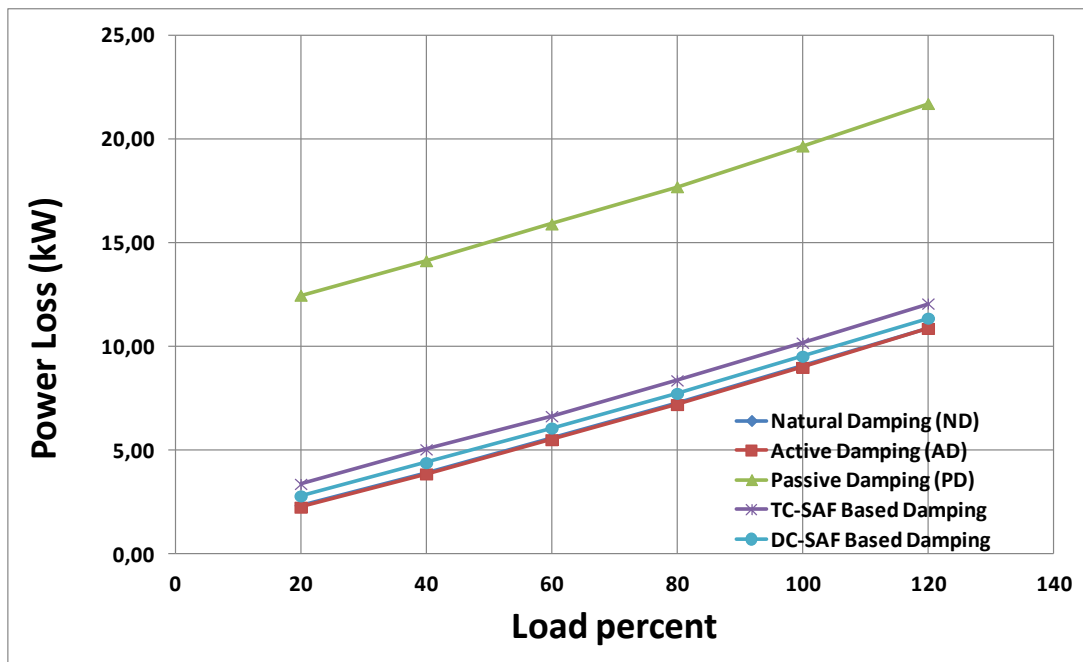


Figure 6.12 Power loss comparison of damping methods under various load conditions

6.5. Efficiency Comparison

Efficiencies of ND, AD, PD, TC-SAF compensated, and DC-SAF compensated systems at various load conditions are analyzed and the results are shown in Figure 6.13. SAF compensated systems have an efficiency rating higher than 99% at the rated load. The difference between efficiencies gets bigger as the load percent decreases. Due to less number of switches, elimination of SIT, and lower DC-bus

voltage, the DC-SAF outclasses the TC-SAF in terms of the efficiency. PD has the worst efficiency rating due to damping resistors inserted in the *LCL* filter. The efficiencies of ND and AD methods are at the highest level due to the elimination of resonance by the controllers. Since any additional elements are not placed in the system, power losses are due to semiconductor losses for ND and AD. The efficiencies of these two systems are almost the same for all load conditions.

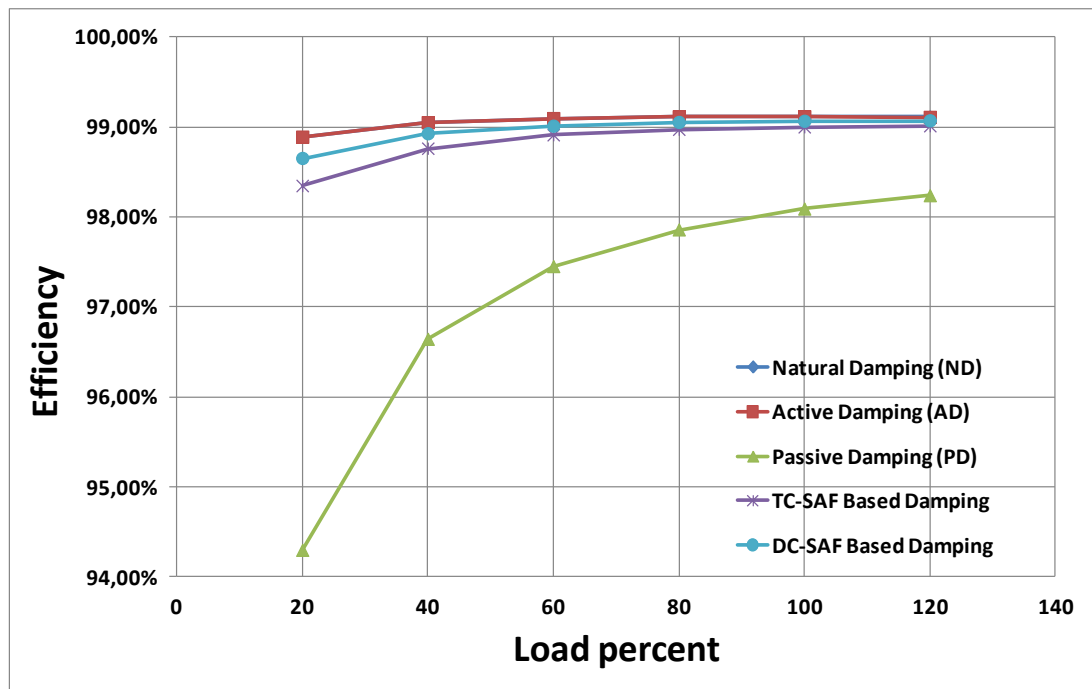


Figure 6.13 Efficiency comparison of damping methods under various load conditions

6.6. Performance Evaluation

In this section, the operational efficiency and the operational current harmonic distortion ratings of 1 MW PWM-VSI for each damping method is evaluated. The annual workload of the system is defined using the capacity factor of the wind turbine. Then, the performance of the system with ND, AD, PD, and SMCD is evaluated. To evaluate the performance of the investigated system, power output vs.

wind speed curve of a WT is needed. The selected WT is Mitsubishi's MWT62/1.0 model [73].

Capacity factor is defined as the actual output over a period of time as a proportion of a WECS's maximum capacity. The capacity factor information of MWT62/1.0 can be obtained from Figure 6.14 (a). The annual energy production in MWh is shown in Figure 6.14 (b).

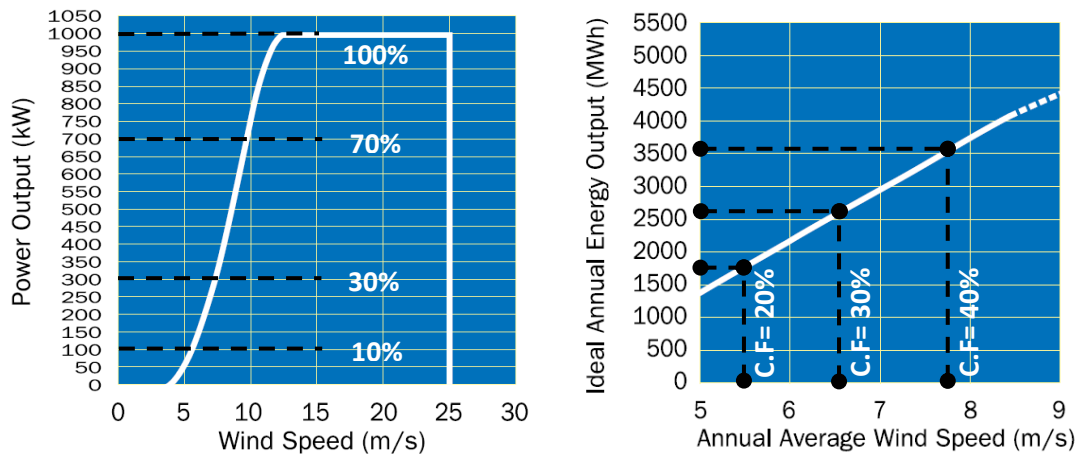


Figure 6.14 (a) Power curve **(b)** Annual energy production and capacity factor of MWT62/1.0

The power curve is modified in Figure 6.15 assuming the capacity factor is constant within the corresponding wind speed intervals (i.e. the output power changes linearly within specified wind speed intervals). Then, the curve is converted into rectangular boxes. In this way, the area under the curve is not changed while the calculations are made easier using linear equations. The red vertical slices from c_1 to c_5 reflect the segments that the WT is working at the corresponding wind speed interval when wind speed is between 3.5 m/s and 25m/s.

The mean capacity factor is calculated by using the width of these slices and the equivalent power outputs as shown in (6.1). The operation time, σ (i.e. when the WECS is active) is defined in (6.2). As the modified power curve represents the time

intervals of power generation, summing the constants from c_1 to c_5 gives the operation time as stated in (6.3). The maximum operation time of the WECS is assumed to be 60% of the year in hours ($\sigma=0.6$). The capacity factors analyzed in this study are 20%, 30%, and 40%.

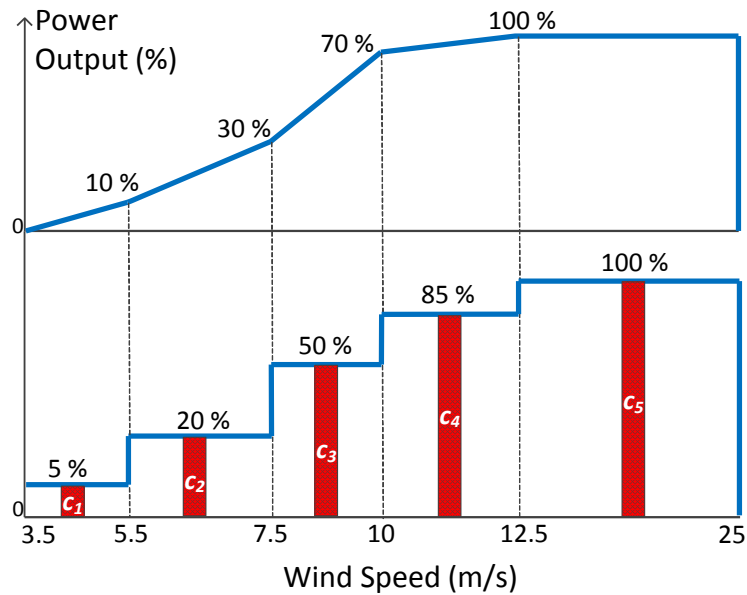


Figure 6.15 Modified power curve of MWT62/1.0

$$C.F(\%) = c_1 * 5 + c_2 * 20 + c_3 * 50 + c_4 * 85 + c_5 * 100 \quad (6.1)$$

$$\sigma = \frac{\text{Duration of active power generation per annum [hour]}}{\text{One year [hour]}} \quad (6.2)$$

$$\sum_{m=1}^5 c_m = \sigma \quad (6.3)$$

Table 6.2 gives the wind speed intervals classified according to Figure 6.15 and the coefficients corresponding to each wind speed interval. The weighted sum of power levels at which the WECS is operating is equal to the capacity factor. It should be

noted that the sum of the coefficients from ϕ_1 to ϕ_5 are equal to 1 whereas the sum of c_1 to c_5 is equal to 0.6. The normalized coefficients are utilized in the next step where the operational efficiency is calculated.

Table 6.2 Capacity factors calculated using different power levels

| <i>C.F</i> (%) | Wind Speed Coefficients (ϕ_n) | | | | |
|----------------|--------------------------------------|-------------------------|------------------------|-------------------------|-------------------------|
| | ϕ_1 3.5-5.5 m/s | ϕ_2 5.5-7.5 m/s | ϕ_3 7.5-10 m/s | ϕ_4 10-12.5 m/s | ϕ_5 12.5-25 m/s |
| 20 % | 0.30 | 0.30 | 0.20 | 0.10 | 0.10 |
| 30 % | 0.20 | 0.25 | 0.15 | 0.15 | 0.25 |
| 40 % | 0.10 | 0.10 | 0.20 | 0.25 | 0.35 |

The operational efficiency, η_{op} of the system is calculated using the normalized wind speed coefficients as given in (6.4).

$$\eta_{op} = \phi_1 \cdot \eta_{5\%} + \phi_2 \cdot \eta_{20\%} + \phi_3 \cdot \eta_{50\%} + \phi_4 \cdot \eta_{85\%} + \phi_5 \cdot \eta_{100\%} \quad (6.4)$$

where $\eta_{5\%}$, $\eta_{20\%}$, $\eta_{50\%}$, $\eta_{85\%}$, and $\eta_{100\%}$ are the efficiencies at 5%, 20%, 50%, 85%, and 100% load, respectively.

Using the information given in Figure 6.13, the efficiencies of each damping method at 20%, 30%, and 40% capacity factor for a 1 MW PWM-VSI is given in Table 6.3. For all capacity factors, the efficiency rating of ND and AD are superior to other three damping methods since additional lossy elements are not used. On the other hand, TC-SAF and DC-SAF based damping methods are more efficient than PD due to the elimination of damping resistors as stated in the previous sections. The efficiency ratings of all methods increase as the capacity factor increase.

The operational current harmonic distortion ratings of each damping method are given for the same capacity factors in Table 6.4. For low capacity factor values the

percent of the ripples injected to the grid increase; however, it should be noted that the fundamental current magnitude is also low for such capacity factor values. The harmonic attenuation capability of the filter is not disturbed for ND and AD methods hence the ripple magnitudes are always lower than that of PD for all capacity factor values. In addition, TC-SAF provides a better filter characteristic than DC-SAF.

Table 6.3 Operational efficiencies of 1 MW PWM-VSI with different damping methods for various capacity factors

| Capacity Factor | ND | AD | PD | TC-SAF | DC-SAF |
|------------------------|-----------|-----------|-----------|---------------|---------------|
| 20 % | 98.85% | 98.85% | 94.31% | 98.47% | 98.60% |
| 30 % | 98.92% | 98.93% | 95.38% | 98.61% | 98.73% |
| 40 % | 99.02% | 99.02% | 96.70% | 98.80% | 98.90% |

Table 6.4 Operational current harmonic distortion ratings of 1 MW PWM-VSI with different damping methods for various capacity factors

| Capacity Factor | ND | AD | PD | TC-SAF | DC-SAF |
|------------------------|-----------|-----------|-----------|---------------|---------------|
| 20 % | 4.31% | 5.19% | 8.11% | 5.34% | 8.23% |
| 30 % | 3.43% | 4.13% | 6.47% | 4.25% | 6.49% |
| 40 % | 2.29% | 2.75% | 4.33% | 2.83% | 4.22% |

6.7. Cost Evaluation

The cost evaluation of damping methods is assessed using the initial cost and running cost. For each damping method the initial cost is analyzed first than the running cost is calculated using the operational efficiency stated in the previous section.

The initial cost for a 2L PWM-VSI design includes semiconductors, IGBT gate drives, heat sink, blower, air duct, current/voltage transducers, electronic boards, mechanical enclosure, and grid side filter prices. There is a variety of semiconductors from different manufacturers which can replace each other. Although the prices differ for each product, an average price can be estimated. 1800

A IGBTs cost around \$690 while 2400 A IGBTs cost around \$780. For 1 MW system, the grid side current's peak value is about 1150 A, hence IGBTs having 1700 V and 1800 A ratings can be used. The plug and play type gate drives cost around \$180 per IGBT and common for all power ratings. The heat sink price; on the other hand, depends on the efficiency rating of the system at rated load. The power loss on IGBTs is the main criterion for determining the cooling. An average cost of \$200/kW is accepted for cooling of the power unit with an additional cost of \$250 for air duct and \$400 for blower. For current and voltage control loops minimum 2 voltage sensors and 2 current sensors at the grid side, 2 current sensors and 1 voltage sensor at the DC-link side are required. Average prices for current and voltage sensor are around \$200 and \$240 respectively. DC-link capacitors of at least 1200V rating should be selected for this application and a suitable capacitor bank consisting of parallel-connected film capacitors cost around \$1050. Damping resistors for 1 MW PWM-VSI is selected according to Figure 6.12. The power loss exerted on damping resistors is at least 10 kW. Such a three-phase resistor's price is approximated as \$700. The reactive components both in grid side *LCL* filter and auxiliary transformer are approximated as \$3200 and \$800 respectively. Three single-phase transformers and additional SRF in TC-SAF cost around \$2550 while coupling inductors cost around \$150 in DC-SAF. Electronic boards consisting of microprocessors and peripherals cost around \$600. The mechanical enclosure including the interior mechanical parts of the PWM-VSI cost roughly as \$6000.

AD methods usually employ 2 additional current sensors (2 out of 3 phases) whereas PD methods need passive damping elements. SMCD methods employ auxiliary IGBTs, reactive components, and transformers where necessary. TC-SAF employs an additional electronic board controlling 3 single-phase inverters. One additional voltage sensor and 3 additional current sensors are used in TC-SAF. On the other hand, DC-SAF utilizes an additional electronic board controlling a three-phase inverter. One additional voltage sensor and 2 additional current sensors are used in DC-SAF.

By considering the number of components common in each method and additional components, Table 6.5 is given. Apart from the abovementioned prices, cabling, connector, electrical protection, auxiliary mechanical and electrical components are combined as a single item in the same table. The cost of these components are accepted more or less the same for all damping methods.

Table 6.5 Initial cost analysis of 1 MW PWM-VSI for various damping methods

| | ND | AD | PD | TC-SAF | DC-SAF |
|--|----------------|----------------|----------------|----------------|----------------|
| IGBTs | \$4140 | \$4140 | \$4140 | \$4140 | \$4140 |
| Gate driver | \$1080 | \$1080 | \$1080 | \$1080 | \$1080 |
| Heat sink, blower, and air duct | \$2250 | \$2250 | \$2250 | \$2650 | \$2450 |
| Current/voltage transducers | \$1520 | \$1920 | \$1520 | \$1520 | \$1520 |
| DC-link capacitors | \$1050 | \$1050 | \$1050 | \$1050 | \$1050 |
| Damping resistors | - | - | \$700 | - | - |
| Auxiliary IGBTs | - | - | - | \$1200 | \$1600 |
| Auxiliary reactive components | - | - | - | \$2550 | \$150 |
| Auxiliary current/voltage transducers | - | - | - | \$840 | \$640 |
| Electronic boards | \$600 | \$600 | \$600 | \$1200 | \$1200 |
| Mechanical enclosure | \$6000 | \$6000 | \$6000 | \$7000 | \$7000 |
| Grid side filter | \$3200 | \$3200 | \$3200 | \$3200 | \$3200 |
| Other | \$2500 | \$2500 | \$2500 | \$3000 | \$3000 |
| TOTAL | \$22340 | \$22740 | \$23040 | \$29430 | \$27030 |

As ND and AD methods provide the least power losses and the initial costs of these methods are the lowest among five distinct damping methods, the return on investment is not investigated for ND and AD methods. Since the long term stability of a WECS can be satisfied by additional hardware such as PD, the comparison is

mainly between PD and SMCD methods. The annual power losses of PD, TC-SAF, and DC-SAF compensated systems are calculated for various capacity factors in Table 6.6.

Table 6.6 Annual power losses of PD, TC-SAF, and DC-SAF compensated systems for various capacity factors

| Capacity Factor | PD | TC-SAF | DC-SAF |
|------------------------|------------|---------------|---------------|
| 20 % | 104.99 MWh | 38.05 MWh | 34.35 MWh |
| 30 % | 122.15 MWh | 50.18 MWh | 45.87 MWh |
| 40 % | 140.69 MWh | 63.68 MWh | 58.74 MWh |

In Turkish Energy Market, the average price for electricity produced from wind energy sources is 7.9 U.S. cents/kWh. In order to see whether SMCD damping methods can replace PD or not, Table 6.7 is presented. The initial cost differences and the annual savings of SMCD methods over PD are given for 20%, 30%, and 40% capacity factors. Moreover, the return on investment periods of TC-SAF and DC-SAF compensated systems are given in the same table.

Table 6.7 Return on investment calculation of SMCD methods

| | TC-SAF | DC-SAF |
|------------------------------------|---------------|---------------|
| Initial Cost Difference | \$6390 | \$3990 |
| Annual Savings for 20% C.F | \$5288.3 | \$5580.6 |
| Annual Savings for 30% C.F | \$5685.9 | \$6026.4 |
| Annual Savings for 40% C.F | \$6084.1 | \$6474.1 |
| Return on Investment Period | ≈ 1 year | ≈ 8 months |

The operational life of a WECS is approximated as 20 years. Hence the cost savings throughout the whole operational life of WECS for each SMCD method are more than \$100000 and the return on investment periods are very short. In addition to lower power loss and reduced initial cost of DC-SAF compensated system, the shorter return on investment period and smaller size are two important factors to utilize DC-SAF rather than TC-SAF.

It should also be noted that, the return on investment duration becomes shorter as the capacity factor of the WECS increases beyond 40%.

CHAPTER 7

CONCLUSION AND FUTURE WORK

The penetration of wind power to the utility is greater than before and it is continuously increasing. Variable speed wind turbines dominate the market at present. Although doubly-fed induction generator based wind turbines are used previously, wind turbines using full-scale converters are more preferred nowadays due to their superior performance during grid faults. Grid support by means of 100% reactive current injection to the utility can only be supported by the full-scale converter. The main advantage of doubly-fed induction generator based wind turbines; on the other hand, is the use of partial scale power converters.

LCL filters connected as the grid interface of full-scale back-to-back PWM-VSIs in order to mitigate the current harmonics injected to the utility have an inherent resonance problem causing large oscillations in the system if not damped properly. A variety of damping methods are presented in the literature but none of them offered an appropriate solution for high power systems without additional power loss.

In this thesis, the design and resonance damping of *LCL* filtered three-phase 2L PWM-VSI widely used in grid-connected renewable energy systems are investigated. The design procedure starts from the converter's power rating and ends with the selection of suitable converter topology, switching frequency, pulse-width modulation technique, DC-link voltage level, and *LCL* filter parameters. The controller design for grid-connected PWM-VSIs is also stated to present a complete analysis.

The resonance phenomena; however, is not a minor problem that the controllers can deal with for multi-megawatt systems. The limited phase margins of the controllers

due to low switching frequencies make the active damping of the resonance impractical. Because of high efficiency target of multi-megawatt systems, the switching frequency cannot be increased so as to obtain a sufficient phase margin. Therefore, passive damping methods should be applied. Enormous resistive losses due to damping resistors inserted in the *LCL* filter are not well-accepted since the cooling and thermal design costs of the WECS increase as the losses increase.

In the literature, advance passive damping methods are proposed via insertion of reactive components in various ways with the *LCL* filter. The frequency responses are modified such that low frequency harmonics pass through the damping inductors and high frequency harmonics flow through the damping capacitors. Only resonant harmonics flow through the damping resistors. In that way, the resistive losses are diminished.

Reduced damping losses owing to advanced passive damping methods are still too high for multi-megawatt systems. Further decrease in the damping losses can be achieved using switch mode converters emulating series damping resistors. Auxiliary converters connected to the *LCL* filter provide the necessary impedance path for the resonant harmonics while other frequency components are allowed to pass without any modification by the auxiliary converters. Two novel methods are presented in this thesis for the resonance damping of multi-megawatt systems where the switching frequency is limited to only a few kilohertz. A transformer-coupled method together with three auxiliary single-phase inverters and a directly-connected method with a three-phase inverter are described in operation and analyzed thoroughly.

A top to bottom design methodology for the grid side converter of the WECS both on hardware and software is given in this study. The resonance problem due to grid side *LCL* filter is emphasized. An optimized but not yet practically verified method, SMCD is introduced and developed. The comparison of various damping methods is made by computer simulations and detailed cost analysis.

Wind turbines are typically installed in the form of wind farms rather than individually at multi-MW ratings and the best selling range for wind turbines is 1.5-3 MW. For such high power ratings, the application of active damping methods is not feasible while SMCD methods are verified to be major alternatives to passive damping due to their outnumbered advantages. Therefore, the main contribution of this study is to present alternative damping methods to the inherent resonance issue of the *LCL* filter providing reduced resistive losses and smaller filter size.

The comparison of various damping methods on a 1 MW PWM-VSI leads to the conclusion that passive damping is the least efficient damping method. On the other hand, natural and active damping methods do not produce additional losses for the damping of the *LCL* filter hence have the highest efficiency ratings. As an improvement on the efficiency of the overall system, SMCD methods can be applied. Nearly 1% of the 1 MW system's rated power is lost due to passive damping. SMCD methods reduce the damping losses by 95% hence the overall efficiency of the system is improved nearly by 1% at rated load conditions. Different capacity factors are also analyzed in Chapter 6 and the operational efficiency ratings of various damping methods are presented. Especially for low capacity factors, the efficiency of the system is improved by 4% due to DC-SAF which results in 70 MWh energy saving per annum.

In terms of THD rating, all damping methods have more or less the same performance on 1 MW system. However, THD performances of natural damping, active damping, and TC-SAF compensated damping methods outclass passive damping and DC-SAF compensated damping methods at rated load conditions. Reduced attenuation capability of the *LCL* filter at frequencies above the resonant frequency due to passive damping and DC-SAF compensated damping leads to higher current ripples on the grid side currents. The operational current harmonic distortion ratings of various damping methods demonstrated for three distinct capacity factors and the abovementioned results are also valid for all capacity factors. As the capacity factor increases, the grid side current THD ratings in percentage decrease.

The detailed cost analysis of various damping methods on a 1 MW PWM-VSI is presented in Chapter 6. The initial costs and the running costs are investigated. Since additional damping elements are not used in natural and active damping, the minimized costs are obtained for these two methods. Auxiliary switching elements, auxiliary controllers, and auxiliary transformers utilized in TC-SAF and DC-SAF compensated systems bring extra costs hence the initial costs of these two methods are more than other damping methods. Long term stability of the system is not provided by natural or active damping; therefore, the comparison of the running costs are made among passive, TC-SAF compensated, and DC-SAF compensated damping methods. The return on investment analysis shows that the total saving per annum for DC-SAF compensated system is around \$6000 and the amortization time is nearly 8 months.

To conclude, DC-SAF compensated system is a major alternative of passive damping generally applied in low-voltage, multi-megawatt grid connected systems. In terms of grid side current THD rating, efficiency, amortization time, size, and weight, DC-SAF compensated system is very dominant and can easily be implemented. The return on investment time of the investigated SMCD method is also analyzed for distinct capacity factors and it decays as the capacity factor increases. For every 10% increase in the capacity factor, the return on investment time decays nearly 1 month.

For 3 MW PWM-VSI, the comparison of passive damping, advanced passive damping and SMCD based damping methods is made. The resistive losses due to passive damping are around 2% of the system's rated power this time. It can be concluded that the annual savings due to SMCD methods are higher than 1 MW system hence the return on investment time is shorter. For even higher power levels than 3 MW, the resistive losses due to passive damping further increase and the feasibility of SMCD methods becomes more apparent. Although higher power ratings require three-level converters, the losses due to passive damping are expected to be similar. Therefore, SMCD methods may also be used for damping for higher level converters.

The steps to the conclusion can be summarized as follows:

First chapter goes over the global wind energy capacity and a typical wind turbine design. The motivation behind this study, damping of *LCL* filter resonance is stated. The damping methods available in the literature are mentioned. Moreover, the efficiency criterion on high power WECS is highlighted with two efficiency curves against switching frequency for 1 MW and 3 MW systems.

The basics of WECS are given in Chapter 2. Different types of wind turbines are covered and the importance of variable speed wind turbines with full-scale converters is stated. Power quality problems and grid codes are specified as well as the short-circuit ratio of the grid. Power converter topologies used in WECS are briefly introduced with their specific properties. A detailed comparison of the power converter topologies is given. Moreover, review of back-to-back connected converters is stated. The requirements on the power converters; grid code compliance, fast power response, controllable reactive power, low THD level, cost effectiveness, and reduced design complexity are covered. Converter topologies for low-voltage grid connection with numerical examples of various manufacturers are stated. Besides, the trends and perspectives in WECS are discussed.

Chapter 3 covers design and control of grid-connected PWM-VSIs. In particular, grid side converter of WECS is discussed. The switching frequency range is determined using the efficiency criterion. The modulation and controller types are defined. Moreover, the grid side filter topologies for multi-megawatt systems are presented. Mathematical models of *L* and *LCL* filters are given and the frequency characteristics are demonstrated. A review in the hardware design part is introduced. The selection of DC-link capacitor and the *LCL* filter parameters are given. In the control overview part, space vector transformations from three-phase rotating signals to two-phase stationary signals are expressed. The sub blocks of the converter's controller are discussed in detail. Phase-locked loop, current and voltage control blocks are reviewed specific to wind turbine applications. The parameters of the controllers are formulated and the tuning of the parameters is given together with some assumptions. The sampling of the analog signals to digital domain is clarified.

In addition, the stability of the controllers is discussed using an exemplary bode plot and a pole-zero diagram.

In Chapter 4, resonance damping methods, namely natural damping (ND), active damping (AD), and passive damping (PD) are reviewed and specific to high power systems, advanced passive damping methods are given. Transfer functions and bode plots of each damping method are provided. AD gain adjustment is stated with the equations. Switch mode converter based resonance damping (SMCD) methods are introduced. The need for SMCD methods is explained. The control algorithm and the single-phase equivalent circuits are explained. Besides, the frequency responses of transformer-coupled and directly-connected SMCD methods are sketched.

The verification of passive damping and SMCD methods are presented in Chapter 5. Simulation results for passive damping and advanced passive damping methods on 3 MW PWM-VSI is given. The verification of all methods, steady-state waveforms, load dynamic responses, THD analysis, and efficiency comparison are demonstrated. Stability of TC-SAF and DC-SAF compensated systems is examined by an instant activation of the proposed methods. Steady-state current and voltage waveforms are presented. Besides, load dynamic responses are demonstrated. The efficiency and THD ratings of the proposed methods reflect the contribution of novel SMCD methods. Frequency spectrums of grid side currents are shown that they are compatible with the bode plots demonstrated in Chapter 4. Verification of SMCD methods on 3L PWM-VSI is also given. Under grid current feedback (GCF) and converter current feedback (CCF), the proposed methods are verified with time domain signals. Moreover, distorted and unbalanced grid conditions are examined on 3L 3 MW SMCD systems.

Lastly, Chapter 6 gives a complete comparison of ND, AD, PD, and SMCD methods on a 1 MW system. Load dynamic responses, grid current FFT results, THD and efficiency curves against load percent are demonstrated. In addition, power losses of each damping method are compared. The estimated cost analysis of damping methods is also given at the end of the chapter. The cost of a 2L 1 MW PWM-VSI is found approximately as \$22000. Depending on the damping method, the cost of the

system increase further but the efficiency of the system for each damping method should not be ignored. Due to limited efficiency rating of passive damping, the annual losses of the system cannot be neglected. SMCD methods provide higher efficiency ratings hence the running cost of the system is minimized. The return on investment calculation reflects that the initial cost of SMCD methods can be paid off within one year.

As future work, the experimental verification of SMCD methods might be investigated. Detailed simulation results and performance analyses of these methods are studied; however, an experimental setup to reflect the feasibility of two novel SMCD methods on hardware would be a nice subject.

Moreover, application of SMCD methods on 3L converters are not investigated in detail throughout this thesis. For higher power ratings than 3MW, the application of 3L converters is advantageous over 2L ones. Detailed performance analyses of SMCD methods for various load conditions might be another future work to deal with.

SMCD with different topologies could also be studied. For instance, reduced switch count SMCD methods would further minimize the power losses on the auxiliary converter. Alternatively, techniques utilized on the extraction of resonant frequency harmonics would be improved. Time delays introduced by digital filters in the control algorithm of SMCD methods do not make any significant effect on the performance of the SMCD methods; however, enhanced harmonic extraction techniques used in power quality conditioners can also be used in SMCD methods.

REFERENCES

- [1] Global Wind Energy Council - Global Cumulative Installed Capacity 1996-2013
[online] Available: <http://www.gwec.net/> [Accessed: November, 2014].
- [2] M. Liserre, R. Cardenas, M. Molinas, and J. Rodriguez, "Overview of multi-MW wind turbines and wind parks," *IEEE Trans. Ind. Electron.*, vol. 58, no. 4, pp. 1081-1095, Apr. 2011.
- [3] M. Liserre, F. Blaabjerg, and S. Hansen, "Design and control of an *LCL*-filter based three-phase active rectifier," *IEEE Trans. Ind. Appl.*, vol. 41, no. 5, pp. 1281-1291, Sep./Oct. 2005.
- [4] B. G. Cho and S. K. Sul, "*LCL* filter design for grid-connected voltage-source converters in high power systems," *Energy Conversion Congress and Exposition (ECCE), 2012 IEEE*, pp.1548-1555, Sep. 2012.
- [5] J. Dannehl, F. W. Fuchs, S. Hansen, and P. B. Thogersen, "Investigation of active damping approaches for PI-based current control of grid-connected pulse width modulation converters with *LCL* filters," *IEEE Trans. Ind. Appl.*, vol. 46, no. 4, pp. 1509-1517, Jul./Aug. 2010.
- [6] Y. Tang, P. C. Loh, P. Wang, F. H. Choo, and F. Gao, "Exploring inherent damping characteristics of *LCL*-filters for three-phase grid-connected voltage source inverters," *IEEE Trans. Power Electron.*, vol. 27, no. 3, pp. 1433-1443, Mar. 2012.
- [7] R. Pena-Alzola, M. Liserre, F. Blaabjerg, R. Sebastian, J. Dannehl, and F. W. Fuchs, "Analysis of the passive damping losses in *LCL*-filter-based grid converters," *IEEE Trans. Power Electron.*, vol. 28, no. 6, pp. 2642–2646, Jun. 2013.

- [8] S. G. Parker, B. P. McGrath, and D. G. Holmes, "Regions of active damping control for *LCL* filters" *IEEE Trans. Ind. Appl.*, vol.50, no.1, pp.424-432, Jan./Feb. 2014.
- [9] E. Kantar, S. N. Usluer, and A.M. Hava, "Control strategies for grid connected PWM-VSI systems," *Electrical and Electronics Engineering (ELECO), 2013 IEEE 8th International Conference on*, pp.220-224, Nov. 2013.
- [10] E. Kantar, S. N. Usluer, and A.M. Hava, "Design and performance analysis of a grid connected PWM-VSI system," *Electrical and Electronics Engineering (ELECO), 2013 IEEE 8th International Conference on*, pp.157-161, Nov. 2013.
- [11] S. N. Usluer and A. M. Hava, "Series active filter based resonance damping of high power three-phase, *LCL* filtered, grid connected voltage source inverters," *Industrial Electronics (ISIE), 2014 IEEE 23rd International Symposium on*, pp.643-648, Jun. 2014.
- [12] S. N. Usluer and A. M. Hava, "Investigation on Series Active Filter Compensated High Power Grid-Connected Voltage Source Inverters with *LCL* Filter," *Energy Conversion Congress and Exposition (ECCE), 2014 IEEE*, vol., no., pp.381,388, 14-18 Sept. 2014.
- [13] E. Kantar and A. M. Hava, "Design of grid connected PWM converters considering topology and PWM methods for low-voltage renewable energy applications," *Power Electronics Conference (IPEC-Hiroshima 2014 - ECCE-ASIA), 2014 International*, vol., no., pp.2034, 2041, 18-21 May 2014.
- [14] K. Ma, M. Liserre, and F. Blaabjerg, "Comparison of multi-MW converters considering the determining factors in wind power application," *Energy Conversion Congress and Exposition (ECCE), 2013 IEEE*, pp.4754-4761, Sep. 2013.
- [15] F. Blaabjerg, Z. Chen, R. Teodorescu, and F. Iov, "Power Electronics in Wind Turbine Systems," *International Power Electronics and Motion Control Conference (IPEMC), 2006 CES/IEEE*, vol.1, no., pp.1,11, Aug. 2006.
- [16] L. H. Hansen, L. Helle, F. Blaabjerg, E. Ritchie, S. Munk-Nielsen, H. Bindner, P. Sørensen, and B. Bak-Jensen, "Conceptual survey of Generators and

Power Electronics for Wind Turbines,” Risø National Laboratory, Roskilde, Denmark, Dec. 2001.

- [17] The Inside of a Wind Turbine [online] Available: <http://energy.gov/eere/wind/inside-wind-turbine-0> [Accessed: November, 2014].
- [18] F. Iov and F. Blaabjerg, “Power electronics control of wind energy in distributed power systems,” Department of Energy Technology, Aalborg University, Denmark.
- [19] EN 50160 ed. 2 - "Voltage characteristics of electricity supplied by public distribution networks," English version 2007.
- [20] IEC 61400-21, "Wind turbine generator system - Part 21: Measurement and assessment of power quality characteristics of grid connected wind turbines", 2008.
- [21] "IEEE Std. 519-1992", IEEE Recommended Practices and Requirements for Harmonic Control in Electric Power Systems, 1993.
- [22] P. Lipnicki and T. M. Stanciu, “Reactive power control for wind power plant with STATCOM” Institute of Energy Technology, Aalborg University, Denmark Master Thesis 2010.
- [23] “Elektrik piyasası şebeke yönetmeliğinde değişiklik yapılmasına ilişkin yönetmelik” Resmi Gazete, 3 January 2013, Number: 28517.
- [24] S. Grunau and F.W. Fuchs, " Effect of wind-energy power injection into weak grids," in Proc. Generation Transmission and Distribution, 2006, pp.599-609.
- [25] F. Blaabjerg and Z. Chen “Power Electronics for Modern Wind Turbines” Synthesis Lectures On Power Electronics #1, Institute of Energy Technology, Aalborg University, Denmark.
- [26] R. Teodorescu, M. Liserre, and P. Rodriguez, “Grid Converters for Photovoltaic and Wind Power Systems” Wiley, 2011.
- [27] S. Khomfoi and L. M. Tolbert “Multilevel Power Converters” Chapter31, The University of Tennessee.

- [28] F. Blaabjerg, M. Liserre, and K. Ma, "Power electronics converters for wind turbine systems," *IEEE Trans. Ind. Appl.*, vol. 48, no. 2, pp. 708–719, Mar./Apr. 2012.
- [29] Z. Chen, J. M. Guerrero, and F. Blaabjerg "A review of the state of the art of power electronics for wind turbines", *IEEE Trans. Power Electron.*, vol.24, no.8, pp.1859 -1875, Aug. 2009.
- [30] Wind energy market share [online] Available: <http://www.enercon.de/en-en/247.htm> [Accessed: November, 2014].
- [31] Standard slip ring generator for doubly-fed concept from 1.5-3.6 MW, "AMK/L series," brochure, last access on [November 2014].
- [32] High speed PM generator series for full converter concept from 1.5 MW upwards, "AMG 500 and 560 series," brochure, last access on [November 2014].
- [33] Wind power generators - high speed PM generator, "HS-PMG," product note, last access on [November 2014].
- [34] ENERCON wind energy converters, product overview, last access on [November 2014].
- [35] GE power conversion, "Generators 2,500 to 80,000 kVA up to 22,000 Volts," brochure, last access on [November 2014].
- [36] Siemens Wind Turbine SWT-6.0-154 [online] Available: <http://www.energy.siemens.com/hq/en/renewable-energy/wind-power/platforms/d6-platform/wind-turbine-swt-6-0-154.htm> [Accessed: November, 2014].
- [37] Siemens Wind Turbine SWT-4.0-130 [online] Available: <http://www.energy.siemens.com/hq/en/renewable-energy/wind-power/platforms/g4-platform/wind-turbine-swt-4-0-130.htm> [Accessed: November, 2014].
- [38] Siemens Wind Turbine SWT-3.6-120 [online] Available: <http://www.energy.siemens.com/hq/en/renewable-energy/wind-power/platforms/g4-platform/wind-turbine-swt-3-6-120.htm> [Accessed: November, 2014].
- [39] Siemens Wind Turbine SWT-3.3-130 [online] Available: <http://www.energy.siemens.com/hq/en/renewable-energy/wind-power/platforms/d3-platform/wind-turbine-swt-3-3-130.htm> [Accessed: November, 2014].

- [40] Siemens Wind Turbine SWT-3.2-113 [online] Available: <http://www.energy.siemens.com/hq/en/renewable-energy/wind-power/platforms/d3-platform/wind-turbine-swt-3-2-113.htm> [Accessed: November, 2014].
- [41] ABB low-voltage wind turbine converters, “ACS800 0.6 to 6 MW,” brochure, last access on [November 2014].
- [42] ABB low-voltage wind turbine converters, “ACS880 800 kW - 8 MW,” brochure, last access on [November 2014].
- [43] Mitsubishi IGBT Modules, “CM2400HCB-34N,” datasheet, last access on [November 2014].
- [44] Fuji IGBT Modules, “1MBI2400U4D-170,” datasheet, last access on [November 2014].
- [45] ABB IGBT Modules, “5SNA 2400E170305,” datasheet, last access on [November 2014].
- [46] Infineon IGBT Modules, “FZ2400R17HP4_B29,” datasheet, last access on [November 2014].
- [47] The 10 Biggest Wind Turbines in the World [online] Available: <http://www.windpowermonthly.com/10-biggest-turbines> [Accessed: November, 2014].
- [48] The world’s 10 biggest wind turbines [online] Available: <http://www.power-technology.com/features/featurethe-worlds-biggest-wind-turbines-4154395/> [Accessed: November, 2014].
- [49] The five-level converter, “ANPC-5L technology and the ACS 2000 drive,” brochure, last access on [November 2014].
- [50] F. Blaabjerg, R. Teodorescu, M. Liserre, and A. V. Timbus, “Overview of Control and Grid Synchronization for Distributed Power Generation Systems” *IEEE Trans. Ind. Electron.*, vol. 53, no. 5, pp.1398-1409, Oct. 2006.
- [51] J. Dannehl, M. Liserre, and F. W. Fuchs, “Filter-Based Active Damping of Voltage Source Converters with *LCL* Filter” *IEEE Trans. Ind. Electron.*, vol. 58, no. 8, pp. 3623-3633, Aug. 2011.

- [52] J. Dannehl, C. Wessels, and F. W. Fuchs, "Limitations of voltage-oriented PI current control of grid-connected PWM rectifiers with *LCL*-filters," *IEEE Trans. Ind. Electron.*, vol. 56, no. 2, pp. 380–388, Feb. 2009.
- [53] A. A. Rockhill, M. Liserre, R. Teodorescu, and P. Rodriguez, "Grid-Filter Design for a Multimegawatt Medium-Voltage Voltage-Source Inverter," *IEEE Trans. Ind. Electron.*, vol.58, no.4, pp.1205,1217, April 2011.
- [54] R. Teodorescu, F. Blaabjerg, M. Liserre, and A. Dell'Aquila, "A stable three-phase *LCL*-filter based active rectifier without damping," *Industry Applications Conference, 2003, Conference Record of the*, vol.3, no., pp.1552, 1557 vol.3, 12-16 Oct. 2003.
- [55] J. Dannehl, F. W. Fuchs, and P. B. Thogersen, "PI state space current control of grid-connected PWM converters with *LCL* filters," *IEEE Trans. Power Electron.*, vol. 25, no. 9, pp. 2320–2330, Sep. 2010.
- [56] E. Kantar, "Design and control of PWM converter with *LCL* type filter for grid interface of renewable energy systems" Master Thesis, 2014.
- [57] F. Iov , R. Teodorescu , F. Blaabjerg , B. Andersen , J. Birk, and J. Miranda "Grid code compliance of grid-side converter in wind turbine systems", *Proc. IEEE PESC*, pp.1 -7 2006.
- [58] AVX medium power film capacitors for power applications [online] Available: <http://www.avx.com/docs/masterpubs/mdpwrflm.pdf> [Accessed: November, 2014].
- [59] Electronicon, "PK16TM and E61 high density dc film capacitors," datasheet, last access on [November 2014].
- [60] E. Twining and D. G. Holmes, "Grid current connected regulation of a three-phase voltage source inverter with an *LCL* input filter," *IEEE Trans. Power Electron.*, vol. 18, no. 3, pp. 888–895, May 2003.
- [61] V. Kaura and V. Blasko, "Operation of a phase locked loop under distorted utility conditions," *IEEE Trans. Ind. Appl.*, Vol. 33, No. 1, pp. 58-63, Jan./Feb. 1997.

- [62] L. R. Limongi, R. I. Bojoi, C. Pica, F. Profumo, and A. Tenconi, "Analysis and comparison of phase locked loop techniques for grid utility applications," in *Proc. PCC APOS, Nagoya, Japan, 2007*, pp. 674–681.
- [63] M. Liserre, F. Blaabjerg, and A. Dell'Aquila, "Step-by-step design procedure for a grid-connected three-phase PWM voltage source converter," *International Journal of Electronics*, vol. 91, no. 8, pp. 441–460, Aug 2004.
- [64] N. Hoffman, F. W. Fuchs, and J. Dannehl, "Models and effects of different updating and sampling concepts to the control of grid connected PWM converters - A study based on discrete time domain analysis," in *Proc. IEEE European Conference on Power Electronics (EPE), Birmingham, UK, 2011*.
- [65] V. Blasko and V. Kaura, "A novel control to actively damp resonance in input LC filter of a three-phase voltage source converter," *IEEE Trans. Ind. Appl.*, vol.33, no.2, pp.542,550, Mar/Apr 1997.
- [66] S. G. Parker, B. P. McGrath, and D. G. Holmes, "A general discrete time model to evaluate active damping of grid converters with *LCL* filters," *Power Electronics Conference (IPEC-Hiroshima 2014 - ECCE-ASIA), 2014 International*, vol., no., pp.2019,2026, 18-21 May 2014.
- [67] A. M. Hava, R. J. Kerkman, and T. A. Lipo, "Simple analytical and graphical methods for carrier-based PWM-VSI drives," *IEEE Trans. Power Electron.*, vol.14, no.1, pp.49,61, Jan 1999.
- [68] J. Holtz, "Pulsewidth modulation for electronic power conversion," *Proc. IEEE*, vol. 82, no. 8, pp. 1194–1214, Aug. 1994
- [69] A. M. Hava and E. Ün, "Performance analysis of reduced common-mode voltage PWM methods and comparison with standard PWM methods for three-phase voltage-source inverters," *IEEE Trans. Power Electron.*, vol.24, no.1, pp.241,252, Jan. 2009.
- [70] A. M. Hava and N. O. Çetin, "A generalized scalar PWM approach with easy implementation features for three-phase, three-wire voltage-source inverters," *IEEE Trans. Power Electron.*, vol.26, no.5, pp.1385,1395, May 2011.

- [71] B. Terzic, G. Majic, and A. Slutej, "Stability analysis of three-phase PWM converter with *LCL* filter by means of nonlinear model," in *Automatika* vol.51, no.3, pp.221-232, 2010.
- [72] A. Julean, "Active damping of *LCL* filter resonance in grid connected applications" Master Thesis, 2009.
- [73] Mitsubishi Heavy Industries, "Mitsubishi Wind Turbine Generator," MWT62/1.0 datasheet, last access on [November 2014].
- [74] Fresh Wind from an Ancient Land (Wind Power in Turkey) [online] Available: http://www.siemens.com/innovation/apps/pof_microsite/_pof-spring-2013/_html_en/wind-energy-in-turkey.html [Accessed: November, 2014].